THE PHYSICAL REVIEW

VOLUME 86 Second Series NUMBER

APRIL 15, 1952

Published for the

AMERICAN PHYSICAL SOCIETY

by the

AMERICAN INSTITUTE OF PHYSICS

Lancaster, Pa., and New York

THE PHYSICAL REVIEW

A journal of experimental and theoretical physics established by E. L. Nichols in 1893

Published by the American Institute of Physics
for the

AMERICAN PHYSICAL SOCIETY

Officers

President

J. H. VAN VLECK
Harvard University
Cambridge, Massachusetts

Vice-President

ENRICO FERMI
Institute for Nuclear Studies
University of Chicago
Chicago 37, Illinois

Secretary

K. K. DARROW
Bell Telephone Laboratories
Office:
Columbia University
New York 27, New York

Treasurer

G. B. PEGRAM
Columbia University
New York 27, New York

Local Secretary
for the Pacific Coast

J. KAPLAN
University of California at Los Angeles
Los Angeles, California

Managing Editor

S. A. GOUDSMIT
Brookhaven National Laboratory
Upton, Long Island
New York

BOARD OF EDITORS

Editor

S. A. GOUDSMIT

Associate Editors

HARVEY BRACKETT — M. GOLDHABER — W. P. ALLIS
R. F. CHRISTY — R. HOFSTADTER — F. G. MARKHAM
C. L. CRITCHFIELD — A. W. LAWSON — W. E. PARKINS
M. DEUTSCH — A. PAIS — CONYERS HERRING
T. H. JOHNSON — R. SERBER — H. W. LEWINTER
BRUNO ROSSI — C. H. TOWNES — ARNOLD NORDSIECK

Manuscripts for publication should be submitted to S. A. Goudsmit, Brookhaven National Laboratory, Upton, Long Island, New York. The authors' institutions are requested to pay a publication charge of $6 per page which, if honored, entitles them to 100 free reprints. Instructions will be sent with galley proofs.

Proof and all correspondence concerning papers in the process of publication should be addressed to the Publication Manager, American Institute of Physics, 57 East 55 Street, New York 22, New York.

Subscription Price

United States and Canada $15.00
Elsewhere $17.00

Back Numbers[1]

Yearly back number rate when complete year is available:
Prior to 1949: $20.00
Thereafter: $27.00

Single copies: $2.00 each, prior to July, 1929;
$1.00 each, July, 1929–December, 1941;
$2.00 each, January, 1942–December, 1946;
$1.00 each, January, 1947–December, 1948;
$1.25 each, thereafter.
General index, 1893–1930: $4.00.

Subscriptions, renewals, and orders for back numbers should be addressed to the American Institute of Physics, 57 East 55 Street, New York 22, New York.

Changes of address in the case of members of the American Physical Society should be addressed to the Treasurer; in the case of other subscribers to the American Institute of Physics.

[1] Set Ruhl's Index of Physics Department, Cornell University, Ithaca, New York.

The Physical Review is published semi-monthly at Prince and Lemon Streets, Lancaster, Pennsylvania.

Entered as second-class matter October 6, 1948, at the Post Office at Lancaster, Pennsylvania, under the Act of March 3, 1879.

Acceptance for mailing at special rate of postage provided for in paragraph (d-2), section 34.40, P. L. & R. of 1948, authorized January 20, 1949.

THE
PHYSICAL REVIEW

A journal of experimental and theoretical physics established by E. L. Nichols in 1893

SECOND SERIES, VOL. 86, NO. 2 APRIL 15, 1952

A New Kind of Radio Propagation at Very High Frequencies Observable over Long Distances

D. K. BAILEY, *National Bureau of Standards, Washington, D. C.*
R. BATEMAN, *National Bureau of Standards, Washington, D. C.*
L. V. BERKNER,* *Carnegie Institution of Washington, Washington, D. C.*
H. G. BOOKER, *Cornell University, Ithaca, New York*
G. F. MONTGOMERY, *National Bureau of Standards, Washington, D. C.*
E. M. PURCELL, *Harvard University, Cambridge, Massachusetts*
W. W. SALISBURY,† *Collins Radio Company, Cedar Rapids, Iowa*
AND
J. B. WIESNER, *Massachusetts Institute of Technology, Cambridge, Massachusetts*

(Received August 31, 1951)

The discovery and some results of a preliminary investigation of a new type of weak vhf propagation by means of the ionosphere is reported. This form of propagation appears to be observable over ranges out to about 2000 kilometers from the transmitter but is likely to be masked by other kinds of propagation at distances much less than about 1000 kilometers. The initial experiments on a frequency of 49.8 Mc/sec reveal the uninterrupted presence of observable signal over a test path of 1245 kilometers, irrespective of season, time of day, or geomagnetic disturbance, though showing dependence in intensity on these factors, and possibly on the meteor activity as well.

Some preliminary speculations suggest that the mechanism of this type of propagation may be scattering caused by ever-present irregularities in the *E* region, and an approximate transmission equation is derived in terms of parameters describing inhomogeneities in the *E* region. Measured signal intensities during periods of hf radio fadeouts associated with solar flares never show any reduction in signal. On the contrary, there is usually an enhancement of signal intensity accompanied by a simultaneous weakening of the background noise. This result suggests strongly that the signals are returned from a part of the *E* region near or just below the absorption region for ordinary hf radio waves.

I. INTRODUCTION

THE propagation of vhf radio waves (frequencies of 30 to 300 Mc/sec) to distances substantially beyond the horizon has been observed for many years. These observations can nearly always be attributed to one of two causes. At short and intermediate ranges, special conditions prevailing at times in the troposphere usually provide the explanation. Propagation to greater distances is usually attributable to ionospheric reflections. Very high values of the *F*2-layer critical frequency account satisfactorily for occasional cases of fairly strong fields at distances of several thousand kilometers, while sporadic *E*-layer ionization often accounts for erratic but strong fields out to distances of the order of 2000 kilometers. These occasional types of ionospheric reflections are practically never observed at great distances for frequencies much above about 100 Mc/sec. It is the object of this paper to describe a type of long-distance ionospheric propagation at vhf such as might be expected from a weak sporadic *E* region which is not sporadic, being apparently present at all times.

It is well known from the work of Ratcliffe[1,2] and co-workers that the distribution of ionization in the ionosphere has a fine structure capable of producing incoherent scattering. Even under quiet ionospheric conditions there are turbulent motions in the ionosphere

* Now with Associated Universities, Inc., Upton, Long Island, New York.
† Now with University of California, Berkeley, California.

[1] J. A. Ratcliffe and J. L. Pawsey, Proc. Cambridge Phil. Soc. **29**, 301 (1933).
[2] J. A. Ratcliffe, Nature **162**, 9 (1948).

which lead to fading of single "rays" quite apart from fading due to interference between two or more rays. Might it not be that scattering arising from turbulence in the ionosphere could be detected at vhf when other forms of ionospheric transmission are absent? A similar phenomenon has come to light in recent years in connection with tropospheric propagation, and a theory to explain it has been presented by Booker and Gordon.[3]

In Sec. II of this paper this theory is adapted to calculate ionospheric scattering at vhf. Section III describes preliminary measurements undertaken as a result of the encouraging calculations given in Sec. II. The phenomenon thereby uncovered is described more fully in Secs. IV and V.

II. TRANSMISSION EQUATION—THEORETICAL SPECULATIONS

Before presenting and discussing results it is useful to consider the theoretical deductions which were made in advance of the initial experimentation concerning ionospheric scattering of very high frequency radio waves caused by irregularities (perhaps attributable to turbulence) in the spatial distribution of electron density. The starting point is the formula for the scattering cross section, per unit volume, of an inhomogeneous dielectric, given in reference 3:

$$\sigma=\frac{\langle(\Delta\epsilon/\epsilon)^2\rangle_{Av}(2\pi l/\lambda)^3\sin^2\chi}{\lambda[1+(4\pi l/\lambda)^2\sin^2\frac{1}{2}\theta]^2}, \tag{1}$$

where σ = the scattered power per unit incident power density, per unit macroscopic element of volume, and per unit solid angle in a direction making an angle θ with the direction of incidence; l = scale of fine structure; χ = the angle between the incident electric field and the direction of scatter, and $\sin^2\chi$ is a polarization factor, henceforth omitted since it is nearly unity in the application to be considered; $\langle(\Delta\epsilon/\epsilon)^2\rangle_{Av}$ = mean squared variation in dielectric constant; and λ = wavelength of radio wave.

To apply Eq. (1) to the ionosphere it is necessary to use the value of ϵ appropriate to an ionized medium. Neglecting the effect of the earth's magnetic field, this leads to

$$\sigma=\frac{\langle(\Delta N/N)^2\rangle_{Av}(2\pi l/\lambda_N)^2}{\lambda_N[1+(4\pi l/\lambda)^2\sin^2\frac{1}{2}\theta]^2}, \tag{2}$$

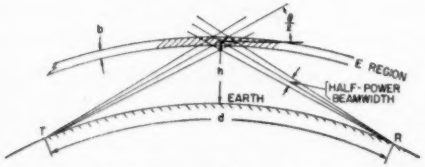

FIG. 1. Geometry of E-region scattering.

[3] H. G. Booker and W. E. Gordon, Proc. Inst. Radio Engrs. 38, 401 (1950).

where $\langle(\Delta N/N)^2\rangle_{Av}$ = mean square fractional variation in electron density from average, and λ_N = plasma wavelength corresponding to the mean electron density N. More detailed discussions of what is involved in Eq. (2) will be given in a separate paper. For the present application only directions of scatter outside the main scattering beam are of interest, that is, values of θ for which

$$(4\pi l/\lambda)\sin\tfrac{1}{2}\theta\gg 1. \tag{3}$$

Subject to this condition Eq. (2) becomes

$$\sigma=\left\langle\left(\frac{\Delta N}{N}\right)^2\right\rangle_{Av}\left(\frac{\lambda}{\lambda_N}\right)^4\frac{1}{32\pi l\sin^4\frac{1}{2}\theta}. \tag{4}$$

Expressed in terms of the wave frequency f and the plasma frequency f_N corresponding to the mean electron density, Eq. (4) becomes

$$\sigma=\left\langle\left(\frac{\Delta N}{N}\right)^2\right\rangle_{Av}\left(\frac{f_N}{f}\right)^4\frac{1}{32\pi l\sin^4\frac{1}{2}\theta}. \tag{5}$$

Now if P_t is the total power in a transmitted beam passing at an angle of $\frac{1}{2}\theta$ through a slab of ionization of thickness b (see Fig. 1) having an irregular or turbulent character described by l and $\langle(\Delta N/N)^2\rangle_{Av}$, the scattered power P_s per unit solid angle is given by

$$P_s=(\sigma b/\sin\tfrac{1}{2}\theta)P_t. \tag{6}$$

Therefore,

$$P_s=\left\langle\left(\frac{\Delta N}{N}\right)^2\right\rangle_{Av}\left(\frac{f_N}{f}\right)^4\frac{b}{32\pi l\sin^5\frac{1}{2}\theta}P_t. \tag{7}$$

Equation (7) may now be applied to scattering in a layer of vertical thickness b above the midpoint of a path, assuming identical transmitting and receiving antennas, each with an equivalent aperture area A, or a gain $G=4\pi A/\lambda^2$ over an isotropic antenna. If the received power is P_r, then the transmission equation is approximately

$$\frac{P_r}{P_t}=\left\langle\left(\frac{\Delta N}{N}\right)^2\right\rangle_{Av}\left(\frac{f_N}{f}\right)^4\frac{Ab}{D^2l}\frac{1}{8\pi\sin^5\frac{1}{2}\theta}, \tag{8}$$

where D is the ray length; for reasonably oblique scatter-paths D is practically identical with the surface transmission-distance d (Fig. 1). Equation (8) is based on the assumption of a scattering volume within which the scattering parameters are everywhere those appropriate to the midpoint of the path.

With the aid of the approximate transmission equation above, it was possible to make some numerical calculations. The following rough characteristics for the scattering medium were considered plausible: b = 5 km; h = height of scattering layer (assuming E region) = 100 km; $\langle(\Delta N/N)^2\rangle_{Av}=10^{-4}$, corresponding to simple turbulence as deduced from hf radio fading (reference 2); l = 100 meters, corresponding to hf fading correla-

tion observed with separated receivers (reference 1); $f_N = 1.5$ Mc/sec (presumed variable diurnally, seasonally, etc.). Making reasonable assumptions regarding antenna dimensions and transmitter power, it was deduced that received signals at a distance of 1500 kilometers would easily exceed cosmic noise. This type of propagation would, however, be limited by the curvature of the earth to distances of the order of, say, 2000 kilometers. With decreasing distances below about 1000 kilometers, the type of propagation should be increasingly masked by tropospheric propagation.

III. THE EXPERIMENTAL ARRANGEMENT AND INITIAL RESULTS

The need for experimental work was evident, and on January 23, 1951, experimental transmissions were initiated to test these views. The experimental arrangements are summarized as follows:

transmitter location:	Cedar Rapids, Iowa (Collins Radio Company)
receiver location:	Sterling, Virginia (National Bureau of Standards)
path length:	1245 km
frequency:	49.800 Mc/sec
emission:	continuous wave
rf power to antenna:	23 kw (estimated). This has varied slightly and in a known manner during the course of the experimental program.
antennas:	Identical horizontal rhombics at both terminals as follows: height: 41.2 feet; leg length: 500 feet; tilt angle: 83° (i.e., rhombic interior angles of 166° and 14°); gain over dipole at same height ≈18 db; main lobe maximum at vertical angle of 7°; main lobe total width to half-power points: vertical section 5°, horizontal section 6°; calculated effective area: $A = 299$ m².
receiver noise figure:	3 db
receiver band width:	nominally 3 kc/sec

For this arrangement of the transmitter and receiver, and for an ionospheric height of 100 km, $D = 1270$ km, $\frac{1}{2}\theta = 11.8°$, and from Eq. (8)

$$P_r = 2.0 \times 10^{-12} \text{ watt}$$
$$= -117 \text{ dbw (117 db below 1 watt).}$$

For the same distance and system, the inverse distance received power would be 3.5×10^{-5} watt $= -45$ dbw, which indicates a transmission loss of 72 db.

The initial tests were intended to cover a period of a few days. Signals were received, and it was immediately apparent to all concerned that the tests should be continued in order to establish the seasonal as well as diurnal characteristics of the received signals and to establish the behavior of the signals during ionospheric disturbances. During the first hf fadeout that occurred after the commencement of the vhf observations, it was found that the vhf signals were strengthened. This surprising result at least confirmed ionospheric influence. To make possible an extended observing program, it was necessary to suspend the tests temporarily so that the transmitting installation could be placed in suitable condition for prolonged and continuous operation.

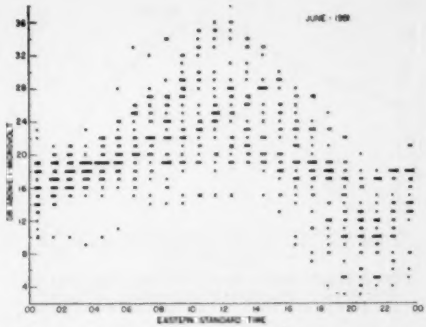

FIG. 2. Mass plot of hourly signal intensities, June, 1951, for 49.8 Mc/sec transmission over a distance of 1245 km. Crosses represent interpolated values for times of sporadic E transmission.

IV. EXPERIMENTAL RESULTS

During the experimental transmissions there was no failure resulting from conditions in the medium to receive easily measurable signals over the 1245-kilometer experimental path. Occasional loss of record occurred when terminal equipment or power failed.

A striking characteristic of the received signal, which exhibits fading characteristics that seem to follow a Rayleigh distribution, is the presence at all times of day of random heterodyne whistles, mostly descending in pitch and caused by reflections from the moving head of ionization accompanying meteors in their passage through the E region and somewhat lower parts of the atmosphere. These whistles, which vary enormously in intensity according to the geometry of the situation, and the size and velocity of the meteor, are relatively infrequent and of long duration in the evening, and frequent and of short duration in the dawn hours, as would be expected from their meteoric nature. Furthermore, a meteor giving a strong whistle often causes the signal level to rise abruptly (sometimes to the extent of blocking the receiver) and remain high for periods ranging from several seconds to occasionally a minute or more. This enhancement of the signal accompanying strong meteor whistles practically always endures till long after the end of the whistle, and it is certain that this meteoric residue makes an important contribution to the mean signal level.

The received signal power was recorded automatically using an averaging circuit having a time constant of 12 seconds. This long time constant facilitated the reduction of the data by averaging the rapid fading of the signal before recording. The stability of the receiving equipment was such that calibration was necessary only once each day. The estimated average of the

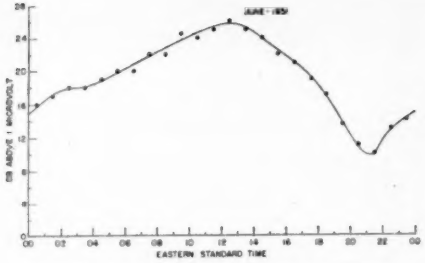

FIG. 3. Hourly median signal intensities, June, 1951, for 49.8 Mc/sec transmission over a distance of 1245 km.

recorded signal level was tabulated by hourly periods. Corrections, when necessary, were made to the results to allow for variation in the transmitted power. Figure 2 is a mass plot showing the individual hourly measurements for the month of June. Figure 3 represents their medians. The crosses plotted in Fig. 2 represent cases when the recorder nearly saturated, presumably because of the occurrence of strong sporadic *E* propagation during part or all of the hour. The signal level represented by a cross is that estimated by interpolation for the hour, had sporadic *E* been absent. The data are shown on a decibel scale with zero corresponding to one microvolt open circuit antenna voltage. One microvolt corresponds to a received available power of 4.2×10^{-16} watt or -154 dbw.

In general the signal power received exhibits a maximum near midday and a pronounced minimum between 20 and 22 hours EST. Following the minimum, the signal increases fairly steadily throughout the night. There appears to be some tendency for a second maximum in the forenoon.

The records were examined with interest and care during times of magnetic disturbances and hf radio fadeouts (now known commonly as SID's or sudden ionospheric disturbances). During the most severe magnetic disturbance for which observations were available, the signal showed pronounced enhancement. During more moderate disturbances the signal occasionally shows some enhancement, or appears normal. Analysis of hf records during April and May shows 24 SID's occurring between 1½ hours after sunrise, and 1½ hours before sunset, for which simultaneous vhf data are available on the experimental path. In seventeen of these events, the received signal showed a noticeable enhancement ranging from 3 to 9 db during the period of the SID, as established by fadeout observations on ordinary hf radio communication paths. This enhancement becomes noticeable within a few minutes of the onset of the SID and the received signal returned to normal at the end of the fadeout. In the remaining seven cases of hf fadeout, the records of received vhf signal did not show any certain enhancement, but rather appeared to be normal. An important point is that there was no evidence of any weakening of the signal for these cases.

Figure 4(a) shows the vhf record during an SID on May 19, and Fig. 4(b) the simultaneous hf fadeout record (also made at Sterling) of a station located in Ohio operating at 6.08 Mc/sec. Figure. 4(a) shows that the transmissions were interrupted for a two-minute period every half-hour. During these interruptions the level of background noise was recorded. The diminution in recorded background noise (mainly cosmic) during the SID shown in Fig. 4(b) can be seen.

These results are a strong indication that the received signal is returned from a part of the *E* region below the level of maximum ionization, and perhaps even from below the absorbing region, sometimes referred to as the *D* region. This is further substantiated by earlier and independent observations of cosmic noise, which suffers a small but noticeable attenuation at the same frequency during SID's.

Some additional experimental results are of interest. Observations of the received signal power using a horizontal dipole antenna at different heights between 12 and 80 feet indicated no pronounced height-gain effects, and were inconclusive as regards evidence on predominant angle of arrival of the signal. Comparison of the instantaneous signals received on spaced antennas showed a correlation coefficient of about 0.5 for a 50-foot separation and about 0.3 for a 100-foot separation. The

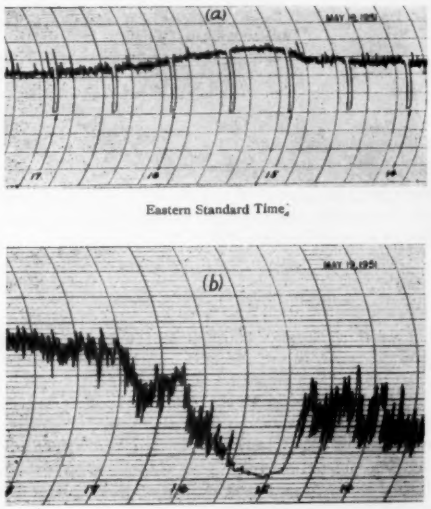

FIG. 4. (a) Record showing enhancement of signal intensity for 49.8 Mc/sec transmission over a distance of 1245 km during the SID of May 19, 1951, commencing at 1450 EST and ending approximately at 1615 EST. (b) Record showing SID fadeout for 6.08 Mc/sec transmission over a distance of 525 km during the SID of May 19, 1951, commencing at 1450 EST and ending at approximately 1615 EST.

observations with 100-foot separation were not, however, made simultaneously with those at 50 feet. Observations made simultaneously with vertical and horizontal dipoles at the same height above ground showed that the horizontal polarization of the transmitted signal was largely preserved.

Other observations of the experimental transmission have been made, notably by the Bell Telephone Laboratories, by the School of Electrical Engineering, Cornell University, and by the radio amateurs. It is evident from these observations that the signal can be received reliably over a considerable area. During a short period, receiving tests were made in Bermuda at a distance of 2600 kilometers from Cedar Rapids. Signals were received sporadically, and only at times associated with intense sporadic E ionization at some point along the path.

V. DISCUSSION OF RESULTS IN TERMS OF THE TRANSMISSION EQUATION

In the pre-experimental calculations it was estimated that the received signal power corresponding to a critical frequency $f_N = 1.5$ Mc/sec and coming from a height of about 100 kilometers would be 2.0×10^{-12} watt. Inspection of records revealed that the maximum median values of received signal varied, in the middle of the day, from about 10 to about 26 db above 1 microvolt corresponding to power levels of 4.2×10^{-15} and 1.7×10^{-13} watt. These values occurred at times when the critical frequency of the E layer varied from 3.2 to 3.6 Mc/sec. It is thus apparent that the pre-experimental speculations were too optimistic. The behavior of the signal during SID's suggests that the ionospheric region responsible for the transmission is lower than 100 kilometers. In such a lower region, the values of f_N corresponding to the electron densities normally present are substantially lower, though probably exhibiting similar diurnal and seasonal variations. It would appear, therefore, that the transmission equation of Eq. (8) could better account for the experimental results if values of f_N were used which are appropriate to the lower heights from which the signals seem to come.

The earlier reference to the contribution made by meteors to the received signal can now be further elaborated. The pronounced evening minimum of signal intensity and the tendency to show a fairly steady rise during the night, together with the tendency for a second maximum in the forenoon, seen in Fig. 5, besides the midday maximum, suggest that the received signal can be thought of as resulting from at least two distinct causes. The diurnal variation of the solar ultraviolet radiation produces a midday maximum. The ionization produced by meteors varies roughly sinusoidally with a maximum at about 0600 hours local time, and a minimum at about 18 hours local time. A superposition of the diurnal variations associated with these two causes, with relative importance varying according to season, etc., would account reasonably for many features of the observed monthly diurnal trends.

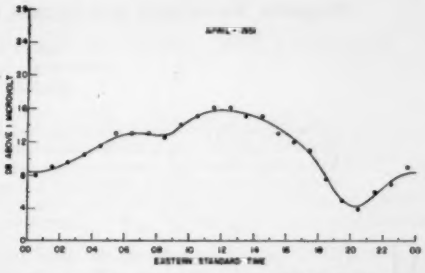

FIG. 5. Hourly median signal intensities, April, 1951, for 49.8 Mc/sec transmission over a distance of 1245 km.

VI. PLANS FOR FUTURE EXPERIMENTS

Results of experimentation to date, while of considerable interest, leave many questions unanswered. For future experimentation tests of frequency and distance dependence are envisaged, together with more detailed study of the nature of the received signal, with the objective of improving understanding of the transmission mechanism and the parameters of the medium.

ACKNOWLEDGMENT

The pre-experimental study discussed in this paper was supported by the International Broadcasting Division of the Department of State and carried out at the Massachusetts Institute of Technology. The continuing program is being conducted cooperatively by the National Bureau of Standards and the Massachusetts Institute of Technology. The early assistance and continuing cooperation of the Collins Radio Company is acknowledged.

Magnetic Resonance in a System Containing Two Magnetic Sublattices*

ROALD K. WANGSNESS
U. S. Naval Ordnance Laboratory, White Oak, Maryland
(Received January 7, 1952)

The normal frequencies are calculated classically including exchange, demagnetizing, and anisotropy fields. Ferromagnetic and antiferromagnetic resonance conditions are shown to be special cases of a general formula which is obtained. Conditions under which the Kittel ferromagnetic frequency should be applicable to the two-lattice system are discussed, as well as the possibility of resonance in the exchange field.

MAGNETIC resonance experiments have been recently performed on some antiferromagnetic materials[1] and various ferrites.[2] The results of the latter have been generally discussed from the point of view of Kittel's theory of ferromagnetic resonance.[3] Néel, however, has proposed an explanation of the magnetic properties of the ferrites based on the fact that the magnetic ions are unequally distributed between the two different crystallographic sites available to them.[4] The resulting model is one in which the magnetic system consists of two generally dissimilar interpenetrating sublattices which presumably are antiferromagnetically coupled; in addition, there are interactions among the members of each sublattice. As a result, it is of interest to determine the resonant frequencies of this particular system in order to learn how the standard ferromagnetic formula[3] is modified, if at all.

Actually, we shall give below a classical calculation of the normal frequencies of a general two-sublattice system subject to a static magnetic field. One can thus expect to obtain a unified derivation of the ferro-, ferri-,[4] and antiferromagnetic resonance conditions, the simple two-sublattice model of an antiferromagnet having proven to be quite adequate in many respects.[5] The effects of the anisotropy energy will be described by the familiar artifice of effective demagnetizing factors,[3] which will, however, be separately defined for each sublattice.

THE NORMAL FREQUENCIES

The static external field H_0 defines the positive z axis of our coordinate system. The magnetizations of the two sublattices, $\mathbf{M}_1$ and $\mathbf{M}_2$, are assumed to be predominantly along this direction. This provides sufficient generality as Keffer and Kittel[6] have discussed ways of extending results of this case to situations in which H_0 and the magnetizations are no longer nearly parallel.

Let the molecular field coefficients be λ_{11}, λ_{22}, $\lambda_{12}=\lambda$, and the common demagnetizing factors be N_x, N_y, N_z. The effective demagnetizing factors resulting from anisotropy are N_{1x}, N_{1y}, $\cdots$, N_{2z}. If $\mathbf{H}_1$, $\mathbf{H}_2$ are the resultant fields acting on the sublattices, we have

$$\begin{aligned}\mathbf{H}_1=H_0\mathbf{k}&+\lambda_{11}\mathbf{M}_1+\lambda\mathbf{M}_2-N_x(M_{1x}+M_{2x})\mathbf{i}\\&-N_y(M_{1y}+M_{2y})\mathbf{j}-N_z(M_{1z}+M_{2z})\mathbf{k}\\&-N_{1x}M_{1x}\mathbf{i}-N_{1y}M_{1y}\mathbf{j}-N_{1z}M_{1z}\mathbf{k}\end{aligned}\quad(1)$$

with a similar expression for $\mathbf{H}_2$.

If we neglect damping, the equations of motion are $d\mathbf{M}_i/dt=\gamma\mathbf{M}_i\times\mathbf{H}_i$, where γ is the electron gyromagnetic ratio and $i=1, 2$. Substituting for $\mathbf{H}_i$ from (1) and neglecting product terms like $M_{1x}M_{2y}$,[7] we find that $M_{iz}\simeq\text{const}=M_i$. If we now assume that all of the remaining components are proportional to $e^{i\omega t}$, write ω for ω/γ, let $M=M_1+M_2=\chi_{\|}H_0$, and solve the secular equation which is obtained from the equations of motion, we find the two normal frequencies to be given by

$$2\omega^2=F\pm[F^2-4(A_xB_x-C_xD_x)(A_yB_y-C_yD_y)]^{\frac{1}{2}},\quad(2)$$

where

$$\left.\begin{aligned}&F=A_xA_y+B_xB_y+C_xD_y+C_yD_x,\\&A_j=H_0+(\lambda-N_z)M+E_j,\\&B_j=H_0+(N_j-N_z)M+E_j,\\&2C_j=(N_{1j}-N_{1z})M_1-(N_{2j}-N_{2z})M_2,\\&D_j=(N_j-\lambda)(M_1-M_2)+C_j,\\&2E_j=(N_{1j}-N_{1z})M_1+(N_{2j}-N_{2z})M_2;\quad j=x, y.\end{aligned}\right\}\quad(3)$$

We note that Eq. (2) contains explicitly only that molecular field coefficient, λ, which describes the interaction between the sublattices, although λ_{11} and λ_{22} will in general be involved in the expressions for M_1 and M_2. We shall consider below a few important special cases of Eq. (2)

THE FERROMAGNETIC CASE

If $C_j=0$ or can be neglected, we find at once from (2) and (3) that

* Supported in part by the ONR.

[1] Trounson, Bleil, Wangsness, and Maxwell, Phys. Rev. **79**, 542 (1950); C. A. Hutchison, Jr., private communication; Okamura, Torizuka, and Kojima, Phys. Rev. **82**, 285 (1951).

[2] W. H. Hewitt, Jr., Phys. Rev. **73**, 1118 (1948); H. G. Beljers, Physica **14**, 629 (1949); L. R. Bickford, Jr., Phys. Rev. **78**, 449 (1950); Yager, Galt, Merritt, and Wood, Phys. Rev. **80**, 744 (1950); T. Okamura and V. Torizuka, Phys. Rev. **83**, 847 (1951); D. W. Healy, Jr., Technical Report No. 135 (Cruft Laboratory, Harvard University, Cambridge, Massachusetts, 15 August, 1951); Okamura, Torizuka, and Kojima, Phys. Rev. **84**, 372 (1951).

[3] C. Kittel, Phys. Rev. **73**, 155 (1948); J. H. Van Vleck, Phys. Rev. **78**, 266 (1950).

[4] L. Néel, Ann. phys. **3**, 137 (1948).

[5] J. H. Van Vleck, J. Chem. Phys. **9**, 85 (1941); J. phys. et radium **12**, 262 (1951).

[6] F. Keffer and C. Kittel, Phys. Rev. **85**, 329 (1952).

[7] J. H. Van Vleck, Phys. Rev. **74**, 1168 (1948).

$$\omega_+^2=A_xA_y=[H_0+(\lambda-N_x)M+(N_{1z}-N_{1x})M_1]\times[H_0+(\lambda-N_z)M+(N_{1y}-N_{1z})M_1], \quad (4)$$

$$\omega_-^2=B_xB_y=[H_0+(N_x-N_z)M+(N_{1z}-N_{1x})M_1]\times[H_0+(N_y-N_z)M+(N_{1y}-N_{1z})M_1]. \quad (5)$$

If one replaces $(N_{1j}-N_{1z})M_1$ by $(N_j^e-N_z^e)M$, Eq. (5) becomes just the frequency obtained in the Kittel theory of ferromagnetic resonance.[3] With the fact that $C_j=0$, this replacement can always be made by defining these "reduced" demagnetizing factors by

$$(N_j^e-N_z^e)^{-1}=(N_{1j}-N_{1z})^{-1}+(N_{2j}-N_{2z})^{-1}. \quad (6)$$

Thus we have seen that, formally at least, for our double sublattice system to be correctly described by the Kittel theory, its nature must be such that the condition $(N_{1j}-N_{1z})M_1=(N_{2j}-N_{2z})M_2$ can be fulfilled.

The frequency given by (4) does not seem to have been previously discussed for the case of ferromagnetic resonance. If the Curie temperature is greater than about 0.1°K, the "exchange field," λM, will be the dominant part of (4). For ordinary ferromagnetic materials where $M\approx10^3$ oersted, $\lambda M\approx10^7$ oersted, so that the detection of this resonance at ordinary field strengths would require a frequency $\omega_+\approx10^{14}$ sec^{-1}, corresponding to a wavelength ≈0.02 mm. For the simple case $D_j=0$, and in the normal mode associated with ω_+, $\mathbf{M}_1$ and $\mathbf{M}_2$ precess about the z axis in the same sense but exactly out of phase; the projection of either on the xy plane sweeps out an ellipse with $(A_x/A_y)^{\frac{1}{2}}$ as the ratio of major and minor axes. Since $\mathbf{M}_1$ and $\mathbf{M}_2$ are not parallel in this mode, the exchange field on $\mathbf{M}_1$ as a result of $\mathbf{M}_2$ will also not be parallel to $\mathbf{M}_1$; hence there will be a nonzero torque on $\mathbf{M}_1$ caused by the exchange which leads to this high frequency precession. In contrast to this, $\mathbf{M}_1$ and $\mathbf{M}_2$ precess in phase in the corresponding mode associated with ω_-, the ratio of axes being $(B_x/B_y)^{\frac{1}{2}}$.

THE ANTIFERROMAGNETIC CASE

An important class of frequencies corresponds to A_j, B_j, and C_j being independent of j and equal, respectively, to A, B, and C. Equation (2) then becomes

$$2\omega^2=A^2+B^2+C(D_x+D_y)\pm\{(A+B)^2[(A-B)^2+2C(D_x+D_y)]+C^2(D_x-D_y)^2\}^{\frac{1}{2}}. \quad (7)$$

I. $A=B$

This assumption includes the case of an antiferromagnet at 0°K for which the "anisotropy field" H_A is along the z axis and equal for both lattices; to show this let us assume that

$$-N_{1x}M_1=N_{2x}M_2=H_A; \quad N_{1x,y}=N_{2x,y}=0 \quad (8)$$

so that $E_j=0$. At 0°K we have $M_1=-M_2=M_s$, making $M=0$, and $-\lambda M_1=\lambda M_2=H_E$ since λ is here assumed to be negative; H_E is then the "exchange field." Equation (3) then gives

$$A=B=H_0, \quad C=H_A, \quad D_j=H_A+2H_E+2N_jM_s.$$

Therefore,

$$\omega^2=H_0^2+H_A[H_A+2H_E+(N_x+N_y)M_s]\pm H_0\{4H_A[H_A+2H_E+(N_x+N_y)M_s]+(H_A/H_0)^2(N_x-N_y)^2M_s^2\}^{\frac{1}{2}}. \quad (9)$$

This agrees with the result of Keffer and Kittel,[6] and as they remark, if $N_x=N_y=N$, it simplifies considerably and yields

$$\omega=H_0\pm[H_A(2H_E+H_A+2NM_s)]^{\frac{1}{2}}. \quad (10)$$

It is interesting to note that Eq. (10) clearly shows that the demagnetizing effects enter formally at least into the resonance condition for a sphere, in contrast to the ferromagnetic case. If we neglect the demagnetizing effects, we obtain the resonance condition first given by Nagamiya[8] and Kittel.[9]

II. $A\neq B$, D_j Independent of j

In this case, Eq. (7) gives

$$\omega=\tfrac{1}{2}(A+B)\pm[\tfrac{1}{4}(A-B)^2+CD]^{\frac{1}{2}}.$$

This result is suitable for discussing a ferri- or antiferromagnetic material at an arbitrary temperature. If, for simplicity, we neglect demagnetizing effects and use the assumptions of Eqs. (8), we find that[9]

$$\omega=H_0+\tfrac{1}{2}\lambda M\pm\{H_A[H_A-\lambda(M_1-M_2)]+\tfrac{1}{4}(\lambda M)^2\}^{\frac{1}{2}}. \quad (11)$$

DISCUSSION

These few examples serve to illustrate the generality of the result given by (2) and how (2) can be simplified by appropriate and judicious choice of conditions—corresponding to what can then be often obtained experimentally. Explicit formulas for other cases can be found similarly, and it is here that suitable knowledge or guesses about the microscopic properties will be of value. If we compare (4) and (5), we see that the Kittel ferromagnetic frequency which can be obtained from (5) is the only specific case discussed here which turns out to be explicitly independent of the interlattice coupling coefficient, λ, since it requires only a knowledge of M, while in (4), λM is predominant for ordinary fields and Curie temperatures. Having noted this, it is then perhaps easier to understand why the Kittel ferromagnetic theory has been used so successfully in the analysis of results obtained with ferrites[10] in spite of the presumed antiferromagnetic character of λ; on the other hand, it is hard to visualize such a situation for

[8] T. Nagamiya, Prog. Theor. Phys. **6**, 350 (1951).
[9] C. Kittel, Phys. Rev. **82**, 565 (1951).
[10] This statement should probably be qualified somewhat as the values of g obtained for ferrites by using Eq. (5) are often surprisingly larger than 2, e.g., as high as 2.49 (see Healy, reference 2), which may be a result of using resonance conditions not strictly applicable to ferrites.

which $C_J=0$ as would be required. In this connection, it is interesting to observe that the "ferromagnetic case" can be included in the assumptions of Eqs. (8) by letting $M_2=0$. Then both (5) and (11) lead to the same frequency H_0+H_A, if one first assumes a sphere in (5), and then neglects demagnetizing effects as was done in (11).

I wish to thank Dr. J. S. Smart for several interesting discussions on the magnetic properties of the ferrites, and Dr. L. R. Maxwell for his continued interest.

PHYSICAL REVIEW VOLUME 86, NUMBER 2 APRIL 15, 1952

The Effects of Configuration Interaction on the Atomic Hyperfine Structure of Gallium*†

G. F. KOSTER‡
Physics Department, Massachusetts Institute of Technology, Cambridge, Massachusetts
(Received December 4, 1951)

The effects on the hyperfine structure of the mixing of higher configurations with the ground configuration $(4s)^2 4p$ of gallium is studied. It is found that the only configuration which need be considered is the $4s4p5s$. A Hartree wave function for the excited $5s$-state of gallium is calculated, and the extent of the mixing of this excited configuration with the ground configuration is determined. The coupling constants for magnetic and electric quadrupole hyperfine structure are computed with the use of the wave function for the ground state of gallium including the excited configuration. The determination of quadrupole moments from atomic hyperfine structure measurements is discussed and various methods of making this calculation compared. Beside the determination of the quadrupole moments of gallium, the quadrupole moments of aluminum, indium, and chlorine are estimated.

I. INTRODUCTION

THE splitting of the fine structure levels of an atom due to the hyperfine interactions can be written (in units of $\sec^{-1}$) as[1]

$$\left(\frac{E}{h}\right)_F=\frac{aC}{2}+b\left\{\frac{(3/4)C(C+1)-I(I+1)J(J+1)}{2IJ(2I-1)(2J-1)}\right\}, \quad (1)$$

where

$$C=F(F+1)-I(I+1)-J(J+1).$$

Here J is the total electronic angular momentum, I is the nuclear spin, and F is the total angular momentum of the nucleus and the electrons. The first term in Eq. (1) arises from the interaction of the magnetic dipole moment of the nucleus and the magnetic field at the nucleus because of the surrounding electrons. The second term arises from the interaction of the electric field at the nucleus, due to the electrons, and the electric quadrupole moment of the nucleus. The quantities a and b are two coupling constants which measure the strength of the interaction between the nucleus and the atomic electrons. They are given by[2]

$$a=-(\mu/IJ)\langle\textstyle\sum_i H_{iz}\rangle_{Av} \quad (2)$$

$$b=-e^2Q\langle\textstyle\sum_i(3\cos^2\theta_i-1)/r_i^3\rangle_{Av}. \quad (3)$$

Here μ is the magnetic moment of the nucleus, and H_{iz} is the z component of the magnetic field at the nucleus caused by the ith electron. The summation extends over all the atomic electrons. Q is the quadrupole moment of the nucleus and θ_i, ϕ_i, and r_i are the spherical coordinates of the ith electron. The average values which appear in these formulas are to be taken for the electrons in the state $m_J=J$. If we assume that our electronic wave function arises from a single configuration, and that this configuration contains one electron outside of closed shells, we find that[2]

$$a=(\mu\mu_0/I)[2L(L+1)/J(J+1)]\langle 1/r^3\rangle_{Av}\mathfrak{F} \quad (4)$$

where $\mu_0=eh/4\pi mc$. Here L is the orbital angular momentum of the electron outside the closed shells and the average value is taken with respect to this electron's wave function. $\mathfrak{F}$ is a small relativistic correction (~ 1) given by Casimir.[2] The constant b is given by[2]

$$b=e^2Q(2L/2L+3)\langle 1/r^3\rangle_{Av}\mathfrak{R}, \quad (5)$$

if we assume that the wave function is separable into a product of a radial and an angular part. $\mathfrak{R}$ is another small relativistic correction given by Casimir. For the atoms with one p-electron outside of closed shells, we

* Supported by the ONR and the Research Laboratory in Electronics.
† Part of a thesis submitted in partial fulfillment of the requirements for the Ph.D. degree at the Massachusetts Institute of Technology.
‡ Present address: Brookhaven National Laboratory, Upton, New York.
[1] H. Kopfermann, *Kernmomente* (Akademische Verlagsgesellschaft M.B.H., Leipzig, 1940), Chapter I.
[2] H. B. G. Casimir, *On the Interaction between Atomic Nuclei and Electrons* (Teylers Tweede Genootschap, Haarlem, 1936).

find, on the basis of Eqs. (4) and (5), (setting $J=\frac{3}{2}$) that the quadrupole moment can be expressed in terms of the experimentally measured value of the ratio of a to b.

$$Q=(8/3)(b/a)(\mu\mu_0/e^2I)(\mathfrak{F}/\mathfrak{G}). \quad (6)$$

These equations also predict that

$$(a_{\frac{3}{2}})/(a_{\frac{1}{2}})=5(\mathfrak{F}_{\frac{3}{2}})/(\mathfrak{F}_{\frac{1}{2}}). \quad (7)$$

The use of Eq. (6) to determine the quadrupole moment tas first suggested by Davis, Feld, Zabel, and Zacharias,[3] who also noticed that for aluminum, gallium, and indium the ratio in Eq. (7) differed considerably from the value predicted. This leads one to suspect that the assumptions underlying the use of Eq. (6) to determine the quadrupole moments of substances may be in error. The aspect which we shall investigate is the assumption that the ground-state wave function of these atoms can be taken as though it arises from a single configuration. In particular, we shall consider the effect of configuration interactions on the ground states of gallium. Fermi and Segrè[4] first carried out a calculation of configuration interaction for thallium, which shows similar anomalies.

II. CALCULATION OF THE MIXING OF CONFIGURATIONS

The mixing of configurations is caused by the electrostatic interactions between electrons. The Hamiltonian for the electrons in an atom, neglecting magnetic interactions, is given by

$$H=\sum_i -\nabla_i^2-\frac{2Z}{r_i}+\frac{1}{2}\sum_{i\neq j}\frac{2}{r_{ij}}, \quad (8)$$

where r_{ij} represents the distance between two electrons and Z is the atomic number of the atom. The units in the equation are atomic units.[5] There exist matrix elements of this Hamiltonian between different configurations. The choice of gallium for a calculation of configuration interaction was governed by the existence of numerical wave functions for the ground configuration of this atom[6] and of accurate hyperfine structure measurements in both the $^2P_{\frac{3}{2}}$ and the metastable $^2P_{\frac{1}{2}}$ states. Matrix elements of the Hamiltonian [Eq. (8)] vanish if the states arising from the two configurations differ in either multiplicity, total orbital angular momentum (L), total angular momentum (J), or parity. Since the ground state of gallium is a ^2P-state, we need only consider ^2P-states arising from excited configurations as being mixed with the ground configuration. (The ground configuration of gallium is $(1s)^2(2s)^2(2p)^6(3s)^2(3p)^6(3d)^{10}(4s)^24p$.) In our choice of an excited configuration, we are also limited to those which are strongly coupled to the nucleus and which are energetically close to the $(4s)^24p$ configuration. The $4s4p5s$ configuration has all the desired properties. It can produce relatively great hyperfine structure splittings since it contains two s electrons outside of closed shells which need no longer, because of the exclusion principle, have paired spins. The only other nearby configuration which has the desired properties is the $4s4p4d$ configuration. We shall not include it in our calculations since it does not interact as strongly with the $(4s)^24p$ configuration[7] and also because it is further removed in energy from the $(4s)^24p$ configuration than is the $4s4p5s$ configuration. The $4s4p5s$ configuration can give rise to two different ^2P-states, depending on how the spins of the $4s$, $4p$, and $5s$ electrons are combined to give a system of angular momentum $S=\frac{1}{2}$. Let us denote these two states by $\Psi^1(^2P_J)$ and $\Psi^2(^2P_J)$. The $(4s)^24p$ ^2P-state we shall denote by $\Psi^0(^2P_J)$. Our ground-state wave function must be written, if configuration interaction is included, as

$$\Phi(^2P_J)=\alpha_0\Psi^0(^2P_J)+\alpha_1\Psi^1(^2P_J)+\alpha_2\Psi^2(^2P_J). \quad (9)$$

The α's are calculated by minimizing the expectation value of the Hamiltonian [Eq. (8)] subject to the constraint

$$\alpha_0^2+\alpha_1^2+\alpha_2^2=1. \quad (10)$$

Details of this calculation, along with the specific forms of the wave functions $\Psi^i(^2P_J)$ for $J=\frac{3}{2}$, $\frac{1}{2}$ in terms of one electron wave functions, are contained in Appendix I. There we find that

$$\alpha_0=0.995; \quad \alpha_1=0.0307; \quad \alpha_2=-0.102 \quad (11)$$

for both $J=\frac{1}{2}$ and $J=\frac{3}{2}$.

III. EFFECT ON THE HYPERFINE COUPLING CONSTANTS

The effect that this mixture of configurations has on the magnetic hyperfine coupling constant, a, is now sought. The coupling constants for the states $J=\frac{1}{2}$ and $J=\frac{3}{2}$ will be given by

$$\begin{aligned} a_{\frac{1}{2}}&=-(\mu/IJ)\int \Phi^*(^2P_{\frac{1}{2}}, m_J=\tfrac{1}{2}) \\ &\quad\times\textstyle\sum_i H_{is}\Phi(^2P_{\frac{1}{2}}, m_J=\frac{1}{2})d\tau_1\cdots d\tau_{31} \\ a_{\frac{3}{2}}&=-(\mu/IJ)\int \Phi^*(^2P_{\frac{3}{2}}, m_J=\tfrac{3}{2}) \\ &\quad\times\textstyle\sum_i H_{is}\Phi(^2P_{\frac{3}{2}}, m_J=\frac{3}{2})d\tau_1\cdots d\tau_{31}. \end{aligned} \quad (12)$$

These integrals can be reduced to a sum of integrals over one electron coordinates by use of the explicit

[3] Davis, Feld, Zabel, and Zacharias, Phys. Rev. 76, 1076 (1949).
[4] E. Fermi and E. Segrè, Rendiconti della R. Academia d'Italia 4, 18 (1933–XI); E. Fermi and E. Segrè, Z. Physik 82, 729 (1933).
[5] D. R. Hartree, Reports on Progress in Physics 11, 113 (1946–1947). The unit of energy is Rhc. R is the Rydberg.
[6] Hartree, Hartree, and Manning, Phys. Rev. 59, 299 (1941).
[7] The off-diagonal terms for the matrix of the interaction of this configuration with the ground configuration are about 1/20 of the similar terms for the $4s4p5s$ configuration. This result was obtained by using Slater's analytic wave functions [J. C. Slater, Phys. Rev. 36, 57 (1930)].

forms of $\Psi^i(^2P_J)$ in Appendix I. For the integrals of single electron wave functions with $l=1$, we shall use as the operator for the magnetic field at the nucleus due to a single electron[8]

$$\mathbf{H}_i=-(2\mu_0/r_i^3)\{\mathbf{L}_i-\mathbf{S}_i+[3(\mathbf{S}_i\cdot\mathbf{r}_i)/r_i^2]\mathbf{r}_i\}. \quad (13)$$

For the expectation values involving s electrons, use of this operator would not yield finite results. Instead we shall use the relativistic expression for the magnetic field at the nucleus[8]

$$\mathbf{H}_i=e(\boldsymbol{\alpha}\times\mathbf{r}_i)/r_i^3. \quad (14)$$

Here α_x, α_y, and α_z are the well-known matrices appearing in the Dirac equation.[9] For a four-component wave function, we shall use the approximation of a Dirac wave function by a Schrödinger wave function for a central field given by Darwin.[9,10]

$$\psi_{4s}(\text{Dirac})=\left[\left(\frac{ih}{4\pi mc}\right)\cos\theta\frac{\partial}{\partial r}\psi_{4s};\ \left(\frac{ih}{4\pi mc}\right)(\sin\theta)e^{i\varphi}\frac{\partial}{\partial r}\psi_{4s};\psi_{4s;0}\right]. \quad (15)$$

This expression will replace $\psi_{4s}\alpha$.

TABLE I. Quadrupole moments of Al, Ga, and In (all quadrupole moments in units of 10^{-24} cm^2).[a]

Nucleus	Z	Z_i	I	II	III	IV
Al^{27}	13	10.0	0.156	0.153	0.155	
Ga^{69}	31	27.4	0.232	0.178	0.186	0.189
Ga^{71}	31	27.4	0.146	0.112	0.118	0.119
In^{115}	49	45.1	1.17	0.759	0.834	
In^{113}	49	45.1	1.15	0.746	0.820	

[a] The shielding correction (see reference 15, Table II) would increase the values of the quadrupole moments by a factor of 1.105 for Al, 1.032 for In, and 1.046 for Ga.

If we use the explicit forms of the angular parts of our one-electron wave functions as given in Condon and Shortley,[11] we can evaluate the integrals (12) using the s wave function (15) and the form of the magnetic field at the nucleus given in Eqs. (13) and (14). We find

$$\begin{aligned}a_{\frac{1}{2}}=&-(2\mu\mu_0/3I)\{\alpha_0^2[-(8/5)\mathfrak{F}\langle 1/r^3\rangle]\\&+\alpha_2^2[-(8/5)\mathfrak{F}\langle 1/r^3\rangle]\\&+\alpha_1^2[-(16\pi/9)\{s^2(0)+\sigma^2(0)\}-(32/15)\mathfrak{F}\langle 1/r^3\rangle]\\&+2\alpha_1\alpha_2[(1/3)^{\frac{1}{2}}(8\pi/3)\{s^2(0)-\sigma^2(0)\}]\\&+2\alpha_1\alpha_0[(1/6)^{\frac{1}{2}}(16\pi/3)s(0)\sigma(0)]\}\\a_{\frac{3}{2}}=&-(2\mu\mu_0/I)\{\alpha_0^2[-(8/3)\mathfrak{F}\langle 1/r^3\rangle]\\&+\alpha_2^2[-(8/3)\mathfrak{F}\langle 1/r^3\rangle]\\&+\alpha_1^2[(16\pi/27)\{s^2(0)+\sigma^2(0)\}-(8/3)\mathfrak{F}\langle 1/r^3\rangle]\\&+2\alpha_1\alpha_2[-(1/3)^{\frac{1}{2}}(8\pi/9)\{s^2(0)-\sigma^2(0)\}]\\&+2\alpha_1\alpha_0[-(1/6)^{\frac{1}{2}}(16\pi/9)s(0)\sigma(0)]\}.\end{aligned} \quad (16)$$

In these equations, $s(0)$ represents the value of the $4s$ wave function at $r=0$ and $\sigma(0)$ represents the value of the $5s$ wave function at $r=0$. We have also that

$$\langle 1/r^3\rangle=\int_0^\infty[P_{4p}^2(r)/r^3]dr.$$

We notice that terms in addition to that appearing in Eq. (4) have appeared in the coupling constant arising from the unpaired spins in the excited configuration.

The quadrupole coupling constant will be given by

$$b=-e^2Q\int\Phi^*(^2P_{\frac{1}{2}},m_J=\tfrac{3}{2})\textstyle\sum_i[(3\cos\theta_i-1)/r_i^3]\times\Phi(^2P_{\frac{1}{2}},m_J=\tfrac{3}{2})d\tau_1\cdots d\tau_{31}. \quad (17)$$

Performing the indicated integrations, we find that

$$b=e^2Q(2/5)\langle 1/r^3\rangle(\alpha_0^2+\alpha_1^2+\alpha_2^2)\mathfrak{R}. \quad (18)$$

This yields, by use of the normalization condition [Eq. (10)], that

$$b=e^2Q(2/5)\mathfrak{R}\langle 1/r^3\rangle.$$

This is exactly the same form which the coupling constant would have if the configuration interaction were neglected ($\alpha_1=\alpha_2=0$; $\alpha_0=1$). The excited configuration differs from the ground configuration only in that one of the $4s$ electrons is excited to a $5s$ state. The s electrons, because of their spherical symmetry, do not contribute to the quadrupole interaction energy. In this way we can understand this result.

IV. QUADRUPOLE MOMENT OF GALLIUM

In order to determine the quadrupole moment of gallium from the measured value of b, we need the value of $\langle 1/r^3\rangle$. We shall determine the value of this quantity from the measured value of $a_{\frac{1}{2}}$ by estimating $s(0)$ and $\sigma(0)$. We can estimate these quantities by two means. They are given directly from the Hartree $4s$ and $5s$ functions for gallium. This gives the values $s(0)=2.70a_0^{-\frac{3}{2}}$ cm$^{-\frac{1}{2}}$ and $\sigma(0)=0.956a_0^{-\frac{3}{2}}$ cm$^{-\frac{1}{2}}$. a_0 is the Bohr radius. We can also determine these quantities from the formula of Fermi and Segrè[4]

$$[\psi_{ns}{}^0(0)]^2=\frac{1}{a_0{}^3\pi}\frac{Z}{n^{*3}}\frac{dn^*}{dn}\left[\frac{1}{1-\beta^2Z^2}\right]. \quad (19)$$

Here β is the fine structure constant and n^* is defined by the equation

$$E_n=-(R/n^{*2})\text{ cm}^{-1},$$

where E_n is the term energy of the electron under consideration, and R is the Rydberg. Using the Hartree energies for E_n and the estimate of dn^*/dn given by Kopfermann,[1] we find that $s(0)=2.82a_0^{-\frac{3}{2}}$ cm$^{-\frac{1}{2}}$ and $\sigma(0)=1.07a_0^{-\frac{3}{2}}$ cm$^{-\frac{1}{2}}$. These values are in good agreement with those obtained from the Hartree functions.

[8] E. Fermi, Z. Physik **60**, 320 (1930).
[9] L. I. Schiff, *Quantum Mechanics* (McGraw-Hill Book Company, Inc., New York, 1949).
[10] C. G. Darwin, Proc. Roy. Soc. (London) **118**, 654 (1928).
[11] E. U. Condon and G. H. Shortley, *Theory of Atomic Spectra* (Cambridge University Press, London, 1935).

If we insert the Hartree values along with the values of α_0, α_1, and α_2 that we have determined into Eq. (16), we obtain

$$a_{\frac{1}{2}}=-(2\mu\mu_0/I)[-0.280a_0^{-3}-2.67\mathfrak{F}_{\frac{1}{2}}\langle 1/r^3\rangle]$$
$$a_{\frac{1}{2}}=-(2\mu\mu_0/3I)[0.837a_0^{-3}-1.61\mathfrak{F}_{\frac{1}{2}}\langle 1/r^3\rangle]. \quad (20)$$

We notice the effect of the configuration interaction is smaller in the $J=\frac{1}{2}$ state. This is a reflection of the fact that in the $J=\frac{1}{2}$ state the probability of finding an s electron with spin "up" is more nearly equal to the probability of finding it with spin "down" than it was in the $J=\frac{3}{2}$ state. The smaller correction resulting from configuration interaction in this state provides the reason for calculating $\langle 1/r^3\rangle$ from the $J=\frac{3}{2}$ rather than the $J=\frac{1}{2}$ state. For gallium, we have the values[12–14]

Ga^{69}:

$$a_{\frac{1}{2}}=1338.78 \text{ Mc/sec}, \quad a_{\frac{3}{2}}=190.790 \text{ Mc/sec},$$
$$\mu=2.001 \text{ (in nuclear magnetons)}, \quad I=\tfrac{3}{2},$$
$$b=62.518 \text{ Mc/sec}.$$

Ga^{71}:

$$a_{\frac{1}{2}}=1701.05 \text{ Mc/sec}, \quad a_{\frac{3}{2}}=242.424 \text{ Mc/sec},$$
$$\mu=2.543 \text{ nm}, \quad I=\tfrac{3}{2}, \quad b=39.398 \text{ Mc/sec}.$$

Using these values in Eq. (20) for the $J=\frac{1}{2}$ state we find that $\langle 1/r^3\rangle=3.46a_0^{-3}$ cm^{-3} for Ga^{69}. Substituting this value into the formula for the coupling constant for the $J=\frac{3}{2}$ state in (20), we find $a_{\frac{3}{2}}=201$ Mc/sec. Neglecting the configuration interaction, we had $a_{\frac{1}{2}}/a_{\frac{3}{2}}=5.41$. Including the configuration interaction, we find $a_{\frac{1}{2}}/a_{\frac{3}{2}}=6.67$, while the experimental value of this ratio is 7.02.

From the experimental value of b and the value of $\langle 1/r^3\rangle$ that we have determined, we calculate the quadrupole moments of gallium to be[15]

$$Q(Ga^{69})=0.190\times 10^{-24} \text{ cm}^2$$
$$Q(Ga^{71})=0.120\times 10^{-24} \text{ cm}^2.$$

V. QUADRUPOLE MOMENTS OF OTHER NUCLEI

We have four possible ways that we can use to estimate the quadrupole moments of nuclei in other elements with an electronic structure similar to that of gallium.

Method I: From the measured value of $b/a_{\frac{1}{2}}$

$$Q=(8/3)(b/a_{\frac{1}{2}})(\mu\mu_0/e^2I)(\mathfrak{F}_{\frac{1}{2}}/\mathfrak{R}). \quad (21)$$

Method II: From the measured value of $b/a_{\frac{3}{2}}$

$$Q=(40/3)(b/a_{\frac{3}{2}})(\mu\mu_0/e^2I)(\mathfrak{F}_{\frac{3}{2}}/\mathfrak{R}). \quad (22)$$

Method III: The theoretical formula for the fine structure splitting, δ, will be unaffected by this type of configuration interaction. The reason for this is that s electrons do not contribute to the fine structure separations. Exciting an s electron by raising it to an s state with principal quantum number increased by one will, therefore, not change the formula for this splitting. Calculation of the fine structure coupling constant for our many configuration wave function bears out this result. We have that

$$\delta=(3\mu_0^2/e)\langle(1/r)(dV/dr)\rangle\mathfrak{C}. \quad (23)$$

V is the potential in which the electron outside of the spherically symmetric shells moves, and

$$\langle(1/r)(dV/dr)\rangle=\int_0^\infty P_{np}^2(r)(1/r)(dV/dr)dr$$

for elements with one p electron outside of closed shells. $\mathfrak{C}$ is a small relativistic correction given by Casimir.[3] We can define a quantity Z_i by the relation

$$\langle(1/r)(dV/dr)\rangle=Z_i\langle 1/r^3\rangle \quad (24)$$

TABLE II. Quadrupole moments of the chlorine isotopes.[a,b]

Nucleus	Z	Z_i	I	II	III′
Cl^{35}	17	13.7	−0.0789	−0.0778	−0.0782
Cl^{37}	17	13.7	−0.0621	−0.0612	−0.0616

[a] The values of the coupling constants used in this calculation were obtained from a private communication from V. Jaccarino and J. G. King and also from V. Jaccarino and J. G. King, Phys. Rev. **83**, 471 (1951).
[b] The shielding correction (see reference 15, Table III′) would increase the values of the quadrupole moments of Cl by a factor of 1.079.

Z_i can be determined from the formula of Casimir[3]

$$\delta/R=(dn^*/dn)[Z_i^2/n^{*3}L(L+1)]\beta^2, \quad E_n=-n^{*-2}. \quad (25)$$

Here E_n is expressed in Rydbergs and the fine structure splitting in cm^{-1}. From the term values of the configurations $(4s)^2np$ $(n=4, 5, 6, \cdots)$ values of n^* and dn^*/dn are estimated. From the measured value of δ for each of these terms a value of Z_i is calculated by use of Eq. (25). To determine the quadrupole moment, we use the formula

$$Q=(b/\delta)(\mu_0^2/e^2)(15/2)(\mathfrak{C}/\mathfrak{R})Z_i.$$

The values of Z_i for the higher values of n are used in this formula, since the uncertainties in the values of dn^*/dn disappear because this ratio approaches unity as n increases. This method was applied by Renzetti[12] to gallium.

Method IV: This method is the method carried out for gallium in this paper and involves the calculation of the mixing of configurations.

Table I contains the values of the quadrupole moments of elements in the same column of the periodic table as gallium along with the values of Z_i determined by the use of Eqs. (25).

[12] N. A. Renzetti, Phys. Rev. **57**, 753 (1940).
[13] G. E. Becker and P. Kusch, Phys. Rev. **73**, 584 (1948).
[14] J. E. Mack, Revs. Modern Phys. **22**, 64 (1950).
[15] Values of the quadrupole moments in this article do not include shielding corrections of the type considered by R. Sternheimer, Phys. Rev. **84**, 244 (1951); **80**, 102 (1950). This correction, on the basis of Sternheimer's Thomas-Fermi calculation, increases the values of the quadrupole moments of gallium by a factor 1.046.

If we assume that these elements undergo the same type of configuration interaction as gallium, we can expect that method I will yield a value too large whereas method II will yield a value too small. This we can see by noticing that the sign of the correction terms in Eq. (31) is different from the $J=\frac{3}{2}$ state than it is for the $J=\frac{1}{2}$ state.

In Table II are given the quadrupole moments of the chlorine isotopes. Chlorine has one electron missing from a closed p shell, so that all of the methods except method III are applicable except for those changes of sign arising from the fact that we are considering a missing p electron.[3] Method III is not applicable since there is nothing in chlorine similar to the series $(4s)^2np$. Instead of method III, we used a method III′. In this method, we determined the value of Z_i for chlorine by interpolation between the values we obtained for aluminum, gallium, and indium.

VI. CONCLUSION

In gallium, we have seen that the only type of configuration interaction that we must consider is the type in which one of the $4s$ electrons is excited to a $5s$ state. This type of mixing has a large effect on the theoretical value of the magnetic hyperfine coupling constant. In the $J=\frac{3}{2}$ state of the atom, it decreases the value of the coupling constant below the value computed without the inclusion of the interaction. In the $J=\frac{1}{2}$ state, it increases the value of the coupling constant. The inclusion of this type of mixing of configurations does not change the form of either the fine structure or electric quadrupole coupling constants. This mixing of states is able to explain in a quantitative manner the deviation of the measured value of $a_{\frac{1}{2}}/a_{\frac{1}{2}}$ from the theoretical value calculated without the mixing.

We can also draw the conclusion that the hope that $\langle 1/r^3\rangle$ will cancel from the ratio of either $a_{\frac{1}{2}}$ to b or $a_{\frac{1}{2}}$ to b is not realized. The quadrupole moments calculated on the basis of this assumption will be in error. If $a_{\frac{1}{2}}$ is used, a value of the quadrupole moment too large will be obtained. If $a_{\frac{1}{2}}$ is used a value will be obtained which is too small. Since the correction is smaller in the $\frac{1}{2}$ state the value of Q obtained by method II will be more reliable.

Calculation of $\langle 1/r^3\rangle$ from the magnetic hyperfine structure with the inclusion of configuration interaction affords the most reliable method of evaluating this quantity and from it the quadrupole moment of the nucleus. We have also seen that, in the case of gallium, the calculation of $\langle 1/r^3\rangle$ from the observed doublet separation, through the use of Z_i, affords a method which gives a result in good agreement with the value obtained using the configuration interaction.

Since we might expect that the type of configuration interaction will be the same for all elements in the same column of the periodic table, some of the conclusions we have derived for gallium can be applied to these elements. The effect of the configuration interaction is greater the higher the nuclear charge. This we judge from the increase of the deviation of $a_{\frac{1}{2}}/a_{\frac{1}{2}}$ from the value predicted by Eq. (7). We conclude that, in the absence of a quantitative calculation of the mixing of the configurations for these elements, the most reliable method of calculating Q is method III involving the fine structure splitting. In every case for which this calculation was carried out, the value of the quadrupole moment obtained was between the values obtained by methods I and II. This, coupled with the agreement between the value of the quadrupole moment of gallium by method III and the more exact method involving configuration interaction, seems to indicate that is method is fairly reliable.

The author wishes to express his gratitude to Professor B. T. Feld, who suggested this problem and offered much helpful advice during its study. He also wishes to thank Mrs. Neria Ryder for performing many of the numerical computations.

APPENDIX I.

By compounding the spins and the orbital angular momenta of the individual electrons, we find that

$$
\begin{aligned}
&\Psi^0(^2P_{\frac{1}{2}},\ m_J=\tfrac{3}{2})\\
&\quad=\{\psi_{4s}{}^0(1)\alpha(1)\psi_{4s}{}^0(2)\beta(2)\psi_{4p}{}^1(3)\alpha(3)\}\{\text{core}\}\\
&\Psi^1(^2P_{\frac{1}{2}},\ m_J=\tfrac{3}{2})\\
&\quad=\{(\tfrac{1}{6})^{\frac{1}{2}}[\psi_{4s}{}^0(1)\beta(1)\psi_{5s}{}^0(2)\alpha(2)\psi_{4p}{}^1(3)\alpha(3)\\
&\qquad+\psi_{4s}{}^0(1)\alpha(1)\psi_{5s}{}^0(2)\beta(2)\psi_{4p}{}^1(3)\alpha(3)\\
&\qquad-(\tfrac{2}{3})^{\frac{1}{2}}\psi_{4s}{}^0(1)\alpha(1)\psi_{5s}{}^0(2)\alpha(2)\psi_{4p}{}^1(3)\beta(3)]\}\{\text{core}\}\\
&\Psi^2(^2P_{\frac{1}{2}},\ m_J=\tfrac{3}{2})\\
&\quad=\{(\tfrac{1}{2})^{\frac{1}{2}}[\psi_{4s}{}^0(1)\beta(1)\psi_{5s}{}^0(2)\alpha(2)\psi_{4p}{}^1(3)\alpha(3)\\
&\qquad-\psi_{4s}{}^0(1)\alpha(1)\psi_{5s}{}^0(2)\beta(2)\psi_{4p}{}^1(3)\alpha(3)]\}\{\text{core}\}\\
&\Psi^0(^2P_{\frac{1}{2}},\ m_J=\tfrac{1}{2})\\
&\quad=\{(\tfrac{1}{3})^{\frac{1}{2}}\psi_{4s}{}^0(1)\alpha(1)\psi_{4s}{}^0(2)\beta(2)\psi_{4p}{}^0(3)\alpha(3)\\
&\qquad-(\tfrac{2}{3})^{\frac{1}{2}}\psi_{4s}{}^0(1)\alpha(1)\psi_{4s}{}^0(2)\beta(2)\psi_{4p}{}^1(3)\beta(3)\}\{\text{core}\}\\
&\Psi^1(^2P_{\frac{1}{2}},\ m_J=\tfrac{1}{2})\\
&\quad=\{-\tfrac{2}{3}\psi_{4s}{}^0(1)\beta(1)\psi_{5s}{}^0(2)\beta(2)\psi_{4p}{}^1(3)\alpha(3)\\
&\qquad+\tfrac{1}{3}[\psi_{4s}{}^0(1)\beta(1)\psi_{5s}{}^0(2)\alpha(2)\psi_{4p}{}^1(3)\beta(3)\\
&\qquad+\psi_{4s}{}^0(1)\alpha(1)\psi_{5s}{}^0(2)\beta(2)\psi_{4p}{}^1(3)\beta(3)]\\
&\qquad+\tfrac{1}{3}(\tfrac{1}{2})^{\frac{1}{2}}[\psi_{4s}{}^0(1)\beta(1)\psi_{5s}{}^0(2)\alpha(2)\psi_{4p}{}^0(3)\alpha(3)\\
&\qquad+\psi_{4s}{}^0(1)\alpha(1)\psi_{5s}{}^0(2)\beta(2)\psi_{4p}{}^0(3)\alpha(3)]\\
&\qquad-\tfrac{1}{3}(2)^{\frac{1}{2}}\psi_{4s}{}^0(1)\alpha(1)\psi_{5s}{}^0(2)\alpha(2)\psi_{4p}{}^0(3)\beta(3)\}\{\text{core}\}\\
&\Psi^2(^2P_{\frac{1}{2}},\ m_J=\tfrac{1}{2})\\
&\quad=\{(\tfrac{1}{2})^{\frac{1}{2}}[\psi_{4s}{}^0(1)\beta(1)\psi_{5s}{}^0(2)\alpha(2)\psi_{4p}{}^0(3)\alpha(3)\\
&\qquad-\psi_{4s}{}^0(1)\alpha(1)\psi_{5s}{}^0(2)\beta(2)\psi_{4p}{}^0(3)\alpha(3)]\\
&\qquad-(\tfrac{1}{3})^{\frac{1}{2}}[\psi_{4s}{}^0(1)\beta(1)\psi_{5s}{}^0(2)\alpha(2)\psi_{4p}{}^1(3)\beta(3)\\
&\qquad-\psi_{4s}{}^0(1)\alpha(1)\psi_{5s}{}^0(2)\beta(2)\psi_{4p}{}^1(3)\beta(3)]\}\{\text{core}\}.
\end{aligned}
\tag{26}
$$

These wave functions must be antisymmetrized and multiplied by $(1/31!)^{\frac{1}{2}}$ in order to normalize. In Eq. (26) $\alpha(i)$ denotes the spin eigenfunction for the ith electron

with the z component of spin $+\frac{1}{2}$ and $\beta(i)$ the spin eigenfunction with z component of spin $-\frac{1}{2}$. $\psi_{nl}{}^{m_l}(i)$ is the Hartree wave function of θ_i, φ_i, and r_i, with n the radial quantum number, l the orbital angular momentum quantum number, and m_l the z component of orbital angular momentum. By the symbol {core}, we mean the product of the Hartree wave functions with spin for all the core electrons up through the closed shell. $\psi_{nl}{}^{m_l}(i)$ are solutions of the equations

$$(-\nabla^2-Z_p(nl,r)/r)\psi_n{}^{m_l}=-\epsilon_{nl}\psi_{nl}{}^{m_l} \tag{27}$$

and are written in the form

$$\psi_{nl}{}^{m_l}=[P_{nl}(r)/r]\Theta(l,m_l;\theta)\Phi_{m_l}(\varphi). \tag{28}$$

Θ and Φ_{m_l} are the usual spherical harmonics.[11] $Z_p(nl,r)/r$ is the potential arising from the nuclear charge at the origin and the charge distribution described by the spherical parts of the wave functions of all but the electron under consideration. Ψ^1 and Ψ^2 differ in that in Ψ^1 the spins of the $4s$ and $5s$ electrons are combined to form a system with angular momentum 1 which is then combined with the spin of the $4p$ electron to form a system of angular momentum $\frac{1}{2}$. In Ψ^2 the spins of the $4s$ and $5s$ electrons form a system of angular momentum 0 which forms, upon combination with the spin of the $4p$ electron, a system with angular momentum $\frac{1}{2}$.

We determine the α's by the condition that

$$\int\Phi^*({}^2P_{\frac{1}{2}})[H-E]\Phi({}^2P_{\frac{1}{2}})d\tau_1\cdots d\tau_{31} \qquad d\tau_i=r_i^2\sin\theta_i d\theta_i d\varphi_i dr_i \tag{29}$$

should be a minimum subject to the normalization requirement

$$\alpha_0^2+\alpha_1^2+\alpha_2^2=1. \tag{30}$$

The integrations in Eq. (29) include a summation over the spin coordinates.

In order to calculate the integrals appearing in (29) use was made of the Hartree wave functions for gallium. The $5s$ radial wave function necessary for the calculation was calculated numerically by the methods used by Hartree.[5] The potential $Z_p(5s,r)/r$ which is necessary for this calculation was taken to be identical with $Z_p(4s,r)/r$. This is a good approximation since one would not expect that exciting a $4s$ electron to a $5s$ state would seriously alter the charge distribution of the remaining 30 electrons. This also has the advantage that now the $4s$ and $5s$ wave functions are orthogonal. Table III contains the values of $P_{5s}(r)$ along with the value of the normalization integral and the energy value ϵ_{5s}.

TABLE III. The $5s$ Hartree wave function for gallium (not normalized).

r	$P_{5s}(r)$	r	$P_{5s}(r)$	r	$P_{5s}(r)$
0.000	0.000	1.6	−5.90	26.0	0.07
0.005	0.427	1.8	−6.10	28.0	0.04
0.010	0.724	2.0	−5.84	30.0	0.02
0.015	0.914	2.2	−5.22	32.0	0.01
0.020	1.016	2.4	−4.34	34.0	0.00
0.025	1.046	2.6	−3.26		
0.030	1.017	2.8	−2.07		
0.035	0.943	3.0	−0.81		
0.040	0.832	3.2	0.47		
		3.4	1.74		
0.05	0.537	3.6	2.98		
0.06	0.187	3.8	4.16	$\epsilon_{5s}=0.201$	
0.07	−0.180	4.0	5.27		
0.08	−0.535				
0.09	−0.861	4.5	7.67		
0.10	−1.15	5.0	9.52	$\int_0^\infty P_{5s}{}^2(r)dr=873$	
		5.5	10.82		
0.12	−1.57	6.0	11.62		
0.14	−1.78	6.5	12.00		
0.16	−1.81	7.0	12.03		
0.18	−1.67	7.5	11.80		
0.20	−1.41	8.0	11.35		
0.22	−1.07	8.5	10.76		
0.24	−0.66	9.0	10.07		
0.26	−0.22	9.5	9.33		
0.28	0.23	10.0	8.55		
0.30	0.67	10.5	7.78		
		11.0	7.03		
0.35	1.65	11.5	6.31		
0.40	2.38	12.0	5.63		
0.45	2.82	12.5	4.99		
0.50	2.99	13.0	4.41		
0.55	2.92				
0.60	2.67	14.0	3.40		
		15.0	2.58		
0.7	1.79	16.0	1.93		
0.8	0.64	17.0	1.43		
0.9	−0.58	18.0	1.05		
1.0	−1.76	19.0	0.77		
1.1	−2.84	20.0	0.56		
1.2	−3.77	21.0	0.40		
1.3	−4.54	22.0	0.29		
1.4	−5.15	24.0	0.14		

By varying the α's to minimize (29) we are led to the set of linear homogeneous equations

$$\begin{aligned}(H_{00}-E)\alpha_0+H_{01}\alpha_1+H_{02}\alpha_2&=0\\ H_{10}\alpha_0+(H_{11}-E)\alpha_1+H_{12}\alpha_2&=0\\ H_{20}\alpha_0+H_{21}\alpha_1+(H_{22}-E)\alpha_2&=0.\end{aligned} \tag{31}$$

Here

$$H_{ij}=\int\Psi^{i*}H\Psi^j d\tau_1\cdots d\tau_{31}\quad i,j=0,1,2. \tag{32}$$

In order that these equations have a nontrivial solution, the determinant of the coefficients of the α's must vanish. If we make the substitution $H_{00}-E=-E'$, and also simplify our matrix elements by use of the equations that $\psi_{nl}{}^{m_l}$ satisfy and the definition of $Z_p(nl,r)$, we find that this determinant can be written as

$$\begin{vmatrix}-E' & G_{01} & G_{02}\\ G_{10} & G_{11}-E' & G_{12}\\ G_{20} & G_{21} & G_{22}-E'\end{vmatrix}=0. \tag{33}$$

TABLE IV. Values of $R^k(n^al^a, n^bl^b; n^cl^c, n^dl^d)$.

n^a	l^a	n^b	l^b	n^c	l^c	n^d	l^d	R^k
4	0	1	0	1	0	4	0	0.00419
4	0	2	0	2	0	4	0	0.00645
4	0	3	0	3	0	4	0	0.0185
4	0	5	0	5	0	4	0	0.00807
4	0	2	1	2	1	4	1	0.00800
4	0	3	1	3	1	4	1	0.0219
4	0	4	1	4	1	4	1	0.126
4	0	3	2	3	2	4	2	0.0408
4	0	1	0	1	0	5	0	0.00148
4	0	2	0	2	0	5	0	0.00227
4	0	3	0	3	0	5	0	0.00628
4	0	2	1	2	1	5	1	0.00283
4	0	3	1	3	1	5	1	0.00753
4	0	4	1	4	1	5	1	−0.0273
4	0	3	2	3	2	5	2	0.0129
5	0	1	0	1	0	5	0	0.000524
5	0	2	0	2	0	5	0	0.000800
5	0	3	0	3	0	5	0	0.00213
5	0	2	1	2	1	5	1	0.000997
5	0	3	1	3	1	5	1	0.00260
5	0	4	1	4	1	5	1	0.0383
5	0	3	2	3	2	5	2	0.00422

Here the G's are given by

$$\begin{aligned}
G_{11}&=\epsilon_{4s}-\epsilon_{5s}-2K_{4s,0}{}^{5s,0}+K_{5s,0}{}^{4p,1}+3K_{4s,0}{}^{4p,1}\\
&\quad+2\sum{}'[K_{4s,0}{}^{n'l',m'}-K_{5s,0}{}^{n'l',m'}]\\
G_{12}&=G_{21}=(3)^{\frac{1}{2}}[K_{4s,0}{}^{4p,1}-K_{4s,0}{}^{4p,1}]\\
G_{22}&=\epsilon_{4s}-\epsilon_{5s}+2K_{4s,0}{}^{5s,0}+K_{4s,0}{}^{4p,1}-K_{5s,0}{}^{4p,1}\\
&\quad+2\sum{}'[K_{4s,0}{}^{n'l',m'}-K_{5s,0}{}^{n'l',m'}]\\
G_{10}&=G_{01}=(6)^{\frac{1}{2}}N_{4p,1}\\
G_{20}&=G_{02}=(2)^{\frac{1}{2}}[N_{4p,1}+2\sum{}'N_{n'l',m'}],
\end{aligned}\tag{34}$$

where

$$\begin{aligned}
K_{nl,m}{}^{n'l',m'}&=\int\psi_{nl}{}^{*m}(1)\psi_{n'l'}{}^{*m'}(2)[1/r_{12}]\\
&\quad\times\psi_{nl}{}^{m}(2)\psi_{n'l'}{}^{m'}(1)d\tau_1d\tau_2\\
N_{nl,m}&=\int\psi_{5s}{}^{*0}(1)\psi_{nl}{}^{*m}(2)[1/r_{12}]\\
&\quad\times\psi_{4s}{}^{0}(2)\psi_{nl}{}^{m}(1)d\tau_1d\tau_2.
\end{aligned}\tag{35}$$

In Eqs. (34) the primed summations extend over the core electrons through the closed d shell. The integrals in Eqs. (35) are all of the well-known type[11]

$$\begin{aligned}
&\int\psi_{n^al^a}{}^{*m_l{}^a}(1)\psi_{n^bl^b}{}^{*m_l{}^b}(2)[1/r_{12}]\psi_{n^cl^c}{}^{m_l{}^c}(1)\\
&\qquad\times\psi_{n^dl^d}{}^{m_l{}^d}(2)d\tau_1d\tau_2\\
&=\delta(m_l{}^a+m_l{}^b,\,m_l{}^c+m_l{}^d)\sum_{k=0}c^k(l^a,m^a;l^a,m^c)\times\\
&\quad c^k(l^d,m_l{}^d;l^b,m_l{}^b)R^k(n^a,l^a,n^b,l^b,n^c,l^c,n^d,l^d).
\end{aligned}\tag{36}$$

This result is obtained by expanding $1/r_{12}$ in spherical harmonics. The c^k are the known result[11] of integration over angles and

$$\begin{aligned}
&R^k(n^a,l^a,n^b,l^b,n^c,l^c,n^d,l^d)\\
&\quad=\int_0^\infty\int_0^\infty(r_<{}^k/r_>{}^{k+1})P_{n^al^a}(1)P_{n^bl^b}(2)P_{n^cl^c}(1)\\
&\qquad\times P_{n^dl^d}(2)dr_1dr_2,
\end{aligned}\tag{37}$$

where $r_<$ is the smaller and $r_>$ the greater of r_1 and r_2. Table IV contains a list of the values of those integrals which were necessary in the calculation. Numerical integration using Simpson's rule was used to obtain these values from our numerical wave function.

Solving the determinant for the lowest value of E' and our set of homogeneous equations for the α's, we find

$$\begin{aligned}
-E'&=0.00894,\\
\alpha_0=0.995,\quad\alpha_1&=0.0307,\quad\alpha_2=-0.102.
\end{aligned}\tag{38}$$

We can now see that the mixing of the configurations is small and that the energy of the ground state is only lowered slightly. The α's for the linear combination of Ψ's for the $J=\frac{1}{2}$ state are exactly the same as those we have calculated for the $J=\frac{3}{2}$ state.

Angular Distribution of Neutrons Scattered by Helium*

ROBERT K. ADAIR
University of Wisconsin, Madison, Wisconsin
(Received December 28, 1951)

A proportional counter filled with helium was irradiated with monoenergetic fast neutrons produced by bombarding thin lithium and tritium-filled zirconium targets with protons from the electrostatic generator. Angular distributions of the neutrons scattered by helium were determined by measuring the distribution in energy of the pulses from recoiling alpha-particles with a differential discriminator. Measurements were made for eleven different neutron energies from 400 kev to 2730 kev. The angular distributions were consistent with a description of the neutron-helium interaction in terms of an inverted $P_{\frac{1}{2}}-P_{\frac{3}{2}}$ doublet in He^5, split by about 5 Mev.

I. INTRODUCTION

AN examination of the interaction of neutrons and protons with alpha-particles can provide information on the virtual ground states of He^5 and Li^5. According to the quasi-atomic model of nuclei the lowest state of He^5 or Li^5 should be a ^2P state. The sign and magnitude of the splitting in energy of the $P_{\frac{1}{2}}$ and $P_{\frac{3}{2}}$ components of the doublet is of particular interest since the characteristics of the splitting may be related to specific nucleon-nucleon spin orbit forces.

Measurements of the $n-\alpha$ back-scattering cross section by Staub and Tatel[1] showed some indication of a doublet structure near 1-Mev neutron energy. These authors interpreted their results in terms of a form of dispersion theory introduced by Bloch[2] and concluded their data could be fitted by either a regular or inverted $P_{\frac{1}{2}}-P_{\frac{3}{2}}$ doublet split by about 300 kev. However, Wheeler and Barschall[3] showed that the $n-\alpha$ angular distribution measurements of Barschall and Kanner[4] at a neutron energy of 2.4 Mev indicated a much stronger spin orbit coupling than could be expected from the level assignments of Staub and Tatel. Hall and Koontz[5] measured the $n-\alpha$ angular distribution and total cross section at neutron energies from 0.6 to 1.8 Mev. They attempted to analyze their data in terms of a close doublet but did not succeed in obtaining a fit to their measurements. The presence of the low energy group of neutrons from the Li(p,n) reaction affected their results adversely.[6]

From an analysis of more quantitatively reliable data on the $p-\alpha$ differential cross section and the $n-\alpha$ total cross section it was concluded that an inverted $P_{\frac{1}{2}}-P_{\frac{3}{2}}$ doublet is formed in He^5 and Li^5 with a splitting of the order of 5 Mev.[7] In view of the uncertainties in the angular distribution measurements and their usefulness in corroborating the level assignments, it seemed desirable to make further measurements of these distributions.

II. EXPERIMENTAL PROCEDURE

Monoenergetic neutrons were used to bombard helium in a proportional counter, and the angular distribution of the scattered neutrons was determined by measuring the distribution in energy of the helium recoils. Barschall[4] has pointed out that the distribution in energy of the alpha-particle recoils in the laboratory system is proportional to the differential scattering cross section per unit solid angle as a function of $\cos\vartheta$, where ϑ is the angle of scattering in the center-of-mass system. Therefore, the distribution of pulses from the counter represents the differential scattering cross section as a function of the cosine of the scattering angle.

Figure 1 shows the proportional counter used in these measurements. The most important difference between this counter and that described by Koontz and Hall[8] is the utilization of guard sleeves held at an intermediate potential. An important limitation on the use of proportional counters with gas amplification is the reduction of the gas multiplication near the ends of the counter caused by distortion of the field by wire supports and guard sleeves held at the potential of the wire. An attempt was made to reduce this effect by using guard sleeves held at an intermediate potential.[9] The sleeves used on this counter consisted of ceramic tubing which had an outside diameter of 0.040 inch and an inside diameter of 0.010 inch. The outside surface was coated with Aquadag to provide a conducting surface, and held at an appropriate intermediate potential. Since the dielectric constant of the cermic was about four, it was necessary to coat the inside of the ceramic, which was in contact with the wire, to preclude the production of excessive fields in small gaps between the ceramic and wire. Such fields could cause small gas breakdowns.

The chamber was used in conjunction with a Model 100 amplifier and preamplifier. The rise time of the amplifier was 0.5 microsecond and the clipping time 32 microseconds. Pulse-height distributions were

* Work supported by the AEC and the Wisconsin Alumni Research Foundation.
[1] H. Staub and H. Tatel, Phys. Rev. **57**, 936 (1940).
[2] F. Bloch, Phys. Rev. **58**, 829 (1940).
[3] J. Wheeler and H. H. Barschall, Phys. Rev. **58**, 682 (1940).
[4] H. H. Barschall and M. H. Kanner, Phys. Rev. **58**, 590 (1940).
[5] T. A. Hall and P. G. Koontz, Phys. Rev. **72**, 196 (1947).
[6] T. A. Hall, Phys. Rev. **72**, 196 (1947).
[7] R. K. Adair, Phys. Rev. **82**, 750 (1951).
[8] P. G. Koontz and T. A. Hall, Rev. Sci. Instr. **18**, 643 (1947).
[9] A. L. Cockroft and S. C. Curran, Rev. Sci. Instr. **22**, 37 (1951).

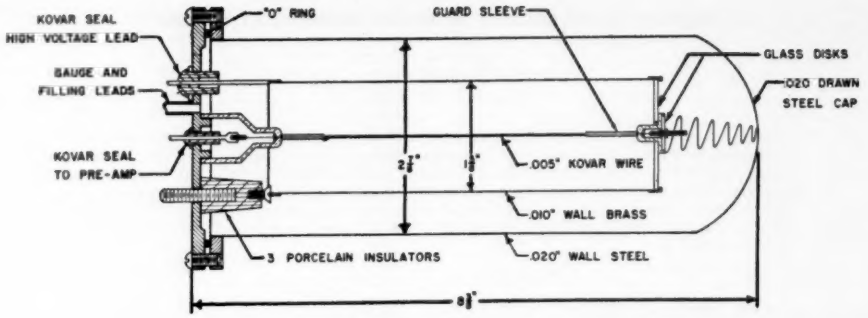

FIG. 1. Proportional counter.

measured with a single channel differential discriminator. A channel width of 1½ volts, held constant by a dry cell, was used. The position of the bottom of the channel could be varied from 0 to 50 volts.

The energy resolution of the counter was checked by measuring the pulse-height distribution from the nitrogen (n,p) reaction when nitrogen was introduced into the counter, and by measuring the pulse distributions of the α-particles from a polonium source on the counter wall. In both cases the pulse distributions had a width at half-maximum of about five percent of the pulse energy.

Measurements of the $n-\alpha$ angular distribution were made at neutron energies of 1000 kev, 1200 kev, 1400 kev, 1700 kev, 2000 kev, 2400 kev, and 2730 kev by irradiating the counter with fast neutrons from the $T(p,n)$ reaction. The tritium was absorbed in a zirconium film which had been evaporated onto a wolfram backing. Two-Mev protons lost about 30-kev energy in passing through this target. Monoenergetic neutrons of the required energies were produced by bombarding the target with protons accelerated by the electrostatic generator. It is in this region above 1 Mev that the results of Hall and Koontz were obscured by the low energy group of neutrons from the $Li(p,n)$ reaction which they used. For the present measurements the counter was filled with 1½ atmospheres of argon, 1½ atmospheres of helium, and 1.4 cm of CO_2. With this filling, the most energetic alpha-particle recoils from the highest neutron energy used had a range of about 7 mm. The CO_2 was added to reduce the rise time of the pulses from about 50 microseconds to about 5 microseconds. Since the clipping time was 32 microseconds, the maximum height of the pulse was not sensitive to the small variations in pulse rise time which are caused by differences in electron collection time from different recoil tracks. The counter was placed in position so that the axis of the counting volume was aligned with the direction of the proton beam, the center of the counting volume being about 4 inches from the target. A gas multiplication of about 15 was obtained with 2000 volts between the center wire and the wall and 400 volts between the wire and sleeve. The potential was supplied by dry cells. Pulse-height distributions were obtained by recording the number of counts which fell into the discriminator channel as a function of the bias of the channel. The neutron flux was monitored indirectly by measuring the proton current incident on the target. The crosses on Figs. 4, 5, and 6 represent the distributions obtained in this way; the ordinate of each point is proportional to the number of counts in the channel per unit neutron flux; the abscissa is proportional to the bias voltage measured to the center of the channel.

Slightly different procedures were used to obtain the angular distributions at energies of 400 kev, 600 kev, 750 kev, and 865 kev. Since the low energy group of neutrons from the $Li(p,n)$ reaction does not seriously interfere with the measurements at these energies, it seemed advantageous to make use of the larger neutron flux available from the $Li(p,n)$ reaction. The counter was again placed in line with the proton beam, but with the center of the counting volume 7 inches from the target. For these measurements the counter was filled with 3 atmospheres of helium and 2.4 cm of CO_2. A gas multiplication of about 15 was produced with 1200 volts between the wall and wire. The crosses on Figs. 2 and 3 show the distributions obtained in this fashion.

III. EXPERIMENTAL RESULTS

Corrections must be applied to the pulse-height distribution before one can relate them to differential cross sections. In particular, allowance must be made for tracks which enter or leave the active volume expending only part of their energy in this volume. Effects produced by the distortion of the field near the guard sleeves are also important. Measurements reported by Rossi and Staub[10] show that under unfavorable conditions the reduction in field near a wire support of larger diameter than the wire will produce a region of reduced

[10] B. Rossi and H. Staub, *Ionization Chambers and Counters* (McGraw-Hill Book Company, Inc., New York, 1949).

gas multiplication which may extend as much as a cm from the support. In the counter used in the present experiment the inside of the guard sleeve is held at the potential of the wire. Since the inside diameter of the sleeve is twice the size of the wire, distortion will occur. However, the field variation is much smaller than in the example presented by Rossi and Staub, and the gas multiplication is less sensitive to the field. The extent of this region was then estimated rather arbitrarily as 4 mm.

The fraction of the pulses of energy e which were reduced in energy was calculated and added to channel e. This addition represents pulses which fell into lower channels and must therefore be subtracted from these channels. The distribution from the lower channels will depend upon the spectrum of energies of the degraded pulses. Pulses lost to a channel by the wall effect would have a spectrum of energies such as to distribute them evenly among the lower channels if the ionization density along the track were constant. The correction to the distribution was made by assuming all of the degraded pulses including those which were reduced in energy by the end effect would have a distribution such that the counts added to channel e were contributed equally by the lower channels. This contribution was therefore subtracted from the lower channels. The lack of knowledge of the behavior of the gas multiplication at the ends of the counter makes a more detailed study of the correction seem unprofitable. A correction was also applied for the recoils caused by collisions of the neutrons with the carbon and oxygen from the CO_2. The uncertainty in the whole correction is estimated to be about one-half the value of the correction and is larger than the purely statistical errors. The distribution curve is, of course, affected by the energy resolution of the counter. The uncertainty in this resolution is so large that it seemed best not to attempt such a correction.

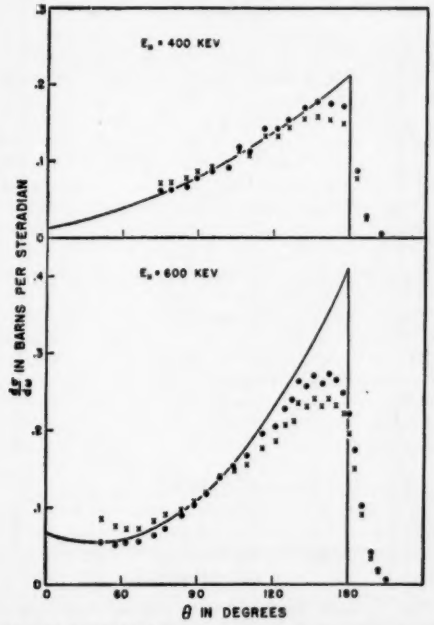

FIG. 2. Angular distribution in the center-of-mass system of neutrons scattered by helium at neutron bombardment energies of 400 kev and 600 kev. The crosses represent the uncorrected data. The solid circles represent the data corrected for end effects and wall effects. The solid curve shows the distribution calculated from Eqs. (1) and (4).

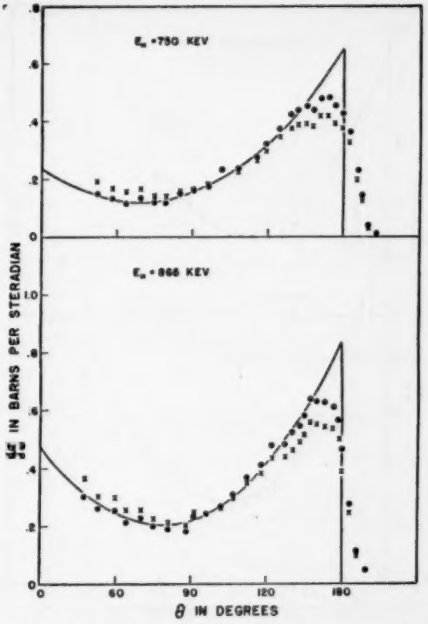

FIG. 3. Angular distribution in the center-of-mass system of neutrons scattered by helium at neutron bombardment energies of 750 kev and 865 kev. The crosses represent the uncorrected data. The solid circles represent the data corrected for end effects and wall effects. The solid curve shows the distribution calculated from Eqs. (1) and (4).

The solid circles on Figs. 2–6 represent the corrected distributions. When allowance is made for the effect of the low energy group of neutrons in the measurements of Hall and Koontz,[5] the present results are in good agreement with theirs over the energies which they measured. The agreement of the distributions with those of Barschall and Kanner at 2.4 Mev and the measurements of Huber[11] at neutron energies of 0.52, 0.7, 1.91, 2, 2.5, and 2.6 Mev is quite good.

[11] P. Huber (private communication).

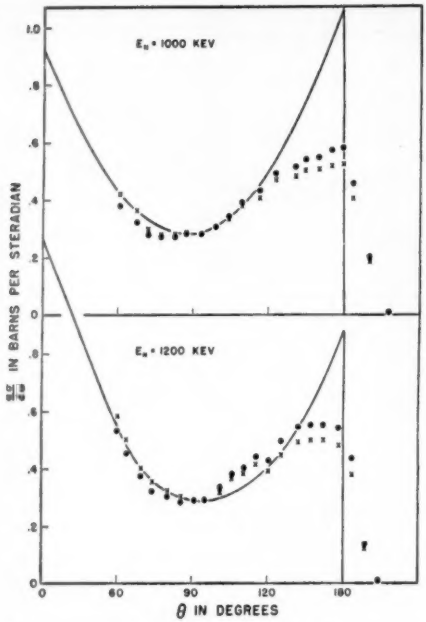

FIG. 4. Angular distribution in the center-of-mass system of neutrons scattered by helium at neutron bombardment energies of 1000 kev and 1200 kev. The crosses represent the uncorrected data. The solid circles represent the data corrected for end effects and wall effects. The solid curve shows the distribution calculated from Eqs. (1) and (4).

IV. INTERPRETATION

When coupling between spin and orbital angular momentum is taken into account, the differential scattering cross section for a neutron scattered by a nucleus of spin zero can be written,

$$d\sigma/d\Omega = k^{-2}|e^{i\delta_0}\sin\delta_0 + \cos\vartheta(2e^{i\delta_+}\sin\delta_+ + e^{i\delta_-}\sin\delta_-)|^2 + k^{-2}|\sin\vartheta(e^{i\delta_-}\sin\delta_- - e^{i\delta_+}\sin\delta_+)|^2, \quad (1)$$

where k is the wave number of the neutron, δ_0 is the s-wave phase shift, and δ_+ and δ_- are the phase shifts for the $P_{\frac{3}{2}}$- and $P_{\frac{1}{2}}$-waves, respectively. The interaction of waves associated with an angular momentum greater than one will be neglected at the energies of interest here. Since Eq. (1) is a second-order equation in $\cos\vartheta$, the pulse-height distributions should take the form of parabolas. The three coefficients determining the parabola are completely specified at any energy by the measured angular distributions and the total cross section. Although one can then solve for the three unknown phase shifts, the experimental uncertainties in the distribution measurements are large and it appears more useful to use them in a corroborative manner, comparing them with differential cross sections estimated from other considerations.

Nuclear reactions in general are conveniently discussed in terms of the wave function at the nuclear surface. According to Wigner and Eisenbud[12] one can set up Hermitian boundary conditions on the nuclear surface which determine a complete set of eigenfunctions. The scattering matrix can then be expressed in terms of the values of the eigenfunctions on the nuclear surface and their characteristic energies. The choice of boundary conditions is somewhat arbitrary. A convenient choice is,

$$\varphi = (d\ln r\chi/d\ln r)_{r=a} = -l, \quad (2)$$

where χ is the normalized internal wave function and a is the nuclear radius. A function R may be defined which is equal to $a/(\varphi+l)$. For elastic scattering R can be expanded in a series $R=\sum \gamma_\lambda^2/(E_\lambda - E)$, where the E_λ are characteristic energies associated with the eigenfunctions χ_λ determined by the nuclear Hamiltonian and the boundary conditions of Eq. (2) and $\gamma_\lambda = (\hbar^2/2m)^{\frac{1}{2}} \times \int \chi_\lambda V dS$, where V is the exterior radial wave func-

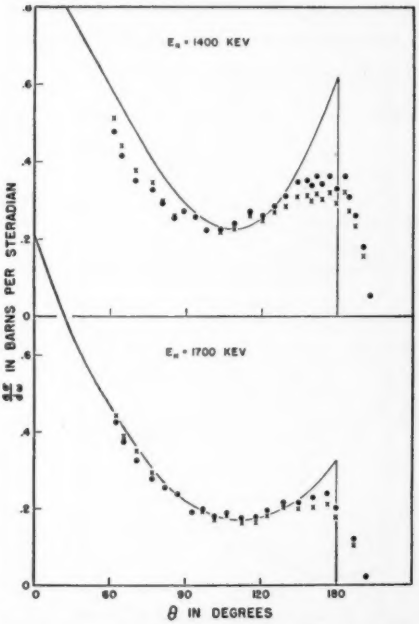

FIG. 5. Angular distribution in the center-of-mass system of neutrons scattered by helium at neutron bombardment energies of 1400 kev and 1700 kev. The crosses represent the uncorrected data. The solid circles represent the data corrected for end effects and wall effects. The solid curve shows the distribution calculated from Eqs. (1) and (4).

[12] E. P. Wigner and L. Eisenbud, Phys. Rev. **72**, 29 (1947).

tion of the two particles normalized over the nuclear surface.

When the only reaction which can occur is elastic scattering, the S-matrix is defined uniquely by the scattering phase shifts, $S_{l,j}=\exp(2i\delta_{l,j})$. We can express δ in terms of the logarithmic derivative, φ,

$$\delta=-\tan^{-1}[(\varphi F-aF')/(\varphi G-aG')],$$

where F and G are the regular and irregular free particle wave functions[13] evaluated at a and the prime indicates the derivative with respect to r. Using $R_{l,j}=a/(\varphi_{l,j}+l)$ we can write

$$\delta=\tan^{-1}\frac{ka/(F^2+G^2)}{(a/R)-d\ln(F^2+G^2)^{\frac{1}{2}}/d\ln(ka)-l}-\tan^{-1}\frac{F}{G}. \quad (3)$$

When E is near E_λ, we can approximate R by one term in the expansion and obtain the single level Breit-Wigner formula

$$\delta=\tan^{-1}\frac{k\gamma^2/(F^2+G^2)}{E_\lambda-E+\Delta}-\tan^{-1}\frac{F}{G}, \quad (4)$$

where

$$\Delta=-\frac{\gamma^2}{a}\left(\frac{d\ln(F^2+G^2)^{\frac{1}{2}}}{d\ln ka}+l\right).$$

In general, a resonance energy, E_r, can be defined in different ways. A convenient definition is $E_r=E_\lambda+\Delta$. This will not, in general, be the energy at which the scattering cross section is a maximum, but it will be very near the energy at which the reaction particles have the highest probability of forming a compound state. Since the variation of the phase shift, and hence the cross section, will be large near resonance, the most reliable and easily interpreted experimental measurements are made near resonance. The level shift, Δ, represents the difference between the energies associated with the boundary condition and that which results in a resonance in the reaction. In order that R can be adequately represented by one term in the series at energies near resonance, the shift Δ should be much smaller than γ^2/a. It is then important to choose boundary conditions which will result in a small level shift. The boundary condition given in Eq. (2) was chosen to insure an adequately small level shift in the examples considered here.

Critchfield and Dodder[14] have shown that the $p-\alpha$ differential cross-section measurements of Freier *et al.*[15] are consistent with two sets of phase shifts, one representing an inverted doublet with an undetermined large splitting, the other corresponds to a regular doublet with a splitting of about one Mev. Measurements of the polarization of the scattered protons[16] show that the former alternative is correct. The points on Fig. 7 represent Critchfield and Dodder's values of the phase shifts for the inverted doublet together with their estimate of the probable error. The curves represent the best fit to the points obtained by trial and error from Eq. (4). Corresponding values of the parameters were $a=2.9\times10^{-13}$ cm, $\gamma^2(P_{\frac{1}{2}})=\gamma^2(P_{\frac{3}{2}})=17.6\times10^{-13}$ Mev cm, $E_\lambda(P_{\frac{3}{2}})=3.65$ Mev, and the doublet splitting $E_\lambda(P_{\frac{1}{2}})-E_\lambda(P_{\frac{3}{2}})=5$ Mev. It is clear that the parameters for the $P_{\frac{1}{2}}$ level are somewhat arbitrary. The s-wave curve was computed using $R_s=0$. A small negative value of R_s, as might be expected from the contributions of high-lying levels, would improve the fit.

The total $n-\alpha$ cross section will equal

$$\sigma=2\pi k^{-2}\sum_{l,j}(2j+1)\sin^2\delta_{l,j}, \quad (5)$$

where $\delta(P_{\frac{1}{2}})$ and $\delta(P_{\frac{3}{2}})$ are calculated from Eq. (4). The points on Fig. 8 are the experimental values of Bashkin *et al.*,[17] while the solid curve represents the fit of Eq. (5) to the data, using the values of the parameters a, γ^2, and the doublet splitting deduced from the $p-\alpha$ analysis. The discrepancy between the data and the

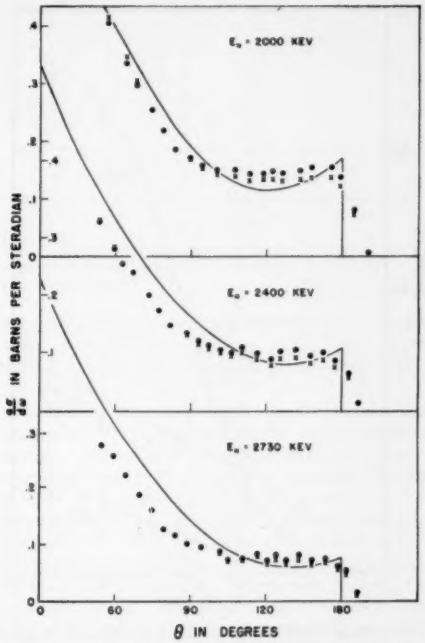

FIG. 6. Angular distribution in the center-of-mass system of neutrons scattered by helium at neutron bombardment energies of 2000 kev, 2400 kev, and 2730 kev.

[13] These functions were computed with the aid of tables prepared by Bloch, Hull, Broyles, Bouricius, Freeman, and Breit, Revs. Modern Phys. **23**, 147 (1951).

[14] C. L. Critchfield and D. C. Dodder, Phys. Rev. **76**, 602 (1949).

[15] Freier, Lampi, Sleator, and Williams, Phys. Rev. **75**, 1345 (1949).

[16] M. Heusinkveld and George Freier, Phys. Rev. **85**, 80 (1952).

[17] Bashkin, Mooring, and Petree, Phys. Rev. **82**, 378 (1951).

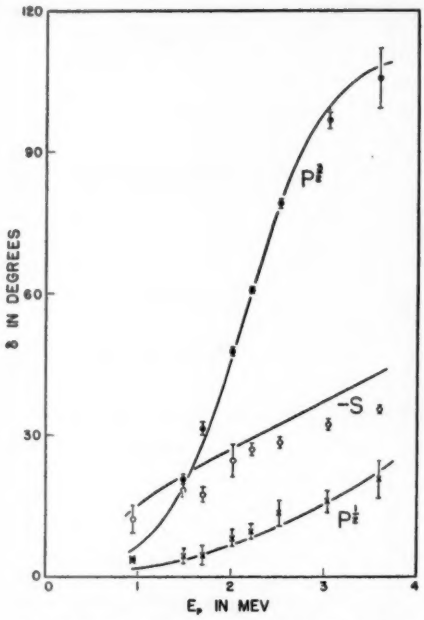

FIG. 7. Phase shifts for p–α scattering as a function of proton bombardment energy. The points represent the results of the analysis of Critchfield and Dodder, the solid curves show the phase shifts calculated from Eq. (4).

curve at 1.2 Mev is qualitatively accounted for by the lack of homogeneity in energy of the neutrons from the Li(p,n) reaction which were used in the measurement of the total cross section. The effect of the low energy group of neutrons from this reaction reduces the experimental cross section. The He^5 levels are 1.25 Mev lower than the Li^5 levels, a shift attributable quantitatively to the difference in Coulomb energy. The $n-\alpha$ S-wave phase shifts were calculated by requiring the wave function to have the same logarithmic derivative at the nuclear surface as the $p-\alpha$ S-wave.

It seems reasonable to assume that the influence of higher angular momentum phase shifts is small. Critchfield and Dodder found no evidence for their presence in the analysis of the $p-\alpha$ scattering data. Since a/λ is only about one at 4 Mev, the penetration factor of neutrons with two units of orbital angular momentum will be of the order of five percent and one might expect D-wave phase shifts of a few degrees. The presence of such a D-wave phase shift will then affect the angular distribution at energies over 3 Mev through interference with the S- and P-waves. Since waves of different angular momentum do not interfere in total cross section the effect of D-waves on the total cross section should be negligible.

The description of the $n-\alpha$ interaction in terms of an inverted $P_{\frac{1}{2}}-P_{\frac{3}{2}}$ doublet in He^5, split by about 5 Mev, is in qualitative agreement with the n-angular distribution measurements. The solid curves on Figs. 2–6 show the differential cross sections calculated from Eq. (5) using the parameters derived from the analysis of the $p-\alpha$ differential cross section and the $n-\alpha$ total cross section data. The experimental distributions are roughly normalized to facilitate comparison with the theoretical differential cross sections. When the poor angular resolution and the rather large general uncertainties of the measurements are considered, their agreement with the curves seems satisfactory. A slightly smaller splitting and a lower value of $E_\lambda(P_{\frac{1}{2}})$ would result in a somewhat better fit, but the measurements are not sufficiently reliable to justify such a conclusion.

The angular distribution data of Huber *et al.* at energies over 3 Mev are not adequately represented by the phase shifts of Eq. (2). It appears to me, however, that these data may be fitted by reasonably small changes in these phase shifts and are not inconsistent with the general conclusions of the analysis.

DISCUSSION

The doublet splitting in He^5 has also been investigated by measuring the energy spectrum[18] of neutrons produced in the bombardment of tritons by tritons. Two groups of neutrons were noted corresponding to the formation of broad states in He^5, unbound by about 0.9 Mev and 3.5 Mev, respectively. A similar investigation has been made of the doublet splitting in Li^5. Titterton and Brinkley[19] observed the breakup of Li^5 produced by the $Li^6(\gamma,n)$ reaction and found evidence that Li^5 is produced in its lowest state and in a state

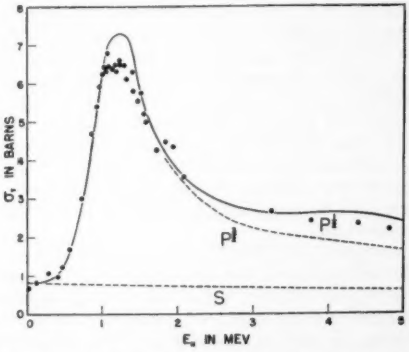

FIG. 8. n–α total cross section as a function of neutron bombardment energy. The points represent the experimental data of Bashkin *et al.* while the solid curve shows the cross section calculated from Eqs. (4) and (5). The dotted lines separate the contributions of the various partial cross sections.

[18] W. J. Leland and H. M. Agnew, Phys. Rev. **82**, 558 (1951).
[19] W. E. Titterton and T. A. Brinkley, Proc. Roy. Soc. (London) **A64**, 202 (1951).

about 2.5 Mev higher. A complete description of these processes would require a more detailed knowledge of nuclear mechanics than is available, but as a first approximation it might be expected that the nucleus He^5 or Li^5 would be preferentially produced at the energy at which the extra nucleon has the highest probability of being found in the field of the alpha-particle. This energy will be near E_r, where $E_r=E_\lambda+\Delta$. For He^5, $E_r(P_\frac{1}{2})\approx 0.95$ Mev and $E_r(P_\frac{3}{2})\approx 4$ Mev. For Li^5, $E_r(P_\frac{1}{2})\approx 2.1$ Mev and $E_r(P_\frac{3}{2})\approx 5.3$ Mev. The splittings in E_r are smaller than the splittings in E_λ because of the change in Δ with energy. Considering the approximations made, the splittings in E_r of about 3 Mev are in satisfactory agreement with the experimental values obtained from the analysis of reaction products.

The difference between the resonance energy splitting of about 3 Mev and the characteristic energy splitting of about 5 Mev is dependent upon the value of the derivative of the wave function at the nuclear surface.[20] This value is sensitive to the choice of nuclear radius. A radius larger than the rather small value of 2.9×10^{-13} cm, determined from the shape of the $P_\frac{3}{2}$ resonances and the magnitude of the Coulomb energy shift between the He^5 and Li^5 states, would result in a smaller difference between the two splittings. However, the value of the characteristic energy difference, $E_\lambda(P_\frac{3}{2})-E_\lambda(P_\frac{1}{2})$, must in any case be larger than the resonance energy splitting of about 2.7 Mev found from the reaction data, and probably lies between 4 and 5 Mev.

Since the E_λ are energies characteristic of the nuclear Hamiltonian and boundary conditions at the nuclear surface, the splitting, $E_\lambda(P_\frac{3}{2})-E_\lambda(P_\frac{1}{2})$, can be regarded as the spin-orbit interaction energy averaged over the nuclear volume. Feingold and Wigner[21] have estimated the splitting which might be expected from tensor forces. They find that this splitting, which occurs only in the second order of perturbation theory, can be only a few hundred kev. The ordinary relativistic Thomas splitting will be of the order of 50 kev.

According to Rosenfeld[22] the Møller-Rosenfeld mixed-meson theory may lead to splittings of about M/m times the Thomas splitting, where M is the nucleon mass and m is the meson mass. This would still be an order of magnitude too small. Blanchard and Avery[23] have investigated the effect of specific nucleon-nucleon, $(\mathbf{L}\cdot\mathbf{S})$, spin-orbit forces on the splitting of the energy levels of a single particle outside of a closed shell. They find that if the strength of this velocity dependent interaction is comparable to that usually assumed for the static forces, then splittings of the necessary order of magnitude might be expected. Strong spin-orbit forces

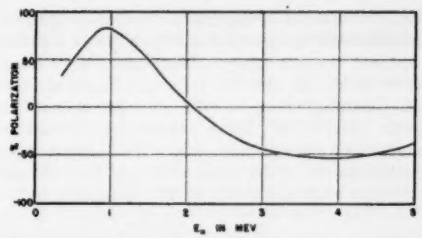

FIG. 9. Neutron polarization as a function of incident neutron energy of neutrons scattered by α-particles through 90° in the center-of-mass system.

have been used by Mayer[24] and Haxel *et al.*,[25] to explain certain characteristics of heavy nuclei. Low excited states of light nuclei also provide evidence[26] for strong spin-orbit forces.

Calculations such as those of Blanchard and Avery assume that the interaction can be represented adequately by the model of a single particle moving in the average potential of the closed shell core, and that the nucleon-meson coupling is sufficiently weak so that many-body forces can be neglected. The value obtained for the reduced width, γ^2, characteristic of the $n-\alpha$ and $p-\alpha$ scattering is approximately equal to $\hbar^2/Ma$, where M is the reduced mass of the system. With this value of γ^2 and for $|E-E_\lambda|<\gamma^2/a$, Eq. (4) takes the same form as the result for scattering by a square well of depth E', where $(E'+E)=\pi^2(l+1)^2\hbar^2/8Ma^2=37$ Mev, indicating that the interaction and the model of a nucleon moving in the average field of the alpha-particle may be a reasonably good approximation.

Schwinger[27] has pointed out that the strong spin orbit forces observed in the $n-\alpha$ interaction should result in a polarization of the scattered neutrons. The percent polarization in the X direction will equal

$$100\frac{\vartheta_x}{d\sigma/d\Omega}=100P, \tag{6}$$

where ϑ_x is the expectation value for the spin in the X direction and $d\sigma/d\Omega$ is the differential scattering cross section. For neutrons scattered out of an unpolarized beam

$$\begin{aligned}\vartheta_x=2k^{-2}[&\sin\varphi\sin\vartheta\{\sin\delta_0\sin\delta_-\sin(\delta_0-\delta_-)\\&-\sin\delta_0\sin\delta_+\sin(\delta_+-\delta_0)\}\\&+\sin\varphi\cos\vartheta\{3\sin\delta_+\sin\delta_-\sin(\delta_--\delta_+)\}],\end{aligned} \tag{7}$$

where only S- and P-waves are considered.[28]

[20] The importance of this effect has been discussed by J. Ehrman [Phys. Rev. **81**, 412 (1951)] and R. G. Thomas [Phys. Rev. **80**, 136 (1950)] with particular regard to the energy levels of C^{13} and N^{13}.

[21] E. P. Wigner, private communication.

[22] L. Rosenfeld, *Nuclear Forces* (Interscience Publishers, Inc., New York, 1949).

[23] C. H. Blanchard and R. Avery, Phys. Rev. **81**, 1067 (1951).

[24] M. G. Mayer, Phys. Rev. **75**, 1969 (1949).

[25] Haxel, Jensen, and Suess, Phys. Rev. **75**, 1766 (1949).

[26] Koester, Jackson, and Adair, Phys. Rev. **83**, 1250 (1951).

[27] J. S. Schwinger, Phys. Rev. **69**, 681 (1946).

[28] The calculational procedure is similar to that used by Wolfenstein in his analysis of reactions involving polarized protons. L. Wolfenstein, Phys. Rev. **75**, 1664 (1949).

Figure 9 shows the polarization of neutrons scattered from helium in the direction $\varphi=\vartheta=90°$, as a function of incident neutron energy. Polarizations were calculated from Eq. (6) and Eq. (7) using the phase shifts which described the $n-\alpha$ total cross section and the angular distribution. These polarizations should be quantitatively reliable below 2 Mev. At higher energies the uncertainties in the phase shifts and the influence of D-waves make the results of only qualitative value. It may also be possible to use helium to analyze the polarization of fast neutrons, since the scattering of a polarized beam of neutrons from helium will show a left right asymmetry equal to $(1+P'P)/(1-P'P)$, where P' is the polarization of the incoming beam.

I wish to thank Professor H. H. Barschall for his advice on the experimental techniques involved in this work. I also wish to express my appreciation to Professor P. Huber for discussion of his measurements.

PHYSICAL REVIEW VOLUME 86, NUMBER 2 APRIL 15, 1952

The Isotope Effect in Superconductivity. II. Tin and Lead*

B. SERIN, C. A. REYNOLDS, AND C. LOHMAN†
Physics Department, Rutgers University, New Brunswick, New Jersey
(Received December 13, 1951)

The critical magnetic fields, H, of various isotopic mixtures of tin and of lead have been measured as a function of temperature, T.

For tin, the critical temperature T_c at zero field, is related to the average mass number, M, by the relation $M^{0.46}T_c=$const. The critical magnetic fields, H_0, at absolute zero are proportional to the critical temperatures. The normalized values of critical field, H/H_0, are the same function of the variable T/T_c for all the isotopes. An analytic expression for this function giving the best fit to the experimental data is given.

The measurements on lead were made in the temperature range 1.6°K to 4.2°K. The data clearly indicate that the isotope effect is present in this superconductor.

1. INTRODUCTION

THIS investigation was a continuation of our work on the dependence of superconducting properties on isotopic mass which was originally discovered in mercury. The details of experimental technique and a bibliography are contained in our first paper,[1] which will be referred to as I. The present work was briefly reported at low temperature conferences[2] and is in general agreement with the work of Lock, Pippard, Shoenberg,[3] Maxwell,[4] and Olsen-Bär.[5]

TABLE I. Critical field data for tin. The critical temperatures T_c, the critical fields at 0°K, H_0, and the slope of the critical field-temperature curves at T_c, $(dH/dT)_{T_c}$, are tabulated as a function of the average mass number, M. The purities and H_0/T_c are also listed.

M	Purity (% Sn)	T_c(°K)	H_0 (oersteds)	H_0/T_c	$(dH/dT)_{T_c}$ (oersteds/°K)
113.6	99.50	3.805	312	82.0	145
118.7	99.995	3.752	304	81.5	144
123.8	99.76	3.659	298	81.4	144

2. MEASUREMENTS ON TIN

(a) Samples

The two samples of tin metal which had isotope distributions differing from the distribution occurring in nature were obtained from the AEC.[6] The natural metal ($M=118.7$) was obtained from the Johnson, Matthey Company. The purities of the samples are listed in Table I.

The metal was cast under vacuum into thin-walled glass capillary tubes. The tin samples were about 0.8 mm in diameter and about 4 cm long. The wall thickness of the capillary tubing was about 0.2 mm.

(b) Experimental Results

The techniques used to determine the critical magnetic fields as a function of temperature were identical with those described in I. In addition to the two isotope samples, measurements were made on two samples of natural tin. The results for these two samples were the

* This work has been supported by the joint program of the ONR and AEC, the Rutgers University Research Council, and the Radio Corporation of America.

† The parts of this paper dealing with the measurements on lead are based on an M.S. thesis submitted by C. Lohman to the Graduate Faculty of Rutgers University.

[1] Reynolds, Serin, and Nesbitt, Phys. Rev. **84**, 691 (1951).

[2] Serin, Reynolds, and Nesbitt, *Proceedings of the Low Temperature Symposium* (National Bureau of Standards, March 27 to 29, 1951); C. A. Reynolds and B. Serin, *Proceedings of the International Conference on Low Temperature Physics* (Oxford, England, August 22 to 28, 1951).

[3] Lock, Pippard, and Shoenberg, Proc. Cambridge Phil. Soc. **47**, 811 (1951).

[4] E. Maxwell, *Proceedings of the International Conference on Low Temperature Physics* (Oxford, England, August 22 to 28, 1951).

[5] M. Olsen-Bär, Nature **168**, 245 (1951).

[6] The isotopes were produced by Carbide and Chemical Division, Oak Ridge National Laboratory, Y-12 Area, Oak Ridge, Tennessee, and were obtained on allocation.

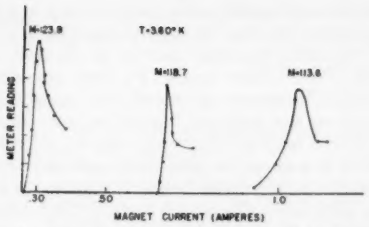

FIG. 1. Curves of detected signal *vs* current in the Helmholtz coil for three isotopes of tin.

same over the whole range of temperature, so that we give the data only for one of the samples of natural metal.

The shape of the curves of detected signal for the three samples as a function of current through the Helmholtz coil at a given temperature are shown in Fig. 1. The critical magnetic field is given by the field corresponding to the current value at the peak of each curve. The magnetic field in oersteds equals 27.6 times the current value. The large separation and the narrowness of the peaks are noteworthy. The half-widths of all peaks are very close to the ideal width calculated assuming a discontinuous increase in susceptibility at the critical field. The more impure samples, $M=123.8$ and $M=113.6$ tend to have broad tails on either side of the maximum. The positions of the peaks at any temperature could be determined to an absolute accuracy of about 0.5 per cent.

The critical fields, H, were measured at about 60 values of the temperature, T, in the range 1.27°K to 3.80°K. The critical temperatures, T_c, obtained by extrapolating the critical field temperature curves to zero magnetic field are given in Table I. Below 2°K the critical magnetic fields were proportional to the square of the temperature. Hence, the critical magnetic fields at 0°K, H_0, were obtained by plotting H as a function of T^2 and extrapolating to zero temperature. Values for H_0, as well as the values of the slopes of the critical field-temperature curves at the critical temperatures, are given in Table I.

The values of H_0/T_c and $(dH/dT)T_c$ given in Table I are in good agreement with these reported by Lock *et al.*[3] for tin isotopes of different average mass numbers.

Fitting the critical temperature data to a relation of the form $M^{\alpha}T_c=\text{const}$, gives $\alpha=0.46\pm0.02$.

In agreement with Lock *et al.*,[3] we find that the normalized critical field $h=H/H_0$ is the same function of the normalized temperature $t=T/T_c$ for all the isotopes. This result is illustrated in Fig. 2, where h is plotted as a function of t^2. The dashed line is the extrapolation of the slope of the curve at temperatures below 2°K. The data for temperatures above 2°K clearly deviate appreciably from the parabolic behavior at low temperatures. In order to avoid confusion, less than one-third of the data have been plotted in Fig. 2.

We have 175 values of h in the interval $0.34<t<1.0$. Because of the large number of experimental points available and the excellent consistency of the data, it seemed worthwhile to derive an analytic expression fitting the data. In order to do this simply, h was assumed to be an even function in the interval $-1.0<h<1.0$; and the function was expanded in Legendre polynomials. This method is equivalent to fitting the data by the method of least squares.[7] Since h was chosen to be an even function, no odd function can be present in the series expansion, so that the expansion may not converge as rapidly as the usual type of least squares expansion. We do not feel that the particular form of the expansion is of great physical significance, so that we preferred the polynomial method because of its great simplicity. The data were thus interpolated to give central differences, and the coefficients of the Legendre polynomials[8] were determined by numerical integration to give

$$h(t)=0.652P_0-0.681P_2+0.0213P_4 \\ -0.00372P_6-0.00429P_8 \\ =1.000-1.083t^2-0.0659t^4+0.349t^6-0.216t^8,$$

where P_n is the Legendre polynomial of order n. The rms deviation of the data from the expression, $h(t)$, is 0.0025.

3. MEASUREMENTS ON LEAD

(a) Samples

The lead isotopes were obtained in the form of lead oxide from the AEC.[6] The oxide was reduced to lead

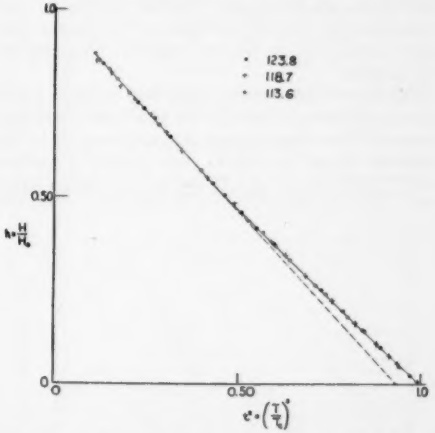

FIG. 2. The normalized critical magnetic fields for the various isotopes of tin are plotted as a function of the square of the normalized temperatures.

[7] See, e.g., A. Sommerfeld, *Partial Differential Equations of Physics* (Academic Press, Inc., New York, 1949), pp. 21–25.

[8] We used the excellent tables of Legendre polynomials of H. J. Tallqvist, Acta Societatis Scientiarium Fennicae, NSA **2**, No. 4.

TABLE II. The average mass numbers, M, and the purities of the lead samples.

M	Purity (% Pb)
206.15	99.88
207.2	99.998
207.9	99.7

metal by heating in a hydrogen atmosphere. The metal was then cast under vacuum into thin-walled capillary tubes. Two samples were also cast from natural metal obtained from the Johnson, Matthey Company. The average mass numbers and the purities of the samples are listed in Table II. The natural metal has an average mass number of 207.2. The data for the two samples of natural metal were the same over the whole range of temperature.

(b) Experimental Results

The critical magnetic field measurements were made in the temperature range 1.6°K to 4.2°K, so that the critical fields varied between about 550 and 760 oersteds. The Rutgers precision electromagnet[9] was used to provide these relatively large magnetic fields. Using this magnet, it was possible to determine, with an accuracy of 1 percent, differences of 5 oersteds between magnetic fields having magnitudes of about 500 oersteds.

The measuring techniques were the same as those described in I, except that the samples were mounted horizontally in the liquid helium Dewar flask so that the axes of the samples could be oriented parallel to the field of the electromagnet. The best orientation was determined by rotating the flask into the position that gave minimal widths for the magnetic transitions of the samples.

The half-widths of the magnetic field transitions were about 4 oersteds greater than the ideal width, probably because of the strains introduced in the samples by the tendency of lead to stick to glass. Further it was not possible to distinguish in any consistent way at a given temperature between the critical fields of $M=207.9$ and $M=207.2$, probably because of the very poor purity of the former sample. To check the effect of impurities, a sample of natural lead containing 0.2 percent tin was prepared. The tin impurity increased the critical fields at all temperatures by 1.2 oersteds relative to a sample of high purity lead. An impurity effect of this magnitude is large enough and is in the right direction to obscure the magnetic field difference expected on the basis of the isotope effect.

However, the peaks of the transitions of the samples of $M=207.2$ and $M=206.15$ were clearly and consistently resolvable. We found the critical field of $M=206.15$ was 5.1 ± 0.5 oersteds greater than the critical field of $M=207.2$. This difference was constant over the whole range of temperature used in these experiments.

The critical field difference of 5.1 oersteds is more than twice as great as would be calculated by assuming that the critical field at 0°K is proportional to $M^{-\frac{1}{2}}$. This result is consistent, however, with the results of Olsen-Bär,[5] who on the basis of measurements of the critical temperatures, found that M and T_c were related as $M^{0.72}T_c=\text{const}$. Considering the larger separation of the critical temperatures, our results also lend support to the assumption that the critical magnetic fields at absolute zero are proportional to the critical temperatures.

Despite the poor quality of the data, we are convinced that the isotope effect is present in the superconductor lead, in contradiction to the results of the earlier workers.[10]

4. ACKNOWLEDGMENT

In conclusion we wish to thank Mr. J. Teza and Mr. L. B. Nesbitt for technical assistance, and Dr. M. P. Garfunkel, Mr. W. H. Wright, and Mr. J. Gittleman for help in making the measurements.

[9] Sommers, Weiss, and Halpern, Rev. Sci. Instr. **22**, 612 (1951).

[10] H. Kamerlingh Onnes and W. Tuyn, Leiden Communications, No. 160*b* (1922); E. Justi, Physik. Z. **42**, 325 (1941).

Beta- and Gamma-Radiation of Al^{28}*

HENRY T. MOTZ AND DAVID E. ALBURGER
Brookhaven National Laboratory, Upton, New York
(Received December 14, 1951)

The beta- and gamma-rays occurring in the decay of Al^{28} have been measured by means of lens spectrometers using sources activated by the (n, γ) and (d, p) reactions on aluminum. The gamma-ray has an energy of 1.782±0.010 Mev and the beta-ray end point is found to be 2.865±0.010 Mev. The total disintegration energy is consistent with nuclear reaction Q-values linking Al^{28} and Si^{28}. It is shown that a discrepancy of 0.4 mMU in the $Si^{28}-Al^{27}$ mass difference exists when reaction data is compared to mass spectroscopic values. A mass for Al^{27} of 26.990 140±0.000 035 is proposed, based on Si^{28}, P^{31}, and S^{32} as standards.

INTRODUCTION

THE beta- and gamma-rays of 2.30-minute Al^{28} have been studied by several observers during the past ten years. Itoh[1] found one gamma-ray of energy 1.82±0.02 Mev from the distribution of the Compton electrons from a carbon radiator using a 180° magnetic spectrometer. Watase showed[2] that beta-gamma coincidences were present and found no gamma-gamma coincidences. By using a cloud chamber, Eklund and Hole found[3] a simple beta-spectrum with an end point of 2.98±0.18 Mev and a single gamma-ray of energy 2.05±0.15 Mev. Bleuler and Zünti investigated[4] the absorption of the beta- and gamma-rays and obtained a value 2.75±0.10 Mev for the beta end point and 1.80±0.10 Mev for the gamma-ray. These authors also found beta-gamma coincidences. Benes, Hedgran, and Hole found[5] a beta end point of 3.01 Mev and a gamma-ray energy of 1.80 Mev using a thin lens spectrometer. The simple cascade nature of the radiations and their approximate energy values are well established by these investigations.

Recent mass values[6] based on mass spectroscopic and reaction data indicated that the $Al^{28}-Si^{28}$ mass difference was 4.39±0.08 Mev, which is outside the range of the observed values previously quoted. Though this predicted value of 4.39 Mev is now known to be in error, it was thought necessary to have a more accurate experimental value of the total energy in order to reliably check the mass difference of Al^{28} and Si^{28}.

GAMMA-RADIATION

Commercially available 2S aluminum irradiated in the Brookhaven Nuclear Reactor was found to have an initial long-lived activity due to impurities of less than 1 percent for a four minute exposure. This material was considered sufficiently pure for the purposes of this experiment. The externally converted electrons from successive 20- to 30-second exposures of 700 mg samples were studied with a thin lens beta-ray spectrometer. Uranium foil converters of 21- and 42-mg/cm² thickness were used with a resolution of 2 percent in momentum. The electron spectrum was observed over the range of 0.1 to 4.0 Mev, and only one gamma-ray was found in agreement with previous observers. A typical spectrum of the Compton end point and the K and L photoelectron peaks is shown in Fig. 1. In order to integrate the source strength over a counting interval, a monitor counter was used. The spectrometer yield for a fixed number of monitor counts above background was recorded for each setting of the magnet current. Overlapping points were taken for each exposure, and a total of about 15 exposures of each aluminum sample was necessary to complete a run. The spectrometer was calibrated with the internal conversion line of Cs^{137} and the external conversion lines of Na^{24}, ThC″, and Co^{60}. The gamma-ray energy calculated from both the peak and extrapolated momenta of the K photoelectric peak was found to be 1.782±0.010 Mev. The less accurate values obtained from the Compton end point and the L photoelectric peak agree well with this value.

BETA-SPECTRUM

Two independent experiments were carried out to investigate the beta-ray spectrum. The first was done

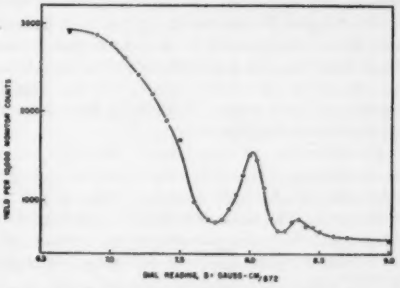

FIG. 1. External conversion electrons from Al^{28} gamma-ray using a 42-mg/cm² uranium converter.

* Research carried on under contract with the AEC.
[1] J. Itoh, Proc. Phys.-Math. Soc. Japan **23**, 605 (1941).
[2] Y. Watase, Proc. Phys.-Math. Soc. Japan **23**, 618 (1941).
[3] S. Eklund and N. Hole, Arkiv, Mat. Astr. Fys. **29**, No. 26 (1943).
[4] E. Bleuler and W. Zünti, Helv. Phys. Acta **20**, 195 (1947).
[5] Benes, Hedgran, and Hole, Arkiv Mat. Astr. Fys. **35**, No. 12 (1948).
[6] H. T. Motz, Phys. Rev. **81**, 1061 (1951).

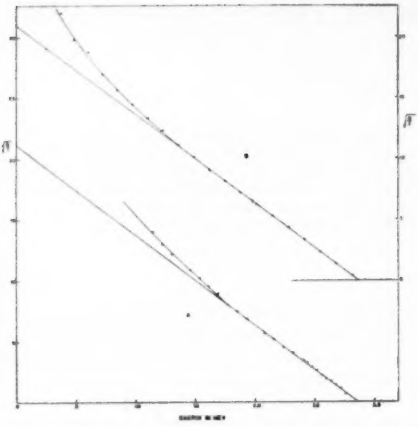

FIG. 2. Kurie plot of Al^{28} beta-spectrum. Curve *A*, (n, γ) activation; Curve *B*, (d, p) activation.

with reactor-activated sources and the second with the Brookhaven electrostatic accelerator and a similar but different lens spectrometer. The reactor experiment utilized 2-mg/cm² aluminum foils exposed for two to three minutes. The sources had an initial activity of about 500 microcuries and could be used for four or five momenta settings for a fifteen minute counting period before the background correction became too large. New foils were used for each exposure to avoid the build-up of long-lived activities. The beta-rays entered the spectrometer vacuum chamber through a 10-mg/cm² aluminum port. A thin-window monitor counter was used to determine the average source strength as for the gamma-ray observations. The effect of the aluminum port and source thickness was studied with the use of a source of P^{32} mounted on 2-mg/cm² aluminum foil. The Kurie plot[7] for P^{32} deviated from a straight line below 800 kev and gave an end point of 1.70±0.01 Mev. The Kurie plot obtained from one of the three runs on Al^{28} is shown in Fig. 2, Curve A. The deviation from a straight line is not inconsistent with the results from P^{32}. Some of the scatter in the points is probably due to slight misalignment of the sources and is somewhat greater than the expected statistical variation of yield. By means of a least squares fit, the observed end point is found to be 2.859±0.020 Mev from the reactor-activated samples.

In the second set of experiments, using the electrostatic accelerator, the activity was formed in aluminum foils by the $Al^{27}(d, p)Al^{28}$ reaction using a 2.0-Mev deuteron beam. The foils were 0.22 and 0.9 mg/cm² in thickness, and the corresponding beam currents of 6 and 1.5 microamperes gave similar source strengths. The lens spectrometer was connected to the beam tube of the accelerator in such a way that the foils were located at the normal source position of the spectrometer. A baffle system in the beam tube defined the region of activation to a spot 5 mm in diameter, and the deuteron current passing through the target was collected and measured by means of an insulated Faraday cup attached to the center lead baffle of the spectrometer.

The procedure consisted of irradiating the target for about 2 minutes, turning off the beam, and counting for several minutes. In order to normalize the spectrometer yield to a standard number of disintegrations a gamma-ray monitor was placed near the source, and the data were taken in a manner similar to that described in the reactor experiments.

In initial tests the presence of 10-minute N^{13} positron activity formed by deuteron bombardment of carbon deposits on the target was detected. This caused inconsistency in the data below 1.2 Mev (the positron end point) because of the monitoring technique and resulted in excessive low energy deviations in the Kurie plot. The positrons were finally removed by the installation of a spiral baffle system. The baffles were also found to reduce considerably the background of scattered beta-rays beyond the end point of the spectrum and permit an estimate that not more than 2 percent of the Al^{28} beta-decays go to the ground state of Si^{28}.

The Kurie plot of the beta-ray spectrum is shown in Fig. 2, Curve B, for a 0.22-mg/cm² source. Deviations from linearity occur below 1.2 Mev and vary with the thickness of the source used. From the straight line portion of the curve a least squares analysis gives an end point energy of 2.866±0.010 Mev. The 2.76-Mev Na^{24} gamma-ray was used for calibration. The combined results of all data using both spectrometers gives the value 2.865±0.010 Mev for the Al^{28} beta-ray end point. Using this figure and the measured half-life, the log *ft* value of the transition is 4.92 as calculated from the graphs given by Moszkowski.[8] This value and the linearity of the Kurie plot show that the beta-decay is of the allowed type.

DISCUSSION

By means of several nuclear reaction *Q*-values reported by the MIT Group[9] it is possible to calculate the expected total disintegration energy of Al^{28}. Table I lists the observed *Q*-values and the predicted total disintegration energy as derived from two combinations of the data. The *p*, *d*, and α masses given by Li *et al.*[10] were used in these calculations. The observed beta-decay value agrees well with the two calculated from the reaction values and is somewhat more accurate. These data can be used to find the mass difference

[7] The accurate relativistic Fermi functions kindly furnished by the Computation Laboratory of the National Bureau of Standards were used in all of the Kurie plot calculations.

[8] S. A. Moszkowski, Phys. Rev. **82**, 35 (1951).

[9] MIT Progress Report, May 1951.

[10] Li, Whaling, Fowler, and Lauritsen, Phys. Rev. **83**, 512 (1951).

$Si^{28}-Al^{27}$ by combining the Al^{28} decay energy with the other Q-values. The result is a mass difference $Si^{28}-Al^{27}$ = 0.995 702±0.000 018 MU. The mass of Si^{28} has been reported as 27.985 810±0.000 080[11] and 27.985 792 ±0.000 032 MU.[12] The average of these is 27.985 795 ±0.000 032 MU. The mass doublet $C_2H_3-Al^{27}$ has been given as 42.35±0.065 mMU.[13] Using recent values[10] for C and H, a mass of 26.989 684±0.000 070 is found for Al^{27}. From these mass spectrographic data, one finds $Si^{28}-Al^{27}$ 0.996 111±0.000 080 MU. The reaction mass difference 0.995 702±0.000 018 MU is not in agreement with this and indicates that either the absolute value for Al^{27} or that for Si^{28} must be in error by about 0.4 mMU.

The most accurately measured Q-values linking Si^{28} to P^{31} and S^{32} indicate that the Si^{28} mass is consistent with the P^{31} and S^{32} masses[12] to 0.000 04 MU, which is less than the combined probable errors of the observed quantities. Similarly the mass of Si^{28} is consistent with the mass of the Ne^{20}[12] within the same limit. Thus it seems reasonable to accept the Si^{28} mass spectrographic value and reject the Al^{27} value. Using the Si^{28}, P^{31}, and S^{32} masses as standards, one can derive a mass for Al^{27} that is consistent with the known Q-values linking these isotopes.[14] Such a fit gives a value of 26.990 140±0.000 035 for Al^{27}.

TABLE I. Calculated and observed disintegration energy of Al^{28}.

Disintegration energy (Mev)	Reaction chains and decay energies	Reference
4.657±0.019	$Si^{28}(d,p)Si^{29}$ $Si^{29}(d,\alpha)Al^{27}$ $Al^{27}(d,p)Al^{28}$	a
4.637±0.020	$Si^{28}(d,p)Si^{29}$ $Si^{29}(d,p)Si^{30}$ $Si^{30}(d,\alpha)Al^{28}$	a
4.647±0.014	Beta endpoint 2.865±0.010 Mev Gamma-ray 1.782±0.010 Mev	present work

[a] See reference 9.

We are indebted to Dr. I. Feister and Miss Irene Stegun of the National Bureau of Standards for supplying the Fermi functions in advance of publication.

[11] H. E. Duckworth and R. S. Preston, Phys. Rev. **79**, 402 (1950).
[12] H. Ewald, Z. Naturforsch. **6a**, 293 (1951).
[13] S. Flügge and J. Mattauch, Physik. Z. **42**, 1 (1941).
[14] H. T. Motz, Phys. Rev. **85**, 501 (1952).

PHYSICAL REVIEW VOLUME 86, NUMBER 2 APRIL 15, 1952

Stars Initiated by High Energy Protons and Neutrons

HERBERT FISHMAN AND ALFRED MORRIS PERRY, JR.
Department of Physics, University of Rochester, Rochester, New York
(Received December 20, 1951)

Stars initiated in nuclear emulsions by 240-Mev protons and 180-Mev neutrons have been studied. Size-frequency distributions of the stars and angular distributions of prongs in various energy intervals have been obtained. Comparison with similar results obtained at different energies shows that the star size distribution is more sensitive to incident energy for protons than for neutrons.

I. INTRODUCTION

STARS in photographic emulsions have been studied by several investigators for a variety of incident particles.[1-5] In such experiments, it is hoped, from the average properties of large numbers of stars, to gain insight into the manner in which energetic nucleons interact with nuclei, and to test various nuclear models.

In the present experiment stars initiated by protons of about 240 Mev and neutrons of about 180 Mev have been examined in sensitive emulsions.

II. EXPERIMENTAL PROCEDURE

A. Protons

Ilford G-5 plates, 200, 300, and 600 microns thick were exposed to the proton beam of the 130-in. cyclotron by a method first used by Bernardini, Booth, and Lindenbaum[6] at Columbia. The plates were placed parallel to the median plane of the cyclotron, about $\frac{7}{8}$ in. above and below it, and in the neighborhood of the cyclotron radius at which $-d(\ln H)/d(\ln R)=0.2$. At this radius large vertical oscillations of the proton beam occur, and in the absence of other targets, a parallel beam of protons is spread out over the plates. In azimuth the plates were placed as far as possible from the "up-beam" edge of the dee, to reduce background caused by knock-on neutrons. Exposures were for one to two seconds with arc source and hydrogen supply turned off.

Microscopic scanning for events was done in two ways: by a systematic search over the area of the plate, and by following individual proton tracks which were selected in an unprejudiced manner near the leading edge of the plate. The latter method, while far more tedious, is much more reliable for events with few

[1] E. Gardner and V. Peterson, Phys. Rev. **75**, 364 (1949).
[2] E. Gardner, Phys. Rev. **75**, 379 (1949).
[3] L. S. Germain, Phys. Rev. **82**, 596 (1951).
[4] E. W. Titterton, Phil. Mag. **42**, 109 (1951).
[5] Bernardini, Booth, and Lindenbaum, Phys. Rev. **80**, 905 (1950); **83**, 669 (1951).
[6] S. J. Lindenbaum (private communication).

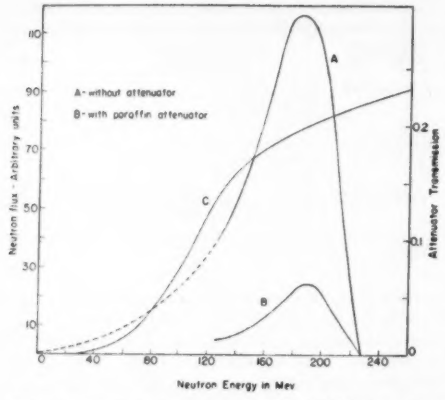

FIG. 1. Spectrum of neutrons produced by 240-Mev protons on ½-in. Be target. Curve *B* shows spectrum behind 107 cm of paraffin; curve *C* shows the transmission of the paraffin.

prongs, and indeed is mandatory for the observation of small scatters and stoppings (in which the proton track vanishes in flight, presumably suffering a charge exchange scatter).

Star prongs were roughly classified by inspection into three groups: (1) black, including protons of about 30 Mev or less, deuterons less than 60 Mev, and all alpha-particles likely to be encountered in this experiment; (2) gray-black, including protons between 30 and 70 Mev, deuterons from 60 Mev; and (3) gray, consisting of protons above about 70 Mev. Only tracks greater than 5 microns in length were counted as prongs.

Criteria for judging the tracks were established partly by the ranges of a few long prongs, and partly by an empirical relation for grain density *vs* ionization, calibrated by 240-Mev protons. This relation, first brought to our attention by Dr. David Ritson, is

$$N=N_0(1-e^{-I/I_0}),$$

where N_0 is a saturation grain density, I the specific ionization of the proton, and I_0 a parameter depending on the sensitivity and development of the emulsion. The single calibration at 240 Mev is evidently not sufficient to determine both N_0 and I_0. However, a choice of $N_0=150$ grains/50μ gives a curve which matches the grain counts of a few long prongs, and which agrees quite well with a series of values $N/N_{\min}$ *vs* $I/I_{\min}$ given by Bernardini.[7] ($N_{\min}$ is the grain density of a proton with minimum ionization, $I_{\min}$.) The accuracy of energy assignments was not better than ±10 Mev in the neighborhood of 30 Mev, or ±20 Mev in the neighborhood of 70 Mev.

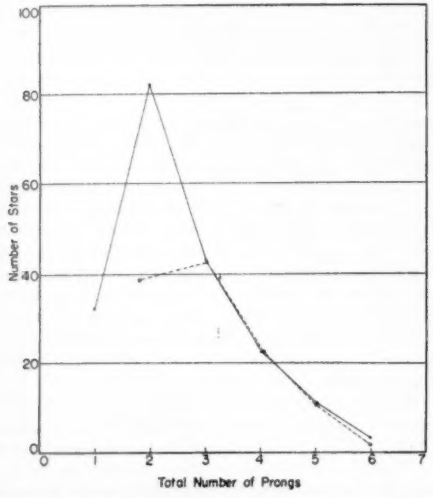

FIG. 2. Size-frequency distributions for neutron and proton stars. Solid curve: 240-Mev protons. Dashed curve: 180-Mev neutrons. Curves normalized at 3 prongs.

TABLE I. Number of stars *vs* total number of prongs.

Number of prongs	1	2	3	4	5	6	Total
No. of proton stars	32	82	43	23	11	3	194
No. of neutron stars	···	199	225	117	55	10	606

B. Neutrons

Neutrons were produced by interposing a ½-in. beryllium target at 58½-in. radius in the 240-Mev proton beam. Plates being exposed to the neutron beam were placed 29 ft away from the target, inside a concrete block-house.[8] The front wall of the block-house consists primarily of 3-ft of copper, lined with 1-ft thick concrete. In front of the block-house is a 6-ft copper collimator. As further insurance against background, the plates were surrounded by a cave of lead bricks. Placed in the neutron beam, as close as possible to the target, was a column of paraffin, 107 cm long, the effect of which was to reduce the relative intensity of low energy neutrons in the beam.

While a reliable neutron spectrum has not yet been obtained, the neutron scattering group[9] believe that their final spectrum will not differ greatly from the preliminary one shown in Fig. 1. Also shown is the spectrum of the neutrons after passing through the paraffin, obtained from the incident spectrum by the transformation,

$$N(x, E)=N(0, E)\exp-(\sigma_C N_C+\sigma_H N_H)x,$$

where $x=107$ cm and σ_C, σ_H, N_C, and N_H are the total

[7] G. Bernardini (private communication to Dr. S. W. Barnes).
[8] Clifford Swartz, Rochester thesis (1951).
[9] Guernsey, Mott, and Nelson, private communication.

neutron cross sections and numbers per cm^3 of carbon and hydrogen atoms in the paraffin.

As in the case of the proton stars, it was necessary to calibrate the plates so that the neutron star prongs could be classified in broad energy intervals, even though they left the emulsion. In place of the 240-Mev calibration point which was found convenient in the proton-star plates, reliance was placed on the grain density of one very long proton track which ended in the emulsion, and on the range-energy curve for protons in G-5 emulsion.[10,11] While the grain density of a second, somewhat shorter, track differed from the first in the range 30–55 Mev by a somewhat greater amount than would be expected from statistics, they agreed within statistics elsewhere, and it was possible to ascertain in six cases of fast star prongs ending in the emulsion that the average error in deducing the energy from the grain count was 5 Mev. As in the case of proton stars, the prongs were then classified by inspection as black, gray-black, or gray, corresponding approximately to protons below 30 Mev, between 30 and 70 Mev, or above 70 Mev. Only tracks greater than 5 microns were counted as prongs.

TABLE II. Number of stars *vs* number of black prongs.

Number of black prongs	0	1	2	3	4	5	6
No. of proton stars	24	63	47	32	19	6	3
No. of neutron stars	···	89	184	175	107	39	7

Since the incident particle is not visible in the case of neutron stars, it was not feasible to record one-pronged stars. Moreover, the two-pronged events also offered some difficulty, since it was not possible in all cases to distinguish between true neutron stars and low energy scatters. Such events were considered to be neutron stars if: (1) it was possible to discern at the vertex of the star a prong less than 5 microns in length, which was considered to be a "recoil" prong; (2) it was possible to observe a difference in grain density between the two tracks; and (3) it was possible to observe an increase in grain density along both tracks in the direction away from the star. By comparison with the proton-star plates, it has been possible to exclude from consideration the alpha-particle disintegrations of thorium, which is present in the emulsion as an impurity. Hence, we can conclude that analysis of the neutron star data should: (1) not include one-pronged stars; (2) consider two-pronged events with the reservations stated above; and (3) include all events with three or more prongs as bonafide neutron stars.

III. RESULTS

Altogether 596 neutron stars were found with a total of 1847 prongs, giving an average of 3.1 prongs per star

[10] F. H. Tenney, private communication (based on reference 11).
[11] Aaron, Hoffman, and Williams, University California Radiation Laboratory Report No. 121 (1951).

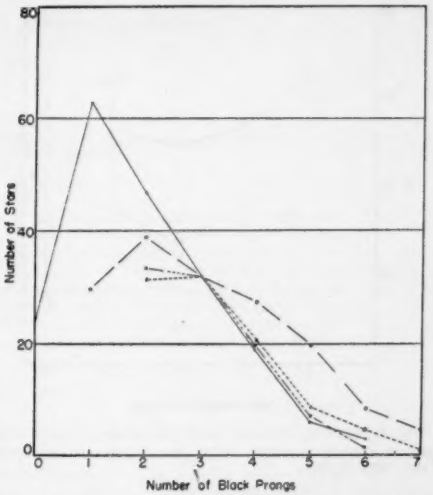

FIG. 3. Size-frequency distributions for neutron and proton stars, normalized at 3 black prongs. ○—380-Mev protons. ●—240-Mev protons. △—300-Mev neutrons. ×—180-Mev neutrons.

for stars with two or more prongs. 194 proton stars were found by the track scanning method and 321 by the area scanning method. Stars found by area scanning have been included only in the angular distribution of prongs, which we have shown to be essentially independent of star size for black and gray-black prongs, and nearly so for gray prongs.

By considering only stars with three or more prongs, we find an average of 3.6 prongs per star for neutrons and 3.7 prongs per star for protons. Size-frequency distributions for neutron and proton stars are shown

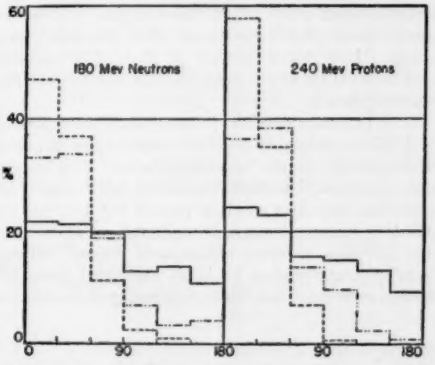

FIG. 4. Angular distributions of star prongs. Solid curves: black prongs. Dash-dotted curves: grey-black prongs. Dashed curves: grey prongs. Area under each histogram equals 100 percent.

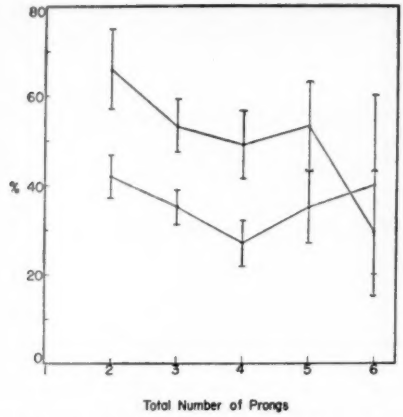

FIG. 5. Percentage of stars with N prongs having one or more gray or gray-black prongs. Upper curve: proton stars. Lower curve: neutron stars.

in Table I and in Fig. 2, in which the abscissa is the total number of prongs (excluding, of course, the incident proton). In order to compare our results with data for proton and neutron stars obtained at Columbia,[5,6] we have also plotted the number of stars against the number of black prongs as shown in Table II and in Fig. 3. The curves of Fig. 3 are normalized at three-pronged stars. The energy of the protons in the Columbia work was about 380 Mev and of the neutrons about 300 Mev.

The striking feature of this comparison is the similarity of the prong distributions for 180-Mev neutrons and for 300-Mev neutrons. The distribution obtained for 150-Mev neutrons by Titterton[4] at Harwell is also almost identical with the 180-Mev neutron curve. Furthermore, the prong distribution for 180-Mev neutron stars is essentially the same as that for 240-Mev proton stars. (While the proton data are based on a comparatively small number of stars, they are well corroborated for two or more black prongs by the area-scanning data.)

It is probably possible to understand these results in detail by making Monte Carlo calculations like those of Bernardini, Booth, and Lindenbaum.[5] This has not been done yet. The similarity in the neutron-star distributions may be a result in part of the fact that the 300-Mev neutron beam was unfiltered, while the 180- and 150-Mev neutron beams were filtered through paraffin, and therefore probably contained fewer low energy neutrons. The difference in energy dependence of the neutron- and proton-star distributions may be a result in part of the fact that the $n-p$ scattering cross section decreases with energy up to 200 Mev or above,[12] while the $p-p$ cross section is essentially independent of energy above 100 Mev.[13,14] Since protons will predominate in the first two or three generations of collisions inside the nucleus if the incident particle is a proton, while neutrons will predominate for incident neutrons, it can be seen that the effect of the energy dependence of the $n-p$ cross section is of greater consequence for neutron stars than for proton stars.

The angular distributions of star prongs in the three energy groups are shown in Fig. 4. While the distributions for neutron and proton stars are quite similar, it is seen that the gray prongs are more strongly peaked forward in the proton stars than in the neutron stars. This is probably caused in part by the difference in incident energy in the two cases, but it is also a result of the fact that the proton distribution includes stars with zero or one black prong, which contain 60 percent of all the gray prongs. (The proton distribution does not, however, include scatters resulting in a single outgoing gray track; these were not classified as stars.) For proton stars with fewer than two black prongs, the gray prongs are about 10 percent more peaked in the 0–30° interval than for proton stars with two or more black prongs.

If we consider crudely that the incident particle suffers only a single collision inside the nucleus, and that $p-p$, $p-n$, and $n-n$ collisions are equally probable at these high energies, we are led to expect three times as many visible fast prongs for incident protons as for incident neutrons. This effect is, of course, reduced by subsequent collisions inside the nucleus, but we may expect nonetheless that a higher percentage of proton than of neutron stars will exhibit fast prongs. This is confirmed by the results shown in Fig. 5.

It would doubtless be a useful extension of this work to determine the energies of the prongs more carefully in order to obtain a good energy spectrum of the prongs. It would also be desirable with the use of less sensitive emulsions to identify deuterons, alpha-particles, and heavier fragments which may be ejected as well as protons.

The authors wish to thank Dr. Sidney W. Barnes, under whose guidance the work was performed, and Dr. Robert E. Marshak, for valuable discussions. Thanks are due Mrs. Jane Button and Mr. Raymond Doughty, who assisted with the scanning.

[12] J. DeJuren and B. J. Moyer, Phys. Rev. **81**, 919 (1951).
[13] Chamberlain, Segrè, and Wiegand, Phys. Rev. **83**, 923 (1951).
[14] R. W. Birge, Phys. Rev. **80**, 490 (1950).

The Production of Positive Mesons by Photons*

J. STEINBERGER
Columbia University, New York, New York

AND

A. S. BISHOP
University of Zurich, Zurich, Switzerland

(Received October 26, 1951)

Experimental results are presented on the production of positive mesons in hydrogen and carbon, as a function of meson angle and energy. The principal results are as follows: The angular distribution in the case of hydrogen is rather flat in the region 45°–135° in the laboratory system, slightly peaked near 90°. This demonstrates that the pion is not a scalar. The excitation function at 90° rises approximately linearly to a plateau which starts at photon energies of about 260 Mev. This rise is slower than expected on the basis of a phase space argument. The total cross section for 255-Mev photons in hydrogen is $1.9\pm0.3\times10^{-28}$ cm². The cross sections in carbon are lower, per proton, by a factor of approximately three. With respect to hydrogen, the meson energy distribution is shifted to lower energies and the angular distribution is shifted to the backward angles.

I. INTRODUCTION

THE construction of x-ray machines of sufficient energy has made it possible to study the process of meson production by photons. Photomesons were first found by McMillan, Peterson, and White.[1] We report here the results of more detailed experiments, especially on the process $p+h\nu\rightarrow n+\pi^+$. The experiments were carried out in the hope that this process, which seems particularly suited to analysis because of its simplicity, may shed some light on the interaction of mesons with nucleons.

The following data are presented: (1) The energy dependence of the mesons produced at 90° to the beam direction, both for carbon and hydrogen targets and the excitation function for the production of positive mesons on hydrogen. (2) The angular dependence of the production cross section. (3) The total cross section for meson production by 255-Mev photons on hydrogen.

The experiments have been in part reported.[2]

II. X-RAY CHARACTERISTICS

The x-rays employed in these experiments are produced in the Berkeley synchrotron. This machine accelerates electrons to an energy of 325 Mev and then permits them to strike a target of 0.020-in. platinum. About 15 percent of the electron energy is converted to x-rays with an angular spread of 1° half-width, and characteristic bremsstrahlung spectrum. Figure 1 shows the spectrum, as calculated and corrected for the effects of finite target thickness, and variation of the magnetic field during expulsion of the beam. Cloud-chamber measurements of the spectrum by Powell, Hartsough, and Hill[3] are in agreement with the theoretical results. The expulsion time is purposely made long in order to minimize the accidental coincidence rate in counting experiments.[4] The machine is pulsed 5 times/sec, each beam pulse lasting approximately 0.003 sec. The duty cycle is therefore ~0.015 (Fig. 2).

The beam is monitored by a self-cycling ionization chamber, calibrated by Blocker and Kenney against the ionization chamber used in an absolute measurement of the beam intensity.[5] Their calibration, which has an uncertainty estimated to be less than 10 percent, has been used in all determinations of absolute cross section.

III. KINEMATICS

We study the reaction $p+h\nu\rightarrow n+\pi^+$ for free protons as well as those bound in carbon nuclei. In the case of the reaction with free protons, there are only two

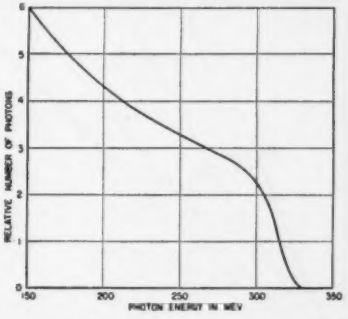

FIG. 1. Calculated x-ray spectrum, corrected for finite target thickness and variation of magnetic field during the expulsion period.

* Research supported by the AEC.

[1] McMillan, Peterson, and White, Science **110**, 579 (1949).

[2] J. Steinberger and A. S. Bishop, Phys. Rev. **78**, 493 (1950). **78**, 494 (1950); Bishop, Steinberger, and Cook, Phys. Rev. **80**, 291 (1950).

[3] Powell, Hartsough, and Hill, Phys. Rev. **81**, 213 (1951).

[4] This is accomplished, on the suggestion of E. M. McMillan, by shaping the envelope of the rf accelerating voltage. G. Gauer and C. Nunan, University of California Radiation Laboratory Report No. 714 (1950).

[5] Blocker, Kenney, and Panofsky, Phys. Rev. **79**, 419 (1950).

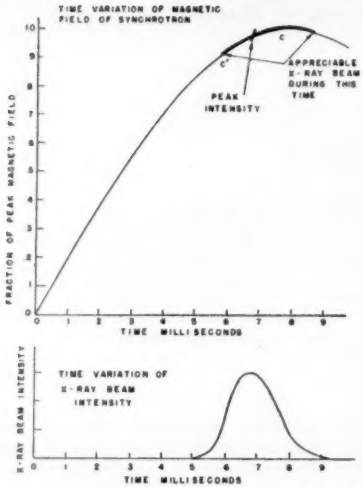
TIME VARIATION OF MAGNETIC FIELD OF SYNCHROTRON
FRACTION OF PEAK MAGNETIC FIELD
TIME MILLISECONDS
PEAK INTENSITY
APPRECIABLE X-RAY BEAM DURING THIS TIME
TIME VARIATION OF X-RAY BEAM INTENSITY
X-RAY BEAM INTENSITY
TIME MILLISECONDS

FIG. 2. Duty cycle of the synchrotron.

outgoing particles, and, by the conservation laws, a knowledge of the meson energy and production angle suffice to determine the reaction kinematics, and in particular, the energy of the responsible light quantum.

$$h\nu=\left(E-\frac{\kappa^2}{2M}\right)\Big/\left(1-\frac{E}{M}+\frac{2k\cos\theta}{M}\right), \qquad (1)$$

neglecting the n-p mass difference. Here $h\nu$=photon energy; k, E=meson momentum, energy; κ=meson rest energy; M=proton rest energy; $\hbar=c=1$. This fact makes it possible to measure the proton cross sections as a function of γ-ray energy, despite the continuous nature of the x-ray spectrum. (See Fig. 3.)

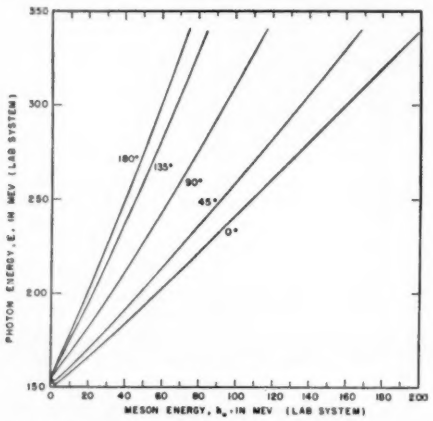

FIG. 3. Photon energy as a function of meson energy and emission angle in the laboratory system, for the reaction,

$$p+h\nu\rightarrow\pi^++n.$$

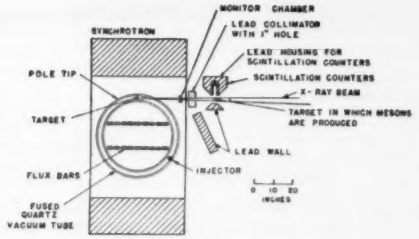

FIG. 4. Arrangement of apparatus.

IV. EXPERIMENTAL ARRANGEMENT

a. General

The x-ray beam is collimated to a diameter of 1 in. at a distance of five feet from the internal target. It is then allowed to strike a target of the material whose meson production cross section is being measured. (See Figs. 4 and 5.) The meson detector consists of three crystal counters, anthracene or stilbene, each approximately $1\frac{3}{4}$ in.$\times 1\frac{3}{4}$ in.$\times\frac{3}{8}$ in., and with attached photomultiplier. The central crystal is about 9 in. from the target. The whole telescope may be rotated about an axis through the center of the target and perpendicular to the x-ray beam.

As is well known, stopped π^+ mesons disintegrate with a mean lifetime of 2.6×10^{-8} sec. The μ^+ mesons

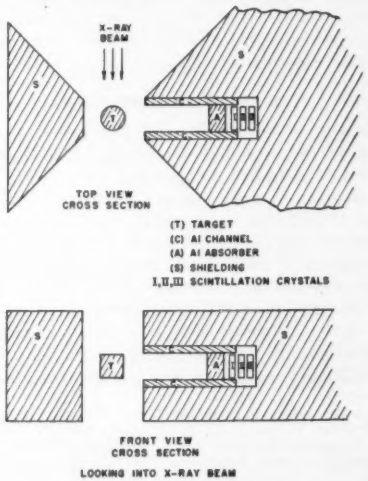

FIG. 5. Details of meson detector.

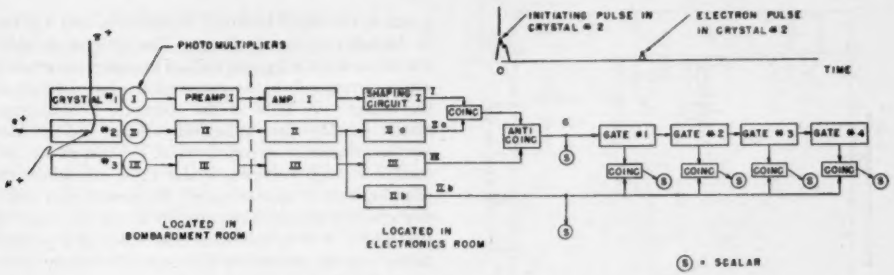

FIG. 6. Block diagram of electronics.

so produced disintegrate with a mean life of 2.2×10^{-6} sec, emitting positrons. On the other hand, π^- mesons coming to rest in condensed matter immediately form stars and have no delayed decay products. Our apparatus detects π^+, μ^+, and μ^- mesons, and does not distinguish between these. A particle is registered if it penetrates the aluminum absorber (Fig. 5), and crystal I, comes to rest in crystal II, and its decay electron appears within the time interval of one of several successive gates, each two microseconds long, initiated by the first event. A block diagram is shown in Fig. 6. Only standard electronic apparatus is required except, perhaps, for the discriminator in the decay electron pulse channel. This must have a short recovery time, since the decay electron pulse is always preceded by that of the stopping meson. For this purpose a biased positive feedback amplifier was used, with 5×10^{-7} sec recovery time, of a design by Wouters.

b. Accidental Counting Rate

Not all observed coincidences are due to time correlated events, but some, varying from between one and twenty percent of the counting rate in the first delay channel, are due to two uncorrelated events which have the proper time delay. The number of such events is calculated statistically as the product of the known single counting rates, resolving time, and reciprocal duty cycle. The quotient of resolving time and duty cycle is determined by testing the apparatus under conditions in which the number of time correlated events is small compared to the random events.

c. Experimental Checks on the Detection Method

Removal of the target, or of the liquid hydrogen from its container, resulted in a decrease in the meson counting rate by at least a factor of 100. Plateau characteristics (delay coincide rate as a function of minimum pulse height in a particular channel) are reproduced in Figs. 7, 8, and 9. They show that the pulses due to stopping mesons are rather uniform in height, but that those due to the decay electrons have a large spread. This is expected, since the decay electron ranges are large compared to crystal dimensions and the electrons leave the crystal in all directions with various path length. The shape of Fig. 10 has been checked theoretically.

The scintillation detectors are operated at the indicated pulse-height levels during all experiments. The levels are calibrated by means of a radium source. With the help of the plateau curves it is possible to calculate absolute cross sections, if it is assumed that the intercepts of the plateau curves with the abscissa corresponds to 100 percent detection efficiency. We estimate that the error in the absolute cross sections due to uncertainty in the detection efficiency is of the order of 10 percent. The differences in the absolute cross sections between previously reported results[2] and those of this paper are due to incorrect estimates of the decay electron detection efficiency before the experimental determination of Fig. 9.

The relative counting rates in the delay channels should reproduce the exponential $\mu\rightarrow e$ decay. This datum is obtained simultaneously with all measurements, some of it is shown in Fig. 10. Although statistically superior to previous measurements, they suffer from systematic error.[6] The lifetime determinations

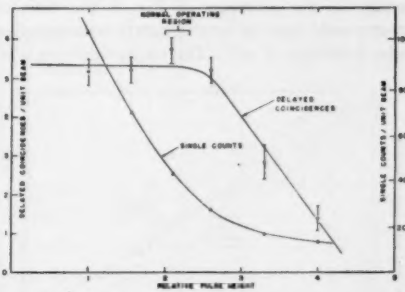

FIG. 7. Integral counting rates as a function of pulse height in crystal 1.

[6] This error is due to the fact that the pulse circuits do not trigger with uniform sensitivity for 1–2μ seconds after the initial (meson stopping) event. The decay electron is therefore not counted with the same efficiency in the first channel as in the others.

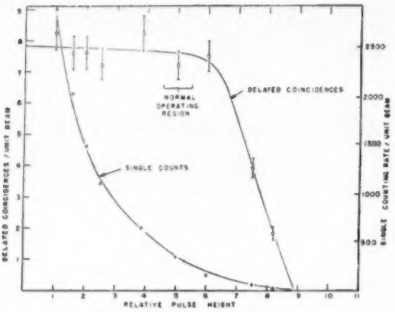

FIG. 8. Integral counting rates as a function of pulse height in channel II*a*.

serve as a check on the method, rather than as a better determination of the $\mu \rightarrow e$ decay constant.

In this connection it may be pointed out that although the apparatus detects π^+, μ^+, and μ^- mesons, all but 2–3 percent are π^+ mesons. μ^- mesons are produced at most in minute amounts, as shown by the experiments using photographic emulsion detectors.[1] The μ^- mesons which are counted are due to the 2–3 percent of the π^- mesons decaying in flight. Since both range and direction are approximately preserved in the decay, the chief effect is that besides the positive π-mesons, 2–3 percent of the negative pions are also counted. The hydrogen cross sections are not at all affected, since it is known from the work by Cook[7] in photographic emulsions that negative mesons are not produced by photons in hydrogen.

d. Angular and Energy Resolutions

The intensity of the x-ray beam limits the resolution which can be obtained without sacrificing statistical accuracy. In the geometry of Fig. 5, the detectors subtend a solid angle of approximately 0.03 sterad, an angular resolution of $\pm 7°$. The target thickness is 0.4 g/cm² in the liquid hydrogen experiments and 4 g/cm² in the subtraction experiments. The detector in which the meson stops is 2 g/cm² thick. The energy uncertainty which corresponds to this range uncertainty depends on the energy. For most of the spectrum it is approximately ± 3 Mev for the liquid hydrogen, and ± 5 Mev for the subtraction experiments. It is larger at low and smaller at high energies. Under these conditions the counting rate is approximately 10 mesons/min and a day's bombardment is required to obtain one point by subtraction with a statistical inaccuracy of 5 percent. Better angular resolution, and especially energy determination by magnetic analysis are difficult to achieve with present intensities.

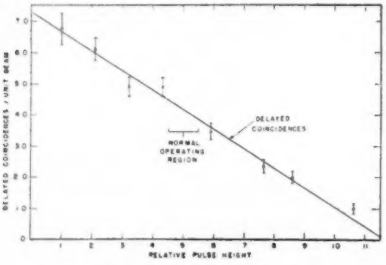

FIG. 9. Integral counting rate as a function of pulse height in channel II*b*.

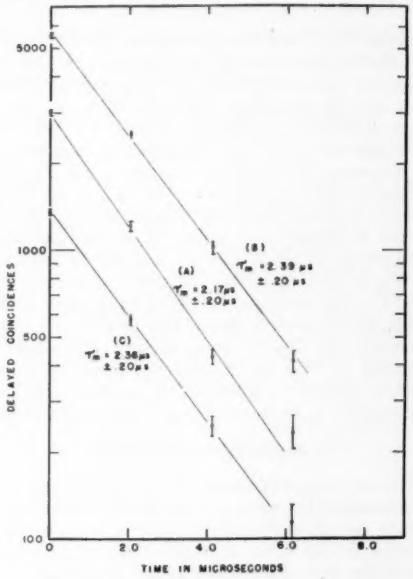

FIG. 10. Relative counting rate in the four delay channels for three sets of data.

e. Effects of Nuclear Interaction of Mesons

All methods of detecting mesons which depend on observing it at the end of its range suffer from the fact that the meson may be scattered or absorbed in nuclear collisions in the material which brings it to rest. The mean free path of 90-Mev mesons in aluminum, the absorbing material used in these experiments, has been measured and is 70 g/cm².[8] The data have been corrected for this absorption.

[7] L. J. Cook, to be published.

[8] Chedester, Isaacs, Sachs, and Steinberger, Phys. Rev. **82**, 958 (1951).

V. EXPERIMENTAL RESULTS

a. Energy Distribution of π^+ Mesons at 90° to the Beam Direction

The experiment was performed with carbon, paraffin, and liquid hydrogen targets. The geometry of the subtraction experiment is shown in Fig. 4. The targets are cylinders 2 in. high and 2 in. in diameter. The carbon target is laminated so that the ionization loss of the meson in the two targets is the same. The attenuation of the incident beam, chiefly due to pair creation, is 7 percent in the carbon, 5 percent in the paraffin target. The angular resolution is triangular, $\pm 10°$ at the base. The results are shown in Fig. 11.

Figure 12 represents the geometry, using a liquid hydrogen target. The target is designed and constructed by Cook. The energy resolution is ± 3 Mev and the angular resolution is triangular with $\pm 10°$ width at the base. Results are given in Fig. 13.

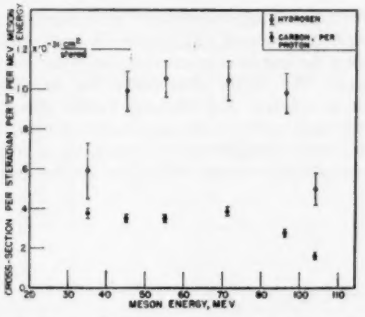

FIG. 11. Energy distribution of mesons produced at 90° by 325-Mev max energy x-rays on carbon and on hydrogen by subtraction.

As was pointed out in Sec. III, it is possible to derive the excitation function of the differential cross section from these data. Let the photon spectrum, $\phi(h\nu)$ be normalized so that

$$\int_0^{h\nu_{\max}} h\nu\phi(h\nu)dh\nu = h\nu_{\max} = 1\text{“}Q\text{”}.^9$$

Let $N(E)$ = number of mesons per unit meson energy per steradian per Q and per target atom. Then

$$d\sigma(h\nu)/d\Omega = [N(E)/\phi(h\nu)](dE/dh\nu),$$

where $h\nu$ and E are related [Eq. (1)] through the conservation laws.

The excitation function of the differential cross section for the production of π^+ mesons on hydrogen is shown in Fig. 14. Because of their superior statistical accuracy and energy resolution, only the liquid hydrogen results were used in the determination of the excitation function.

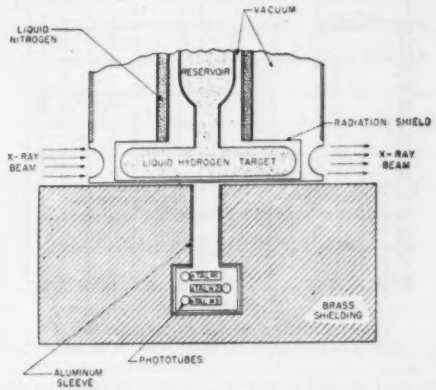

FIG. 12. Hydrogen target and geometry used in energy distribution measurements at 90°.

b. Angular Distribution

The angular distribution was also measured both by subtraction and with a liquid hydrogen target. At the various angles the meson range was chosen so that the responsible incident photons have the energy 255 Mev in the laboratory system, or 204 Mev in the center-of-mass system. The angular range was limited in the forward direction by an increasing accidental counting rate, and in the backward direction by the geometry of the apparatus. The liquid hydrogen target was designed by V. Peterseon and is shown in Fig. 15. The hydrogen is contained in an aluminum cup $1\frac{1}{2}$ in. in diameter, $1\frac{3}{4}$ in. high, and with 0.0015-in. wall thickness. The meson production in the walls of the cup is approxi-

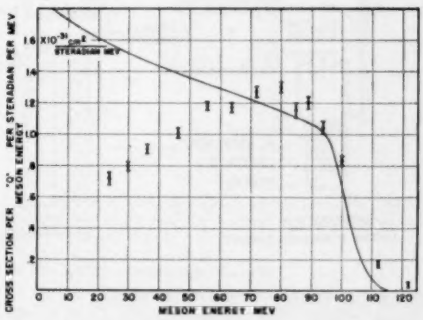

FIG. 13. Energy distribution of mesons produced by 325-Mev max energy x-rays on hydrogen, using liquid hydrogen target. Solid curve represents number of photons per unit meson energy. $\phi(h\nu)dh\nu/dE$. The derivative is calculated on the basis of formula (1).

[9] The "Q" is a unit of x-ray flux. The number of Q's incident on a target is equal to the total incident x-ray energy divided by the maximum x-ray energy.

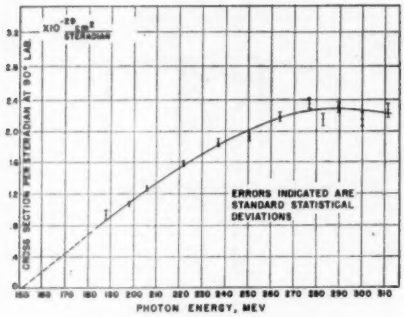

FIG. 14. Excitation function for the production of mesons by photons on hydrogen, at 90° to the beam.

mately 1 percent of that in hydrogen. The angular dispersion is triangular, ±6.5° at the base. Results are shown in Figs. 16 and 17.

c. Total Cross Section

Except for the missing experimental data at very large and very small production angles, the angular distribution data can be integrated to yield a total cross section. Twenty percent of the total solid angle lies in the unexplored region. Extrapolating the data linearly to small and large angles, we get a total cross section of $1.9\pm0.3\times10^{-28}$ cm² for the production of positive mesons on hydrogen by 255-Mev γ-rays.

VI. DISCUSSION OF RESULTS

We compare here briefly several theoretical suggestions with the experimental results. The photomeson production reaction provides a new domain for testing the theory of the interaction of the π-meson with nucleons, and it may be hoped that it will provide some new insight, and this because the reaction is particularly simple in the frame of the current approximate methods. The comparison need be made only for scalar and pseudoscalar mesons, since it is known that the pion has spin zero.[10]

The reaction has been studied theoretically from at least three points of view, which differ in the approximations used in the solution of the same equations of motion of the meson, nucleon, and electromagnetic fields.

1. Perturbation approximation.[11] It is assumed that the coupling of mesons and nucleons is weak, and the solution is the first term in an expansion in the coupling parameter. The higher order terms are increasingly difficult to evaluate. For the large known interaction of mesons and nucleons, the convergence is either slow or nonexistent. Pseudoscalar and pseudovector coupling of the pseudoscalar meson field to the nucleus give the

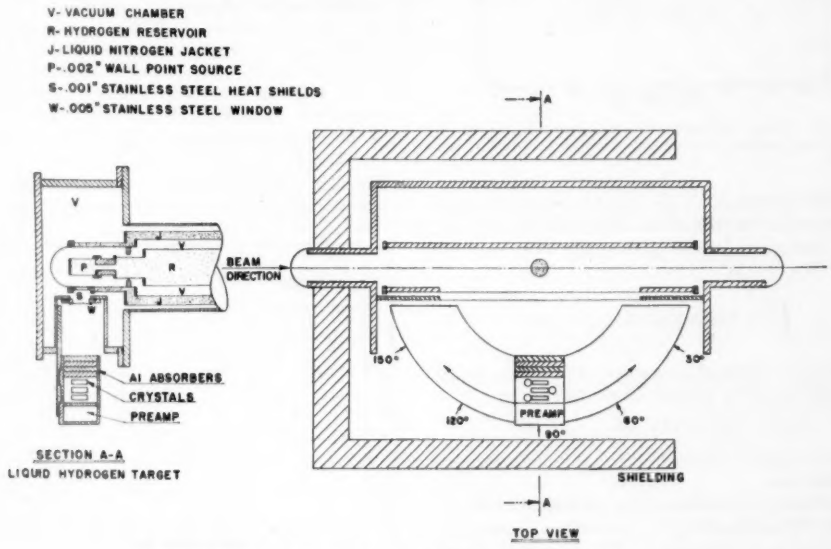

FIG. 15. Hydrogen target used in angular distribution measurements.

[10] Durbin, Loar, and Steinberger, Phys. Rev. **83**, 646 (1951); Clark, Roberts, and Wilson, Phys. Rev. **83**, 649 (1951).
[11] Perturbation theoretical results have been published by H. Feshbach and M. Lax, Phys. Rev. **76**, 134 (1949); K. A. Brueckner, Phys. Rev. **79**, 641 (1950); G. Araki, Prog. Theor. Phys. **5**, 507 (1950).

same result in the first order. The pseudovector coupling theory diverges in higher order.

2. Strong coupling or classical approximation, in the strong coupling theory[12] it is assumed that the coupling parameter is large; in the classical approximation[13] the meson field is not quantized, but the strength of the coupling is arbitrary. These approximations are equivalent and give the same results. In order to permit a solution of the equations, it must be further assumed that the nucleons are infinitely heavy (neglect of recoil) and it is necessary to introduce an effective nuclear radius of the order of the nucleon Compton wavelength to allow the convergence of certain integrals.

3. In the Tomonaga intermediate coupling approximation[14] the field equations are integrated in successive steps; the first corresponds to no mesons in the self field of the nucleon, the second to one meson, and so on. The approximations involve chiefly the choice of the approximate solutions for the meson field wave functions, as well as neglect of nuclear recoil. Because of the nonrelativistic approximations (nuclear recoil neglect), the classical (strong coupling) and Tomonaga calculations are possible only in pseudovector coupling in the case of pseudoscalar mesons.

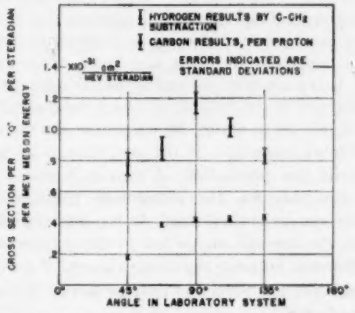
HYDROGEN RESULTS BY C-CH2 SUBTRACTION
CARBON RESULTS, PER PROTON
ERRORS INDICATED ARE STANDARD DEVIATIONS
CROSS SECTION PER 'C' PER STERADIAN PER MEV MESON ENERGY
ANGLE IN LABORATORY SYSTEM

FIG. 16. The production of mesons on carbon and on hydrogen by subtraction, at five angles. The meson energies are 48 Mev at 135°, 57 Mev at 112.5°, 67 Mev at 90°, 82 Mev at 67.5°, and 96 Mev at 135°, chosen so that the responsible photon energy in the free proton collision is 255 Mev.

Except for minor relativistic corrections present only in the perturbation theory, all three approximations give the same results. These are

$$\frac{d\sigma}{d\Omega}=-\alpha\frac{1}{4}\frac{g^2}{4\pi}\frac{k^2\sin^2\theta}{E^2h\nu^2(1-v\cos\theta)^2}\times\text{const (scalar)}, \quad (2)$$

$$\frac{d\sigma}{d\Omega}=\alpha\frac{f^2}{4\pi}\frac{k^2}{\kappa^2h\nu^2}\left[1-\frac{\kappa^2k^2\sin^2\theta}{2E^2h\nu^2(1-v\cos\theta)^2}\right]\times\text{const (pseudoscalar)}, \quad (3)$$

[12] Y. Fujimoto and H. Miyazawa, Prog. Theor. Phys. 5, 1052 (1950).

[13] K. A. Brueckner and K. M. Case, to be published. Also H. W. Lewis, private communication.

[14] K. M. Watson and E. W. Hart, Phys. Rev. 79, 918 (1950).

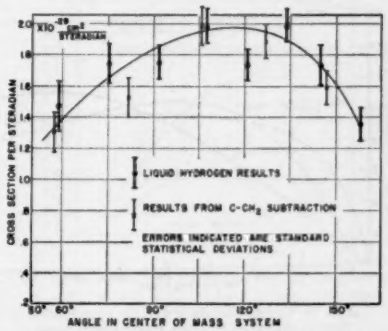
LIQUID HYDROGEN RESULTS
RESULTS FROM C-CH2 SUBTRACTION
ERRORS INDICATED ARE STANDARD STATISTICAL DEVIATIONS
CROSS SECTION PER STERADIAN
ANGLE IN CENTER OF MASS SYSTEM

FIG. 17. Angular distribution for the production of mesons by photons on hydrogen. The meson energies are as in Fig. 16.

where $\hbar=c=1$; $\alpha=1/137$; E, k=meson energy, momentum; $h\nu$=photon energy; v=meson velocity; θ=production angle of meson with respect to photon; g, f=coupling constants in scalar and pseudoscalar theory (pseudovector coupling). In pseudoscalar coupling f should be replaced by $\kappa g/2M$.

The constant is unity in the weak coupling (perturbation) limit, and has been evaluated by Watson and Hart[14] in the transition region of weak to strong coupling. In the limit of strong coupling the constant is $\frac{1}{4}$ in the scalar theory, and $\frac{1}{8}$ in the pseudoscalar theory. In Fig. 18 Watson and Hart's results are reproduced for the pseudoscalar theory in the transition region from weak to strong coupling. The relativistic perturbation result[15] is compared with the experiment in Figs. 19 and 20. The angular distribution in the scalar theory has a dipole character and is peaked at small angles because of the retardation factor $(1-v\cos\theta)^{-2}$. In

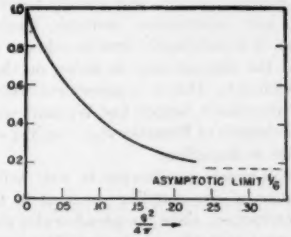

FIG. 18. The ratio of photomeson production in the Tomonaga approximation to its value in the weak coupling approximation (after Watson and Hart).

[15] The result in perturbation theory is:

$$\frac{d\sigma}{d\Omega}=\frac{\alpha}{4}\frac{f^2}{4\pi}\frac{k}{h\nu E_N E_p[1+E/M-(h\nu-p_0)E\cos\theta/kM](1+p_0/E_p)}\left\{\frac{k^2\sin^2\theta(\pm M-\mathbf{p}\cdot\mathbf{p}_0)}{E^2h\nu^2(1-v\cos\theta)^2}-\frac{k^2\sin^2\theta}{(1-v\cos\theta)Eh\nu}+\frac{\mathbf{p}\cdot h\nu}{\mathbf{p}_0\cdot h\nu}\right\}$$

where the + and − signs refer to scalar and pseudoscalar theory respectively. $\mathbf{A}\cdot\mathbf{B}$ are four-vector products. $\mathbf{p}_0$ and $\mathbf{p}$ are energy-momentum vectors of incoming and outgoing nucleons, respectively.

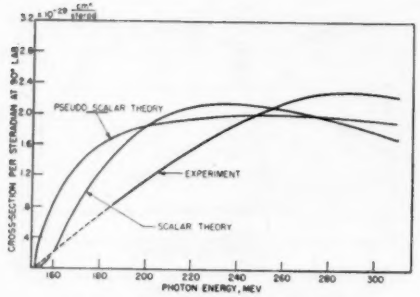

FIG. 19. Energy distribution in the perturbation theory, compared with the experimental result.

pseudoscalar theory there is also the dipole term, but the predominant term involves a change of the nucleon spin, and is isotropic. The two interfere destructively. The excitation function differs chiefly in that the scalar theory starts at threshold as $(h\nu-h\nu_0)^{\frac{1}{2}}$ and the pseudoscalar theory more steeply as $(h\nu-h\nu)_0^{\frac{3}{2}}$. Neither theory gives good experimental agreement at low meson energies in the excitation function. The energy dependence of the matrix element in pseudoscalar theory is very small, so that the pseudoscalar result in Fig. 19 is almost entirely kinematical. Comparison with the experimental results shows that the square of the matrix element actually increases with energy by a factor of approximately two in the observed energy range.

In the angular distribution, the pseudoscalar theory is in fair agreement with the experimental result, although the experimental points fall considerably below the theoretical at backward angles. The scalar results are, however, in violent disagreement. We wish to argue, that since the theoretical result is independent of the approximation used, and actually follows directly from the spin independent isotropic meson-nucleon interaction, it is sufficiently firm to rule out the possibility that the charged pion is scalar, on the basis of these experiments. This is in agreement with the conclusion of Brueckner, Serber, and Watson[16] on the basis of the experiments of Panofsky *et al.*[17] on the absorption of π-mesons in deuterium.

The photomeson production is well suited for a determination of the coupling constant in the meson nucleon interaction, since the pseudoscalar theory is in fair agreement with the experiment. The pseudovector coupling constant which gives best agreement with the angular distribution at 255-Mev photon energy is $f^2/4\pi=0.37$ in the relativistic weak coupling limit.[16] The nonrelativistic weak coupling result (Eq. (3)) requires $f^2/4\pi=0.16$. However, it may be seen from the result of Watson and Hart, Fig. 18, that this is much too high for the validity of the weak coupling approximation, and that the approximation of strong coupling is more nearly valid. The value of the coupling constant to be used in theories which do not assume its smallness must then be six times greater, or $f^2/4\pi=1.0$, in order to maintain agreement with this experiment. The inadequacies of the theory, however, prevent one from attaching significance to the exact result.

We turn to a discussion of photomeson production in a complex nucleus. Experimentally we see that the differential cross section per proton in carbon is lower than the elementary process by a factor five at 45°, and by a a factor two at 135°. The mean energy of the mesons produced in carbon is approximately 3.5 Mev lower than that in hydrogen, at 90° in the laboratory system and integrated over the continuous spectrum of the meson beam.

The additional nucleons act in two ways: (1) They interfere in the creation of the meson. (2) They may reabsorb the meson before it escapes. Effect 1 is discussed by Feshbach and Lax[18] and by Chew and Lewis.[19] The latter treats specifically the deuteron, but the arguments can be extended to more complex nuclei. It is shown, especially by Chew and Lewis, that the chief effect in the complex nucleus is the exclusion principle interference in the final state, which reduces the cross section for those states, in which the nucleons have small total momentum in the final state. This reduces markedly the production of mesons in the forward directions, because the momentum transfer to the nuclear system is then small. It has also the effect of raising the average energy left to the nuclear system, and therefore reducing the average energy of the meson, as observed. The reduction in cross section is given by a form factor

$$\sigma=\sigma_0[1-F(D)]; \quad F(D)\simeq\int\psi^2\exp(i\mathbf{D}\cdot\mathbf{r})d\mathbf{r};$$

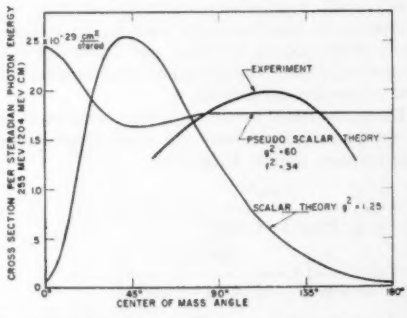

FIG. 20. Angular distribution of photomesons (photon energy 255 Mev) in the perturbation theory, compared with the experimental result.

[16] Brueckner, Serber, and Watson, Phys. Rev. **81**, 575 (1951).
[17] W. K. H. Panofsky, Phys. Rev. **81**, 565 (1951).
[18] H. Feshbach and M. Lax, Phys. Rev. **76**, 134 (1949).
[19] G. Chew and H. W. Lewis, Phys. Rev. **84**, 779 (1951).

where σ_0 = differential cross section for the elementary act; σ = differential cross section in carbon, per proton; $\mathbf{D}$ = total momentum of final nuclear system; ψ = wave function of protons in a carbon nucleus.

The simplicity of the form factor is due to a closure approximation.[19] The relation (1) is a good approximation for nuclei larger than helium. In the case of deuterium the connection is more complicated. It depends on the form of the meson-nucleon interaction, specifically, on whether or not the spin state of the nucleon changes in the process of meson emission. In the case of heavier nuclei, the Pauli interference does not depend on a possible spin change. To compare with the experiment, we need to know ψ. We use the wave function empirically determined by Chew and Goldberger[20] in an analysis of the deuteron pick-up reaction

$$\psi=(\alpha_p^3/\pi)^{\frac{1}{2}}e^{-\alpha_p r};\quad \alpha_p=1.3(\kappa c/\hbar).$$

Then

$$F(D)=\alpha_p^4/(\alpha_p^2+\tfrac{1}{4}D^2)^2.$$

It is also necessary to know the correspondence between the nuclear recoil D and the meson production momentum k, which is observed experimentally. There is no one-to-one correspondence between these quantities; except in the elementary process. However, as Chew and Lewis[19] point out, the average nuclear recoil D will be approximately equal to the corresponding recoil momentum in the case of photoproduction in hydrogen. With these assumptions it is possible to make the comparison between the theoretical and experimental results, shown in Fig. 21. The solid line shows the effect of the Pauli principle alone. The absorption mean free path for mesons of this energy is approximately 4×10^{-13} cm,[21] so that about 50 percent of the mesons produced in carbon should be reabsorbed. This correction brings the theoretical expectation below the experimental points (dotted curves, Fig. 22).[13] The theory is in agreement with the observed angular distribution, and although it overestimates the interference effect slightly, the basic assumptions are confirmed.

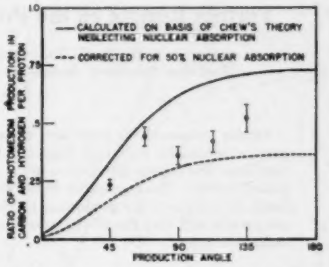

FIG. 21. Experimental and theoretical ratio of the photomeson production cross section in carbon, per proton, with respect to hydrogen.

We wish to thank Professor E. B. McMillan for the use of the synchrotron, and for his kind assistance during the course of the experiments. We are indebted to Dr. L. Cook and Dr. V. Peterson for the use of liquid hydrogen targets, and to Dr. W. Blocker and Dr. R. Kenney for the absolute calibration of the beam monitor. The bombardments were made by the operating crew of the Berkeley synchrotron under the direction of W. Gibbins and J. McFarlane.

[20] G. Chew and M. Goldberger, Phys. Rev. **77**, 470 (1950).

[21] Byfield, Lederman, and Kessler, unpublished; Isaacs, Sachs, and Steinberger, unpublished.

Further Results on the Production of Neutral Mesons by Photons*

W. K. H. PANOFSKY,† J. N. STEINBERGER,‡ AND J. STELLER
Radiation Laboratory, Department of Physics, University of California, Berkeley, California

(Received December 14, 1951)

Further measurements have been made on the photoproduction of neutral mesons using the gamma-gamma coincidence technique. New data have been obtained on the gamma-gamma correlation curves in beryllium. The angular distribution of the photomesons in Be has been determined and found to be strongly peaked forward. The dependence on the atomic number A of production has been found to obey an $A^{\frac{2}{3}}$ law. Some data obtained for production in hydrogen show that the π^0 and π^+ production cross sections are comparable and that the π^0 excitation curve starts more slowly from threshold than does the π^+ photo-excitation curve.

A. INTRODUCTION

IN a previous paper[1] we have discussed the evidence for photoproduction of neutral mesons. Since the time of our last report, considerable progress has been made concerning our information on this particle. The charge exchange reaction[2] has given evidence as to the mass of the π^0 meson. Sachs and Steinberger[3] have shown that the π^0 formed by π^- capture in hydrogen gives gamma-gamma coincidences, as has been established for photoproduced π^0's. Also, further data on the production of π^0 mesons from proton collisions are available.[4] Cosmic-ray evidence[5] in photographic plates has shown that $\pi^\pm$ mesons are produced by primaries in comparable numbers if one infers that single electron-positron pairs correlated to high energy stars are evidence of π^0 mesons. Thus there is now evidence as to the existence of a π^0 meson and also as to its spin.

B. INSTRUMENTATION

This paper deals with further results on the photoproduction in the 325-Mev x-ray beam of the Berkeley synchrotron. The geometrical disposition of internal target, x-ray collimation, π^0 production target, and detectors is essentially the same as previously reported (Fig. 1). The x-ray beam is collimated by lead collimators 6 in. thick inserted in a thick lead wall shielding the detecting apparatus from the stray radiation from the synchrotron. The beam has a diameter of approximately $1\frac{1}{2}$ in. at the point where it strikes the π^0 production target. The detection apparatus consists of two "γ-ray telescopes," each telescope consisting of a set of three crystal counters. The crystals are stilbene units of size $\frac{5}{8}$ in.$\times 1\frac{3}{4}$ in.$\times 1\frac{3}{4}$ in., mounted in light shields with one of their narrow sides facing a 1P21 photomultiplier. Each telescope consists of the following sequence: (a) anticoincidence crystal; (b) converter; (c) coincidence crystal; (d) absorber (usually omitted); (e) coincidence crystal. An event constitutes a "count" if in each of the two telescopes, the crystals (c, e) respond to a particle at minimum ionization or more and (a) does not.

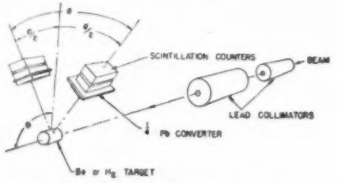

FIG. 1. Geometry of detection apparatus for observing γ-γ coincidences from π^0 disintegrations. The "correlation angle" ϕ and "telescope plane angle" θ (approximately the π^0 production angle) are indicated.

A block diagram of the electronics is shown in Fig. 2. The coincidences and anticoincidences are made in multivibrator circuits of about 10^{-7} sec resolving time developed by Wouters. Each telescope is again put in coincidence with the other, both with a similar circuit as well with a fast (10^{-8} sec) distributed amplifier coincidence circuit developed by Wiegand and described

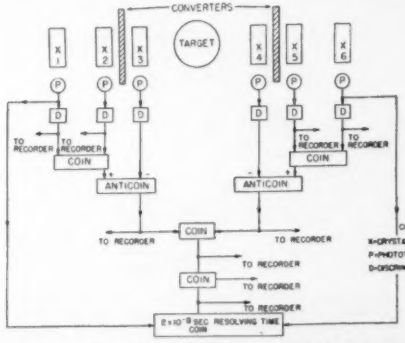

FIG. 2. Block diagram of electronics used in detecting γ-γ coincidences.

* This work was performed under the auspices of the AEC.
† Now at Stanford University, Stanford, California.
‡ Now at Columbia University, New York, New York.
[1] Steinberger, Panofsky, and Steller, Phys. Rev. **78**, 802 (1950). References to earlier evidence concerning the π^0 given in this paper.
[2] Panofsky, Aamodt, and Hadley, Phys. Rev. **81**, 565 (1951).
[3] A. Sachs and J. Steinberger, Phys. Rev. **82**, 973 (1951).
[4] Hales, Hildebrand, Madey, Crandall, Knable, and Moyer, private communication, and Phys. Rev. **83**, 206 (1951).
[5] Carlson, Cooper, and King, Phil. Mag. **41**, 701 (1950).

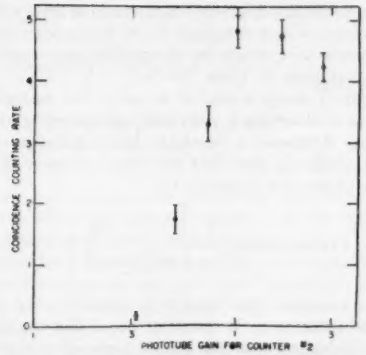

FIG. 3. Observed coincidence counting rate observed as a function of photomultiplier voltage. Within the rather poor statistics a plateau is indicated on this and similar runs.

elsewhere.[6] The accidental coincidence rate is defined by the resolution of this single fast coincidence unit; the coincidence counting rate of each separate telescope corresponds to real events.

Figure 3 shows a curve of quadruple coincidence counting rate as a function of photomultiplier gain. These and similar curves showed that operation took place on a reasonable plateau.

In our previous paper[1] we have discussed the arguments underlying the identification of the quadruple coincidence counts with γ-γ coincidences from the decay of a π^0. This argument is essentially as follows:

(a) The particles counted in each telescope are non-ionizing initially but are converted into ionizing radiation at the converter.

(b) Data on the conversion as a function of converter thickness and converter material are in agreement with the initial non-ionizing radiation being γ-rays but not neutrons.

(c) The range of the ionizing conversion products (for details, see Sec. C), shown to be electrons, corresponds to a γ-ray energy of the correct magnitude in agreement with the disintegration kinematics of a π^0 of mass $\sim$135-Mev into two γ-rays.

(d) The resultant spectra as a function of the correlation angle ϕ, notably the existence of a minimum correlation angle ϕ, (see Sec. C), is in agreement with the kinematical relationship appropriate to π^0 disintegration.

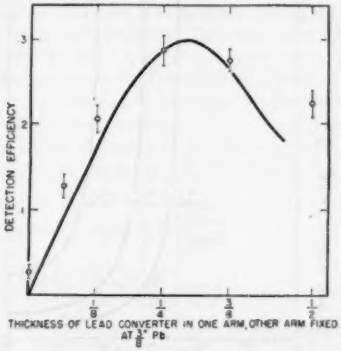

FIG. 4. Calculated and observed detection efficiency of the γ-ray pairs as a function of converter thickness in one telescope arm.

[6] Clyde Wiegand, Rev. Sci. Instr. **21**, 975 (1950).

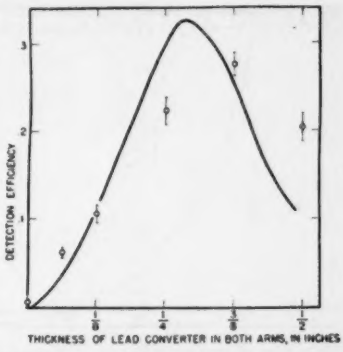

FIG. 5. Calculated and observed detection efficiency of the γ-ray pairs as a function of converter thickness in both telescope arms.

In evaluating absolute cross sections the efficiency of the detector must be evaluated and also the beam must be monitored absolutely. The detection system is such that a γ-ray will be detected if it produces at least one electron which (a) has enough range to penetrate to the second crystal after ionization and radiation loss, and (b) has not scattered out. The efficiency on this assumption is approximately calculable as a function of converter thickness and of γ-ray energy. Figures 4 and 5 show the calculated efficiency as a function of converter thickness in one or both of the telescopes, respectively. These are compared with the experimental transition curves taken at $\phi=\theta=90°$. The corresponding γ-ray energy under this condition is nearly constant

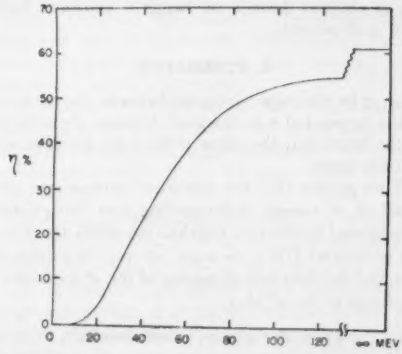

FIG. 6. Calculated detection efficiency of a telescope as a function of γ-ray energy.

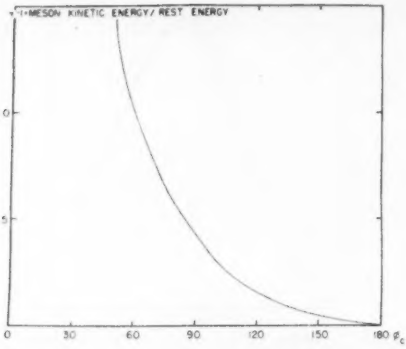

FIG. 7. Plot of the minimum correlation angle ϕ_c against γ = ratio of meson kinetic energy/meson rest energy.

and of order 100 Mev. Figure 6 shows the calculated efficiency as a function of γ-ray energy, for a $\frac{1}{4}$-in. lead converter. Note that the efficiency drops very rapidly for small γ-ray energies; this is a result of the decrease in pair cross sections in conjunction with the requirement as to minimum range of at least one of the electrons.

The average of the γ-rays to be detected lies above half the π^0 rest energy. The reason is that solid angle considerations favor those disintegrations in which the γ-rays are Doppler shifted toward higher energy. A value for the mean efficiency of 0.50 is thus not unreasonable.

The x-ray beam of the synchrotron was monitored by an integrating ionization chamber placed ahead of the collimator in the fringing field of the synchrotron. This chamber was calibrated by the method of Blocker, Kenney, and Panofsky[7] and was recalibrated occasionally during these measurements. The authors are indebted to Blocker and Kenney for carrying out these recalibrations. It is believed that the absolute energy flux of photons through the target is known to better than ± 20 percent.

C. KINEMATICS

Let ϕ be the angle subtended between the telescopes at the target. Let θ be the angle between the direction of the beam and the plane defined by the telescopes and the target.

If we assume that the coincident gamma-rays are a result of π^0 mesons disintegrating into two photons, then several kinematical relations governing the process can be derived. If θ_0 is the angle between the gamma-ray pair and the direction of motion of the π^0 measured in the frame of the π^0, then

$$\sin(\phi/2)=\gamma^{-1}/(\gamma^{-2}\cos^2\theta_0+\sin^2\theta_0)^{\frac{1}{2}}, \qquad (1)$$

where $\gamma=E/E_0=1/(1-\beta^2)^{\frac{1}{2}}$ is the ratio of total relativistic energy to rest energy of the π^0. For a given energy no gamma-rays should be observed at any angle less than that given by $\sin(\phi_c/2)=\gamma^{-1}$.

Figure 7 shows a plot of ϕ_c *vs* γ. The probability $P(\phi)d\phi$ of observing a γ-ray pair corresponding to a π^0 velocity β between a correlation angle ϕ and $\phi+d\phi$ is given (with the fact that the γ-ray emission in the frame of the π^0 is isotropic) by

$$P(\phi)d\phi=\sin\phi\frac{1}{(1-\mu)^{\frac{1}{2}}}\frac{d\phi}{\beta\gamma[(1-\mu)\gamma^{-2}-2]^{\frac{1}{2}}}, \qquad (2)$$

where $\mu=\cos\phi$. This function is shown in Fig. 8 for several values of γ. It should be noted that the probability is highest near the critical correlation angle ϕ_c, and hence we have a near one-to-one correspondence between observed correlation angle and π^0 velocity. This one-to-one correspondence is of course not exact; for a distribution of velocities the probability $P(\phi)$ will be an integral of (2) over a range of velocities from the lowest value permitted for a given ϕ to the highest value energetically possible.

The counting rate of a given counting geometry can be analyzed by treating the problem as if the coincidence resulted from the correlation probability (2) without any further reference to the π^0 motion proper.

Let $\Delta\Omega_1$ and $\Delta\Omega_2$ be the solid angle subtended by the limiting aperture of each telescope at the production target.

Let $N(\gamma)d\gamma d\Omega$ be the probability that a π^0 be emitted between energy γ and $\gamma+d\gamma$ into a solid angle $d\Omega$.

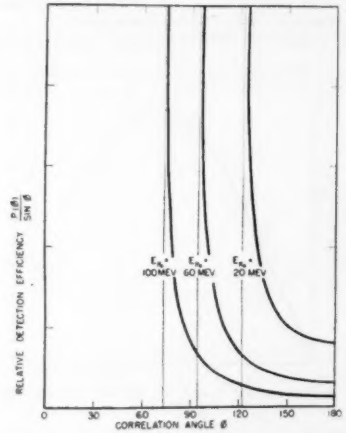

FIG. 8. Plot of $P(\phi)/\sin\phi$ [see Eq. (2)] against the correlation angle ϕ for three values of the meson energy. This function is the relative detection probability for a given correlated γ-ray pair.

[7] Blocker, Kenney, and Panofsky, Phys. Rev. **79**, 419 (1950).

The probability of a coincidence count is then

$$C(\phi)=2\int_{\epsilon}^{\gamma_{max}} P(\phi)d\phi N(\gamma)d\gamma\cdot\Delta\Omega_1\cdot\frac{\Delta\Omega_2}{2\sin\phi d\phi}$$

$$=\frac{\Delta\Omega_1\Delta\Omega_2}{\pi}\int_{\gamma_c}^{\gamma_{max}}\frac{N(\gamma)d\gamma}{\beta\gamma[(1-\mu)\gamma^{-2}-2]^{\frac{1}{2}}}. \quad (3)$$

Here $\gamma_c=[2/(1-\mu)]^{\frac{1}{2}}$ is the lower limit of energy corresponding to a given μ, and γ_{max} is the energetic upper limit of the production process.

Equation (3) constitutes an integral equation between the counting rate and the π^0 production probability as a function of energy. Its inversion will be discussed later. Note that for a given value of the detector plane angle θ (see Fig. 1), the integral (3) averages over a small range of π^0 production angles; only in the case $\theta=\pi/2$ is the production angle fixed. However, for the range of angles used this fact will be ignored and the detector plane angle will be identified with the π^0 production angle.

The curve of efficiency *vs* γ-ray energy (Fig. 6) gives rise to a discriminatory effect on the energy spectrum of the π^0's as calculated from the angular correlation curves by means of Eq. (3). The reason is that near $\phi\approx\phi_c$ both γ-rays will have high energy and thus be detected efficiently, while near $\phi\sim 180°$ one of the two γ-rays will have low energy if the γ^0 energy is large. Hence the one-to-one correspondence between the correlation angle ϕ and the π^0 energy is actually even better than that implied by the integrand of Eq. (3).

D. RANGE OF CONVERSION ELECTRONS FROM γ-RAYS

Figure 9 shows the geometrical arrangement used in measuring the range of the conversion electrons. Space did not permit using beryllium absorbers entirely; for greater ranges than 22 g/cm² Be, a mixture of Be and Cu absorbers was used. The radiation straggling is thus not as small as it could be. The data were taken at $\theta=70°$, $\phi=90°$ with $\frac{1}{16}$-in. Pb converter in the arm of the telescope containing the absorber. Figure 10 shows a plot of the counting *vs* the g/cm² of absorber in one of the arms of the telescope in Fig. 9. For a correlation angle of $\phi=90°$ the mean π^0 velocity is $\beta=0.73$; hence the energy per γ-ray is $\frac{1}{2}E_0/(1-\beta^2)^{\frac{1}{2}}=0.73E_0$. The

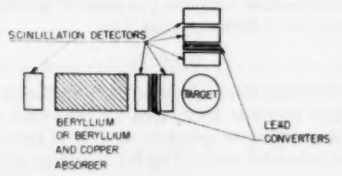

FIG. 9. Disposition of scintillation crystals, lead converter, and absorbers in the experiment attempting to determine the range of conversion electrons from the π^0 γ-rays.

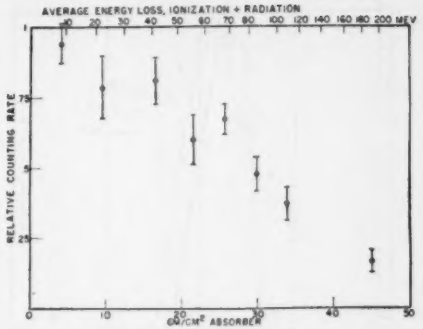

FIG. 10. Absorption curve of conversion electrons as observed in the geometry of Fig. 6.

observed mean electron energy of the more energetic of the pair electrons is 80±12 Mev; the corresponding γ-ray energy is essentially 4/3 of this amount or with the more exact pair energy division probabilities, 110±17 Mev. Hence, $E_0=150\pm23$ Mev, in agreement with the measurements obtained from the γ-ray spectrum from the charge exchange absorption of the π^- meson.[2]

E. PHOTOPRODUCTION IN BERYLLIUM

A series of runs was made studying the yields of photomesons from beryllium. These measurements constitute improvements over the work previously reported.[1] The target was a Be cylinder with its axis perpendicular to the plane defined by the telescopes, 1½ in. long and 4½ in. diameter; the beam diameter at the target was ¾ in. The telescopes were positioned such that the farthest crystal was at a distance of 7 in. from the center line of the Be cylinder. The converters used were lead sheets of ¼-in. thickness and 1½ in.×3 in. in size. The limiting aperture is thus the last crystal which is approximately 1¾ in.×1¾ in. in size.

Figure 11 shows the observed correlation curves. These were taken at three values of the angle θ. Table I shows a typical tabulation of the counting rates observed in the various channels.

The qualitative picture as to the γ^0 disintegration kinematics underlying these spectra is well confirmed. Note that the minimum angle decreases in the forward direction as a result of the increased upper limit of meson energy.

The observed correlation curves enable us to evaluate the energy distribution of the π^0 mesons approximately. Equation (3) constitutes an integral equation for the energy distribution. The $\theta=90°$ curve would yield the energy distribution of π^0 mesons emitted at 90°. The curves at other values of θ correspond to π^0 trajectories in the plane defined by the counters and the target. Not all of these correspond exactly to emission at an

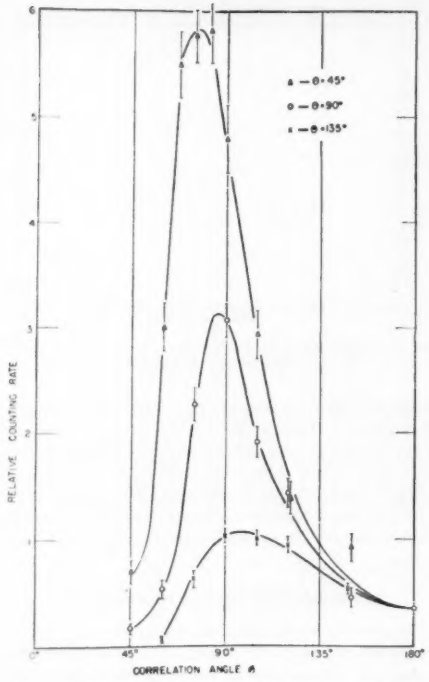

FIG. 11. Relative coincidence counting rates as a function of correlation angle ϕ for three values of the telescope plane angle θ. Beryllium target.

angle θ; however, the deviation is small enough to be neglected here.

The integral equation can be inverted by formal methods. It turns out, however, that the accuracy of the observations is not sufficient to make effective use of such procedures. The most practical means of inversion is to assume that the true energy distribution is "synthesized" out of a finite number (say N) of energy distributions constant over a given energy interval. If we assume such distributions to have arbitrary amplitudes A_N, then the A_N can be determined by fitting the observed correlation curve at N points and solving N linear equations. The correlation curve $\theta=\pi/2$ has been fitted by this means. The assumed distribution is shown in Fig. 12. Figure 13 shows a comparison of the correlation curve calculated on the basis of the energy distribution of Fig. 12 and the experimental data. It is clear that although the observed correlation curves are not very sensitive to details in the energy distribution, they are sufficiently sensitive to give the relative amounts of low energy and high energy contributions in the distribution. The reason is that each high energy component will contribute intensity between the corresponding lower limiting correlation angle and 180°.

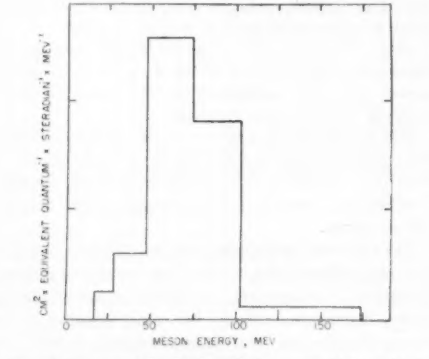

FIG. 12. An energy distribution of π^0 mesons which would give rise to the γ-ray correlation curves of Fig. 11 for $\theta=90°$ in beryllium. The fit is made with six "square step" distributions of suitably adjusted amplitude.

TABLE I. Tabulation of coincidence counting rates corresponding to π^0 photoproduction in beryllium.

ϕ \ θ	Counts per 8.3×10^{13} effective quanta 45°	90°	135°
180°	0.59	0.59	0.59
150°	1.66	0.81	0.97
120°	2.48	2.58	1.71
105°	5.28	3.44	1.83
90°	8.65	5.46	1.87
82½°	10.5	—	—
75°	10.4	4.1	1.14
67½°	9.9	—	—
60°	5.4	0.95	0.12
45°	1.26	0.21	—

Hence if the high energy components already account for the entire intensity at $\phi=180°$, then very little low energy components can be present. This is actually the case here as shown in Fig. 12. Figure 14 shows in contrast the expected correlation curve if the π^0 energy distribution had been identical with the π^+ photomeson distributions reported by Steinberger and Bishop.[8] Clearly the actual π^0 distribution rises more slowly from its limit than does the γ^+ distribution. We shall discuss this point later.

A remark might be made here concerning the meaning of a cross section for these processes. If we define the number Q of "effective quanta"[9] by

$$Q=U/k_0, \qquad (4)$$

there U is the total energy of the x-ray beam and k_0 its upper energetic limit, then we can define a cross section per effective quantum directly in terms of the data as tabulated above. This is a consistent procedure,

[8] J. Steinberger and A. Bishop, preceding paper, Phys. Rev. 86, 171 (1952).
[9] R. F. Mozley, Phys. Rev. 80, 493 (1950).

but one would prefer in the theoretical interpretation of most of these data to have a true cross section per photon at a definite photon energy. Such a cross section can be derived from this data approximately if we assume:

(a) That the one-to-one correspondence between correlation angle ϕ and the meson velocity is exact, i.e., if the curves of Fig. 5 were δ-functions located at a mean correlation angle.

(b) That the production kinematics of the π^0 in various materials is the same as on a free nucleon, i.e., that there is a unique relationship between π^0 and primary photon energy.

We shall shortly obtain the absolute cross sections in these two interpretations.

The estimate of the absolute cross section per effective quantum can be made by use of the curves of Fig. 6. Let η = detection efficiency of each telescope; let $\Delta\Omega$ solid angle subtended by each telescope at the target. The number $P(\phi, \theta)$ of pairs counted is then

$$P(\phi, \theta) = N(\phi, \theta)(\Delta\Omega/2\pi \sin\phi)(\Delta\Omega)\eta^2 \times 2, \qquad (5)$$

where $N(\phi, \theta)$ is the number of gamma-pairs emitted per unit solid angle in θ and per unit plane angle in ϕ. We take $\eta = 0.50$, $\Delta\Omega = 0.063$. If the total number of quanta in the beam passing through the target of N atoms/cm^3 corresponding to the beam is Q, the cross section is thus,

$$d\sigma/d\Omega = (3160/NQ) \int P(\phi, \theta) \sin\phi d\phi$$

$$\sigma = (3160/NQ) \int\int P(\phi, \theta) 2\pi \sin\theta \sin\phi d\phi d\theta. \qquad (6)$$

Numerical integration of the data of Table I gives

θ	$(d\sigma/d\Omega) \times 10^{29}$ cm^2/effective quantum/steradian
45°	4.41
90°	3.13
135°	1.06

$\sigma = 3.7 \times 10^{-28}$ cm^2/effective quantum.

These are the cross sections per effective quantum; to obtain the cross section per quantum at a given energy, some further analysis is necessary. The number of quanta in a primary x-ray energy interval dK is very closely given by

$$dQ = Q(dK/K), \qquad (7)$$

where Q has been defined above. The differential cross section per quantum per unit solid angle of π^0 emission is thus,

$$\frac{d\sigma}{d\Omega} = \left(\frac{\pi \sin\phi d\phi}{\Delta\Omega}\right) \frac{P(\phi, \theta)}{NQ(dK/K)} \frac{1}{\Delta\Omega} \frac{1}{\eta^2}$$

$$= (3160/NQ) P(\phi, \theta) \sin\phi K(d\phi/dK). \qquad (8)$$

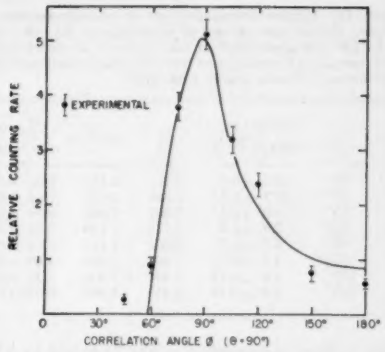

FIG. 13. The smooth curve is the calculated γ-γ correlation curve under the assumption of the energy distribution of Fig. 12. The experimental data are given for comparison.

This can be evaluated if $d\phi/dK = (d\phi/d\gamma)(d\gamma/dK)$ is unique. $d\phi/d\gamma$ can be replaced by the derivative of the mean value of ϕ, averaged over the distributions $P(\phi)$ of the type plotted in Fig. 8. $d\gamma/dK$ can be calculated from the kinematics of photocollisions with single nucleons for a given value of incident photon energy.

If measurements are made at that given ϕ for each value of θ corresponding to the mean value of the correlation curve for a fixed primary photon energy at the particular θ, then this one set of measurements is sufficient to generate an angular distribution $d\sigma/d\Omega$ at that value of photon energy underlying the choice of the ϕ's.

Table II shows the set of measurements made at values of ϕ to correspond to a primary photon energy of 260 Mev.

Since the corresponding data for the angular distributions of π^0's photoproduced in H, are not available

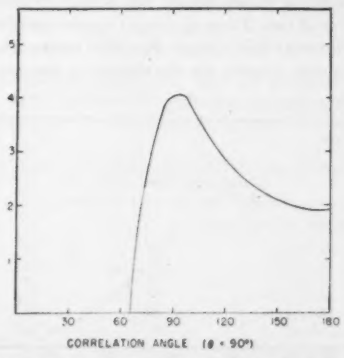

FIG. 14. Correlation curve which would have been expected if the energy distribution of π^0 mesons were identical to the π^+ meson spectrum photoproduced from hydrogen at 90° as observed by Steinberger and Bishop (see reference 8).

TABLE II. Angular distribution of π^0 photoproduction in beryllium. Entries are calculated according to Eq. (8) with $N=6.1\times10^{22}/\sin\theta$ atoms/cm² to take account of the obliquity of the target. $d\gamma/dK$ is computed from the production kinematics on free nucleons. Photon energy = 260 Mev.

θ	ϕ	Counts per 8.3×10^{19} effective quanta	$\frac{d\gamma}{dK}$	$\sin\phi\frac{d\phi}{d\gamma}$	$\frac{d\sigma}{d\Omega}\times10^{29}$ cm²/steradian
34°	70°	10.2 ±0.6	0.911	0.755	4.66 ±0.27
45°	75°	10.5 ±0.5	0.858	0.900	7.64 ±0.36
55°	80°	8.0 ±0.4	0.801	1.060	6.69 ±0.33
67½°	82½°	7.9 ±0.4	0.728	1.150	7.36 ±0.37
90°	90°	5.5 ±0.26	0.602	1.414	5.62 ±0.26
112°	97½°	3.2 ±0.24	0.506	1.660	3.00 ±0.22
135°	105°	1.8 ±0.13	0.444	2.000	1.35 ±0.10
150°	115°	1.36±0.16	0.415	4.000	0.676±0.08

at this writing, the question might be raised to what extent the data of Table II, plotted in Fig. 15, are representative of the angular distributions of π^0's produced on a free proton. Three effects would make the two distributions differ:

1. The Be cross section includes production both from protons and neutrons.

2. The internal motion of the nucleons in Be in combination with the steep excitation of the π^0 photoproduction process would favor π^0's produced from nucleons moving toward the x-ray source.

3. The exclusion principle would modify the distribution somewhat, since the energy available to the proton recoil is a function of the π^0 emission angle. This effect is not very significant since the nucleon retains its identity in π^0 emission.

In agreement with the analogous situation in the case of π^+ production[8] we therefore believe that the photoproduction of π^0 mesons would lead to a still more forward distribution than that given in Fig. 15.

The integrated cross section for 260-Mev photons is 5.55×10^{-27} cm². Note that this is almost twice as large as the value quoted per effective quantum. This is quite reasonable since the excitation of the process rises quite slowly near threshold.

The absolute values quoted here should be accurate to a factor of two. Three significant figures are given to permit internal comparison. Probable errors refer to statistics only. Clearly the distribution is directed well forward in contrast to the corresponding curves for charged meson production.

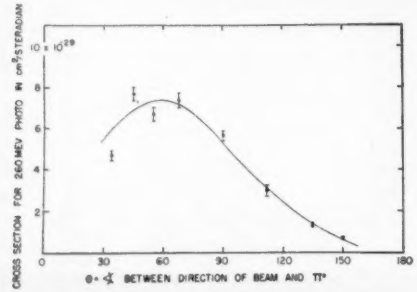

FIG. 15. Cross section per 260-Mev photon for π^0 production in beryllium as a function of production angle.

F. Z DEPENDENCE OF PRODUCTION

The Z dependence of π^0 production was studied by measuring the yield of gamma-gamma coincidences at $\theta=45°$ and $\phi=75°$. The results are tabulated as follows. The targets were either solid cylinders (C and Be) or the material inserted in Bakelite cylinders (Li, Al, Cu, and Pb). Similarly to the experimental difficulties in the work on the Z dependence of charged photomesons,[9] it turned out to be difficult to accumulate satisfactory statistics for heavy elements.

The yield per nucleon is a decreasing function of Z. In fact, if the yield per nucleon is plotted against $A^{-\frac{1}{3}}$ a straight line is obtained. Figure 16 shows a plot of the neutral meson yield per nucleon and a yield of the π^+ yield per proton (according to Mozley[9]) plotted against $A^{-\frac{1}{3}}$. Both sets of data are compatible with a straight line dependence. Since it appears thus that the yield is proportional to the nuclear surface and since the mean free path for photons in nuclear matter is large, we can conclude that the meson mean free path within the nucleus is not in excess of a small multiple of $\hbar/\mu c$. This is in agreement with the recent experiments on nuclear interaction of mesons.[10]

TABLE III. γ-γ coincidence counts as a function of Z of target material.

Material	g/cm²	counts/monitor/nucleon	Number of counts observed
Li	2.71	0.190±0.012	365
Be	8.80	0.148±0.007	458
C	8.09	0.145±0.009	307
Al	1.51	0.126±0.012	129
Cu	0.90	0.077±0.010	74
Pb	0.39	0.051±0.020	20
H (see section G)		0.208±0.029	

G. YIELD FROM HYDROGEN

The data on the π^0 yield from hydrogen are as yet incomplete and the data presented here must be considered preliminary. The hydrogen cross section has been measured by two methods: (a) subtraction method CH_2 (polyethylene) *vs* C and (b) production in liquid H_2.

(a) Subtraction Method.

The two targets employed in the subtraction method were constructed as follows:

1. CH_2 target—cylinder: height—2.000 in.; diameter—1.627 in.; weight—62.97 g; total surface density—4.70 g/cm²; carbon surface density—4.03 g/cm².

2. C target—cylinder constructed of $\frac{1}{16}$ in. graphite layers perforated by $\frac{1}{8}$ in. holes in random fashion: height—1.947 in.; diameter—1.630 in.; weight—54.16 g; surface density—3.94 g/cm².

[10] Bernardini, Booth, and Lederman, Phys. Rev. **83**, 1277 (1951); M. Camac, *et al.*, Phys. Rev. **83**, 1075 (1951); Phys. Rev. **82**, 745 (1951).

The carbon target thus represents the carbon content of the CH_2 target to a fair degree of approximation.

Data tere observed with the telescopes set at $\theta=90°$, $\phi=90°$. The results are given in Table IV. We obtain thus,

$$\sigma_{90°}(\text{hydrogen})/\sigma_{90°}(\text{carbon})=0.120\pm0.025.$$

Assuming that the correlation functions for H and Be are similar, we obtain an estimate for the total cross section,

$$\sigma=0.60\times10^{-28}\ \text{cm}^2/\text{effective quantum at 320 Mev.}$$

Because of the difficulty in obtaining adequate statistics with a subtraction method, no data on the angular distribution and correlation function were taken.

(b) Liquid H_2 Target.

The target used was constructed by Leslie Cook of this Laboratory[11] and the authors are greatly indebted to him for permission to use the instrument. The target essentially constitutes a line source of two in. diameter. This line source was surrounded by a lead cylinder 1 in. thick. A slit cut into the cylinder defined the effective length of the line source. Since the geometry of the

TABLE IV. Data on π^0 yield from CH_2 and C.

	CH_2	C	Difference
Total count	1157	911	···
Accidentals	44	59	···
Net count, corrected to equal carbon content	1098	885	213±45

hydrogen target made a large distance from the target to the counters necessary, larger counters were required to maintain a sufficient solid angle. These counters were made of cylindrical Pyrex containers 4 in. in diameter and 1 in. in height filled with a solution of terphenyl in xylene. 1P28 photomultipliers were used to "look" at the solution through a 1-mm thick Pyrex window sealed onto the edge of the vessel. This system leads to a fairly nonuniform light signal as a function of position of a fast electron track; hence very high photomultiplier gains were required to operate on a plateau. This leads, of course, to an unfavorable ratio of singles to doubles count and hence of accidental coincidences to real events. With this exception, the arrangement and the electronics were as described above and as previously reported.[1]

Data were taken with and without liquid hydrogen in the hydrogen target. The background as a result of the empty target averaged 30±5 percent. Statistics were insufficient to justify point-by-point correction of the observed data. A correction factor of 0.70±0.05 was thus applied to the hydrogen data. Table V shows the data observed. These data are plotted in Fig. 17.

[11] Leslie Cook, University of California Radiation Laboratory Report No. 990 (1950).

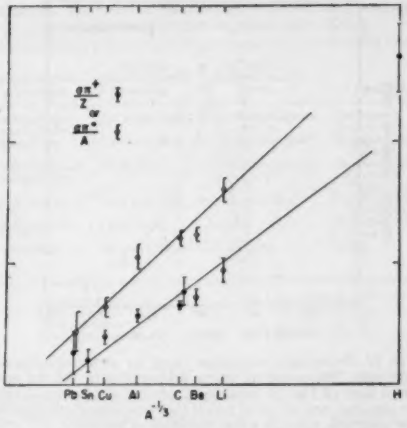

FIG. 16. Cross section of π^0 production per nucleon and cross section of π^+ production per proton according to Moxley (see reference 9) plotted against $A^{\frac{1}{3}}$ where A is the atomic number. Note that the yield varies linearly with nuclear area.

We can again use these data to estimate an absolute cross section. With $\Delta\Omega=0.1$; $\eta=0.50$; effective source length = 5.0 cm, we obtain since

$$\frac{d\sigma}{d\Omega}(\theta)=\frac{\pi}{NQ\eta^2}(\Delta\Omega)^2\int_0^\pi P(\phi,\theta)\sin\phi d\phi$$

$$=4.3\times10^{-30}\int P(\phi,\theta)\sin\phi d\phi$$

$$\text{cm}^2/\text{steradian/effective quantum.} \quad (9)$$

Hence,

$d\sigma/d\Omega(90°)$
$=3.5\times10^{-30}\ \text{cm}^2/\text{steradian/effective quantum};$

$d\sigma/d\Omega(45°)$
$=8.2\times10^{-30}\ \text{cm}^2/\text{steradian/effective quantum.}$

The total cross section can then be estimated to be 0.55×10^{-28} cm²/effective quantum, in good agreement with the result derived from the subtraction method.

TABLE V. Correlation curves for γ-γ coincidences from liquid hydrogen.

ϕ	θ	count/1.39×10⁸ effective quanta
48°	90°	0.11±0.04
67½°	90°	0.76±0.07
90°	90°	0.89±0.09
112°	90°	0.25±0.04
135°	90°	0.17±0.03
157°	90°	0.06±0.03
67°	45°	3.96±0.30
90°	45°	1.14±0.10
135°	45°	0.38±0.07
157°	45°	0.35±0.07

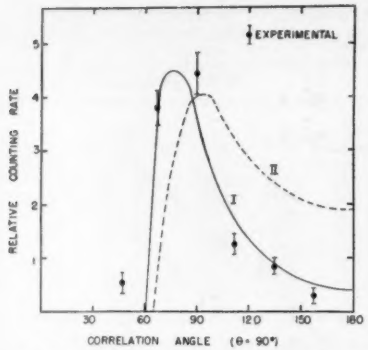

FIG. 17. Preliminary correlation curve for π^0 photoproduction in hydrogen. Shown are (a) the experimental data, (b) the curve (dotted line) of Fig. 14, expected if π^0 and π^+ photoproduction were identical, and (c) (solid curve) the correlation curve expected if the spectrum were the 4-step spectrum of Fig. 18.

The data of Fig. 17 are very similar to the beryllium data of Fig. 11. A step distribution fitting the hydrogen data is shown in Fig. 18. We can therefore conclude definitely that the excitation function for π^0 produced by photons has a higher order contact as compared to the production of charged photomesons.

These data are in agreement as to excitation function with the data reported by Silverman and Stearns.[12] Silverman and Stearns obtain the excitation function in a somewhat more direct manner by measuring the coincidence yield between the recoil proton and one of the two gamma-rays. They confirm the form of the excitation curve and their absolute cross section agrees with ours.

H. DISCUSSION

In their more elementary and "noncontroversial" interpretation, these data principally add to the phenomenology of neutral mesons. The experiments show again that a particle of rest energy of the order of 135 Mev disintegrates into two and only two photons. The particles are of strong nuclear interaction as evidenced by their internal nuclear absorption. The lifetime of the particles is sufficiently long that they are definitely "real," i.e., the decay takes place outside the nuclear field. These properties define the particle and show it to be almost certainly identical with the π^0 inferred from the experiments in high energy nucleon collision in the laboratory and in cosmic rays and identical to the product of charge-exchange scattering of charged π^- mesons.

The two-γ-decay fixes the spin of the π^0 meson as zero or an integer greater than or equal to 2.

In addition to yielding information on the property of the particle itself, these experiments give data on the photoproduction process of π^0 mesons. The more obvious features of the process are:

1. The cross section on nucleons is of the same order; in fact roughly one-third of the production process for positive charged mesons.
2. The excitation function of the π^0 production exhibits a higher order contact near threshold as compared to charged photomeson production. This fact and the absolute cross section is in agreement with the work of Silverman and Stearns.[12]
3. The angular distribution for π^0 photomesons at a given photon energy is strongly peaked forward, in contrast to the π^+ data.
4. The Z dependence of production, other than for exclusion principle effects, of π^0 and π^+ are in agreement.

Because of the similarities between charged and neutral mesons in many respects and also because of the experimental evidence concerning charge independence of nuclear forces, it appears worthwhile to review the relation of these experimental results with the prediction of charge symmetrical meson theory. We shall discuss here only results based on considering the meson to have spin zero and odd intrinsic parity (pseudoscalar); we are thus excluding the possibilities of spin greater than 1.

The mode of π^0 decay precludes spin 1, and recent experimental evidence[13,14] on the reaction $\pi^+ + n \rightleftarrows p + \gamma$ makes the value zero for the π^+ spin a certainty. An even parity spin zero (scalar) meson is ruled out by the results on absorption of π^- mesons in deuterium[2] and also by the photoproduction of π^+ mesons.[3]

In Table VI[15–22] we list the principal calculations on

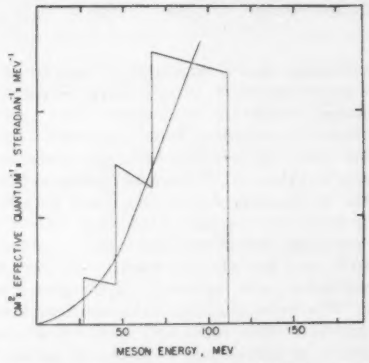

FIG. 18. Step-energy spectrum compatible with the γ-γ correlation data from π^0 photoproduction at $\theta = 90°$.

[12] A. Silverman and M. Stearns, Phys. Rev. **83**, 206 (1951).

[13] Clark, Wilson, and Roberts, Phys. Rev. **83**, 649 (1951).
[14] Durbin, Loar, and Steinberger, Phys. Rev. **83**, 646 (1951).
[15] K. Brueckner, Phys. Rev. **79**, 641 (1950).
[16] G. Araki, Prog. Theoret. Phys. **6**, 507 (1951).
[17] K. Brueckner and K. Watson, private communication.
[18] M. F. Kaplon, Phys. Rev. **83**, 206 (1951).
[19] Aidzu, Fujimoto, and Fukudo, Prog. Theoret. Phys. **6**, 193 (1951).
[20] Y. Fujimoto and H. Miyazawa, Prog. Theoret. Phys. **5**, 1052 (1950).
[21] K. A. Brueckner and K. M. Case, Phys. Rev. **83**, 1141 (1951).
[22] S. D. Drell, Phys. Rev. **83**, 555 (1951).

photomeson production based on charge symmetric, pseudoscalar theory. These calculations were not offered as predictions but rather as possible explanations of these and other data as they became known. Perturbation calculation to order g^2 which had given results in good agreement with the π^+ photoproduction cross section failed to give satisfactory results here;[15,16] such a calculation fails to predict a sufficiently large cross section nor does it give the forward angular distribution observed. Carrying calculations to higher order[17] raises the cross section but also does not give the correct angular distribution. Furthermore it is difficult to take an expansion seriously whose second term exceeds the first and where an estimate of the discarded terms is lacking.

Kaplon[18] and Aidzu, Fujimoto, and Fukudo[19] include the static anomalous magnetic moment of the proton explicitly in a second-order calculation. This gives fair agreement with the absolute cross section, although the angular distribution is still in disagreement with the experimental results. This procedure, as has been pointed out by the authors themselves, is at best an arbitrary one; if the over-all systematics of meson theory were correct, the effect of the anomalous moment, which is in itself a consequence of the interaction of the nucleon with the meson field, would automatically be taken care of in the calculation if it could be carried consistently to 4th order. It is only the difficulties of a consistent meson theoretical calculation of the moments which motivates this phenomenological approach.

Perhaps more interesting is the discovery[20,21] that the isobaric state of the nucleons which is characteristic of strong coupling theory gives rise to resonances in the photoproduction of mesons. This has been shown in the classical[21] and strong coupling[20] approximation. Assuming an isobaric state of excitation 250–300 Mev, rough agreement with all the π^0 production data presented here results. The phenomenological magnetic moments, however, are also used here. At the same time the predicted resonance in the π^+ spectrum is probably contrary to the experimental data.[8] There exists therefore at present no theoretical study of π^0 photoproduction which is free from logical inconsistencies and which fits all the experimental data as they are known at present.

TABLE VI. The principal calculations on photomeson production based on charge symmetric pseudoscalar theory.

Meson-nucleon interaction	Nucleon-electromagnetic coupling	Type of approximation used	Authors
Pseudoscalar or pseudovector	No Pauli term	Perturbation theory to order g^2	Brueckner[a] Araki[b]
Pseudoscalar	No Pauli term	Perturbation theory to order g^4	Brueckner and Watson[c]
Pseudoscalar and pseudovector	Pauli term	Perturbation theory to order g^2	Kaplon,[d] Aidzu, Fujimoto, Fukudo[e]
Pseudovector	No Pauli term	Strong coupling	Fujimoto and Miyazawa[f]
Pseudovector	Pauli term	Classical	Breuckner and Case[g]
Pseudovector	No Pauli term	Spin+charge classical	Drell[h]

[a] See reference 15.
[b] See reference 16.
[c] See reference 17.
[d] See reference 18.
[e] See reference 19.
[f] See reference 20.
[g] See reference 21.
[h] See reference 22.

I. ACKNOWLEDGMENTS

This work has been executed with the cooperation of many members of this laboratory. The authors are particularly indebted to the synchrotron crew under the direction of George McFarland for their efficient cooperation. Alex Stripeika assisted in the maintenance of the electronics. In its later phases Calvin Andre and John Foster assisted in the execution of the experiment. Finally, the authors would like to express their appreciation to Professor Edwin McMillan for his active interest in this experiment.

The Measurement of the In^{113*} Conversion Coefficient with a Scintillation Spectrometer†‡

THOMAS B. COOK, JR.,§ AND SHERWOOD K. HAYNES
Vanderbilt University, Nashville, Tennessee

(Received September 24, 1951)

The internal conversion coefficient of the 0.39-Mev isomeric transition of In^{113*} has been determined with a scintillation spectrometer by measurements which involve only gamma-gamma and electron-electron intensity comparisons. A value of $\alpha = 0.55 \pm 0.03$ is obtained for the total conversion coefficient of this transition. Thus the K-conversion coefficient is 0.46 ± 0.03 if one uses the K to L conversion ratio of 5.4 ± 0.8 as determined by Lawson and Cork. This value is in good agreement with the value of 0.47 which is obtained from Rose's tables for magnetic 2^4-pole radiation.

I. INTRODUCTION

THE measurement of a conversion coefficient is important because it is one of the quantities which may be determined experimentally as a check on the accuracy and internal consistency of present theories of electromagnetic transitions. It is particularly significant to obtain accurate measurements of conversion coefficients now that the accurate theoretical values of K-conversion coefficients are obtainable from Rose's tables.[1]

The fundamental difficulty in measuring conversion coefficients is that gamma-ray and electron intensities must be compared. If this comparison must be made directly, the errors in the determination of the relative efficiencies of the detecting devices for the two radiations result in a somewhat uncertain value of the conversion coefficient. However, in the case of an electromagnetic transition which is immediately preceded or followed by a simple beta-spectrum, the conversion coefficient may be determined with a magnetic beta-ray spectrometer by a comparison of the area under the conversion lines with the area under the beta-spectrum. An accurate determination may be made if the decay scheme is known and is fairly simple, a thin source is used, and the necessary extrapolations and integrations are performed carefully.

When these conditions cannot be fulfilled other methods must be used. Ionization chambers and coincidence-calibrated Geiger counters have frequently been used.[2] Waggoner *et al.*[3] have discussed rather carefully some other methods for measuring conversion coefficients with a magnetic beta-ray spectrometer, all of which involve the absolute determination of gamma-ray intensity.

The determination of the conversion coefficient of transitions which are not immediately preceded or followed by beta-spectra is the subject of this paper. The particular transition which is discussed, illustrative of the application of a scintillation spectrometer to conversion coefficient measurements, is the 0.39-Mev isomeric state of In^{113*} which is produced from Sn^{113} by orbital capture.[4]

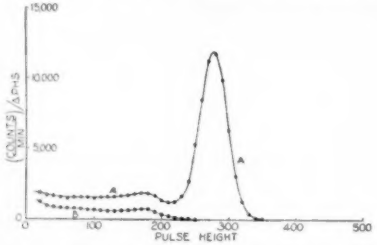

FIG. 1. Sn^{113} data. Curve A represents the total counting rate; curve B represents the counting rate with 0.240-inch Lucite absorber.

II. CONVERSION COEFFICIENTS BY SCINTILLATION SPECTROMETER. ABSOLUTE METHODS

Since an anthracene scintillation spectrometer[5] is sensitive to both electrons and gamma-rays, it seems that such a spectrometer might be useful for the absolute determination of conversion coefficients. The spectrometer used in this study consisted of a rectangular anthracene crystal (1.2 cm thick × 7.6 cm^2), an RCA 5819 photomultiplier, a regulated high voltage power supply, an A1A preamplifier,[6] a Model 204B Atomic Instrument Company linear amplifier, a pulse-height differential analyzer,[7] and an Atomic Instrument Company binary scaler. The negative high voltage for the photomultiplier was monitored by a type K potentiometer. All of the pieces of equipment were operated

† This work has been supported by the Research Corporation and a contract with the AEC.

‡ A preliminary report of this work is given in Phys. Rev. **83**, 875 (1951).

§ This work was carried out in partial fulfillment of the requirements for the degree of Doctor of Philosophy of Thomas B. Cook, Jr. at Vanderbilt University. Present address: Sandia Corporation, Albuquerque, New Mexico.

[1] Rose, Goertzel, Spinrad, Harr, and Strong, Phys. Rev. **83**, 79 (1951).

[2] See the references given in E. Segrè and A. C. Helmholz, Revs. Modern Phys. **21**, 271 (1949).

[3] Waggoner, Moon, and Roberts, Phys. Rev. **80**, 920 (1950).

[4] Thomas, Haynes, Broyles, and Thomas, Phys. Rev. **82**, 961 (1951).

[5] W. H. Jordon and P. R. Bell, Nucleonics **5**, 30 (1949).

[6] W. H. Jordon and P. R. Bell, Rev. Sci. Instr. **18**, 703 (1947).

[7] Francis, Bell, and Gundlach, Rev. Sci. Instr. **22**, 133 (1951).

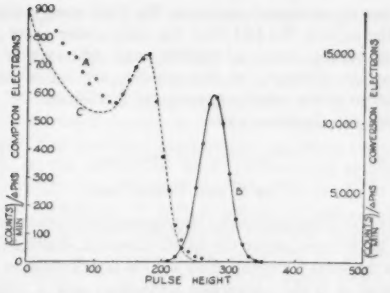

FIG. 2. Isolated conversion and Compton electron curves of In^{113} as taken from the Sn^{113} data: Curve A gives the Compton electron distribution from 0.39-Mev gamma-ray; curve B, the conversion electron lines from the 0.39-Mev transition; curve C is the theoretical Compton distribution corrected for resolving power and fitted to the experimental data at high energies.

from Sola constant voltage transformers. The ΔPHS (the interval on the pulse-height scale in which pulses were recorded) was 10 units on the pulse-height scale.

The first source studied was In^{113*}. A thin source of area$\sim$1 cm^2 was prepared on mica ($\sim$1 mg/cm^2) by the evaporation of a solution of Sn^{113} to dryness. The source was placed 34 mm above the crystal which was covered with a thin aluminum reflector.

The Sn^{113} data are shown in Fig. 1. The peak in the Sn^{113} data is due to electrons ($\sim$0.36 Mev) from internal conversion of the 0.39-Mev gamma-ray of In^{113*}. The lower curve on the Sn^{113} plot was obtained by insertion of a 6-mm Lucite absorber between the source and the crystal. Thus one essentially obtains the pulse-height distribution from the recoil Compton electrons produced in the crystal. The gamma-ray intensity is reduced approximately seven percent by the Lucite absorber.

In principle the conversion coefficient of In^{113*} can be obtained by comparison of the area under the electron spectrum with that under the Compton distribution. In fact, however, many uncertainties enter such a calculation. For instance, it is known from the magnetic electron spectrum of this particular source material[4] that there are no electrons emitted between 0.36 Mev and 28 kev, yet the spectrum of Fig. 4 shows a roughly constant continuum in this region. Presumably this continuum arises from electrons which are backscattered from the mica source backing, from electrons which pass through the corners of the crystal, and to a much greater extent from electrons which are backscattered out of the crystal before dissipating their full energy. These same factors distort the shape of the Compton distribution, and also the absorption of In x-rays increases the counting rate in the low pulse-height region. This is illustrated by Fig. 2 in which the theoretical Compton distribution, after account has been taken of the finite resolution of the spectrometer, is shown.

In addition to these difficulties there remains the effective difference in geometry for electron absorption from that for gamma-ray absorption. This difference is difficult to evaluate accurately.

An almost identical source of Au^{198} was studied to see whether a scintillation spectrometer could be used for conversion coefficient determinations by the comparison of the area under the conversion lines with that under the beta-spectrum as with a magnetic spectrometer. The data are given in Fig. 3, which shows the intense beta-spectrum with an end point of about 0.96 Mev.[8] Superimposed on this are the conversion electron lines from the 0.411-Mev[9] gamma-ray transition of Hg^{198} which follows the beta-decay. After the Compton distribution is subtracted the K and L conversion electron contributions can be resolved by an analysis of the data. The K-conversion electrons have an energy of about 0.33 Mev and the L-conversion electrons about 0.40 Mev. The data taken with the 6-mm Lucite absorber between the source and the crystal again show the energy distribution of the Compton recoil electrons.

A Kurie plot of the electron spectrum of Au^{198} is shown in Fig. 4. The gradual upward curvature of the Kurie plot is largely the result of the same backscattering which distorted the Sn^{113} spectrum. A simple anthracene spectrometer is therefore not suitable for conversion coefficient determinations by area comparisons because the relative areas under the conversion lines and the beta-spectra cannot be accurately determined. If the excited state is not time coincident with the beta-spectrum, a split crystal spectrometer[10] should eliminate this backscattering difficulty. In the time-coincident case, a collimated beta-ray and conversion electron beam entering a hole in an anthracene crystal

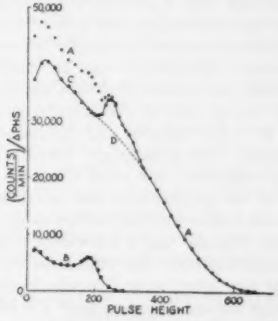

FIG. 3. Au^{198} data. Curve A gives the total counting rate; curve B, the counting rate with a 0.240-inch Lucite absorber; curve C, the total counting rate minus the gamma-ray counting rate (corrected for absorption of gamma-rays in Lucite); curve D, the calculated beta-spectrum.

[8] L. M. Langer and H. C. Price, Jr., Phys. Rev. **76**, 641 (1949).
[9] DuMond, Lind, and Watson, Phys. Rev. **73**, 1392 (1948).
[10] B. H. Ketelle, Phys. Rev. **80**, 758 (1950).

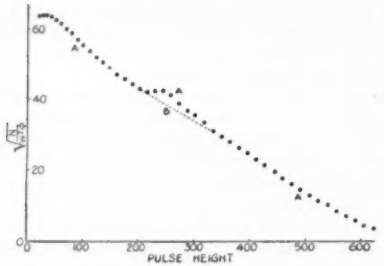

FIG. 4. Kurie plot of the Au^{198} beta-spectrum. Curve A gives the Kurie plot after subtraction of the gamma-ray counting rate; curve B, the assumed Kurie plot if conversion lines were not present.

which traps the backscattered electrons should permit accurate comparisons of areas.[11]

III. CONVERSION COEFFICIENTS BY SCINTILLATION SPECTROMETER. COMPARISON METHOD

Since certain conversion coefficients can be accurately determined by comparison of conversion and beta-ray areas, and since Rose's tables[1] give accurate values of K-conversion coefficients when the multipole order of the transition is known, a method of comparing unknown to known conversion coefficients should prove useful. Such a comparison has been made to determine the conversion coefficient of the 0.39-Mev transition of In^{113*} in terms of the K-coefficient of the 0.411-Mev transition of Hg^{198}.

Although the areas under the electron peaks in Figs. 1 and 3 do not accurately represent the absolute yield of conversion electrons, the percentage backscattering in each should be nearly the same since the transition energies differ by only 5 percent. If the peaks can be isolated, the ratio of the areas will give very closely the ratio of conversion electrons emitted by the two sources.

The Compton distributions can be similarly compared, provided the experimental data are used only at at the high energy end of the distributions so that differences in x-ray energies and intensities do not affect the areas. The pulse-height distribution which should be produced by the recoil Compton electrons from each of the gamma-rays was calculated graphically from the theoretical distribution as given by the Klein-Nishina formula[12] and a knowledge of the resolution of the spectrometer. The resolution curve of the spectrometer was taken to be Gaussian in shape, with with an energy dependence given by:[13] $a^2=kE$, where a is the half-width of the line at $1/\epsilon$ of the maximum, E is the energy of the electrons, and k is a constant. The value of k was determined from the widths of the conversion lines. The calculated distributions were fitted to the experimental curves in the high energy region of the curves. We feel that the areas under these two fitted curves, corrected for the small difference in the detection efficiency of the crystal, are an accurate measure of the relative gamma-ray intensities.

One can therefore write

$$N_{\mathrm{In}}{}^{e}/N_{\mathrm{In}}{}^{\gamma}=Y_1\alpha_{\mathrm{In}}/C_{\mathrm{In}}, \tag{1a}$$

$$N_{\mathrm{Hg}}{}^{e}/N_{\mathrm{Hg}}{}^{\gamma}=Y_2\alpha_{\mathrm{Hg}}/C_{\mathrm{Hg}}, \tag{1b}$$

where N^e is the area under the conversion electron peak, N^γ is the area under the fitted Compton distribution, C is the total Compton cross section per electron in the crystal, α is the conversion coefficient, and Y, which contains all the scattering and geometrical uncertainties, is a slowly varying function of the conversion-electron and gamma-ray energies involved. The difference in the value of Y for the two transitions is difficult to evaluate but should be very small for an energy difference of 5 percent. Therefore, Y_1 is assumed to be the same as Y_2. Hence

$$\alpha_{\mathrm{In}}=\alpha_{\mathrm{Hg}}(N_{\mathrm{In}}{}^{e}/N_{\mathrm{Hg}}{}^{e})(N_{\mathrm{Hg}}/N_{\mathrm{In}})(C_{\mathrm{In}}/C_{\mathrm{Hg}}). \tag{2}$$

Thus the determination of α_{In} in terms of α_{Hg} involves only electron-electron and gamma-gamma comparisons. To determine whether or not the assumption of the equality of Y_1 and Y_2 is valid, data were also taken on the 0.661-Mev[14] isomeric transition of Ba^{137*} as shown in Fig. 5. These data were also used to determine the value of the In^{113*} conversion coefficient. If the value of α given by the Ba^{137*} comparison is near to that given by the Hg^{198} comparison, one may be assured that the difference in the Y values for In^{113*} and Hg^{198} does not cause any appreciable error in the conversion coefficient obtained from the Hg^{198} comparison.

The data taken on Cs^{137} with no absorber (Fig. 5) between the source and crystal show two beta-spectra. The intense low energy spectrum has an upper energy of 0.52 Mev[15] and the weak high energy spectrum has an end point of 1.2 Mev.[16] Superimposed on these beta-spectra is the conversion electron peak (0.624 Mev) due to internal conversion of the 0.661-Mev isomeric transition of Ba^{137*}. The lower curve shows the pulse-height spectrum of the Compton electrons produced in the crystal.

The determination of the areas in Eq. (2) involves separation and isolation of each component. The isolation and area determination of the Compton distributions has already been discussed. Each of the sources presents characteristic difficulties, however, in the isolation of the conversion electron peaks. In the Sn^{113} data the upper and major portions of the peak are free from any other contributing radiations, and the low pulse-height section has been extrapolated to zero intensity on the assumption that the peak is symmetri-

[11] R. C. Davis and P. R. Bell, Phys. Rev. **83**, 483 (1951).
[12] A convenient chart of the Klein-Nishina formula has been compiled by J. A. Wheeler and collaborators at Los Alamos.
[13] J. I. Hopkins, Rev. Sci. Instr. **22**, 29 (1951).
[14] L. M. Langer and R. D. Moffat, Phys. Rev. **78**, 74 (1950).
[15] M. A. Waggoner, Phys. Rev. **82**, 906 (1951).
[16] L. M. Langer and R. D. Moffat, Phys. Rev. **82**, 635 (1951).

cal. The isolated In^{113*} conversion peak is shown in Fig. 2.

The first step in isolating the conversion electron peaks from the Hg^{198} transition was to make a Kurie plot of the Au^{198} data, which is shown in Fig. 4. This beta-spectrum is known to be of the allowed type.[17] A straight line was drawn in under the conversion electron peaks on the Kurie plot. One criterion used to place the straight line was that the ratio of the K to L-plus-M conversion electron intensities fall near to the measured values of this quantity. However, before this ratio could be evaluated it was necessary to allow for the conversion electrons that produce pulses which do not fall under the conversion electron peak. As noted previously in the case of the Sn^{113} data there is a residual continuum of backscattered electrons in the region of the pulse-height scale below the conversion peak about nine percent as high as the maximum of the conversion electron peak. In the analysis of the In^{113*} conversion line the low energy side of the peak was extrapolated to zero intensity on the assumption that the peak is symmetrical. If we assumed that the shape of the beta spectrum in the vicinity of the conversion electron peaks is as given by the dotted straight line on the Au^{198} Kurie plot (Fig. 4), we should be neglecting the effect of this backscattered continuum for the Hg^{198} conversion lines. To correct for this continuum the scattered electron intensity was assumed to be the same percentage of the maximum of the Hg^{198} conversion electron peak as in the case of In^{113*}. Thus the base line for the Hg^{198} conversion lines was made to correspond to the base line which was used for the calculation of the conversion electron intensity of In^{113*}.

By drawing the straight line in the position shown in Fig. 4, performing the inverse of the process used to make the Kurie plot, converting to the same base line as was used for the In^{113*} conversion peak, and assuming a Gaussian line shape to extrapolate the low intensity region of the K-conversion electron peak to zero intensity, we obtain a value of 2.8 to 1 for the ratio of K to L-plus-M conversion electron intensities. The values given in the National Bureau of Standards Circular No. 499 on nuclear data range up to 2.7 to 1, as given by Saxon and Heller.[18] The isolated Hg^{198} conversion electron peaks are shown in Fig. 6.

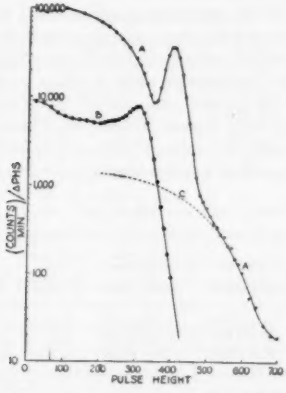

FIG. 5. Cs^{137} data. Curve A gives the total counting rate; curve B, the counting rate with a 0.240-inch Lucite absorber; curve C, the calculated 1.2-Mev beta-spectrum.

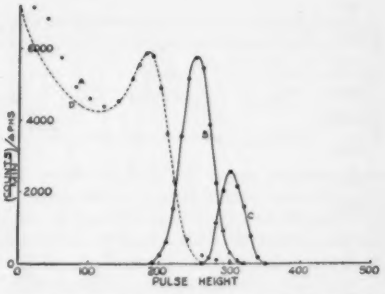

FIG. 6. Isolated conversion and Compton curves from Au^{198} data. Curve A gives the observed Compton electron distribution from the 0.411-Mev gamma-ray of Hg^{198}; curve B, the K-conversion electrons from the 0.411-Mev transition; curve C, the $L+M$ conversion electrons from the 0.411-Mev transition; curve D, the theoretical Compton distribution corrected for resolving power and fitted to the observed distribution at high energies.

The first step in isolating the Ba^{137*} conversion electron peak was to make a Kurie plot of the 1.2-Mev beta-spectrum of Cs^{137}. To simplify the calculations, this high energy contribution has been deducted on the assumption that its distribution follows a straight line allowed Kurie plot. The distribution which has been subtracted from the total counting rate to allow for the high energy spectrum is shown by the dotted line in Fig. 5. After this contribution has been subtracted, the conversion electron peak still overlaps with the lower beta-spectrum. The peak was assumed to be symmetrical, and the shape of the now isolated upper tail was used to extrapolate the lower portion of the curve. This isolated curve is shown in Fig. 7 together with the experimental and theoretical Compton distributions. The areas under the three conversion lines and the three fitted Compton distributions were then numerically evaluated, giving the results shown in Table I.

IV. CALCULATION OF THE In^{113} CONVERSION COEFFICIENT

The conversion coefficient of In^{113*} was determined by substitution of the values of Table I into Eq. (2). However, it is necessary to justify the values given in column 5 for the conversion coefficients of the Hg^{198} and Ba^{137*} transitions. For the Hg^{198} K-conversion

[17] L. M. Langer and H. C. Price, Jr., Phys. Rev. **76**, 641 (1949).

[18] D. Saxon and R. Heller, Phys. Rev. **75**, 909 (1949).

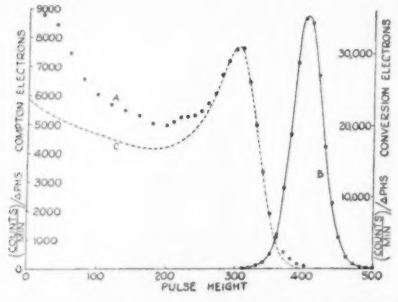

FIG. 7. Isolated conversion and Compton curves form Cs^{137} data. Curve A gives the Compton electron distribution from the Ba^{137} 0.661-Mev gamma-ray; curve B, the conversion electrons from the 0.661-Mev transition; curve C, the theoretical Compton distribution corrected for resolving power and fitted to the observed distribution at high energies.

coefficient the average of the experimental values, which are given in the National Bureau of Standards Circular No. 499 on Nuclear Data, is 0.030. This is in good agreement with the value of 0.031 obtained from Rose's tables[1] for electric quadrupole radiation, and differs by a factor of two and one-half or more from that predicted for any other multipolarity of the radiation. The half-life predicted by Weisskopf's formula[19] for this transition is about 10^{-10} second which is not in disagreement with the half-life value of less than 3×10^{-9} second as determined experimentally by Bell and Petch.[20] Thus, from the agreement between theory and experiment it is reasonable to use the value of 0.031 as the K-conversion coefficient of the Hg^{198} transition.

The K-conversion coefficient of the Ba^{137*} transition was taken to be 0.097 as given by Rose's tables for magnetic 2^4-pole radiation. This is the value recently determined experimentally by Waggoner;[16] however, there is a wide range of values in the literature for this conversion coefficient. The half-life of the Ba^{137*} isomeric state also agrees well with the value obtained from Weisskopf's formula for magnetic 2^4-pole radiation. By the use of a K to L ratio of five as given by Osaba,[11] the total conversion coefficient for this transition becomes 0.116.

In order to determine the conversion coefficient of In^{113*} by comparison with Hg^{198}, it was decided to use only the K-conversion line of Hg^{198} because the area under the K-conversion peak is not very sensitive to the shape of the beta-spectrum which must be subtracted in order to isolate the conversion peaks. This calculation of α for In^{113*} gives a value of 0.55 conversion electrons per gamma-ray. By comparison with the Ba^{137*} data we obtain a value of 0.64 for the conversion coefficient of In^{113*} after a one and one-half percent correction for the difference in absorption of the gamma-rays by the Lucite absorber has been made.

It is difficult to account for the discrepancy between the two values. If the assumed K to $L+M$ conversion ratio for Ba^{137*} is too high, part of the discrepancy can be accounted for. The major energy-dependent factor in the Y's in Eq. (1) is the backscattering of electrons from the crystal. One would expect less scattering for the higher energy and hence a low value of α determined from comparison with Ba^{137*}. A comparison of the intensities of the beta-spectra and conversion electron peaks of Au^{198} and Cs^{137} seems to indicate that the scattering is less in the latter case. Further experimentation is necessary to understand the cause of the discrepancy between the two values of α and to make possible accurate comparisons between conversion lines of very different energies. Since the energy dependence of the Y's in Eq. (1) introduces only about 20 percent difference for an energy difference of about 60 percent it is unlikely that more than 2 or 3 percent error results from an energy difference of only 5 percent. There are also small errors in the values given which arise from the assumption that the electron peaks are symmetrical. However, since this assumption was used only to extrapolate the low intensity sections of the curves and was applied in the same way to all curves, the error involved in the final value could only be one percent or less. The correction to the Hg^{198} data for the scattered electron intensity is only an approximation; however, the total error introduced by neglecting this effect is about ten percent and hence the residual error could be only one or two percent at most. The assumed shape of the beta-spectrum under the Hg^{198} conversion electron peaks is a possible source of error, but again, a reasonable error to be associated with this effect is only a few percent.

In view of the probable errors involved the value which is given for the total conversion coefficient of the 0.39-Mev isomeric transition of In^{113*} is $\alpha=0.55\pm0.03$.[21] If the K to L conversion ratio is taken to be 5.4 as determined by Lawson and Cork,[22] the K-conversion coefficient of In^{115*} is about 0.46 ± 0.03. This is in good agreement with the value of 0.47, which is the value obtained from Rose's tables for magnetic 2^4-pole radia-

TABLE I. Numerical values used in Eq. (2).

Transition	Conversion area counts/min	Compton distribution area counts/min	Compton cross section $(e^2/mc^2)^2$	Conversion coefficient
In^{113*}	61.7×10^3	1.324×10^4	4.05	
Hg^{198}	29.9×10^{3a}	1.128×10^4	4.00	$\alpha_K=0.031$
Ba^{137*}	196.4×10^3	17.9×10^4	3.02	$\alpha_K=0.097$

[a] K-conversion line only.

[19] See R. D. Hill, Phys. Rev. **81**, 470 (1951).
[20] R. E. Bell and H. E. Petch, Phys. Rev. **76**, 1409 (1949).
[21] See reference 4 for a summary of previous measurements of α for In^{113*}. These measurements do not agree with each other or with theory.
[22] J. L. Lawson and J. M. Cork, Phys. Rev. **57**, 982 (1940).

tion. The magnetic 2^4-pole assignment gives the best agreement between the measured half-life and the theoretical half-life calculated from Weisskopf's formula. Table II shows this agreement. Thus, from the agreement between theory and experiment is is reasonable to conclude that the multipolarity of the electromagnetic radiation from the decay of the 0.39-Mev isomeric state of In^{113*} is magnetic 2^4-pole. This assignment predicts an angular momentum change of ± 4 units and a change of parity as shown in the decay scheme of D. A. Thomas *et al.*[4]

It is thought that the comparison method for measuring conversion coefficients, described in this paper, may offer better ultimate accuracy than any other method now used for the determination of the conversion coefficient of an isomeric transition which is not accompanied by a beta-spectrum. The accuracy of the method should be considerably increased by the use of a hollow crystal scintillation spectrometer[11] to reduce the effect of electron scattering out of the crystal.

TABLE II. Half-life of 0.39-Mev radiation from In.

In^{113*}	Electric 2^3	Half-life Electric 2^4	Magnetic 2^4
Weisskopf theory	4.9×10^5 min	0.8 min	6.6×10^2 min
Measured			1.04×10^3 min

Note added in proof:—A recent magnetic beta-ray spectrum of the Cs^{137} used in this work indicates the presence of several (upper limit 7 or 8) percent Cs^{134}. Almost if not all of the Cs^{137} discrepancy can be accounted for by the extra Compton electrons from the Cs^{134} gamma-rays.

VI. ACKNOWLEDGMENTS

The authors wish to acknowledge the generous advice and assistance given by P. R. Bell, J. I. Hopkins, and M. Tidwell. We also wish to acknowledge the help of Dr. G. E. Boyd in obtaining the enriched Sn^{113} activity and of Dr. P. F. Hahn for the Au^{198}

PHYSICAL REVIEW VOLUME 86, NUMBER 2 APRIL 15, 1952

The Shapes of Negative Beta-Spectra at the Low Energy End*

HERMAN M. SCHWARTZ
University of Arkansas, Fayetteville, Arkansas
(Received December 10, 1951)

The disposition of the excess atomic binding energy liberated in a negative beta-decay is of interest in connection with the shape of the low energy end of the beta-spectrum. Previous theoretical work points to the carrying away of this energy by the beta-particle in most cases, with a resulting practical cutoff at the low end of the energy spectrum. However, the present approach, in which the nuclear and atomic electron transitions are treated as a unified process, leads to the conclusion that to the first order that shape is practically unaffected. A possibility for experimental study of this question is pointed out.

I. INTRODUCTION

THIS note is concerned with the following question: What experimentally verifiable predictions can be made at present regarding the low energy end shapes of the spectra of negative beta-emitters for which the beta-decay theory of the corresponding bare nucleus can be taken as known? This question should apply, in the light of presently accumulated evidence, at least to the case of beta-transitions of the theoretically allowed type.

The condition of "experimental verifiability" cannot be applied, of course, with any high degree of precision. It does, however, delimit our problem within certain practical bounds. Thus, it appears to be hardly within the scope of present measuring techniques to determine reliably the effect upon spectral shapes of such second-order processes associated with beta-decay as the so-called inner bremsstrahlung,[1] or the excitation and ionization of the system of atomic electrons surrounding the decaying nucleus.[2] It is possible, in fact, that by thus limiting our discussion only to what can be expected to admit of a reliable check by present experimental means, only two effects have to be considered in connection with the above question: the effect of "screening" by the atomic electrons of the nuclear Coulomb field and the effect of the readjustment of the system of atomic electrons to the changed nuclear charge resulting from the beta-decay. These two effects are obviously not completely independent, but for our purpose they can be treated as such.[3]

The effect of atomic electron screening can be incorporated in the Fermi theory, at least in principle, to any accuracy warranted by the experimental potentialities, inasmuch as this is accomplished by employing as wave functions for the beta-particle the continuum

* This work is supported in part by the AEC.

[1] L. Madansky and F. Rasetti, Phys. Rev. **83**, 187 (1951). This is the latest published report on this effect and deals with its experimental determination; it contains references to the theoretical and earlier experimental work on this problem.

[2] L. Goldstein, J. phys. et radium **8**, 235 and 316 (1937); E. L. Feinberg, J. Phys. (U.S.S.R.) **4**, 423 (1941); A. Migdal, J. Phys. (U.S.S.R.) **4**, 449 (1941). These are theoretical papers. No experimental work on this effect has as yet been announced.

[3] Provided the formulation proposed in this note is essentially correct.

eigenfunctions for the Coulomb potential due to the combined nuclear and atomic electron charge systems of the daughter atom. It is known that this effect is very small in the case of negative beta-decay.[4]

The other effect, that connected with the transition between the ground states of the atomic electron system corresponding to the change in nuclear charge, will be discussed in Sec. II. The conclusion is reached that to the first order the shape of the beta-spectrum is hardly affected. This conclusion is at variance with that to be gathered from previous work related to this problem.[5] Although presumably the approach in each of these papers is different,[6] the results can be seen to imply the following common conclusion: to the first order, the energy

$$D_Z = E_{Z+1} - E_Z \tag{1}$$

(E_Z = numerical binding energy of an atom of atomic number Z), which is liberated in the atomic electron system transition in question,[7] is carried away by the departing beta-particle. From this conclusion it follows that, practically, there should appear a cutoff at the low energy end of negative beta-spectra corresponding to this energy D_Z.

The above conclusion can be readily shown to be a consequence of the assumption, which is tacitly made (except for the first reference 5) in the quoted papers, to the effect that the atomic electron readjustment accompanying beta-decay is a process essentially independent of the nuclear transition and can be considered as taking place subsequent to that transition. Inasmuch as the neutrino has practically no direct coupling with charged particles, one has only to show that the probabilities for electromagnetic radiation or for direct nonradiative absorption of the energy D_Z by the nuclear charges are relatively small, at least in the case of Z large enough for D_Z to be measurably appreciable.

The two alternative conclusions regarding the first-order disposition of the energy D_Z, namely, its being shared by the neutrino and the beta-particle (as is implied by the treatment given in Sec. II), or solely by the beta-particle, are strikingly illustrated by the corresponding consequences regarding the shape of the beta-spectrum of Pu^{241}. On the second view, since D_Z is in this case very nearly of the same order of magnitude as its reported maximum energy, the shape should be practically that of a line spectrum about the end point; whereas on the first view, this shape should be practically that of an allowed, high Z, and small end-point spectrum and thus having an ordinate which increases continuously towards the zero energy point. Recent measurements of the spectrum of Pu^{241} are consistent with this latter shape.[8] There are, of course, other nuclides besides Pu^{241} which are suitable for a test of the question under discussion, and beta-spectrum measuring techniques developed recently make such a test entirely feasible. Moreover, there are already in the literature some relevant measurements and these (with one possible exception), as far as they can be relied upon, appear in fact to confirm the conclusion which is reached in this note, at least in what concerns the nonexistence of a low energy end cutoff. A brief discussion of this published experimental work and an indication of the possibilities for pertinent proportional counter measurements is given in Sec. III.

II. THEORETICAL CONSIDERATIONS

As follows from the discussion of the preceding section, our problem is to determine in the first approximation the probability $P(W)dW$ for the emission by a given nuclide of a negative beta-particle into the kinetic energy range dW at W, when simultaneously the system of surrounding electrons makes a transition from the ground state of the initial atom to that of the daughter atom (singly ionized in its outer shell), it being assumed that the nuclear and atomic transitions can be treated as a combined process.

A precise formulation of this problem would involve the quantized fields of nucleons and leptons (electrons and neutrinos), the latter including the filled bound states corresponding to the available atomic electrons, and subject to proper Fermi and Coulomb couplings.[9] For our present purpose it is possible that it will suffice to employ a phenomenological approach, which corresponds in some respects to the reasoning which enters in the treatment of the atomic electron screening effect. We simply assume that the Fermi interaction operator which involves the change of a neutron into a proton, serves also to change all wave functions pertaining to the nuclear charge specified by Z into the corresponding wave functions related similarly to to $(Z+1)$. It then follows that in forming the first-order matrix element corresponding to the combined nuclear and atomic transitions in question, we obtain the product of the usual matrix element for the beta-transition and of the integral

$$\int \psi_{Z+1}^* \psi_Z d\tau, \tag{2}$$

where ψ_Z, ψ_{Z+1} are the wave functions of the system of

[4] J. R. Reitz, Phys. Rev. **77**, 10 (1950) (contains references to previous papers).

[5] See L. Goldstein, reference 2, and M. H. Hebb, Physica **5**, 701 (1938); R. S. Ingarden, Acta Phys. Polon. **9**, 109 (1948).

[6] It is only in the second of the references in footnote 5 that the reasoning is explicit; the last reference merely contains mention of a relevant calculation, presumably unpublished, of J. Blaton "on the basis of Boltzmann's Virial Theorem"; while in the first reference there is an explicit statement of the assumption of independence of the nuclear and atomic transitions but the conclusion regarding the absorption of the energy D_Z by the departing beta-particle is announced without proof.

[7] The ionization energy of the outer shell of the daughter atom is quite neglible in comparison with D_Z for the Z values of interest to us.

[8] M. S. Freedman, Argonne National Laboratory (private communication).

[9] The transverse electromagnetic field could in general be left out of account in considering only first-order effects.

atomic electrons in the initial and final states, respectively.[10]

The conclusion stated in Sec. I, namely, that to the first order the spectral shape is not affected by the effect under discussion now follows from the following two observations. First, since Dirac perturbation theory here leads to conservation of energy in the combined transition, this energy being the sum of the excess in the nuclear energy levels and of D_Z as defined in (1), and since the atomic electron transition is between discrete states, it follows that the total energy in question is shared between the beta-particle and the neutrino. Secondly, the probability $P(W)dW$ which we are seeking will not be affected to any markedly appreciable extent by the atomic electron transition if the absolute square of the integral (2), which enters as a factor in its expression, differs sufficiently little from unity when ψ_{Z+1} corresponds to the ground state of the product atom. This can be shown indeed to be practically the case for sufficiently large Z.[11]

It is to be noticed that the absolute square of the integral (2) represents the probability for the corresponding atom electron transition on *sudden* perturbation theory. It can be seen indeed that it is consistent with the preceding considerations to think of the combined process in question as a beta-decay accompanied by the atomic readjustment in a time that is compatible with the application of sudden perturbation theory. The essential thing, however, is to account for the disposition of the energy D_Z which is involved in the transition. Sudden perturbation theory in itself does not involve directly any energy considerations and is, in fact, limited in this respect by the time-energy uncertainty relation.

It needs perhaps to be stated that the possibility cannot be ruled out that the simple treatment here given is not adequate and that a strict field-theoretical approach would bring out significant deviations from the shape predicted here, even in the first approximation. Before there is definite experimental evidence pointing in that direction, however, there would perhaps be scant justification for undertaking any highly involved investigation of this sort.

III. EXPERIMENTAL CONSIDERATIONS

There are so far three published results which are perhaps pertinent to our problem.

The cloud-chamber measurements of Richardson and Leigh-Smith[12] of the spectrum of RaD in the form of gaseous lead tetramethyl would be entirely conclusive, at least as to the existence of a low energy end beta-spectrum cutoff, provided we could safely rely on such measurements when they involve track lengths of the order of a millimeter and less. These investigators conclude by an analysis of their photographs, that more than 50 percent of the RaD beta-spectrum lies below 4 kev. Since the value of D_Z for RaD is around 15 kev,[13] the implication of this result, if valid, is quite obvious. Another published result perhaps pointing in the same direction is provided by the measurements of Langer, Motz, and Price[14] of the beta-spectrum of Pm^{147}. They find a straight Kurie plot down to 8 kev and possibly in the case of their windowless counter measurements even down to 6 kev, whereas D_Z for promethium is close to 10 kev.[13] On the other hand, the cloud-chamber investigation of the low energy end beta-spectrum of RaE by Waltner and Rogers[15] appears to confirm the "cutoff" conclusion. Again, the reliability of these low energy measurements must be left an open question.

Of the experimental techniques that are currently being perfected and which may be suitable for the study of appropriate beta-spectra at energies below D_Z, perhaps the most promising at the present time is that involving the use of proportional counters with gaseous sources. The substantial improvements in proportional counter low energy electron spectroscopy developed recently in a number of laboratories, notably at the University of Glasgow,[16] would indeed appear to make the proportional counter a suitable instrument for a completely reliable study of our problem. True, the number of nuclides which can be used to that end with this method is limited. However, unless it turns out that the negative beta-spectral shape at the low energy end is essentially distinct from that so far predicted, it would suffice for our purpose to have such reliable measurements in only a few cases. One example of a nuclide which possibly presents an optimum combination of desirable properties is provided by Ni^{63} which can be used in the form of gaseous nickel carbonyl. Plans for making proportional counter measurements of the low energy end of the spectrum of Ni^{63} are now in progress at the University of Arkansas.[17]

[10] Related discussion is to be found in Feinberg's paper listed under reference 2, although the problem treated there is not the one discussed here.

[11] This is made plausible by the calculations given in the papers listed in reference 2. Results of more extensive calculations that bear out this conclusion will be presented shortly for publication in the *Journal of Chemical Physics*.

[12] H. O. W. Richardson and A. Leigh-Smith, Proc. Roy. Soc. (London) **A160**, 454 (1937).

[13] See, for instance, L. L. Foldy, Phys. Rev. **83**, 397 (1951). An experimental check sufficient for our purpose was obtained by using x-ray level data.

[14] Langer, Motz, and Price, Phys. Rev. **77**, 798 (1950).

[15] A. W. Waltner and F. T. Rogers, Phys. Rev. **75**, 1445 (1949).

[16] A. L. Cockroft and S. C. Currant, Rev. Sci. Instr. **22**, 37 (1951); G. M. Insch and S. C. Curran, Phil. Mag. **42**, 892 (1951). These papers contain references to earlier work.

[17] R. R. Edwards and P. E. Damon (private communication). I wish to express my appreciation of the many stimulating discussions on this subject with Professor R. R. Edwards.

Application of the Fermi Model to Cosmic-Ray Events of Primary Energy Greater Than 10^{13} ev*

W. E. HAZEN, R. E. HEINEMAN, AND E. S. LENNOX
Randall Laboratory of Physics, University of Michigan, Ann Arbor, Michigan
(Received November 28, 1951)

The Fermi model for nucleon-nucleon collisions at high energies has been used to calculate the energy distribution, the energy dependence of the angular distribution, and the number of emitted pions as a function of primary energy and impact parameter. We calculate the effect on the pion distribution of nucleon-antinucleon production in the same collision. The results approach agreement with air-shower observations.

I. INTRODUCTION

EXPERIMENTAL observations of the density structure of air showers[1,2] seem to indicate that the density does not vary appreciably over distances of about one meter or less from the axis of the shower. This result might be explained either by a peculiar density distribution for a single shower core or by a multiplicity of cores with average separations somewhat less than one meter. The latter seems to be the more reasonable explanation.

The most promising model[3] is the customary one in which π^0 mesons are emitted in nuclear interactions of the primary cosmic rays and subsequently decay into photons. If one assumes that the emission is nearly isotropic in the center-of-mass system and merely exploits the relativistic contraction in explaining the observed separation of the air-shower cores, it is necessary to attribute events of shower energy $10^{13}-10^{14}$ ev to primaries of energy 10^{17} ev. The objection to this result is that less than one percent of the energy goes into π^0 mesons, if their number is kept small enough to agree with observed shower sizes. This is apparently in contradiction with estimates from observations at lower energies and with general arguments of equipartition of energy.

Fermi[4] has improved the situation by an order of magnitude in the energy. In this model, conservation of angular momentum already dictates (for a collision with median-impact parameter) a concentration of mesons near the collision axis in the center-of-mass system. The present discussion seeks to show that a more detailed analysis of the Fermi model of single nucleon-nucleon collisions results in an additional gain of nearly another order of magnitude. The angular distribution and number of π^0 mesons emitted "during" a collision will be calculated as a function of energy of the primary nucleons and of the mesons.

Another question that we shall seek to answer is whether or not a reasonable number of mesons of sufficient energy are emitted at the energy required by considerations of the angular separation.

The calculation of the angular distribution and spectral distribution of π-mesons and nucleons produced in a high energy collision of two nucleons follows and extends the work done by Fermi[4] on the statistical theory of multiple meson production for extremely high energies. Only a bare outline of the method is contained here; for a fuller discussion of the ideas and limitations, Fermi's paper should be consulted. The results contained in this paper are obtained mainly by an extension of the ideas presented in Fermi's paper.

We shall consider the question of the angular distribution and the number of particles produced as a function of energy of the primary nucleon and of the secondary particles. In the first part of the work, we assume that statistical equilibrium is attained only by the π-mesons and that the impact parameter is the median one. For extreme relativistic energies calculations have been made in which it is assumed that the incident nucleon energy is high enough to bring the mesons and the nucleon-antinucleon pairs into statistical equilibrium and also for cases with the impact parameter greater than median.

It is found that the angular distribution as a function of the energy of the secondaries is only very weakly dependent upon whether or not one assumes nucleon-antinucleon production in addition to meson production. Of course, the number of mesons produced is smaller if nucleons are produced. If the impact parameter is increased, the angular distribution is found to be more peaked, as Fermi has stated,[4] and the proportion of higher energy mesons is increased.

II. CALCULATIONS

We follow closely the work of Fermi, using as far as possible his notation. Unprimed quantities will refer to the center-of-mass system, primed ones to the laboratory system. The total energy W is deposited initially into a sphere of radius $R=\hbar/\mu c=1.4\times10^{-13}$ cm, which is Lorentz contracted because of the relative motion of the colliding nucleons. This volume we take as

$$V=(2Mc^2/W)(4\pi R^3/3),$$

where Mc^2 is the rest energy of a nucleon. Figure 1

* Supported in part by the joint program of the ONR and AEC.
[1] R. W. Williams, Phys. Rev. **74**, 1689 (1948); J. M. Blatt, Phys. Rev. **75**, 1584 (1948).
[2] W. E. Hazen, Phys. Rev. **85**, 455 (1952).
[3] Lewis, Oppenheimer, and Wouthuysen, Phys. Rev. **73**, 127 (1948).
[4] E. Fermi, Phys. Rev. **81**, 683 (1951).

shows the flattened sphere and the initial direction of motion of the two nucleons (along a and b) having only an angular momentum M_z, along the z axis, which is perpendicular to the plane of the figure and outwards. For the extreme relativistic case, in which we are interested here, the volume is very flattened and the y dimension may be neglected in computing the angular momentum, Z, of a particle produced at the point x, z. Then

$$Z=xp\cos\theta=x(w/c)\eta, \tag{1}$$

where $\eta=\cos\theta$, p is the momentum, w the energy of the emitted particle (assumed relativistic), and θ is the angle between p and the y axis.

We use the thermodynamic approximation and require conservation of energy and of angular momentum. Then the average number of particles in a state of energy w and angular momentum Z is proportional to

$$1/(e^{\beta w-\lambda Z}\pm 1), \tag{2}$$

with $(+)$ for Fermi-Dirac statistics and $(-)$ for Bose-Einstein statistics. We consider both statistics, for we shall consider the formation of pions and nucleon-antinucleon pairs. The parameters β and λ are determined by conservation of energy and angular momentum, respectively. We let

$$\begin{aligned} &\gamma=c\beta=c/kT, \quad \rho=\lambda R/c\beta, \\ &x/R=\xi, \qquad\qquad \zeta=\gamma\rho(1-\rho\eta\xi). \end{aligned} \tag{3}$$

Then using (1), (2), and (3) we may write for the number of particles in a volume element in phase space

$$dN=(AMc^2/W)[g_+F_+(\zeta) +g_-F_-(\zeta)](1-\xi^2)d\xi\rho^2 dpd\eta, \tag{4}$$

where

$$F_\pm(\zeta)=1/(e^\zeta\pm 1) \quad \text{and} \quad A=R^3/(2\pi\hbar^3). \tag{5}$$

The statistical weights g_+ and g_- are taken as $g_+=8$ for the nucleon-antinucleon pairs and $g_-=3$ for the pions.

The angular distribution, if one takes the momentum integral from 0 to ∞, is independent of the statistics and we have

$$N(\eta)=(AMc^2/\gamma^3W)(g_+B_++g_-B_-)f_4(\rho\eta), \tag{6}$$

where

$$f_4(\alpha)=\frac{2}{\alpha^2(1-\alpha^2)}-\frac{1}{\alpha^3}\ln\frac{1+\alpha}{1-\alpha}$$

and

$$B_\pm=\int_0^\infty \zeta^2F_\pm(\zeta)d\zeta. \tag{7}$$

If we integrate (6) over η from -1 to $+1$, we have for the total number of particles

$$N=(AMc^2/\gamma^3W)(g_+B_++g_-B_-)f(\rho), \tag{8}$$

where

$$f(\rho)=\frac{1+\rho^2}{\rho^3}\ln\frac{1+\rho}{1-\rho}-\frac{2}{\rho^2}. \tag{9}$$

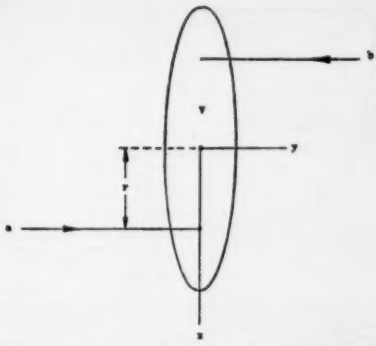

FIG. 1. Diagrammatic view of the interaction volume V of two colliding nucleons, a and b.

Multiplying (4) by cp and integrating over all variables, we have for the total energy

$$W=\tfrac{3}{2}(AMc^3/\gamma^4W)(g_+b_++g_-b_-)f_2(\rho), \tag{10}$$

where

$$f_2(\rho)=\frac{1}{\rho}\ln\frac{1+\rho}{1-\rho}+\frac{2}{1-\rho^2} \tag{11}$$

and

$$b_\pm=\int_0^\infty \zeta^3F_\pm(\zeta)d\zeta. \tag{12}$$

Multiplying (4) by $xp\eta=R\xi p\eta$ and integrating, we find for the total angular momentum

$$M_z=(ARMc^3/\gamma^4W)(g_+b_++g_-b_-)f_1(\rho), \tag{13}$$

where

$$f_1(\rho)=\frac{2}{\rho^3}+\frac{4/(3\rho)}{1-\rho^2}-\frac{1+\frac{1}{3}\rho^2}{\rho^4}\ln\frac{1+\rho}{1-\rho}. \tag{14}$$

One then finds the parameter ρ, which measures the impact parameter, by putting the ratio M_z/W, i.e., the ratio of (13) to (10), equal to r/c. We have then

$$r/R=\tfrac{3}{2}f_1(\rho)/f_2(\rho). \tag{15}$$

Having found ρ for a particular collision, we then find the parameter γ, which depends upon ρ and W, from (10), (11), and (12).

The constants $B_\pm$ and $b_\pm$ are given by

$$B_+=2\sum_{n=1}^{\infty}(-1)^{n+1}\frac{1}{n^3}=1.803,$$

$$B_-=2\sum_{n=1}^{\infty}\frac{1}{n^3}=2.413,$$

$$b_+=6\sum_{n=1}^{\infty}(-1)^{n+1}\frac{1}{n^4}=5.682,$$

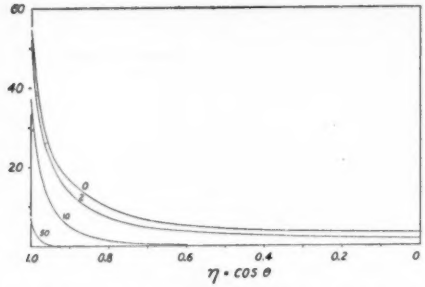

FIG. 2. Angular distribution of pions with no nucleon emission. The number of pions emitted with η between η and $\eta+d\eta$ and having an energy $cp_0 \geq 0$ is $(AMc^2/\gamma^3 W)g_- B_- f_4(0.959\eta)$, and having an energy $cp_0 > 0$ is $(AMc^2/\gamma^3 W)g_- \Sigma_n h_n(\gamma p_0, 0.959\eta)$. We plot $B_- f_4(0.959\eta)$ *vs* η (upper curve) and $\Sigma_n h_n(\gamma p_0, 0.959\eta)$ *vs* η for $\gamma p_0 = 2$, 10, 50.

and

$$b_- = 6\sum_{n=1}^{\infty} \frac{1}{n^4} = 6.494. \tag{16}$$

One notices that the value of ρ for a given impact parameter, r, is independent of whether or not nucleon-antinucleon pairs are formed in addition to the pions. The influence of nucleon-antinucleon pairs is felt only in the effect on γ. This affects the total number of pions of all energies and the angular distribution of pions of momentum $p \geq p_0 > 0$.

To find the angular distribution of pions alone, we write

$$dN_\pi = \frac{AMc^2}{W}\left(g_- \sum_{n=1}^{\infty} e^{-n\xi}\right)(1-\xi^2)d\xi p^2 dp d\eta. \tag{17}$$

For the nucleons, we write

$$dN_N = \frac{AMc^2}{W}\left(g_+ \sum_{n=1}^{\infty} (-1)^{n+1} e^{-n\xi}\right)(1-\xi^2)d\xi p^2 dp d\eta. \tag{18}$$

Integrating (17) and (18) over ξ from -1 to $+1$ and over p from p_0 to ∞, we get, respectively,

$$N_\pi(p_0, \eta) = \frac{A}{\gamma^3}\frac{Mc^2}{W} g_- \sum_{n=1}^{\infty} h_n(\gamma p_0, \rho\eta) \tag{19}$$

and

$$N_N(p_0, \eta) = \frac{A}{\gamma^3}\frac{Mc^2}{W} g_+ \sum_{n=1}^{\infty} (-1)^n h_n(\gamma p_0, \rho\eta), \tag{20}$$

where

$$h_n(\gamma p_0, \rho\eta) = \frac{2\gamma p_0}{n^3\rho^2\eta^2}\left\{\frac{e^{-n\sigma}}{\sigma} + \frac{e^{-n\tau}}{\tau}\right\} - \frac{2}{n^3\rho^3\eta^3}\{-\mathrm{Ei}(-n\sigma) + \mathrm{Ei}(-n\tau)\},$$

$$\sigma = \gamma p_0(1-\rho\eta), \quad \text{and} \quad \tau = \gamma p_0(1+\rho\eta).$$

The convergence of (19) and (20) is quite rapid for $\gamma p_0 = cp_0/kT \gtrsim 2$. We notice that $N_\pi(p_0, \eta)$ depends upon γ and γp_0. It is here that the influence of nucleon-antinucleon pair formation is felt, in its effect on γ.

We should like to describe a collision by taking for r some median value. We take for $P(r)$ the form

$$P(r) = r^2/R^2,$$

where $P(r)$ is the probability of a collision in which the impact parameter is less than r. For the median collision this probability is $\frac{1}{2}$, which gives

$$r = R/\sqrt{2}.$$

With this result and using (15), we find $\rho = 0.959$. Later, in part B, we shall consider collisions for which $\rho = 0.99$. This is not an exceptional case since this corresponds to $P(r) = 0.77$, so that there are still 23 percent of the collisions whose impact parameters are larger.

A. Pion Production Only, Median Impact Parameter, $\rho = 0.959$

Here we calculate the angular distribution and total number of pions above a certain minimum energy with the assumption that no available energy is used for nucleon-antinucleon pair formation. In this case (6), (8), (10), and (13) become, respectively,

$$N_\pi(\eta) = (AMc^2/\gamma^3 W)g_- B_- f_4(\rho\eta), \tag{21}$$

$$N_\pi(\rho) = (AMc^2/\gamma^2 W)g_- B_- f(\rho), \tag{22}$$

$$W = \tfrac{3}{8}(AMc^3/\gamma^4 W)g_- b_- f_2(\rho), \tag{23}$$

and

$$M_Z = (ARMc^2/\gamma^4 W)g_- b_- f_1(\rho). \tag{24}$$

We compute γ from (23) using $\rho = 0.959$. We have then

$$\gamma = 1.23\times 10^{-8}(Mc^2/W)^{\frac{1}{4}} c/\mathrm{ev}. \tag{25}$$

Using this value of γ in (21), we find the total number of emitted pions, one-third of which are neutral pions. Their number is given by

$$N_{\pi^0} = 0.46(W/Mc^2)^{\frac{1}{4}}. \tag{26}$$

One finds the angular distribution of pions with energy greater than a given cp_0 by using (19) if $cp_0 > 0$ or (21) if $cp_0 = 0$. In Fig. 2, we plot for $\gamma p_0 = 0$, the function

$$N_\pi(\eta) \Big/ \left(\frac{AMc^2}{\gamma^3 W} g_-\right) = B_- f_4(\rho\eta),$$

for $\rho = 0.959$ and as a function of η. Also in Fig. 2, for $\gamma p_0 = 2$, 10, and 50, we plot the function

$$N_\pi(p_0, \eta) \Big/ \left(\frac{AMc^2}{\gamma^3 W} g_-\right) = \sum_{n=1}^{\infty} h_n(\gamma p_0, \rho\eta),$$

for $\rho = 0.959$ as a function of η. The curves are sym-

TABLE I. The energies and numbers of emitted π^0 mesons corresponding to the parameter γp_0 for various primary energies and impact parameters.

		Only π-mesons produced. Energy of π^0 mesons in units of 10^{13} ev (cp_0')							
		$\rho=0.959$			$\rho=0.990$			Total number of π^0-mesons (forward and backward)	
Primary energy W/Mc^2	W' ev	50	γp_0 10	2	50	γp_0 10	2	$\rho=0.959$	$\rho=0.990$
50	1.2×10^{12}	0.14	0.03	0.006	0.10	0.02	0.004	3.3	1.7
200	1.9×10^{12}	1.15	0.23	0.05	0.83	0.17	0.034	6.5	3.5
500	1.2×10^{14}	4.6	0.91	0.18	3.3	0.66	0.13	10.3	5.5
1000	4.7×10^{14}	13	2.6	0.52	9.4	1.9	0.38	14.6	7.8
2000	1.9×10^{15}	36	7.3	1.45	26.4	5.3	1.06	21	11.0
5000	1.2×10^{16}	144	29	5.8	104	21	4.2	33	17.3
20,000	1.9×10^{17}	1150	230	46	833	167	3.3	65	35

		Both π-mesons and nucleons produced. Energy of π^0 mesons in units of 10^{13} ev (cp_0')							
		$\rho=0.959$			$\rho=0.990$			Total number of π^0 meson (forward and backward)	
Primary energy W/Mc^2	W' ev	50	γp_0 10	2	50	γp_0 10	2	$\rho=0.959$	$\rho=0.990$
50	1.2×10^{12}	0.104	0.021	0.004	0.053	0.011	0.0021	1.3	0.72
200	1.9×10^{12}	0.853	0.171	0.034	0.44	0.089	0.018	2.6	1.4
500	1.2×10^{14}	3.4	0.68	0.14	1.77	0.354	0.071	4.2	2.3
1000	4.7×10^{14}	9.6	1.92	0.38	5.03	1.0	0.201	5.9	3.2
2000	1.9×10^{15}	26.5	5.4	1.07	19.2	3.9	0.775	8.3	4.5
5000	1.2×10^{16}	107	21.5	4.3	77	15	3.1	13	7.2
20,000	1.9×10^{17}	853	170	34	615	123	24	26	14.3

metrical around $\eta=0$ (in the c.m. system) and we plot only the range $0\leq\eta\leq1$. These plotted curves are independent of the energy of the incoming nucleon, if we consider a given γp_0. The angular distribution for a given cp_0, however, depends on W through γ.

To compare the curves with experimental data, we must translate γp_0 into cp_0', the energy of the emitted pion in the laboratory system. We have (if the colliding nucleon is extreme relativistic)

$$cp_0'=\tfrac{1}{2}(W/Mc^2)(c/\gamma)(1+\eta)\gamma p_0. \tag{27}$$

The factor $(1+\eta)$ in (27) makes those pions emitted in the forward direction with $0.82<\eta<1$ higher in energy by an order of magnitude over those emitted with $-1<\eta<-0.82$. This is the justification for considering only the former, more energetic, group for the interpretation later in the paper.

From Eqs. (25) and (27) we get (using $\eta\approx1$)

$$cp_0'=0.82\times10^8\gamma p_0(W/Mc^2)^{\frac{1}{4}}\text{ ev}. \tag{28}$$

In Table I, (28) is tabulated for various values of γp_0 and W. Also given there is the total number of π^0's, (forward and backward) from (26). We plot in Fig. 3, the integral spectrum of π^0's for several values of W', the laboratory-system energy of the nucleon producing them.

In Table II we give $\eta_{\frac{1}{2}}$, the cosine of the angle within which is emitted one-half of the particles in the forward cone. We include there also the value of η for which the intensity has fallen to one-half the value for $\eta=1$.

B. Pion Production Only; Impact Parameter Largar than Median, $\rho=0.99$

If we increase ρ, there are two effects: (a) The angular distributions become concentrated around $\theta=0$ and $\theta=\pi$, (b) more energy goes into rotation, which lowers the temperature, thereby increasing γ. For $\rho=0.99$, we recompute:

$$\gamma=1.70\times10^{-8}(Mc^2/W)^{\frac{1}{4}}c/\text{ev}. \tag{29}$$

The total number of neutral mesons (forward and backward) becomes

$$N_{\pi^0}=0.25(W/Mc^2)^{\frac{1}{4}},$$

which is almost a factor two less than for the median impact parameter. We have for this case

$$cp_0'=0.59\times10^8\gamma p_0(W/Mc^2)^{\frac{1}{4}}\text{ ev}.$$

In Fig. 4, we plot the same function as Fig. 2, using

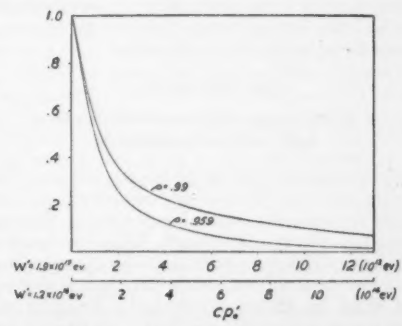

FIG. 3. Integral-energy spectra for emitted pions for two primary energies, considering pion emission only (upper scale $W'=1.9\times10^{13}$ ev) and pion and nucleon emission (lower scale $W'=1.2\times10^{16}$ ev). For other values of W' the cp_0' scale should be varied as $(W')^{3/4}$.

TABLE II. The cosine of the angle within which are emitted one-half of the particles in the forward cone, and the cosine of the angle at half-intensity, as functions of γp_0 and ρ.

γp_0	$\rho=0.959$ $\eta_{\frac{1}{2}}$	η at half intensity
0	0.82	0.958
2	0.865	0.964
10	0.960	0.974
50	0.989	0.989
	$\rho=0.99$	
0	0.89	0.991
50	0.991	0.994

$\rho=0.99$. The dotted line is taken from Fig. 2 with $\gamma p_0=10$ for comparison.

C. Effects of Nucleon-Antinucleon Pairs on Pion Distribution for $\rho=0.959$ and $\rho=0.99$

If the incoming nucleon energy is high enough ($W/Mc^2 \gtrsim 100$) so that nucleon-antinucleon pairs are brought into equilibrium, we must consider their production in addition to the pion production. The effect is to reduce the temperature and hence to reduce the number of π^0's emitted for a given W. In this case we use Eq. (10) to compute γ and Eq. (22) to compute the number of π's, one-third of which are π^0's. We find

$$\begin{aligned} &\rho=0.959 \\ &\gamma=1.66\times10^{-8}(Mc^2/W)^{\frac{1}{2}}c/\text{ev} \\ &N_{\pi^0}=0.19(W/Mc^2)^{\frac{1}{2}} \\ &cp_0'=0.60\gamma p_0(W/Mc^2)^{\frac{1}{2}}\ \text{ev}. \\ &\rho=0.99 \\ &\gamma=2.29\times10^{-8}(Mc^2/W)^{\frac{1}{2}}c/\text{ev} \\ &N_{\pi^0}=0.099(W/Mc^2)^{\frac{1}{2}} \\ &cp_0'=0.44\times10^{8}\gamma p_0(W/Mc^2)^{\frac{1}{2}}\ \text{ev}. \end{aligned} \tag{30}$$

One should note that the angular distribution as a function of γp_0 is not changed, Figs. 2 and 4, but again the energies of the mesons, cp_0', corresponding to a given γp_0 are not the same as any of the other cases. In Fig. 3 the integral energy spectrum for the π's is plotted for an energy $W'=1.2\times10^{16}$ ev.

III. DISCUSSION

A. Comparison of Shower Observations with Fermi's Calculations

Counter observations[5] of the lateral structure of air showers show that there is no multiplicity of singularities of comparable strength separated by distances from a few meters to 200 meters. Ionization chamber[1] measurements show no multiplicity for distances from one meter to about ten meters but there is evidence that either the Molière distribution is wrong or that there is a multiplicity of singularities within distances of about one meter. Cloud-chamber observations show no distinctly resolved singularities for separations less than one meter, but they do confirm the ion-chamber observation that there is a plateau region with very little variation in particle density near the shower axis.[2] Since the cloud-chamber observations should be able to resolve two Molière singularities separated by more than about 20 cm, the cloud-chamber observations of particle densities imply either that there are usually more than two shower cores with separations less than one meter or that the Molière singularities are too sharp.

There is some evidence of multiple cores in the cloud-chamber pictures[2] as evidenced by cases where there are two separate concentration areas for rays of energy $>10^{10}$ ev. Since from the theory of lateral spread of cascade showers the probability is about one-half for rays of energy $>10^{10}$ to lie within 20 cm of the shower axis,[6] concentrations of such rays can be used to identify cores with separations of the order of 50 cm or more.

As a first approximation we shall assume that the major contribution to the air showers observed in the lower atmosphere is made by the secondaries produced in the initial nuclear encounter of a primary. Thus the energy of the initiating rays will be determined with the ordinary cascade shower theory by assuming that the shower originated near the top of the atmosphere. The shower energies involved can be estimated as follows: Both the ion-chamber and cloud-chamber observations are for cases in which the minimum particle densities are ~500 m^{-2} in a region of about 0.2 m^2 surrounding the shower axis. If we use the Molière distribution to obtain the total number of electrons at the observation level and the cascade theory for longitudinal development to obtain the minimum initiating energy therefrom, we obtain 3×10^{13} ev for a single ray or 10^{13} ev for each of four initiating rays.

A satisfactory model should therefore give a multiplicity of 10^{13}-ev rays with angular separations of

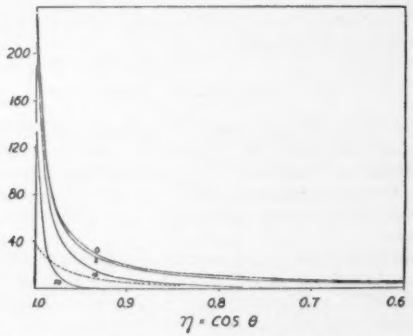

FIG. 4. $B_-f_0(0.99\eta)$ vs η (upper curve) and $\Sigma b_n(\gamma p_0, 0.99\eta)$ vs η for $\gamma p_0=2$, 10, and 50. The dotted curve is for $\gamma p_0=10$ from Fig. 2, for comparison.

[5] Cocconi, Tongiorgi, and Greisen, Phys. Rev. **76**, 1020 (1949).

[6] L. Eyges and S. Fernbach, Phys. Rev. **82**, 23 (1951); **82**, 287 (1951).

roughly 10^{-4} radian or less. The decay of π^0 mesons in flight generates two gamma-rays with an angular separation of about 1.5×10^{-5} radian for photon energies of 10^{13} ev. This mechanism alone would result in a saddle 20 cm long in the density distribution, but it fails to explain a plateau. In order to obtain a plateau, we require a multiplicity of π^0 mesons themselves with an angular spread less than 8×10^{-5} (one meter separation at the observation level of 3000 meters). The angle with the primary axis would be 4×10^{-5} radian.

The relativistic transformation from the rest system (θ) to the observation system (θ') is, for small values of the angles,

$$\theta'=\theta/(2W'/Mc^2)^{\frac{1}{2}}.$$

Thus we need a model that will provide values for θ and W'. As mentioned in the introduction, a model that assumes isotropic emission in the center-of-mass system is probably unsatisfactory.

If we turn to Fermi's calculations, we find $\theta_{\frac{1}{2}}=0.6$ for the angle that includes one-half of the forwardly-emitted mesons of all energies. We disregard the backwardly-emitted mesons because their energy in the laboratory system is an order of magnitude lower, as previously shown. A primary energy of 10^{17} ev is now required in order to effect a contraction of the angle to 4×10^{-5} radian.

Since we really should be considering most probable events, the angle at $\frac{1}{2}$ intensity is perhaps more appropriate than $\theta_{\frac{1}{2}}$. Fermi's angular distribution[4] for mesons of all energies ($\gamma p_0=0$ in Fig. 2) gives 0.28 for the angle at $\frac{1}{2}$ intensity and the corresponding primary proton energy is 2.4×10^{16} ev. Thus, as we go from an isotropic-emission model to the Fermi model, we have a factor of ten reduction (from 3×10^{17} to 2.4×10^{16}) in the energy required to effect the required angular contraction. The question of the number of mesons with energy $>10^{13}$ ev cannot be answered until we consider the results of our detailed analysis in the next section.

B. Comparison of Shower Observations with the Detailed Analysis of the Fermi Model

The observed air-shower effects that are considered here are attributed to the more energetic π^0 mesons ($E>10^{13}$ ev if we assume the showers originate near the top of the atmosphere), whereas the Fermi calculations were for mesons of all energies. Furthermore, the observed showers of a given minimum size are not necessarily caused predominantly by primary events whose average behavior corresponds to the minimum shower size; a more probable origin is one of the more abundant, lower-energy primaries that happens to make a collision with an impact parameter such that $\rho>0.959$ with a consequent hardening of the average spectrum of emitted mesons, or a collision (with any impact parameter) in which the spectrum is harder than average (with a consequent reduction in total number of emitted particles), or a collision in which π^0 mesons carry off more than their average share of the energy.

However, let us first consider an average collision, one with the median value of the impact parameter ($\rho=0.959$). Since the energy is very high, the case of nucleon emission will be considered and we have (from 30) $cp_0'=0.60\times10^{13}\gamma p_0(W/Mc^2)^{\frac{1}{2}}$ and $N_{\pi^0}=0.19(W/Mc^2)^{\frac{1}{2}}$. With the assumptions about the air showers that have previously been stated, we have $cp_0'\gtrsim10^{13}$ ev. We find a minimum value of W' by requiring that we have about two π^0 mesons with energy $\geqslant10^{13}$e v. With $W'=10^{15}$ ev, we have $N(0)=4$ in the forward cone and (Fig. 3) $N(10^{13})=2.8$, which is a reasonable number. The value of γp_0 is then 3 and η for $\frac{1}{2}$ intensity is 0.97. The resulting value of 0.24 for θ together with the relativistic contraction corresponding to $W'=10^{15}$ ev gives $\theta'=1.6\times10^{-4}$, which is only four times larger than the "observed" value, 4×10^{-5}, for air showers. On the other hand, let us first satisfy the angle requirement and then find the number of mesons. The value of η at $\frac{1}{2}$ intensity is about 0.97 for γp_0 in the range from 2 to 10 (Fig. 2). The primary energy required to contract the angle to the observed angle of 4×10^{-5} is $W'=1.8\times10^{16}$ ev. The total number of π^0 mesons is 8 in the forward cone and the number with energy $>10^{13}$ ev is also essentially 8. This number of π^0 mesons of energy $>10^{13}$ ev would produce a shower several times larger than the minimum size under consideration. In summary, an average collision treated according to the Fermi model will, in the limiting cases, give either a lateral spread that is about four times too great when the number of particles is correct or about four times too much energy to the shower component when the lateral spread is correct. An intermediate choice would, of course, give both too many particles and also too large an angle.

Returning to the idea of probable origins as expressed in the opening paragraph of this section, let us consider the results of distant collisions. For a semiquantitative discussion we shall choose $\rho=0.99$ as the impact parameter typifying collisions that contribute strongly to a given-size shower when the emitted particles have an equilibrium energy distribution. Table I shows that the angle at $\frac{1}{2}$ intensity is about 0.14 ($\eta\approx0.99$) for any γp_0 when $\rho=0.99$. The primary energy required to give $\theta'=4\times10^{-5}$ is, therefore, 6×10^{15} ev. The total number of π^0 mesons emitted in the forward direction in the c.m. system is three (Table I) and the average energy is so high (Fig. 3) that the number of secondary particles of energy $>10^{13}$ ev is 9/10 of the total,which is three. Therefore, collisions of this type produce a satisfactory number of particles and they are emitted at satisfactory angles.

The effect of fluctuations in the energy distribution of secondaries could be evaluated quantitatively only by returning to the analysis of the statistical model. Here we shall merely obtain a qualitative estimate by noting that, when we chose a primary energy of $1.8\times$

10^{16} ev for the median impact parameter case, the number of secondaries was too high (eight) but when we chose 10^{15} ev, the angular divergence was too large. Fluctuations of the meson production about the equilibrium might enable the relatively abundant lower energy primaries (10^{15} ev or less) to give showers which would correspond to the equilibrium production properties of less frequent, higher energy primaries. This might occur in the following way: There might be a reduction in the angular divergence in the c.m. system if unusually high energy π^0 mesons are emitted or if an unusually large fraction of the energy goes to π^0 mesons as compared with the other types of particles. On the other hand, since we are forced to choose smaller W' in order to keep the shower energy low enough, the relativistic contraction of angle will be less effective. Thus, there might be two opposing effects on the angular divergence and it is difficult to judge which is larger.

In summary, the detailed analysis of the Fermi model gives results that are almost compatible with the interpretation of existing observations. The main discrepancy is qualitatively similar to the case of an isotropic emission model but quantitatively much less serious, i.e., the primary energy required to give the desired relativistic contraction in angle between π^0 mesons results in too much energy to π^0 mesons.

C. Intensity of Energetic Primaries

In principle, a suitable model enables one to correlate observed shower events with originating primary particles. We have seen that the present model suggests primary energies of the order of 10^{16} ev for the creation of shower energies of the order of 10^{13} ev. The measured intensity[1] is about 2×10^{-5} cm^{-2} sec^{-1} sterad^{-1} for shower energies $\gtrsim10^{13}$ ev if we assume the initiating rays originate near the top of the atmosphere. If we assume a power law for the integral primary spectrum between 1.5×10^{10} ev (where rocket measurements give 0.028 cm^{-2} sec^{-1} sterad^{-1})[7] and 10^{16} ev, there results for the primary spectrum $F(E)=0.028\times(1.5\times10^{10}/E)^{1.08}$ cm^{-2} sec^{-1} sterad^{-1}. The exponent is large enough to escape an infinity in the total energy content even if the same exponent were assumed for greater energies. Actually, if we assume that primary energies are linearly related to average shower energies, the exponent has increased to 1.5–1.9 for primary energies greater than 10^{16} ev.[1]

[7] J. A. Van Allen and S. F. Singer, Phys. Rev. **78**, 819 (1950).

The Solubility of He^3 in Liquid He^4*

J. G. DAUNT AND C. V. HEER
Department of Physics, Ohio State University, Columbus, Ohio
(Received December 26, 1951)

Measurements are reported of the distribution coefficient for He^3 between solutions of He^3 in liquid He^4 and their saturated vapors in the temperature range 1.4°K to 2.6°K. The results obtained below the λ-temperature give values for C_V/C_L higher than those calculable for perfect classical solutions, but in good agreement with the theory previously proposed by Heer and Daunt. Above 2.18°K, the λ-temperature for pure liquid He^4, the measured C_V/C_L also appears greater than that for perfect calssical solutions, as was predicted by Heer and Daunt. A comparison with the theory of de Boer and Gorter is also given.

I. INTRODUCTION

THE experimental study of solutions of He^3 in He^4 has been mainly concerned with measurement of the distribution coefficient, i.e., the ratio of the concentration, C_V, of He^3 in the saturated vapor, to the concentration, C_L, of He^3 in the solution, and this has yielded results which have been both mutually inconsistent and subject to excessive experimental scatter.

A. Above the Lambda-Temperature

Results of measurements[1,2] above the lambda-temperature T_λ for dilute solutions ($C_L \approx 10^{-5}$) indicated values of C_V/C_L in approximate agreement with those calculable from Raoult's law from the equation

$$C_V/C_L = p_3^0/p_4^0, \qquad (1)$$

where p_3^0 and p_4^0 are the vapor pressures of pure liquid He^3 and pure liquid He^4, respectively. More recent work above T_λ by Lane and co-workers[3] and by Weinstock, Osborne, and Abraham[4] using more concentrated solutions (C_L up to 25 percent) indicated qualitatively that the observed C_V/C_L is greater than that calculable from Eq. (1). No exact data however was reported.

B. Below the Lambda-Temperature

It has been in measurements of C_V/C_L below the lambda-temperature that the greatest discrepancies between the various results have been evidenced, and these discrepancies have been mainly the result of a lack of uniformity in the distribution of He^3 throughout the volume of the liquid of the solution. This lack of homogeneity in the liquid phase is primarily the result of (*a*) the much larger heat influxes to the experimental arrangements at temperatures below the λ-temperature and (*b*) the fact that He^3 in solution in liquid He^4 does not partake in superfluid flow.[5,6]

The results obtained by Daunt, Probst, and Smith[2] and by Lane and co-workers[7] for C_V/C_L below T_λ were all much smaller than would be given by Raoult's law; whereas the experimental results by Taconis *et al.*[8] and by Lane and co-workers[9] were very much larger than those predictable form Raoult's law. From their results, Taconis *et al.* proposed the hypothesis that He^3 in liquid He^4 below T_λ could be regarded as being in solution with the "normal" constituent of liquid He^4 only. Assuming such a limited solubility to observe the laws for perfect solutions, this empirical rule leads to the

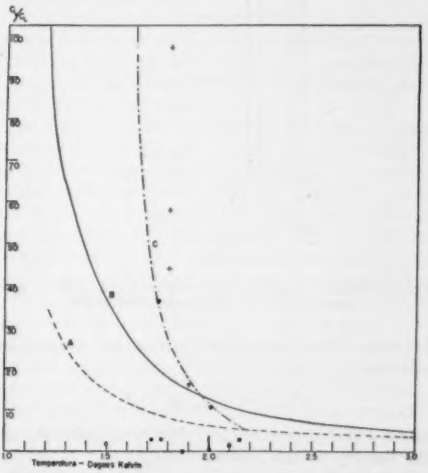

FIG. 1. Plot of C_V/C_L *versus* T from experiment (previous to this paper) and theory for dilute solutions of He^3 in He^4. ($C_L \lesssim 10^{-4}$.) Curve *A*, Raoult's law for perfect classical solutions; Curve *B*, theory of Heer and Daunt (reference 11); Curve *C*, calculated from Taconis's rule (reference 8). ▼ experimental results of Taconis *et al.* (reference 8), + experimental results of Lane and co-workers (reference 9), ■ experimental results of Lane and co-workers (reference 7), and ● experimental results of Daunt and co-workers (reference 2).

* Assisted by a contract between the AEC and the Ohio State University Research Foundation.

[1] Fairbank, Lane, Aldrich, and Nier, Phys. Rev. **71**, 311 (1947).
[2] Daunt, Probst, and Smith, Phys. Rev. **74**, 494 (1948).
[3] Fairbank Reynolds, Lane, McInteer, Aldrich, and Nier, Phys. Rev. **74**, 345 (1948).
[4] Weinstock, Osborne, and Abraham, Phys. Rev. **77**, 400 (1950).
[5] Daunt, Probst, Johnston, Aldrich, and Nier, Phys. Rev. **72**, 502 (1947).
[6] Daunt, Probst, and Johnston, J. Chem. Phys. **15**, 759 (1947).
[7] Fairbank, Lane, Aldrich, and Nier, Phys. Rev. **73**, 729 (1949).
[8] Taconis, Beenakker, Nier, and Aldrich, Phys. Rev. **75**, 1966 (1949) and Physica **15**, 733 (1949). See also Taconis, Beenakker, and Dokoupil, Phys. Rev. **78**, 171 (1950).
[9] Lane, Fairbank, Aldrich, and Nier, Phys. Rev. **75**, 46 (1949).

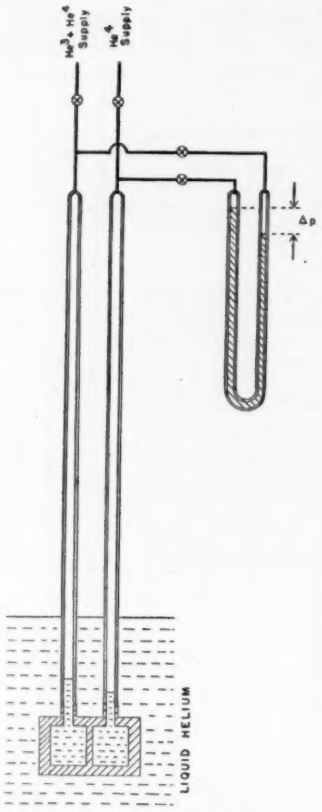

FIG. 2. Diagram of apparatus reported in this paper for measurement of C_V/C_L for solutions of He^3 in He^4.

following formulation for C_V/C_L, for very dilute solutions

$$C_V/C_L=(\rho/\rho_n)(p_3^0/p_4^0), \tag{2}$$

where ρ and ρ_n are the total density of liquid He^4 and the density of the "normal" constituent of He^4, respectively. The value of C_V/C_L according to Eq. (2) is shown in Fig. 1. It should be emphasized that if the laws for classical perfect solutions are continued to be assumed valid, above the λ-temperature there should be no difference between Eqs. (2) and (1), since above the λ-temperature $\rho_n/\rho=1$. This means therefore, according to Taconis, that Raoult's law should be at least approximately valid above the λ-temperature for dilute solutions. de Boer and Gorter[10] have extended this hypothesis of Taconis by calculating the properties of such solutions when the concentration of He^3 may be appreciable.

An entirely different theoretical approach has been made by Heer and Daunt,[11] who have shown that solutions of He^3 in liquid He^4 can be regarded as solutions of model liquids which are represented respectively by ideal Fermi-Dirac and ideal Bose-Einstein gases situated in smoothed potential wells. For such model liquids the quantum effects associated with the degeneracy of the B.E. statistics lead to marked deviations from Raoult's law. The theoretical calculation of C_V/C_L for such dilute solutions is also shown in Fig. 1.

In view of the conflicting experimental data and the interest theoretically in such solutions of He^3 in He^4, the experiments reported herewith were carried out in an attempt to narrow the margin of experimental scatter of results and to measure C_V/C_L over as wide a temperature range as possible.

II. EXPERIMENTAL TECHNIQUE EMPLOYED

The experimental arrangement used by us for the evaluation of C_V/C_L is shown diagramatically in Fig. 2. Two vessels of internal diameter 3.2 mm and volume 40 mm^3 were drilled out of a solid block of pure copper, so that they were in good thermal contact with each other. The vessels were connected to their external gas supplies by capillary tubing of 0.79-mm internal diameter, part of which was of glass so that the levels of the liquids in the two volumes could be observed directly, and the vessels immersed in a bath of liquid helium.

One vessel was filled with pure liquid He^4 and the other with a solution of He^3 in liquid He^4, having a value of C_L of about 1.5 percent, until the levels were visible in the capillaries and at any desired temperature the difference in vapor pressure between the solution and the pure liquid He^4 could be observed with an external differential oil ("Octoil, S") manometer of very small dead (gas) volume (see Fig. 2).

Significant dimensional data are collected together in Table I.

Provision was made also for making a differential comparison between the vapor pressure of the pure liquid He^4 in the vessel and the vapor pressure of the helium bath. (For simplicity this arrangement is not shown in Fig. 2.)

Our experimental arrangement was chosen as one

TABLE I. Dimensional data of apparatus.

Internal diameter of each copper vessel	3.2 mm
Volume of each copper vessel (Experiments of 21st and 22nd December, 1950)	40 mm^3
Volume of each copper vessel (Experiments of 14 December, 1950)	50 mm^3
Diameter of glass capillaries, leading from copper vessels to room temperature	0.79 mm
Average volume of gas "dead" space at room temperature on He^3+He^4 line	3.5 cm^3

[10] J. de Boer and C. J. Gorter, Physica **16**, 228, 667 (1950).

[11] C. V. Heer and J. G. Daunt, Phys. Rev. **81**, 447 (1951).

which would minimize systematic errors for the following reasons:

(a) The maximum height of the solution, measured from the bottom of its containing vessel, was 50 mm, which for 1.0 percent average value of solution concentration would result in ebullition at the bottom of the vessel for a concentration excess of 15 percent at 1.5°K. At 1.8°K the error is 7.5 percent. This would therefore provide adequate automatic stirring, and would provide a surface concentration within 15 percent of the measured average value at the lowest temperature and better accuracy at higher temperatures.

(b) By having both vessles in the same copper block, the temperatures of both vessels should remain the same even above the λ-temperature.

(c) By measuring differential vapor pressure, an equilibrium measurement is made, which also is independent of the two-phase convection in the filling tubes. Moreover, for all temperatures used, the correction for thermo-molecular pressure differences is negligible.

If Δp is the observed excess pressure of the solution over that of pure liquid He^4, then for our dilute solutions,

$$C_V/C_L=[\Delta p/(p_4{}^0+\Delta p)](1/C_L), \quad . \quad (3)$$

to within the accuracy of the experiment.

(d) By observation of the height of the liquid levels, the liquid and vapor volumes could be computed at all temperatures, and hence, C_L could be evaluated from a knowledge of the He^3 concentration in the unrefrigerated gas.

III. THE EXPERIMENTS

He^3, kindly supplied by the AEC, was used, diluted with He^4 ("well" helium) to form a mixture having an unrefrigerated He^3 concentration, C_3, of 1.0±0.10 percent, as estimated by volume measurements made during the dilution process. Subsequent mass-spectrographic analysis of the sample of the unrefrigerated mixture carried out at three different establishments[12] gave values of C_3=0.99 percent; 1.60 percent and 1.65 percent. These discrepancies are disturbing and have forced us to give out results in the form of ranges of C_V/C_L within which the true values of C_V/C_L may be located.

Observations were made on three independent runs. In the last two runs, the vessels were of dimensions given above, whereas in the first run a different copper block was substituted having a vessel volume=50 mm^3, the dimensions of other parts of the apparatus being kept the same.

The temperature of the helium bath was measured by vapor pressure measurements in the usual way, and above the λ-temperature the bath was well stirred and measurements made only on diminishing the temperature from a higher value.

At all temperatures of measurement no measurable difference of vapor pressure was observable between that of the bath and that of the vessel containing the pure He^4, indicating negligible thermo-molecular pressure difference corrections.

The observed results are given in Table II, in which are tabulated the observed temperatures (1949 scale[13]), the observed vapor pressure differences, Δp, between the He^3 and He^4 solution, and the pure liquid He^4, given both in cm of oil and cm of Hg, and the calculated range of values of C_V/C_L obtained from Eq. (3). In this evaluation of C_V/C_L, the numerical value of C_L has been set throughout equal to C_3, the He^3 concentration of the unrefrigerated gas, and the range of values of C_V/C_L has been calculated for C_3=1.0 percent to 1.65 percent. In assessing the possible deviations of C_L from the concentration of the unrefrigerated gas, estimates have been made of the quantity of He^3 present in the vapor phase at each temperature. These estimates have been made in two ways: (*a*) by estimation of the effective (*NTP*) volume available to the vapor from observation of the meniscus heights of liquid in the capillary and in the main liquid helium bath, and (*b*) by noting the change in the meniscus height of the solution in the capillary when the temperature was reduced from the temperature of interest to a low temperature ($T\approx1.4$°K) where the vapor pressure is negligibly small. By both these methods it was concluded that at the highest temperature of measurement, namely $T\approx2.6$°K, (where the "effective" vapor volumes are largest) the amount of He^3 in the vapor phase was not larger than

TABLE II. The results.

Experiment	T°K	Δp cm oil	Δp cm Hg	C_V/C_L[a]
December 14, 1950	2.33	7.60	0.527	5.4– 8.9
	2.27	7.15	0.496	5.8– 9.5
	2.18	5.30	0.368	5.4– 8.9
	1.99	4.60	0.319	7.5–12.4
	1.75	3.90	0.271	12.7–21.0
	1.45	2.70	0.187	23.8–39.3
	2.49	9.20	0.638	4.8– 7.9
December 21, 1950	2.12	4.95	0.344	5.6– 9.3
	1.66	3.95	0.274	12.4–20.4
	1.43	2.70	0.187	25.4–42.0
	2.59	11.50	0.798	4.9– 8.0
December 22, 1950	2.60	8.90	0.617	3.8– 6.3
	2.31	7.70	0.534	5.8– 9.5
	2.19	7.20	0.500	7.0–11.5
	1.93	4.45	0.308	8.5–14.0
	2.30	5.70	0.396	4.4– 7.3
	2.18	5.30	0.368	5.4– 8.9
	1.50	3.0	0.208	23.2–38.2

[a] The two columns under C_V/C_L give the limits of the ranges of the calculated values of C_V/C_L. The lower numerical values of C_V/C_L were obtained by taking $C_L=C_3=1.65$ percent and the higher values were obtained by taking $C_L=C_3=1.00$ percent.

[12] We are indebted to Dr. Mohler of the National Bureau of Standards, to the General Electric Company and to the AEC for the analyses.

[13] H. Van Dijk and D. Shoenberg, Nature **164**, 151 (1949).

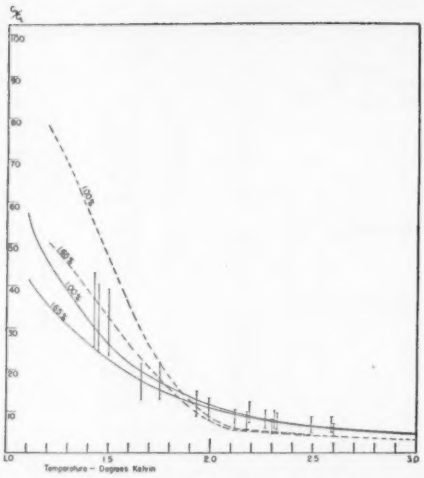

FIG. 3. The full curves are calculated from the theory of Heer and Daunt (reference 11) for He^3 concentrations of 1.00 and 1.65 percent. The broken curves are calculated from the theory of de Boer and Gorter (reference 10) for He^3 concentrations of 1.00 and 1.65 percent. The experimental results (this paper) are given by the vertical lines. The lower ends of the vertical lines correspond to $C_3 = 1.65$ percent and the upper ends to $C_3 = 1.00$ percent.

12 percent of the total amount of He^3. At these temperatures, therefore, C_L may be different from C_3 by 12 percent, and at lower temperatures correspondingly smaller differences must occur. The uncertainty, however, in measurement of the unrefrigerated gas concentration, as detailed above, introduces greater possible errors, and consequently it was not thought worthwhile to make the corrections for the differences between C_L and C_3.

The results are shown in Fig. 3.

IV. CONCLUSION

The results reported herewith on the experimental evaluation of C_V/C_L, although not of high accuracy, do narrow the region of uncertainty and scatter, which was evidenced by previous work (see Fig. 1), and enable a further check with theory to be made. In Fig. 3, the lower numerical values of our results for C_V/C_L correspond to taking the value 1.65 percent for the concentration of the unrefrigerated gas and the higher values correspond to taking 1.00 percent for the same quantity. It seemed natural therefore to make numerical computations from the theories of Heer and Daunt[11] and of de Boer and Gorter[10] for the two liquid concentrations of 1.65 and 1.00 percent. The results of these computations are shown in the curves of Fig. 3.[14]

The comparison of the theories and the experimental results given in Fig. 3 shows that broadly both theories are in general agreement with experiment below T_λ, both showing values of C_V/C_L well above those calculable from the laws for classical solutions.

For temperatures above T_λ the accuracy of the results is unfortunately insufficient to allow a definite conclusion to be drawn; but it might be inferred that the laws for classical perfect solutions are probably insufficient to describe the results. It appears that for the concentration range used in these experiments, the crucial test of theory lies in measurements above T_λ and, consequently, further measurements in this temperature range would be of value.

[14] More extensive computations are to be published by Daunt, Tseng, and Heer.

High Energy Collisions with the Production of Meson Showers

S. BISWAS AND V. D. HOPPER
Physics Department, University of Melbourne, Melbourne, Australia
(Received December 18, 1951)

Eighteen events of meson showers produced in high energy collisions have been analyzed to study the mechanism of the production of mesons. The angles ψ of the mesons have been measured relative to the primary direction or relative to the shower axis for neutron induced showers. The mean value of $\cos\psi$, $\langle\cos\psi\rangle_N$, has been plotted against the number N of the mesons produced. It is found that the observed points can be divided into three regions corresponding to single, double, and triple collisions inside the nucleus. The points representing single collisions lie considerably below the theoretical curve of Heisenberg for completely inelastic collisions and it is concluded that in these collisions only a fraction $(1/K)$ of the incident energy goes to the meson production. For these events the values of K and primary energy E_p have been estimated by applying Heisenberg's theory to partially inelastic collisions. For double and triple collision events the number of mesons produced in successive collisions inside the nucleus has been estimated from the angular dispersions of the single collision events.

I. INTRODUCTION

OUT of a total of 1000 stars obtained in 400 μ Ilford G.5 nuclear plates exposed to cosmic rays at 80,000 feet, 18 high energy stars have been selected for the study of meson shower production. Stars in which the minimum charge, carried by all the evaporation particles, is greater than 8 are ascribed to heavy nuclei and those with less than 8 to light nuclei. Tracks of grain density <1.5 minimum are taken as shower tracks and are assumed to be mesons but occasional slow mesons are also identified and included in the shower. Tracks having grain densities from 1.5 to 5$\times$minimum are classified as medium and are almost exclusively protons. The evaporation particles have grain densities greater than 5$\times$minimum. In these events the initiating particles are protons or neutrons. In the case of proton reactions the angle ψ of each shower track is measured relative to the primary direction, taking into account the shrinkage of the emulsions after processing. For neutron reactions, following Osborne,[1] the shower axis, defined as the "center of gravity" of the meson shower tracks is taken as the primary direction and the angles ψ of the mesons are measured relative to this. The difference in the methods for obtaining ψ for proton and neutron stars does not affect the majority of the events and is discussed later.

II. EXPERIMENTAL OBSERVATIONS AND RESULTS

The mean values of $\cos\psi$, $\langle\cos\psi\rangle_N$, and of ψ, $(\bar{\psi})$ are given in Table I as well as the value of ψ_m, the angle of the meson at the greatest angle from the primary direction. In column 2 of Table I the first number refers to the number of shower tracks (grain density, $g<16/50\mu$), the second to medium tracks ($16<g<50/50\mu$) and the third number of evaporation particles ($g>50/50\mu$). In Fig. 1 the number of shower particles N is plotted against $\langle\cos\psi\rangle_N$. Curve 1A represents the corresponding relation for a completely inelastic nucleon-nucleon collision as given by Heisenberg,[2]

$$\langle\cos\psi\rangle_N \simeq 1-8/n^2, \qquad (1)$$

where n = total number of mesons $=\frac{3}{2}$ times the observed number N of charged mesons from symmetrical theory.

Peyrou *et al.*[3] have pointed out that the maximum angle of the shower particle ψ_m is directly related to the primary energy assuming an isotropic distribution in the c.m. system. When values of ψ_m are plotted against N (Fig. 2) these form a similar pattern to the $\langle\cos\psi\rangle_N$, N plot of Fig. 1.

From Fig. 1 the following are seen:

(1) One set of points lies about the curve 1 which is significantly below the theoretical curve 1A. These events include most of the light nuclei and some of the heavy ones and may be interpreted reasonably as the result of single nucleon-nucleon collisions where only a fraction $1/K$ of the incident energy is used for meson production. This agrees with the conclusion obtained by LePrince-Ringuet *et al.*[4] for a high energy star. The high energy $p-p$ collision denoted by star $L1$ and described previously[5] indicated that about 1/10 of the incident energy of 1000 Bev was used for meson production. If in these events a few fast proton tracks were included in the shower tracks, curve 1 would be displaced further from the theoretical curve indicating higher values of K.

(2) A number of events lie well above the theoretical curve 1A. These events may be reasonably interpreted as because of successive meson producing collisions inside the nucleus. This process of pluro-multiple production of mesons (LePrince-Ringuet *et al.*,[4] Osborne,[1] Kaplon *et al.*[6]) appears to be more probable when only a fraction of the energy of the primary particle is used

[1] L. S. Osborne, Phys. Rev. **81**, 239 (1951).

[2] W. Heisenberg, Nature **164**, 65 (1949); Z. Physik **126**, 569 (1949).

[3] Peyrou, d'Espagnat, and LePrince-Ringuet, Compt. rend. **228**, 1777 (1949).

[4] LePrince-Ringuet, Bousser, Fong, Jauneau, and Morellet, Compt. rend. **229**, 163 (1949).

[5] Hopper, Biswas, and Darby, Phys. Rev. **84**, 457 (1951).

[6] Kaplon, Peters, and Bradt, Phys. Rev. **76**, 1735 (1949).

TABLE I. Summary of data from 18 high energy stars showing the multiplicity classification obtained for the meson showers and the estimated values of K, the ratio of the incident energy to the energy of the shower for single collisions.

Star	Class	Incoming particle	No. of shower particles N	$\langle\cos\psi\rangle_{Av}$	$\bar{\psi}$ deg	ψ_m deg	Multiplicity classification	$N[\langle\cos\psi\rangle_{Av}]_N$	$\Sigma N_1[\langle\cos\psi\rangle_{Av}]_{N_1}$	$\Delta\psi$ deg	Calc. K	E_p (Bev)
L1	7+0+0	p	6	0.992	5.2	15.9	6			1.3	(10)	(1000)[a]
L2	1+3+3	p	2[b]	0.568	71.9	79.6	2			20.5	1.8	4.7
L3	3+1+7	π	3	0.803	35.0	51.0	3				2.0	10
L4	4+1+3	p	3	0.884	26.8	37.0	3			8.0	3.2	16
L5	6+0+6	p	5	0.800	28.9	80.5	3, 2	4.0	3.6	11.5		
L6	5+0+4	p	4	0.959	13.9	22.0	4			5.0	5.9	52
H1	8+3+13	π	8	0.875	26.7	45.3	5,3	7.0	7.4			
H2	12+6+13	p	12[c]	0.754	30.1	94.9	5, 4, 3	9.1	11.1	19.3		
H3	10+1+9	π	10	0.924	19.9	40.0	6, 4	9.2	9.7			
H4	11+8+13	p	10	0.577	51.8	90.7	3, 3, 2, 2	5.8	7.1	36.2		
H5	4+1+11	π	4	0.165	81.5	90.0	2, 2	2.0	2.0			
H6	9+4+15	p	8	0.738	34.9	110.0	3, 2, 2	5.9	6.1	16.1		
H7	4+1+20	π	4	0.953	21.0	27.2	4				5.0	44
H8	14+4+12	π	14	0.818	27.6	84.5	6, 5, 3	11.4	13.3			
H9	6+10+14	p	5	0.875	25.4	46.6	?			5.0		
H10	3+1+17	π	3	0.834	31.6	48.0	3				2.3	11.5
H11	3+1+14	π	3	0.546	49.0	80.0	3				1.0	5.0
H12	5+3+8	π	5	0.963	20.6	28.0	5				4.4	59

[a] Star *L1* refers to a p–p collision (reference 5).
[b] Two of the medium prongs are mesons.
[c] One medium prong is a slow π^- meson.

in a collision. The points may be roughly divided into two regions about the dotted curves 2 and 3. Those around curve 2 may be interpreted as the result of two meson producing collisions inside the nucleus and those around curve 3 to 3 collisions. One isolated point (*H4*) possibly represents a 4-collision process. From the values of ψ_m and $\langle\cos\psi\rangle_{Av}$, it is possible to indicate the type of collision taking place. The total number of mesons N can be subdivided into $N_1+N_2+\cdots$ for successive collisions by using the ψ_m, N curve (Fig. 2) for a single collision and from a study of the number of mesons occurring within a certain angle. In this way the multiplicities N are subdivided for the successive collisions as given in column 8 of Table I. These subdivisions can be checked from the $\langle\cos\psi\rangle_{Av}$ values as follows: If $[\langle\cos\psi\rangle_{Av}]_N$ corresponds to total multiplicity N and $[\langle\cos\psi\rangle_{Av}]_{N_1}$, $[\langle\cos\psi\rangle_{Av}]_{N_2}$, $\cdots$ to numbers N_1, $N_2\cdots$ for single collisions, then

$$N[\langle\cos\psi\rangle_{Av}]_N \simeq N_1[\langle\cos\psi\rangle_{Av}]_{N_1}+N_2[\langle\cos\psi\rangle_{Av}]_{N_2}+\cdots, \quad (2)$$

where $N=N_1+N_2+\cdots$. The numerical values of the two sides of Eq. (2) are given in columns (9) and (10) of the table, which show general agreement, the difference being somewhat large for three events of high plurality. The relation (2) is valid when the nucleons taking part in the successive meson producing collisions inside the nucleus move nearly in the same direction as the primary particle. This is unlikely when a number of successive meson producing collisions occur inside the nucleus. This can be seen from a comparison of the values of $\Delta\psi$, the difference between the direction of the primary and the shower axis, given in column 11 where large values of $\Delta\psi$ occur for 3- and 4-fold collisions. For these events if the angles ψ are measured relative to the shower axis of the star instead of the primary proton direction, the values of $N[\langle\cos\psi\rangle_{Av}]_N$ are closer to the value of $\sum N_1[\langle\cos\psi\rangle_{Av}]_{N_1}$. (For example in events *H2* and *H5*, the $N[\langle\cos\psi\rangle_{Av}]_N$ values are 10.1 and 7.5, respectively, when the angles ψ are meas-

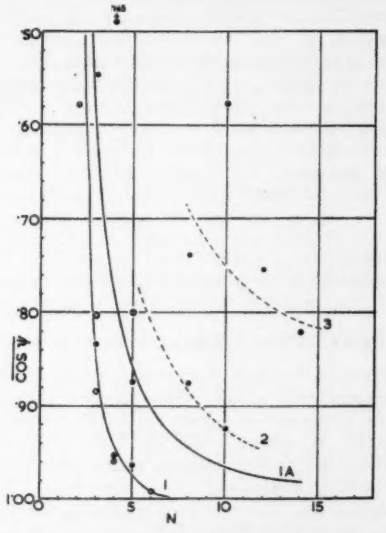

FIG. 1. Number of shower particles N, plotted against $\langle\cos\psi\rangle_{Av}$ for eighteen high energy stars. Blank circles and black circles correspond to light and heavy nuclei, respectively. Curves 1, 2 and 3 represent single, double and triple meson producing collisions in the nucleus. Curve 1*A* represents relation for completely inelastic single collision according to Heisenberg (see reference 2).

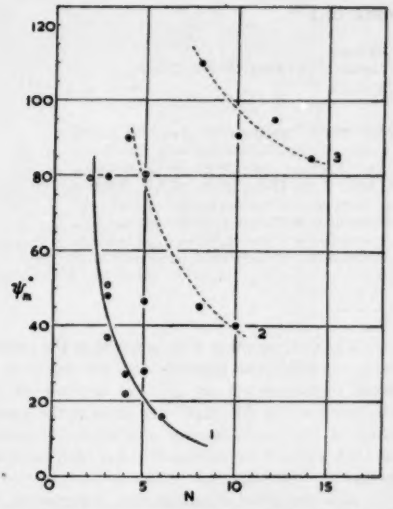

FIG. 2. Number of shower particles N, plotted against $\psi_m°$, the maximum angle of a meson relative to the primary direction or shower axis. Blank circles correspond to light nuclei and black circles to heavy ones. Curves 1, 2, and 3 represent single, double, and triple meson producing collisions.

ured relative to the shower axis.) For single collisions however, it seems better to measure angles ψ relative to the primary proton direction instead of shower axis.

If we apply Heisenberg's theory[2] to partially inelastic collisions the fraction, $1/K$, of the incident energy used for meson production for single collision events can be obtained. For a given number of mesons N, the energy E, available for meson production in the L system, is

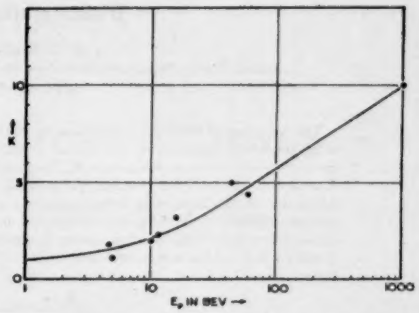

FIG. 3. Energy of the incident particle E_p, plotted against K, the ratio of the energy of the incident particle to the energy of the meson shower for single collisions.

obtained from the N, E curve drawn from the relations

$$N=\tfrac{2}{3}(\epsilon/m)/\ln(\epsilon/m), \quad \epsilon=[2M(M+E)]^{\frac{1}{2}}-2M, \quad (3)$$

where ϵ is the energy available in the c.m. system, m the meson mass, and M the proton mass. The observed value of N and the theoretical value for a completely inelastic collision, are obtained from the value of $\langle\cos\psi\rangle_{Av}$ for any event using curves 1 and 1A of Fig. 1. From the (N, E) curve of relation (3), the corresponding values of E are determined. The ratio of the theoretical to observed E, represents the factor K. The values of K and estimated primary energies E_p are given in Table I. A plot of K *vs* E_p shown in Fig. 3 indicates a general increase of K with increasing energy.

The authors wish to thank Professor L. H. Martin for his continued interest and support, and the Commonwealth Meteorological Service for assistance in exposing the nuclear plates at high altitudes. One of the authors (S.B.) is thankful to the Government of Australia for a UNESCO fellowship.

Disintegration Scheme of I^{131}

R. E. Bell and R. L. Graham
Atomic Energy Project, National Research Council of Canada, Chalk River, Ontario, Canada
(Received December 28, 1951)

The radiations of I^{131} (8-day) have been studied in a pair of lens beta-ray spectrometers placed end to end, with coincidence counting of the focused radiations from a single source. Coincidence beta-spectra are shown with end points at 608±5 kev (87.2 percent), 335±6 kev (9.3 percent), and 250±7 kev (2.8 percent). A weak 812±15 kev beta-spectrum (0.7 percent) apparently leads to the 12-day isomer of X^{131}. Relative intensities of the three main beta-components are obtained from gamma-ray measurements alone. All gamma-rays have their multipolarities assigned on the basis of measured K-conversion coefficients and K/L ratios. A consistent disintegration scheme is proposed which is an extension of that of Metzger and Deutsch. Single-particle orbital assignments are made to the lower excited states of Xe^{131} which agree with shell theory.

I. INTRODUCTION

THE present study of the disintegration of 8-day I^{131} was prompted by the lack of agreement among the many previous publications on the details of this disintegration scheme. The radiations of I^{131} are here examined by coincidence techniques in a pair of lens beta-ray spectrometers placed end to end. In this way the various subcomponents of the I^{131} beta-ray spectrum have been studied separately in coincidence with the Xe^{131} gamma-rays which respectively follow them. Given these results, we arrive at the intensities of the subcomponents of the I^{131} beta-spectrum by gamma-ray measurements alone, so that the intensities found are independent of source thickness effects and spectrum shapes. The disintegration scheme found in the present study is not difficult to reconcile with the results of all previous measurements on I^{131}. An account of the results presented in this paper was given at the annual meeting of the Royal Society of Canada, Montreal, June, 1951. Parts of the work on I^{131} have been published elsewhere.[1,2]

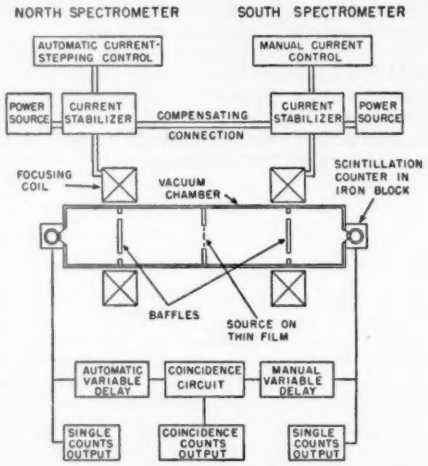

FIG. 1. Pair of end-to-end lens beta-ray spectrometers and associated equipment. This diagram illustrates the functions of the various components of the system but is not to be taken literally either mechanically or electrically. Short Lucite light pipes (not shown above) are used between the scintillating crystals and the 1P21 photomultipliers. As suggested by the diagram, the two lens spectrometers are operated at magnification ~0.7 in order to minimize the interaction effect between them.

The two published disintegration schemes of I^{131} which have found the widest acceptance are those of Metzger and Deutsch[3] and Kern, Mitchell, and Zaffarano.[4] Subsequently, Feister[5] published results lying between the two schemes. Later work by P. R. Bell, Cassidy, and Kelley[6] supports the Kern scheme, while a recent paper by Verster *et al.*[7] agrees with the Metzger-Deutsch result. In the meantime several studies[8–10] have been published on the question of the growth of the 12-day Xe^{131} isomer in low abundance from I^{131}, and this part of the I^{131} disintegration scheme will be accepted here. The accurate gamma-ray energy measurements of Lind *et al.*[11] have assisted in fixing the disintegration scheme and are useful in calibrating the spectrometers.

II. APPARATUS

The chief apparatus was a pair of lens beta-ray spectrometers placed end to end, shown in Fig. 1. The two spectrometers are contained in the two halves of a single vacuum chamber with the source mounted at the center. Simple annular baffles and point focusing are used. Each spectrometer has its own power source and magnet current stabilizer, so that each spectrometer can focus electrons independently of the other. A given

[1] Bell, Graham, and Petch, Can. J. Phys. **30**, 35 (1952).
[2] R. L. Graham and R. E. Bell, Phys. Rev. **84**, 380 (1951).
[3] F. Metzger and M. Deutsch, Phys. Rev. **74**, 1640 (1948).
[4] Kern, Mitchell, and Zaffarano, Phys. Rev. **76**, 94 (1949).
[5] I. Feister, Phys. Rev. **78**, 179 (1950).
[6] Bell, Cassidy, and Kelley, Phys. Rev. **82**, 103 (1951).
[7] Verster, Nijgh, Van Lieshout, and Bakker, Physica **17**, 637 (1951).
[8] Brosi, DeWitt, and Zeldes, Phys. Rev. **75**, 1615 (1949).
[9] I. Bergstrom, Phys. Rev. **80**, 114 (1950).
[10] Zeldes, Brosi, and Ketelle, Phys. Rev. **81**, 643 (1951).
[11] Lind, Brown, Klein, Muller, and DuMond, Phys. Rev. **75**, 1544 (1949).

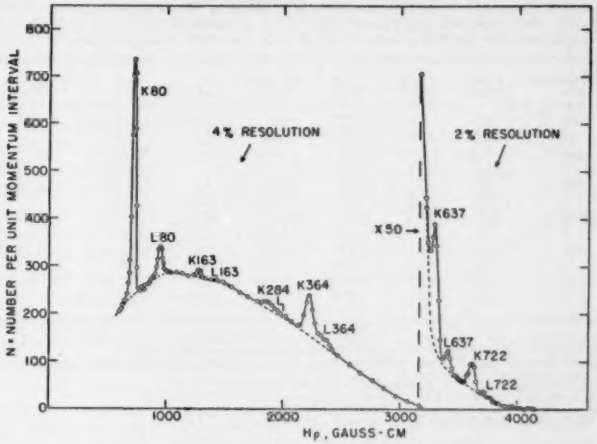

FIG. 2. Observed beta-ray spectrum of I^{131}. The right-hand part of the spectrum was measured with higher resolution in the spectrometer. The standard deviations of the points are everywhere smaller than the radii of the circles.

current in one coil affects by about 0.06 of itself the value of the current required to focus electrons of a given momentum in the other coil. The compensating connection of Fig. 1 balances out this interaction effect by automatically reducing the current in either coil by 0.06 of the amount of the current in the other. There remains a small effect on the transmission of one spectrometer by the current in the other; this effect must be corrected in the observed results.

Either of the magnet current stabilizers (that of the north spectrometer in Fig. 1) may have an automatic current-stepping control replacing the more usual manual current control (south spectrometer in Fig. 1). This unit causes the magnet current to assume a series of equally spaced fixed values in turn, each value being held for a fixed time while counting proceeds. The number of fixed current values may be varied from 10 to 35. A timing switch (not shown in Fig. 1) controls the changes in current.

The detectors for the two spectrometers are stilbene-1P21 scintillation counters connected to a coincidence circuit[1,12] whose resolving time $2\tau_0$ may be varied down to 2×10^{-9} second or less, with the coincidence efficiency remaining greater than 0.9. An automatic variable delay unit[1] is connected in series with the pulses from one of the counters and may be operated by the same timing switch as that used for automatic current switching.

With chart recording of total and coincidence counting rates, the above assembly of apparatus allows us to perform automatically any combination of beta-ray spectroscopy, coincidence spectroscopy, or delayed coincidence experiments on beta-rays and conversion electrons of selected energies. The most frequent types of measurement are

(a) simple automatic beta-ray spectroscopy,

(b) delayed coincidence experiments with the spectrometers held fixed on two desired radiations, and

(c) coincidence spectroscopy in which one spectrometer is held fixed on a particular radiation while the other spectrometer is scanned in steps over some spectrum. In this case it is usual to operate the automatic variable delay unit so as to record in turn true-plus-chance and chance-alone coincidences at each value of the current in the scanned spectrometer.

Chart recording of counting rates is accomplished in the case of high counting rates by recording the output of a counting rate meter. In the case of low counting rates or in cases where the counting rate covers a very wide range, the 1's, 10's, 100's, and 1000's pulses from a scale of 1000 are recorded as pips of different signs and magnitudes on an Esterline-Angus chart.

A subsidiary apparatus was a scintillation gamma-ray spectrometer consisting of a block of NaI(Tl) of dimensions 2×2 cm×1 cm thick, a 5819 photomultiplier, amplifier, and single-channel pulse-height analyzer. In addition, check measurements were made on the gamma-ray intensities emitted by an I^{131} source by lead absorption experiments using scintillation and Geiger counter detection.

III. PROCEDURE AND RESULTS

A. The Beta-Spectrum

The total beta-ray spectrum of I^{131}, shown in Fig. 2, was recorded in the north spectrometer with the current in the south spectrometer shut off. Figure 2 is a composite of results using three different sources and two spectrometer resolution settings. The I^{131} used was chemically separated from n-irradiated Te. Below $H\rho=1000$ the source was of activity ~300 μC, diameter ~8 mm, and average surface density ~125 $\mu g/cm^2$,

[12] R. E. Bell and H. E. Petch, Phys. Rev. 76, 1409 (1949).

TABLE I. Properties of Xe^{131} gamma-transitions following the beta-disintegration of I^{131}. Intensities are given per 100 beta-disintegrations. Each measured figure is accompanied by an estimated percentage probable error in brackets. The K/L values have been calculated assuming that 0.8 of any $L+M+N$ peak is a result of L conversion.

Gamma-energy kev	I total (adopted)	I total (exp)	I_K (exp)	I_{L+M+N} (exp)	I_γ (exp)	α_K (exp)	α_K (theor)[b]	K/L	Multipolarity[a]	Half-life
80	6.3 (10)	6.6 (15)	3.75 (10)	0.67 (20)	2.17 (15)	1.73 (20)	~1.6	7 (20)	$M1$	4.8×10^{-10} sec (40)[e]
163	0.70 (25)	0.70[a] (25)	0.40 (20)	···	···	···	35	···	$M4$[d]	$12d$[f]
284	6.3 (10)	5.6 (20)	0.24 (15)	0.06 (30)	5.3 (20)	0.047 (20)	0.043	5 (30)	$E2$	$<10^{-10}$ sec[g]
364	80.9 (3)	81.6 (5)	1.40 (10)	0.22 (15)	80.0 (5)	0.018 (15)	0.019	8 (15)	$E2(+M1)$	$<10^{-10}$ sec[g]
637	9.3 (15)	9.3 (15)	0.034 (20)	0.005 (30)	9.3 (15)	3.7×10^{-3} (25)	4.1×10^{-3}	9 (20)	$E2$	···
722	2.8 (25)	2.8 (25)	0.0078 (25)	0.0013 (30)	2.8 (25)	2.8×10^{-3} (30)	3.0×10^{-3}	8 (30)	$E2$	···

[a] Deduced from the beta-spectrum. Intensity observed will depend on the age of the source and on the retentivity of the source for Xe atoms. The value 0.40 given under I_K(exp) thus applies only to this particular measurement.
[b] Rose, Goertzel, Spinrad, Harr, and Strong, Phys. Rev. **83**, 74 (1951). An extrapolated value has been used for the 80-kev gamma-ray.
[c] Using the notation of reference d.
[d] M. Goldhaber and A. W. Sunyar, Phys. Rev. **83**, 906 (1951).
[e] R. L. Graham and R. E. Bell, Phys. Rev. **84**, 380 (1951).
[f] Brosi, DeWitt, and Zeldes, Phys. Rev. **75**, 1615 (1949).
[g] Bell, Graham, and Petch, Can. J. Phys. **30**, 35 (1952).

deposited as AgI on a 100 $\mu g/cm^2$ plastic film and covered with 10 $\mu g/cm^2$ of collodion. For $1000<H\rho<3200$ the source was of activity ~200 μC, diameter ~6 mm, and average surface density ~60 $\mu g/cm^2$, deposited as AgI on a 1.5 mg/cm^2 Al foil and covered with 10 $\mu g/cm^2$ of collodion. The spectrometer resolution was ~4 percent for these cases. In spite of its higher average surface density the first of the two sources aforementioned gave cleaner line shapes at low energies, possibly because of chemical attack on the Al backing in the case of the second source. Neither the sources nor the backings are thin enough to guarantee an undistorted spectrum shape. The observed shape is therefore not used to draw firm conclusions about the energies and intensities of the lower energy beta-ray components. Above $H\rho=3200$ the source was of activity ~1 mC, diameter ~4 mm, and average surface density ~1.7 mg/cm^2, deposited as AgI on a thick Al backing and covered with 10 $\mu g/cm^2$ of collodion. For this region the spectrometer resolution was set at ~2 percent. Conversion lines are seen in Fig. 2 due to the well-known gamma-rays of Xe^{131} of energies 80.1, 163, 284.1, 364.2, 637, and 722 kev.[3,9–11] The 177-kev gamma-ray found by Cork *et al.*[13] was not evident. The K-conversion peak of the 364.2-kev gamma-ray was used to calibrate the energy scale. The intensities of the conversion peaks, as determined by their relative areas in Fig. 2, are listed in the columns headed I_K and I_{L+M+N} in Table I, with their estimated probable errors. (Peaks labeled L in Fig. 2 were actually due to $L+M+N$ conversion.)

An allowed Fermi plot of the data of Fig. 2 is shown in Fig. 3, with the conversion peaks of Fig. 2 removed for energies less than 570 kev ($H\rho<3200$). The spectrum splits naturally into four components whose apparent end points and intensities are 812±15 kev (0.7 percent), 608±5 kev (80.5 percent), 335±20 kev (9.4 percent), and 250±25 kev (9.4 percent), assuming that all components have the allowed shape. From this evidence alone it is difficult to be sure that the 250-kev component exists, and we expect that in any case its intensity here appears too high. The beta-ray components of higher energy appear to be on much safer ground. The end points given here have been verified by coincidence measurements (see below, subsection C), except for the weak 812-kev component.

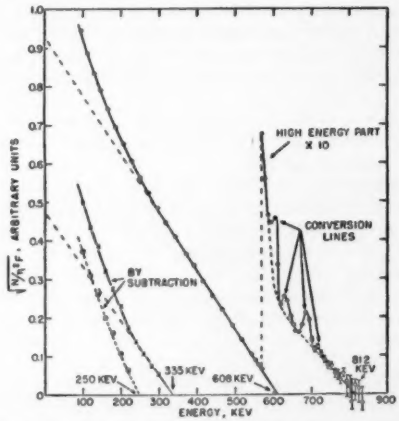

FIG. 3. Allowed Fermi plot of the beta-ray spectrum of I^{131} as observed in Fig. 2. For the part below 570 kev, the conversion lines were omitted as indicated by broken lines in Fig. 2. Where the standard deviations of the points are greater than the radii of the circles, they are indicated by vertical bars. Since the errors of the points of the subcomponents ending at 335 and 250 kev are probably chiefly systematic, no attempt has been made to indicate standard deviations for them.

[13] Cork, Rutledge, Stoddard, Branyan, and Childs, Phys. Rev. **81**, 482 (1951).

B. The Gamma-Spectrum

The secondary electron spectrum of an I^{131} source is shown in Fig. 4. Photoelectrons ejected from an 8 mg/cm² Th radiator were observed in the north spectrometer with the south spectrometer shut off. The beta-rays were stopped by 500 mg/cm² Al. The Compton electron background observed with the Th radiator removed is shown as a broken line in Fig. 4. The relative intensities of the gamma-rays 284, 364, 637, and 722 kev were measured by taking the area of each K peak in Fig. 4 and dividing it by the photoelectric cross section for that energy. The failure to resolve the $L637$ peak from the $K722$ peak is not serious here because Thulin[14] has shown for a Th radiator that the area of the $L637$ peak is almost exactly equal to that of the $K722$ peak.

Absolute quantum intensities of the gamma-rays are found as follows: It is shown later that every beta-ray except those belonging to the 812-kev spectrum is followed by exactly one of the gamma-transitions 284, 364, 637, or 722 kev. The sum of these gamma-transition intensities is therefore 99.3 percent. The sum of their quantum intensities is then equal to 99.3 percent minus the sum of all their internal conversion intensities, found in Table I. The quantum intensities found by this procedure are listed under I_γ, Table I, with estimated probable errors. The least accurate intensity is that of the 284-kev gamma-ray whose K peak in Fig. 4 is weak and awkwardly situated.

According to these results, the sum of the intensities of the 637- and 722-kev gamma-rays is 12.1 percent. This value was checked by absorption measurements in lead, not shown in a diagram, in which the 284- and 364-kev gamma-ray act like a single radiation, and the 637- and 722-kev gamma-rays act like another single

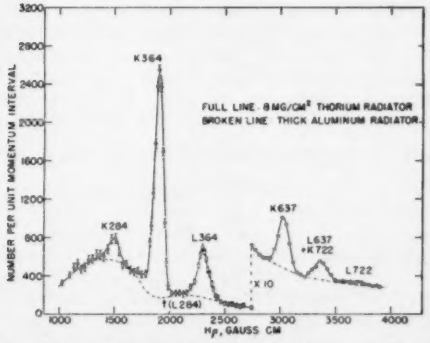

FIG. 4. Secondary electron spectrum of Xe^{131} gamma-rays from an I^{131} source using a Th radiator, 8 mg/cm². The shape of the spectrum observed with the Th radiator removed, leaving a thick Al radiator, is indicated by a broken line. Where the standard deviations of the points are greater than the radii of the circles, they are indicated by vertical bars.

[14] S. Thulin, Phys. Rev. **83**, 860 (1951).

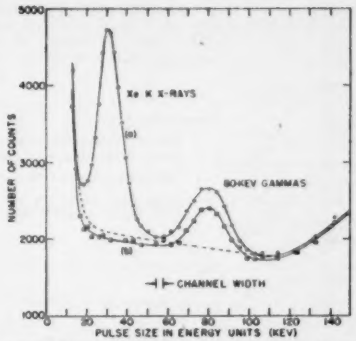

FIG. 5.Scintillation spectrum (low energy region) of the 80-kev gamma-ray and K x-rays of Xe^{131} emitted by a source of I^{131}. The detector was a NaI(Tl) crystal and 5819 photomultiplier connected to a single-channel pulse-height analyser. Curve (a) 280 mg/cm² polystyrene beta-ray absorber over source, curve (b) 410 mg/cm² additional Cu absorber over source to absorb Xe K x-rays. The shape of the background under the x-ray peak in (a) is found by comparison with (b) and shown as a broken line.

radiation. Absorption curves were measured using as detectors a brass-walled Geiger counter and the NaI scintillation counter with its bias set very low (~20-kev equivalent pulse height). The counting rates due to the two equivalent single radiations were separated in the usual way in the absorption experiments and corrected by the respective efficiencies of the two detectors for the two average energies. The relative efficiencies of the Geiger counter were taken from the curves of Bradt *et al.*,[15] and those for the scintillation counter were calculated from the total absorption of NaI. The results for the intensity of the 637+722 gamma-rays were: Geiger experiment, (10.8±1.6) percent; scintillation experiment, (11.7±1.7) percent. These results agree satisfactorily with the figure of 12.1 percent derived from the spectrometer measurement.

The quantum intensity of the 80-kev gamma-ray was measured with the NaI scintillation spectrometer. The thickness of the NaI crystal, 1.0 cm, was great enough to absorb substantially all of the 80-kev gamma-rays falling on it, and all those of lower energy. The low energy part of the scintillation spectrum of an I^{131} source enclosed in 280 mg/cm² of polystyrene to stop the beta-rays is shown in Fig. 5, curve (a). The two peaks are due to Xe K x-rays resulting from K-conversion of gamma-rays in the source and 80-kev gamma-rays. Curve (b) shows the scintillation spectrum with 410 mg/cm² Cu over the source to absorb the K x-rays. Curve (b) is included to show the shape of the background under the K x-ray peak in curve (a). When corrected for absorption in the polystyrene and for fluorescent yield,[16] taken to be 0.80 for Xe, the area of the

[15] Bradt, Gugelot, Huber, Medicus, Preiswerk, and Scherrer, Helv. Phys. Acta **19**, 77 (1946).

[16] H. S. W. Massey and E. H. S. Burhop, Proc. Roy. Soc. (London) **A153**, 661 (1936).

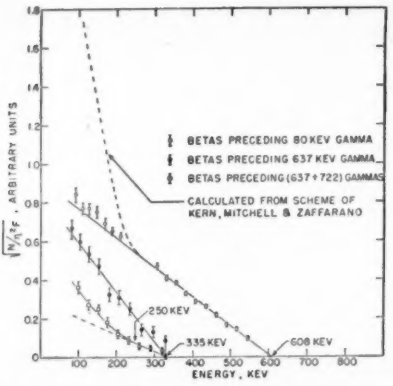

FIG. 6. Coincidence Fermi plots for I^{131}. Upper curve, spectrum of coincidences between beta-rays and 80-kev gamma-rays; the broken line shows what would be expected on the disintegration scheme of Kern *et al.*, reference 4. Middle curve, spectrum of coincidences between beta-rays and 637-kev gamma-rays. Lower curve, spectrum of coincidences between beta-rays, and an equal mixture of 637- and 722-kev gamma-rays. The standard deviations of the points are shown by vertical bars.

K x-ray peak may be equated to the sum of all the K-conversions in the source, $\sum I_K$, already known. The area of the 80-kev peak, corrected for absorption in the polystyrene, then gives directly the quantum intensity of the 80-kev gamma-ray. The result, 2.17 percent, is given under I_γ in Table I, with its estimated probable error.

The K-conversion coefficient of any gamma-ray is the ratio I_K/I_γ and is given in Table I under α_K(exp). The theoretical predictions of Rose *et al.*[17] are given for comparison under α_K(theor) for the multipolarity indicated in the last column of Table I. The K/L ratios in Table I are derived from the experimental results with the assumption that 0.8 of any $L+M+N$ peak is caused by L conversion. The K/L ratios are all consistent with the empirical K/L curves given by Goldhaber and Sunyar[18] for the multipolarities assigned. The total intensities of the gamma-transitions are listed under I total (exp) in Table I. The half-lives of those gamma-transitions which have been measured[2] are also consistent with the assigned multipolarities.

Accurate gamma-ray energy measurements were made only for the 637- and 722-kev gamma-rays, using the accurate energy 364.2±0.1 kev of the 364-kev gamma-ray as a calibration.[11] From Fig. 4, using the extrapolated upper edges of the K lines, the energy of the 637-kev gamma-ray is 637±3 kev. From Fig. 2, the energy difference between 637 and 722 gamma-rays is 85.3±2.0 kev, so that the 722-kev gamma-ray energy is, to the nearest kilovolt, 722±4 kev. The fact that the energy difference between these two gamma-rays is significantly different from 80.1 kev is important in deciding between possible disintegration schemes.[4]

C. Coincidence Measurements

Coincidence measurements have been made in the pair of lens beta-ray spectrometers on most of the radiations from an I^{131} source, in order to establish the correlations existing between the various radiations. Previous coincidence measurements on the internal conversion peaks of the 80, 284, and 364-kev gamma-rays have shown that (1) the 364-kev gamma-ray follows nuclear beta-rays with a half-life less than 10^{-10} seconds;[2] (2) the 80-kev gamma-ray is in cascade with the 284-kev gamma-ray,[1] agreeing with Lind's conclusion[11] that this is a cascade pair of gamma-rays in parallel with the 364-kev gamma-ray; and (3) the 80-kev gamma-ray has a half-life with respect to nuclear beta-rays of $(4.8\pm2.0)\times10^{-10}$ second,[2] and is therefore emitted after the 284-kev gamma-ray.

Measurements have now been made of the beta-ray spectra which precede the 80, 637, and 722-kev gamma-rays. In the case of the 80-kev gamma-ray, the procedure was to use a source on a thin film mounted at the center of the pair of spectrometers and to hold the K-conversion peak of the 80-kev gamma-ray focused in the south spectrometer while scanning the coincidence beta-ray spectrum in the north spectrometer. The results are shown in the form of a Fermi plot in Fig. 6. The coincidence points follow the Fermi plot of the 608-kev component of the total spectrum with a slight rise at low energies, probably as a result of the effect

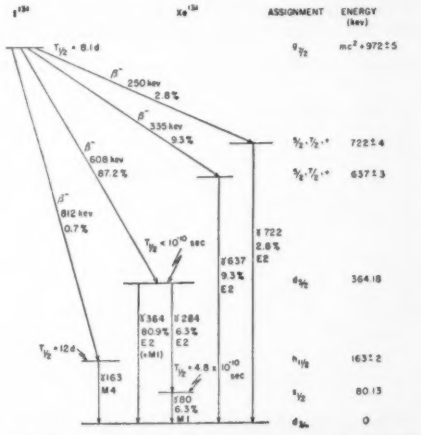

FIG. 7. Proposed disintegration scheme of I^{131}. The detailed properties of the beta-components and gamma-rays are explained in the text and listed in Tables I and II. The orbital assignments are made from experimental results and are consistent with the nuclear shell model. Most of the published observations on I^{131} can be reconciled with this scheme.

[17] Rose, Goertzel, Spinrad, Harr, and Strong, Phys. Rev. **83**, 79 (1951).
[18] M. Goldhaber and A. W. Sunyar, Phys. Rev. **83**, 906 (1951).

TABLE II. Properties of the separate components of the beta-ray spectrum of I^{131}. Intensities are given per 100 beta-disintegrations and are independent of the spectrum shape assumed except in the case of the weak 812-kev spectrum. Figures are included in brackets for two beta-ray spectra which were not observed but which are energetically possible according to Fig. 7.

Maximum energy, kev (adopted)	Intensity (adopted)	$\log f_0 t$	$\log[(W_0^2-1)f_0 t]$	$\log f_0 t$	Spectrum type
812±15	0.7±0.2	9.2	9.9	8.5	First forbidden, (α-shape)
608±5	87.2±3.0	6.6	···	···	*l*-forbidden
335±6	9.3±1.4	6.7	···	···	*l*-forbidden or allowed
250±7	2.8±0.7	6.9	···	···	*l*-forbidden or allowed
(897)	(<0.2) (Unobserved)	(>9.9)	···	···	Second or higher forbidden
(974)	(<0.2) (Unobserved)	(>10.0)	···	···	Second or higher forbidden

of source thickness. Remembering the gamma-ray coincidence results, we conclude that the 80-, 284-, and 364-kev gamma-rays follow only the 608-kev beta-spectrum.

In order to get similar results for the 637- and 722-kev gamma-rays, the I^{131} source on a thick Al backing was used in the pair of spectrometers, the open side of the source facing north. A 42 mg/cm² Th radiator was used on the back of the source holder, facing south. The spectrum in the south spectrometer then resembled that of Fig. 4 except that the photoelectron peaks were more intense and wider as a result of the greater thickness of the radiator. From Fig. 4 it can be seen that the south spectrometer could focus on the $K637$ peak, thus recording the 637-kev gamma-ray alone, or on the $L637+K722$ peak, thus recording 637- and 722-kev gamma-rays in about equal intensity. The north spectrometer was scanned over the coincidence spectrum in the usual way for each of these two settings of the south spectrometer. Fermi plots of the results are shown in Fig. 6. We conclude that the 637-kev gamma-ray follows a beta-ray spectrum of end point 335±15 kev and that the 722-kev gamma-ray follows a beta-ray spectrum of end point 250±20 kev. These observations verify the existence of the 335-kev and 250-kev spectra. However, the intensities of these spectra must be equated to the intensities of the 637- and 722-kev gamma-rays which are, respectively, (9.4±1.4) percent and (2.8±0.7) percent (see Table I).

IV. DISINTEGRATION SCHEME AND DISCUSSION

All the foregoing results are consistent with the disintegration scheme shown in Fig. 7. The scheme agrees in its most intense radiations with that of Metzger and Deutsch,[3] and disagrees with those of Kern, Mitchell, and Zaffarano,[4] Cork *et al.*,[13] and Owen, Moe, and Cook.[19] P. R. Bell *et al.*[6] interpreted their results as favoring a scheme similar to that of Kern *et al.*,[4] but in fact their results are nearly in agreement with this scheme.

Following Fig. 7, the roughly equal measured intensities of the 80 and 284 gamma-transitions have been averaged to give the common intensity assigned to both. This step necessitated a slight change in the intensity of the 364-kev gamma-transition. All the adopted gamma-intensities shown in Table I lie well within the probable errors of the experimental intensities.

From the end point of the 608±5 kev beta-spectrum and the energy of the 364.2-kev gamma-ray, we deduce a total disintegration energy for the I^{131} nucleus of (mc^2+972±5) kev. Since the 637±3 kev gamma-ray has been proved to follow the 335-kev beta-spectrum, we may use the total disintegration energy to obtain a smaller probable error for the energy of the 335-kev component; a similar procedure can be used for the 250-kev component. This procedure would not be allowable without the coincidence measurements of Fig. 6, and therefore cannot be applied to the 812±15 kev beta-spectrum. We thus adopt end points for the low energy beta-components of 335±6 and 250±7 kev, respectively. The adopted intensities for the 608-, 335-, and 250-kev beta-spectra are equal to those of the corresponding gamma-rays in Table I. Table II shows the adopted energies and intensities of the beta-components and their calculated $\log f_0 t$ values. Table II also includes data for two unobserved beta-components that are energetically possible in the disintegration scheme of Fig. 7, but whose intensities from Fig. 2 are less than 0.2 percent.

None of the many possible gamma-transitions between the levels of Fig. 7 were observed other than those already mentioned. The upper limits to be placed on the occurrence of the unobserved gamma-rays vary with the gamma-ray energy, but in any case none of the unobserved gamma-rays can have intensities large enough to upset seriously the intensities adopted for the radiations actually found. These results are consistent with the spins and parities assigned to the states of Xe^{131} (see the following).

Single-particle orbital assignments have been made for most of the levels in Fig. 7 as follows: The ground state of I^{131} is assigned $g_{7/2}$ by analogy with the measured spin and magnetic moment[20] of I^{129}. The ground state of Xe^{131} is $d_{3/2}$ by its measured spin and magnetic moment.[20] The only orbitals which will fit the gamma-ray multipolarity assignments of Table I and explain

[19] Owen, Moe, and Cook, Phys. Rev. **74**, 1879 (1948).

[20] J. E. Mack, Revs. Modern Phys. **22**, 64 (1950).

the beta-ray results of Table II are $d_{3/2}$, $s_{1/2}$, and $d_{5/2}$ for the 0-, 80-, and 364-kev states, respectively. These assignments are consistent with the shell model.[21] The $s_{1/2}$ assignment for the 80-kev state agrees with the observation by Schiff[22] that the angular correlation of the 80- and 284-kev gamma-rays is 0 ± 3 percent. The assignment of $h_{11/2}$ to the 163-kev state follows Goldhaber and Sunyar.[18]

The foregoing orbital assignments make the 812-kev spectrum a first-forbidden, α-type spectrum ($\Delta j=2$, yes), consistent with the observed value of

$$\log[(W_0^2-1)f_0t]=9.9 \quad \text{or} \quad \log f_1t=8.5.^{23}$$

The abundance of this spectrum has been calculated on the assumption of an allowed shape, and if its spectrum is in fact of the α-shape, the abundance should be lowered somewhat from the value 0.7 percent shown in Table II. Since most of the 812-kev spectrum is obscured by more intense spectra of lower energy (Fig. 2), there does not appear to be any experimental way to settle the question of its shape, and the abundance has been left as originally computed.

The 608-kev beta-spectrum becomes an l-forbidden transition[24,25] ($\Delta j=1$, $\Delta l=2$, no) consistent with its $\log f_0t$ value of 6.6.[26] This spectrum seems to have the allowed shape as expected.

Considering the evidence of the 250-kev and 335-kev beta-spectra (Table II) and the multipolarities of the 637 and 722 gamma-rays[27] (Table I), each of the 637- and 722-kev excited states of Xe^{121} may be either 5/2+ or 7/2+. Both beta-components have $\log f_0t$ values suitable for l-forbidden spectra[26] which would suggest 5/2+ for both states. In view of the fact that $\log f_0t$ values for allowed transitions in medium-weight nuclei seem to be separated from those for l-forbidden transitions by less than one unit, on the average,[26] one cannot say that these spectra are not allowed. In that case the value 7/2+ is permissible for either state. It does not seem justifiable to try to make single-particle orbital assignments to these states, but $g_{7/2}$ for one of them is consistent with the shell model.

While this paper was in manuscript, Ketelle, Zeldes, Brosi, and Dandl[28] published coincidence spectra of I^{131} observed with a single magnetic beta-spectrometer and a NaI(Tl) scintillation gamma-spectrometer. Their results are in agreement with those presented in Fig. 6.

We are indebted to the Chalk River Isotopes Branch for the sources of I^{131}, to Dr. Claude Geoffrion for assistance with some of the observations and computations, and to Dr. L. G. Elliott for valuable discussions.

[21] M. G. Mayer, Phys. Rev. **78**, 16 (1950); L. W. Nordheim, Phys. Rev. **75**, 1894 (1949); Hill, Scharff-Goldhaber, and McKeown, Phys. Rev. **84**, 382 (1951); also reference 7.
[22] D. Schiff, Bull. Am. Phys. Soc. **26**, No. 6, 31 (1951).
[23] F. B. Shull and E. Feenberg, Phys. Rev. **75**, 1768 (1949); J. P. Davidson, Phys. Rev. **82**, 48 (1951).
[24] E. Feenberg and K. C. Hammack, Phys. Rev. **75**, 1877 (1949).
[25] R. Bouchez, Compt. rend. **231**, 139 (1950).
[26] Mayer, Moskowski, and Nordheim, Revs. Modern Phys. **23**, 315 (1951).
[27] Verster *et al.* (reference 7) found on the basis of their measured internal conversion coefficient that the 637-kev gamma-ray was electric dipole radiation; however, their value of the conversion coefficient is ~50 percent low because they put the quantum intensity of the 637-kev gamma-ray ~50 percent too high and, in addition, it is inaccurate because their $K637$ internal conversion peak is not cleanly resolved from its background of beta-particles. Their data are not inconsistent with the conclusions of this paper
[28] Ketelle, Zeldes, Brosi, and Dandl, Phys. Rev. **84**, 585 (1951).

Ferroelectricity and Antiferroelectricity in Ceramic $PbZrO_3$ Containing Ba or Sr*

GEN SHIRANE†
Tokyo Institute of Technology, Oh-okayama, Tokyo, Japan
(Received November 16, 1951)

Phase transitions in solid solutions $(Pb-Ba)ZrO_3$ and $(Pb-Sr)ZrO_3$ have been studied by dielectric, dilatometric, and calorimetric measurements. It is shown that when the Ba concentration in $(Pb-Ba)ZrO_3$ compositions exceeds a threshold value of about 5 percent, a ferroelectric intermediate phase begins to appear between the paraelectric and antiferroelectric phases of pure $PbZrO_3$. The temperature range of this intermediate phase increases with the Ba concentration. Though no intermediate phase can be observed in compositions which contain Ba ions with less than this threshold concentration, a forced transition from the antiferroelectric phase to a ferroelectric phase can be caused by the application of a strong electric field at temperatures just below the Curie point. In the $(Pb-Sr)ZrO_3$ system we can also observe an intermediate phase, but this phase proves to be another antiferroelectric phase and not a ferroelectric one. It is concluded, from these situations, that the antiferroelectric phase in pure $PbZrO_3$ must be very peculiar, the free energy of this phase being closely adjacent to those of a ferroelectric phase as well as another antiferroelectric phase.

I. INTRODUCTION

IT has been known that $PbZrO_3$ has several points of resemblance to $BaTiO_3$ in dielectric and structural properties; namely, $PbZrO_3$ has a crystal structure of a tetragonal modification of perovskite type,[1] and its dielectric constant shows a sharp maximum at the Curie point near 230°C.[2] However, our detailed investigations[3,4] on the dielectric properties of this crystal have revealed that the dielectric response of this substance can be explained well if we assume that it is antiferroelectric. Moreover, the x-ray analysis of a single crystal by Sawaguchi *et al.*[5] has shown that the superstructure of this crystal is due to the antiparallel displacement of Pb ions in the plane perpendicular to the c axis.

Very recently, Roberts[6] observed a very weak piezoelectric effect in polarized $PbZrO_3$ ceramic. So, in reference of the foregoing structure analysis, it must be concluded that this crystal is strongly antiferroelectric in the plane perpendicular to the c axis though, possibly, very weakly ferroelectric in the c direction. Nevertheless, we shall continue to use as before the word "antiferroelectric," because the predominant properties of this crystal seem to be properly represented by this word.

A recent study[7] of the $Pb(Zr-Ti)O_3$ system has shown that when Ti ions replace some of the Zr ions in $PbZrO_3$, another transition besides the ordinary Curie point can be observed at lower temperature. The intermediate phase between these two transitions is undoubtedly ferroelectric, because typical hysteresis loops can be observed there.

As stated before, the x-ray analysis has shown that the ions which are responsible for the anomalous dielectric properties of $PbZrO_3$ are Pb ions, and that Zr ions may be considered as a sort of spacer. If the appearance of the ferroelectric intermediate phase in $Pb(Zr-Ti)O_3$ is mainly caused by the replacement of spacer ions, Zr, with smaller Ti ions, a similar phenomenon may be expected upon the replacement of Pb ions with larger ones such as Ba, and at the same time, an inverse situation may be expected upon the replacement of Pb ions with smaller ones such as Sr. Though such a simple interpretation may, of course, be insufficient because the role of the substituted ion depends not only on its ionic radius but also on its polarizability as well as electronic configuration, nevertheless, the study of these $(Pb-Ba)ZrO_3$ and $(Pb-Sr)ZrO_3$ systems will be of some value for elucidating the physical role of the substituted ions in $PbZrO_3$.

The $(Pb-Ba)ZrO_3$ system has already been studied by Roberts[3] and the decrease of the Curie temperature with increasing Ba concentration was reported. However, no special attention was paid to the existence of another transition, because at that time $PbZrO_3$ had been considered as an ordinary ferroelectric. Roberts reported that polarized $(Pb70-Ba30)ZrO_3$ shows a piezoelectric effect at room temperature, and our preliminary dielectric test[3] of $(Pb80-Ba20)ZrO_3$ also revealed that this solid solution shows, in fact, hysteresis loops below its Curie point. If this phase is really of the same nature as the ferroelectric intermediate phase in $Pb(Zr95-Ti5)O_3$,[7] and if it is essentially different from the antiferroelectric phase in pure $PbZrO_3$, there must be a phase boundary somewhere between these two phases.

A re-examination of this $(Pb-Ba)ZrO_3$ system has now been carried out with the special purpose of finding another transition. Moreover, an investigation has been made on the $(Pb-Sr)ZrO_3$ and $(Pb-Ca)ZrO_3$ systems,

* The expense of this research was defrayed from the Scientific Research Expenditure of the Japanese Ministry of Education.
† Now at Department of Physics, Pennsylvania State College, State College, Pennsylvania.
[1] H. D. Megaw, Proc. Phys. Soc. (London) **58**, 113 (1946).
[2] S. Roberts, J. Am. Ceram. Soc. **33**, 63 (1950).
[3] Sawaguchi, Shirane, and Takagi, J. Phys. Soc. Japan **6**, 333 (1951).
[4] Shirane, Sawaguchi, and Takagi, Phys. Rev. **84**, 476 (1951).
[5] Sawaguchi, Maniwa, and Hoshino, Phys. Rev. **83**, 1078 (1951).
[6] S. Roberts, Phys. Rev. **83**, 1078 (1951).
[7] G. Shirane and A. Takeda, J. Phys. Soc. Japan **7**, 5 (1952).

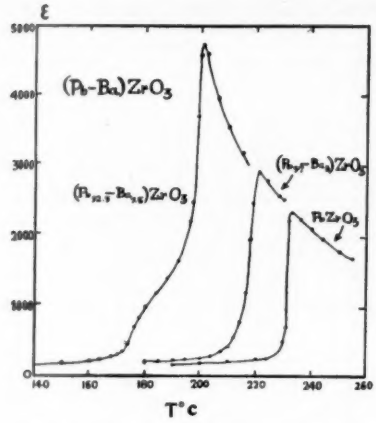

FIG. 1. Permittivity *vs* rising temperature curves of (Pb−Ba)ZrO_3 compositions.

comparing the results with those of the (Pb−Ba)ZrO_3 system.

II. DIELECTRIC STUDY OF (Pb−Ba)ZrO_3

The specimens of (Pb−Ba)ZrO_3 and (Pb−Sr)ZrO_3 composition were made from PbO, ZrO_2, and the respective alkali earth carbonates. Use was made of the same high purity ZrO_2 chemicals as used for the previous study[4] of $PbZrO_3$; this ZrO_2 contains small amount of Ti(0.2 percent), Fe(0.05 percent), and Si(0.03 percent) as impurities. These ingredients were mixed in the desired proportions and sintered at temperatures from 1200° to 1350°C after the preliminary calcination. The higher the Pb concentration, the lower was the sintering temperature.

The dielectric test samples were ceramic disks of 1 mm in thickness and were covered with silver electrodes fired on both faces. The permittivity of these specimens was measured with a beat frequency equipment under an ac field of 1 Mc/sec and 10 v/cm. All of the dielectric measurements were made with the sample immersed in a bath of liquid paraffin, which improved the insulation as well as the constancy of the temperature.

Figure 1 shows the permittivity *vs* rising temperature curves of (Pb−Ba)ZrO_3 compositions together with that of pure $PbZrO_3$. In accordance with the previous data,[2] the Curie temperature decreases with increasing Ba concentration. Whereas the curve for (Pb97−Ba3)-ZrO_3 shows only one sharp maximum at 222°C, the one for (Pb92.5−Ba7.5)ZrO_3 clearly shows another small anomaly at about 175°C besides a sharp maximum at

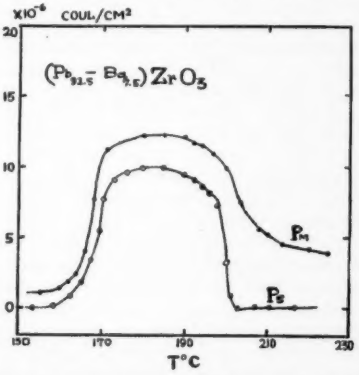

FIG. 3. Maximum polarization P_m and spontaneous polarization P_s of (Pb92.5−Ba7.5)ZrO_3 with rising temperature, estimated from hysteresis loops at $E_{max}=20$ kv/cm.

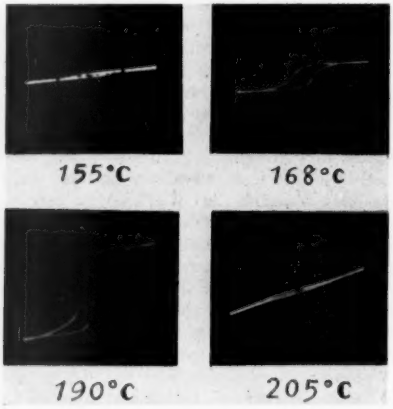

FIG. 2. Hysteresis loops of (Pb92.5−Ba7.5)ZrO_3 at $E_{max}=20$ kv/cm.

200°C. This small anomaly suggests the existence of another transition in this specimen.

The properties of these two transitions in (Pb 92.5−Ba7.5)ZrO_3 were studied more precisely by using a cathode-ray oscillograph. Figure 2 shows a series of *D–E* curves of this specimen under an ac field of 20 kv/cm and 50 cycles/sec. As expected, the *D–E* characteristic is almost linear in the lowest phase, and it shows typical hysteresis loops in the intermediate phase between 175° and 200°C, indicating that this phase is certainly ferroelectric. The spontaneous polarization can be roughly estimated from these figures and is plotted in Fig. 3, together with the maximum polarization at this field strength. It is interesting to note that these hysteresis loops can be easily saturated, and they show relatively large spontaneous polarizations.

The effect of a dc biasing field of 10 kv/cm upon the permittivity of this specimen was studied, with the result shown in Fig. 4. In the antiferroelectric phase

below 175°C, the permittivity is almost independent of the biasing field, except that a slight increase is observed just below the lower transition point. In the ferroelectric region, on the other hand, it decreases considerably with increasing dc bias. The upper transition temperature is raised by dc field, while the lower one is decreased. Namely, the temperature range of the ferroelectric phase is enlarged by the application of a biasing field. This is just the expected result, because the free energy of the ferroelectric phase should be lowered considerably by an electric field as compared with those of the antiferroelectric and paraelectric ones. All of the dielectric properties of this specimen in the three phases are respectively of the same nature as those of the corresponding three phases in $Pb(Zr95-Ti5)O_3$.[7]

The phase diagram of the $(Pb-Ba)ZrO_3$ system obtained from the permittivity measurements at rising temperature is shown in Fig. 5. This figure shows that these solid solutions are ferroelectric at room temperature in the concentration range between about $(Pb85-Ba15)ZrO_3$ and $(Pb65-Ba35)ZrO_3$. This result is consistent with the previous observations of ferroelectricity in the specimens of $(Pb80-Ba20)ZrO_3$[3] and $(Pb70-Ba30)ZrO_3$.[2] The upper phase line in this figure is in good agreement with the previous data obtained by Roberts.[3]

It must be noticed here that the ferroelectric intermediate phase does not appear until the Ba concentration reaches a threshold value which seems to be slightly above 5 percent. In solid solutions derived from $PbZrO_3$, such as $Pb(Zr-Ti)O_3$ and $(Pb-Ba)ZrO_3$, this threshold concentration and consequently the lower phase line seem to depend very sensitively on the impurities already contained even in pure $PbZrO_3$, particularly in ZrO_2 chemicals. For the precise determination of the phase diagram near the $PbZrO_3$ end, we must use the highest purity ZrO_2 chemical, which contains no impurities such as Ti, Ba, Sr, and the like. So the values obtained here for the $(Pb-Ba)ZrO_3$ system are approximate ones, because even our purest ZrO_2 cannot help containing a small amount of Ti.

III. FORCED TRANSITION BY ELECTRIC FIELD

In the course of the previous study[4] of the dielectric properties of pure $PbZrO_3$, anomalous hysteresis loops of very impressive form were obtained at a high field strength and at temperatures just below the Curie point (see Figs. 8 and 9 of reference 4). In these figures we guessed that the central portion of the loop would correspond to the antiferroelectric phase while the outer portion to a ferroelectric phase. Namely, we considered that the forced transition from the antiferroelectric phase to the ferroelectric phase is caused by the application of a strong electric field. These anomalous hysteresis loops can also be observed in the present $(Pb-Ba)ZrO_3$ compositions which contain Ba ions in a concentration less than the threshold value of about

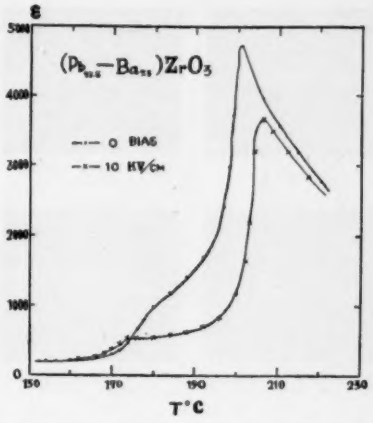

FIG. 4. Effect of a dc biasing field of 10 kv/cm on the permittivity of $(Pb92.5-Ba7.5)ZrO_3$.

5 percent (Fig. 6). We shall define a critical field strength E_c at which the forced transition does occur.

Using a specimen of $(Pb97-Ba3)ZrO_3$ we have estimated E_c as a function of temperature. It is shown in Fig. 7 by open circles. It decreases with increasing temperature and reaches a lowest value E_l near the Curie temperature. This value E_l of varied $(Pb-Ba)ZrO_3$ compositions decreases monotonically with increasing Ba concentration, and seems to reach zero at the concentration at which the ferroelectric intermediate phase begins to appear under zero external field (Fig. 8).

If our foregoing interpretation is right, this forced transition should be caused also by a strong dc biasing field. Figure 9 shows a series of the permittivity *vs*

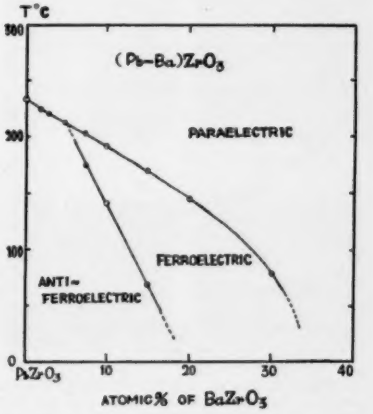

FIG. 5. Phase diagram of the $(Pb-Ba)ZrO_3$ system.

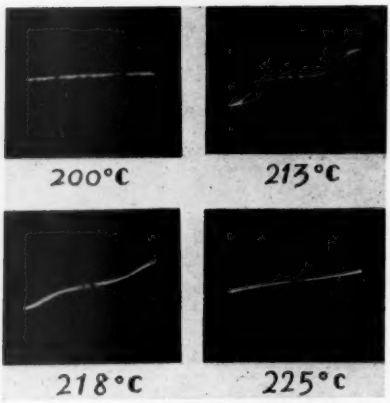

FIG. 6. Hysteresis loops of $(Pb97-Ba3)ZrO_3$ at $E_{max}=20$ kv/cm.

rising temperature curves of a $(Pb97-Ba3)ZrO_3$ specimen under various biasing field strengths. When the applied field is less than a critical value of about 11 kv/cm, which is approximately equal to E_l of this specimen, the Curie temperature decreases slightly with increasing biasing field, accompanied by a slight increase of the permittivity just below the Curie point. On the contrary, when the dc field strength exceeds this critical value, the Curie temperature increases with biasing field strength, and at the same time we can detect another small anomaly in the permittivity curve on the lower temperature side which suggests the existence of another transition. This lower transition temperature decreases with increasing biasing field (Fig. 10). In the new phase between these two transitions, the permittivity decreases considerably with increasing dc field,

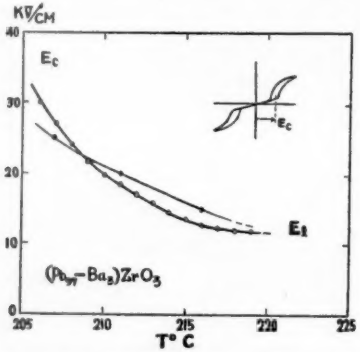

FIG. 7. Threshold field E_e of $(Pb97-Ba3)ZrO_3$ as a function of temperature. Open circles are estimated from the hysteresis loops; solid circles are estimated by the permittivity measurements under the application of a dc biasing field.

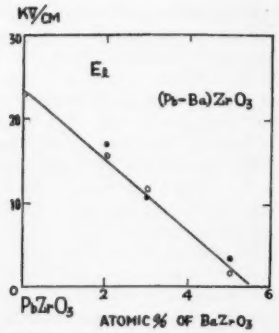

FIG. 8. Threshold field E_t as a function of composition of $(Pb-Ba)ZrO_3$. Open circles are estimated from hysteresis loops; solid circles are estimated by the permittivity measurements under the application of dc biasing field.

just as expected by analogy with the case of the ferroelectric phase in $(Pb92.5-Ba7.5)ZrO_3$. Therefore, it is certain that this new intermediate phase is also ferroelectric.

The critical value of the dc biasing field at which the intermediate phase begins to appear is estimated also for $(Pb98-Ba2)ZrO_3$ and $(Pb95-Ba5)ZrO_3$ by similar measurements, and is shown in Fig. 8 by solid circles. These values are in good agreement with the estimates from the anomalous hysteresis loops. Moreover, it must be noticed here that the lower phase line in Fig. 10 should coincide with the E_e *vs* temperature curve in Fig. 7, because it gives the field strength at which the forced transition occurs at a given temperature, and so

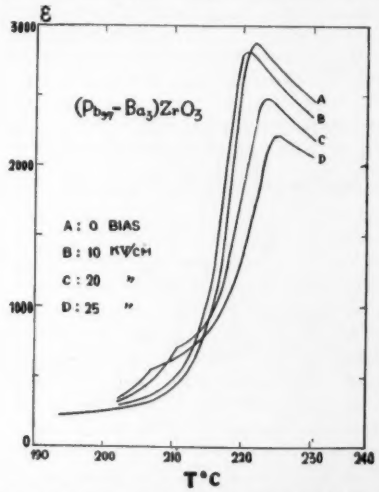

FIG. 9. Effect of a dc biasing field on the permittivity of $(Pb97-Ba3)ZrO_3$.

both curves have the same physical meaning. In Fig. 7 we plotted the lower transition points obtained from Fig. 10 by solid circles, and the qualitative agreement is in fact fairly satisfactory.

We assume that the forced ferroelectric phase may be an extension of the intermediate phase in (Pb92.5−Ba7.5)ZrO_3. The decisive evidence, however, should be given by an x-ray study under the application of a strong dc field, which is now in progress.

IV. DIELECTRIC STUDY OF (Pb−Sr)ZrO_3

Figure 11 shows the permittivity *vs* rising temperature curves for several (Pb−Sr)ZrO_3 compositions. These curves show two anomalies just as in the case of (Pb92.5−Ba7.5)ZrO_3, but a careful comparison reveals the following differences. First, the peak value of the permittivity at the Curie point decreases rapidly with increasing Sr concentration. Secondly, the permittivity change at the lower transition is rather sharp and

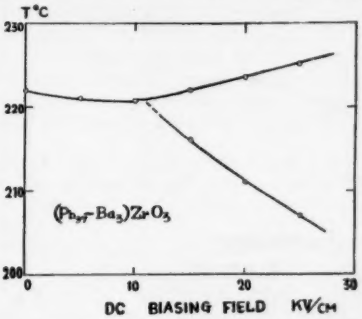

FIG. 10. Transition temperature *vs* dc biasing field curve of (Pb97−Ba3)ZrO_3.

pronounced compared with the small anomaly in the (Pb−Ba)ZrO_3 compositions.

There is no doubt that the lowest phase here is also antiferroelectric, being of the same nature as that of pure $PbZrO_3$. So the foregoing differences should be attributed solely to the essential differences of the respective intermediate phases in both systems. To confirm this point we have carried out a detailed study of the dielectric properties of this intermediate phase with the specimen of (Pb95−Sr5)ZrO_3.

In the first place, we have observed the *D–E* characteristics of this specimen. If the intermediate phase between 222°C and 245°C is of the same ferroelectric phase as that of (Pb92.5−Ba7.5)ZrO_3, typical hysteresis loops should be observed in this temperature range. However, observation under an ac field of 30 kv/cm has shown that the *D–E* characteristic of this specimen is almost linear except just below the upper transition temperature where it shows a slight upward curvature (Fig. 12), suggesting that this intermediate phase may not be ferroelectric. It should be noted here that the

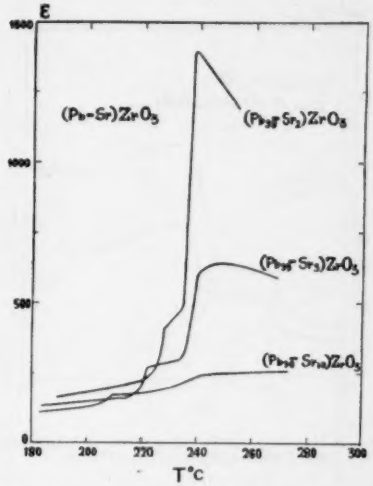

FIG. 11. Permittivity *vs* rising temperature curves of (Pb−Sr)ZrO_3 compositions.

anomalous hysteresis loops, such as observed in (Pb97−Ba3)ZrO_3, cannot be observed for this specimen and for (Pb98−Sr2)ZrO_3 up to an ac field strength of 30 kv/cm. Even in the specimen which contains only 1 percent of Sr ions, we cannot observe the anomalous hysteresis loops up to a field strength of about 40 kc/cm.

Figure 13 shows the maximum polarization P_{max} estimated on cathode-ray oscillograph under maximum ac amplitudes of 20 kv/cm and 30 kv/cm. These curves very much resemble the permittivity *vs* temperature curve of this specimen (Fig. 11). If we reduce these

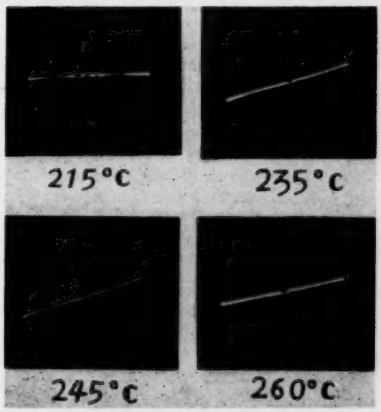

FIG. 12. Hysteresis loops of (Pb95−Sr5)ZrO_3 at E_{max}=30 kv/cm.

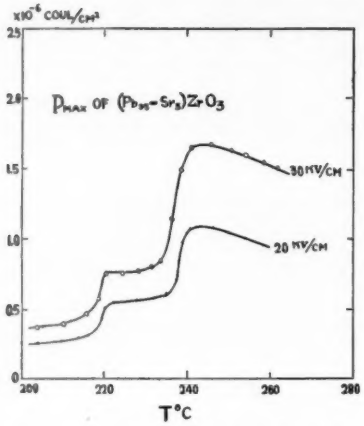

FIG. 13. Maximum polarization of (Pb95−Sr5)ZrO_3 at ac amplitudes of 20 kv/cm and 30 kv/cm.

curves to $4\pi \cdot P_m/E$, they both coincide with each other, and, moreover, they are approximately equal to the permittivity curve. So the two anomalies in these P_{max} curves can be considered as a mere consequence of the corresponding changes in the permittivity at the two transitions, owing to the good linearity of the D–E relation for this specimen. A comparison of these results with those of pure $PbZrO_3$ suggests that the intermediate phase in (Pb95−Sr5)ZrO_3 is also antiferroelectric but not ferroelectric.

To confirm the previous assumption from another point of view, a study was made of the effect of a dc biasing field of 10 kv/cm upon the permittivity of this specimen (Fig. 14). As expected, the results are essentially different from those with (Pb92.5−Ba7.5)ZrO_3.

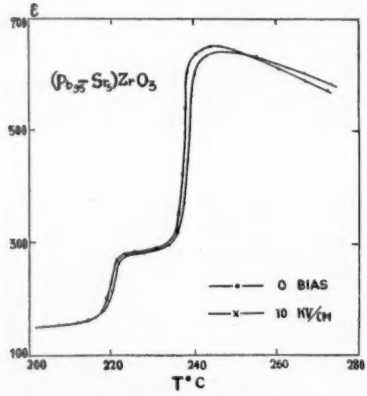

FIG. 14. Effect of a dc biasing field of 10 kv/cm on the permittivity of (Pb95−Sr5)ZrO_3.

The effect near the upper transition point is completely of the same nature as observed in pure $PbZrO_3$. Also, no marked effect was observed around the lower transition point, except a very slight decrease of the transition temperature.

The absence of spontaneous polarization in the intermediate phase was proved directly by a pyroelectric test. A dc field of 10 kv/cm was applied to the specimen while it was being cooled from 270° to 230°C, and both electrodes were connected to a galvanometer circuit while the temperature was maintained at 230°C. After the initial discharging current had disappeared we raised the temperature through the upper transition point near 245°C but no further discharging current could be observed at this point. A similar pyroelectric test on (Pb92.5−Ba7.5)ZrO_3 shows plenty of discharge current at the Curie point. Thus, we conclude that

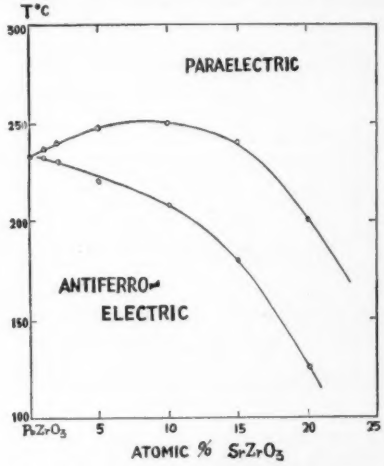

FIG. 15. Phase diagram of the (Pb−Sr)ZrO_3 system.

spontaneous polarization is either absent in (Pb95−Sr5)ZrO_3, or, if it were to exist it must be very small, far less than one-hundredth that of (Pb92.5−Ba7.5)ZrO_3.

The phase diagram of this (Pb−Sr)ZrO_3 system is shown in Fig. 15. It should be noted here that the Curie temperature of this system increases with the Sr concentration up to Sr 10 percent and then decreases, in contrast with the monotonic decrease in the (Pb−Ba)ZrO_3 system. This figure shows that the threshold concentration at which the intermediate phase begins to appear is less than Sr 1 percent. In the course of the former study of the dielectric properties of pure $PbZrO_3$, we observed a small anomaly at 225°C in the cooling curves of the permittivity and of the maximum polarization (Figs. 2 and 6 of reference 4). Now this anomaly can be interpreted reasonably, if we consider that it is

of the same nature as that of the lower transition in the present (Pb−Sr)ZrO_3 system.

V. DILATOMETRIC AND CALORIMETRIC STUDIES

A. Thermal Expansion

The previous study[3] of the thermal expansion of $PbZrO_3$ has shown a large volume expansion at the antiferroelectric *vs* paraelectric transition near 230°C. The linear thermal expansion of (Pb−Ba)ZrO_3 and (Pb−Sr)ZrO_3 compositions has now been measured by the same simple dilatometer that was used for the previous study. Curves for (Pb92.5−Ba7.5)ZrO_3 and (Pb95−Sr5)ZrO_3 are shown in Fig. 16, together with the one for pure $PbZrO_3$. The heating and cooling rates are both about 1°C/min.

The curve for (Pb92.5−Ba7.5)ZrO_3 is completely of the same nature as that for Pb(Zr95−Ti5)O_3.[7] Namely, with rising temperature it transforms from the antiferroelectric phase to the ferroelectric one through the transitional region near 175°C accompanied by a large volume expansion, and further transforms to the paraelectric phase at the Curie point near 200°C accompanied by a relatively small volume contraction. These situations can be made more clear when we extrapolate the linear part in the paraelectric phase to lower temperatures. That is to say, the ferroelectric phase shows an anomalous volume expansion compared with this extrapolation and the antiferroelectric phase shows an anomalous contraction.

TABLE I. Volume expansion coefficient ($\times 10^{-6}$/°C).

Composition	Lowest phase	Cubic phase
$PbZrO_3$	28	23
(Pb92.5−Ba7.5)ZrO_3	27	18
(Pb95−Sr5)ZrO_3	28	34

The situation is very different for (Pb95−Sr5)ZrO_3. In this specimen the volume of the antiferroelectric intermediate phase is between the lowest antiferroelectric phase and the paraelectric phase. Namely, both antiferroelectric phases in this specimen show a volume contraction compared with the extrapolation from the paraelectric phase. Some of the numerical data are shown in Table I and II. Table II gives the aforementioned volume contraction, or expansion, compared with the extrapolation from the cubic phase. It is to be noticed that the value of this anomalous volume contraction at the lowest phase is nearly the same for these three specimens.

The cooling curves are also shown in Fig. 16. The curve for (Pb92.5−Ba7.5)ZrO_3 shows a large temperature hysteresis at the lower transition, just as in the case of Pb(Zr95−Ti5)O_3. On the other hand, we can perceive only a small temperature hysteresis at the lower as well as at the upper transition in (Pb95−Sr5)-ZrO_3. This difference may be the result of a relatively large volume change at the antiferroelectric *vs* ferroelectric transition in the former specimen.

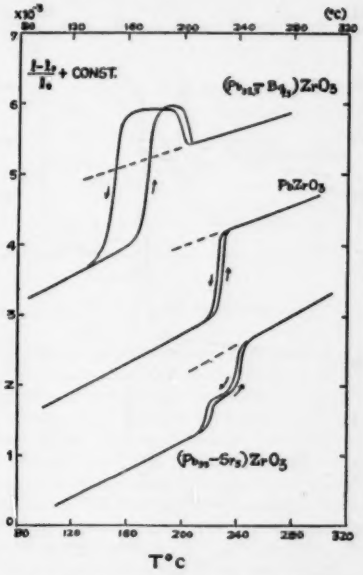

FIG. 16. Linear thermal expansion of $PbZrO_3$, (Pb92.5−Ba7.5)ZrO_3, and (Pb95−Sr5)ZrO_3.

B. Specific Heat

The specific heat *vs* temperature curves of (Pb92.5−Ba7.5)ZrO_3 and (Pb95−Sr5)ZrO_3 were measured by using an adiabatic calorimeter of the Nagasaki-Takagi type,[8] which is an improvement of Sykes' calorimeter.[9] A powdered specimen of about 25 g, contained in a thin glass vessel, was heated by a rate of about 1°–2°C/min. For comparison with the results of these two solid solutions, re-examination of the specific heat curve of pure $PbZrO_3$ was carried out with the high purity specimen. The results obtained are shown in Fig. 17.

The curve for $PbZrO_3$ shows a very sharp maximum at the Curie point at 233°C, in accordance with the very steep changes in the permittivity and dilatometry

TABLE II. Anomalous volume contraction or expansion ($\Delta v/v$), estimated from the extrapolation of the linear part in the cubic phase ($\times 10^{-4}$).

Composition	Lowest phase	Intermediate phase
$PbZrO_3$	−34 at 220°C	...
(Pb92.5−Ba7.5)ZrO_3	−36 at 150°C	+19 at 190°C
(Pb95−Sr5)ZrO_3	−31 at 210°C	−20 at 230°C

[8] S. Nagasaki and Y. Takagi, J. Appl. Phys. Japan **17**, 104 (1948).
[9] C. Sykes, Proc. Roy. Soc. (London) **A143**, 422 (1935).

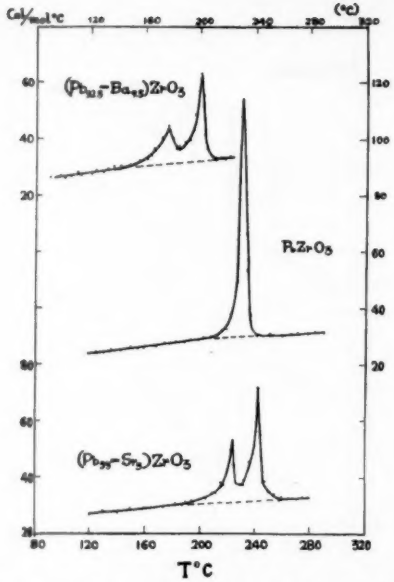

FIG. 17. Specific heat curves of $PbZrO_3$, $(Pb92.5-Ba7.5)ZrO_3$, and $(Pb95-Sr5)ZrO_3$.

curves of this specimen. Though the peak value is finite, it may be certain that the main part of the transition energy consists of the latent heat. By assuming that the normal specific heat corresponds to a broken line shown in the figure, the transition energy is estimated to be about 440 cal/mole, in good agreement with the previous data.[8]

The curves for the two solid solutions clearly show two sharp maxima at their respective two transitions. It is interesting that the same type of specific heat anomaly is observed in these different types of transitions. The transition energies estimated from these curves are given in Table III.

VI. FURTHER STUDY OF $(Pb-Ca)ZrO_3$

Investigations of the $(Pb-Ba)ZrO_3$ and $(Pb-Sr)ZrO_3$ systems have revealed that the phase diagram of solid solutions derived from $PbZrO_3$ can show two different types; namely, the properties of the intermediate phase are either ferroelectric or antiferroelectric according to the nature of the substituted ions. So it seems interesting to study whether the $(Pb-Ca)ZrO_3$ system really belongs to one (more probably to the latter) of these two types of phase diagrams.

The permittivity *vs* temperature curves for $(Pb95-Ca5)ZrO_3$ shows, in fact, two anomalies at 235° and 250°C. The characteristic form of the curve is very similar to that of $(Pb95-Sr5)ZrO_3$, suggesting that the intermediate phase in this system may also be antiferroelectric. The study of the *D*–*E* relation has proved that this is the case. Moreover, the dilatometry curve for this specimen has a very similar form to that of $(Pb95-Sr5)ZrO_3$.

VII. DISCUSSIONS

In the previous study of pure $PbZrO_3$, we assumed the existence of the free energy curve of the ferroelectric phase which lies slightly above that of the antiferroelectric phase (Fig. 18). A further support of this assumption is given by the present study of the $(Pb-Ba)ZrO_3$ system. Namely, the appearance of the ferroelectric intermediate phase and the realization of the forced transition can be well explained if we assume that the free energy of the ferroelectric phase is very close to that of the antiferroelectric phase, so that the former easily becomes lower than the latter either by the replacement of Pb ions with Ba ions or by the application of a strong electric field. Such a situation must be a very special one; namely, $PbZrO_3$ must be a very special example of the antiferroelectricity.

Moreover, the study of the $(Pb-Sr)ZrO_3$ system has shown that there must be another antiferroelectric phase, the free energy of which is also very adjacent to that of the original antiferroelectric phase of pure $PbZrO_3$ (Fig. 18). The effect of the substituted Sr ions seems to lower the free energy of this other antiferroelectric phase, though the inevitability of this effect is not yet fully understood.

The crystal structure of this antiferroelectric intermediate phase must, of course, be different from those of the corresponding phase in $(Pb-Ba)ZrO_3$ and of the antiferroelectric phase of pure $PbZrO_3$, as is actually shown by preliminary comparison of the Debye photographs of these three phases. Detailed results of the x-ray study will be reported in a subsequent paper.

Recently, Kittel[10] has discussed the possibility of realization of an antiferroelectric crystal and has shown that this should be expected to occur in nature. His theory gives some criteria for identifying antiferroelectric crystals. Takagi[11] has also presented a theory of antiferroelectric crystal containing rotatable polar molecules and has added to Kittel's criteria some more criteria helpful for identifying the antiferroelectric crystals. Very recently, Takagi[12] has extended Kittel's theory and has proved that the main conclusions

TABLE III. Transition energy.

Composition	Lower transition	Upper transition
$PbZrO_3$	...	440 cal/mole
$(Pb92.5-Ba7.5)ZrO_3$	190 cal/mole	230 cal/mole
$(Pb95-Sr5)ZrO_3$	180 cal/mole	230 cal/mole

[10] C. Kittel, Phys. Rev. **82**, 729 (1951).
[11] Y. Takagi, Phys. Rev. **85**, 315 (1952).
[12] Y. Takagi, presented at the meeting of the Phys. Soc. Japan on October 5, 1951, held at Tokyo University, Tokyo, Japan.

obtained in his first paper are still valid for more general cases not based upon a specific model of rotatable dipoles. Some of the criteria given by these theories are really satisfied in the two antiferroelectric phases in the present case.

Kittel has also shown that the peak value of the permittivity at the antiferroelectric *vs* paraelectric transition is generally not pronounced for both first and second kinds of transition. In addition to this general case, however, Takagi's theory has emphasized the possibility that the permittivity can in some special cases show a very sharp maximum at the Curie point. In such special cases, a ferroelectric state instead of an antiferroelectric one can be realized by a very small change of the polarizabilities of the constituent ions. This theoretical prediction is in good accordance with the observation of the sharp change of permittivity in pure $PbZrO_3$ and of the appearance of the ferroelectric phase in $(Pb-Ba)ZrO_3$ compositions. It should be added here that Takagi's theory has predicted the possibility of a forced transition by a strong electric field in such special cases.

Attention must now be paid again to the low peak value of the permittivity at the antiferroelectric *vs* paraelectric transition in the $(Pb-Sr)ZrO_3$ system. It has been known that all of the solid solutions, such as $(Pb-Ba)TiO_3$[13,14] and $(Pb-Sr)TiO_3$,[13,15] show the same ferroelectric transition of $BaTiO_3$ type with a large peak value of the permittivity at this point. Moreover, the ferroelectric transition in the $(Pb-Ba)ZrO_3$ system also shows the same type of large permittivity anomaly, though this ferroelectric phase seems to be different from that of $BaTiO_3$. So the observations on the

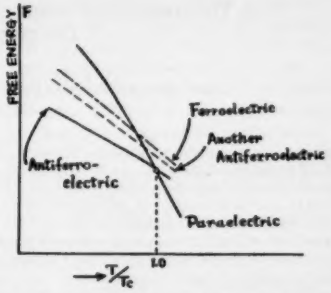

FIG. 18. Free energy curves for $PbZrO_3$.

$(Pb-Sr)ZrO_3$ system must be attributed to the fact that the upper transition in this system is an antiferroelectric *vs* paraelectric transition in contrast with the ferroelectric *vs* paraelectric transition in all other systems. Also, we can consider that $(Pb-Sr)ZrO_3$ compositions show the general characteristic of a small permittivity change at the antiferroelectric Curie point, in accordance with the theoretical prediction. Of course, there exists a suspicion that this low peak value is the result of the sluggishness of the transition, but this possibility has been removed by observation of the sharp changes in the thermal expansion and specific heat curves at this point (Figs. 16 and 17). With decreasing Sr concentration, the situation seems to approach a special case in which a sharp change of permittivity does occur.

The author wishes to thank Professor Y. Takagi for continued encouragement and invaluable advice during the course of this work. Thanks are also due Mr. E. Sawaguchi for his helpful discussions and Dr. S. Roberts and Mr. J. Hori for their very kind communications of unpublished data.

[13] G. H. Jonker and J. H. van Santen, Chem. Weekblad 43, 672 (1947).
[14] G. Shirane and K. Suzuki, J. Phys. Soc. Japan 6, 274 (1951).
[15] S. Nomura and S. Sawada, J. Phys. Soc. Japan 5, 279 (1950).

A Theoretical Estimate of the Effect of Radiation on the Elastic Constants of Simple Metals*

G. J. DIENES†
Atomic Energy Research Department, North American Aviation, Inc., Downey, California
(Received December 13, 1951)

Interstitial atoms and vacancies play an important role in the theory of solids and of radiation damage. It is difficult to separate and measure unambiguously these lattice disturbances in metals. It is suggested that measurements of changes in elastic constants may be appropriate in such investigations.

An approximate theoretical treatment is given of the change in elastic constants of simple metals caused by the presence of a given small fraction of interstitial atoms and vacancies. The elastic coefficients are calculated from atomic interaction potentials (a simple exponential function for copper and a Morse function for sodium) with relaxation effects taken into account. The presence of a small fraction of interstitials and vacancies results in large increases in the elastic coefficients of copper. Lattice vacancies alone were found to decrease the elastic coefficients, the change being essentially a bulk effect. Consequently, increases in the elastic moduli measure primarily the fraction of interstitial atoms. In sodium, large relaxation occurs around an interstitial and this atomic readjustment reduces the effect of the interstitial to the magnitude of a bulk effect.

It is concluded that the theoretically predicted effects should be easily observable in copper or similar metals, provided thermal annealing is prevented. Changes in elastic constants, therefore, may serve as a useful tool for distinguishing between interstitial atoms and lattice vacancies.

I. INTRODUCTION

RADIATION damage may be described briefly as the result of atomic displacements caused by the passage of neutrons or fast charged particles through the material.[1] Many physical properties are drastically changed by the radiation. Our understanding of these effects is still rather rudimentary for two reasons: first, it is by no means clear just what sort of disturbances are left behind in the lattice and, second, the theories which relate atomic displacements to physical properties are themselves poorly developed.

For the purposes of the present study, radiation damage is pictured as the result of the presence of interstitial atoms and vacancies which have been produced by the high energy incident particles. On an atomic scale this must be the primary result of knocking the atoms about within the lattice. If the lattice disturbances cluster, however, either during irradiation or subsequently (by annealing, for example), it may be more profitable to think of radiation damage as akin to cold work or thermal spikes. It is quite likely that differences between radiation damage and cold work in metals, which have been observed experimentally,[2,3] are the result of the presence of interstitials. Such high energies are required for the formation of interstitials in such a substance as copper[4] that their production thermally or even by cold work is most unlikely. They are easily produced, however, by direct knock-ons.

It is clear that it is important to find out whether interstitials exist, in fact, in a close-packed crystalline lattice. The most convenient and best understood physical properties, such as electrical and thermal conductivity of metals, are not well suited to such an investigation since both interstitials and vacancies are scattering centers. It would be very difficult to separate and measure unambiguously the two types of disturbances.

A simple physical argument indicates that elastic constants may be quite sensitive to the presence of interstitial atoms. In general, a bulk property is not expected to be changed appreciably by the displacement of a relatively small percentage of atoms. In close packed metallic substances, however, the elastic constants are determined primarily by the repulsive interactions of the closed ion shells. This potential is of an exponential nature and varies extremely rapidly with interatomic distance. As the interaction distance is shortened, for example by creating an interstitial, the energy of the system increases sharply on the repulsive side of the potential curve. The creation of vacancies by removal of atoms results essentially in the destruction of some normal interactions. Thus, one expects the influence of the interstitials to outweigh heavily the effect of the vacancies.

The main purpose of this paper is to describe some theoretical calculations that have been carried out in an attempt to arrive at a quantitative estimate of the effect of radiation on the elastic coefficients of simple metals. In addition to yielding information concerning interstitials and vacancies, the elastic properties themselves are of interest as influenced by lattice disturbances. It is well known[1,2,5] that many mechanical properties of materials are appreciably changed by irradiation. Mechanical properties, however, are not understood well enough, except in the range of perfect elasticity, to permit a theoretical study of radiation effects. The elastic constants of metals, however, are

* This paper is based on studies conducted under contract with the AEC.
† Now at Brookhaven National Laboratory, Upton, Long Island, New York.
[1] For recent declassified articles on radiation damage in solids see F. Seitz, Disc. Faraday Soc. No. 5, 271 (1949); J. C. Slater, J. Appl. Phys. 22, 237 (1951).
[2] Martin, Austerman, Eggleston, McGee, and Tarpinian, Phys. Rev. 81, 664 (1951).
[3] Eggleston, Bowen, and Kropschot, paper given at Chicago meeting of AIP, October 24, 1951.
[4] H. B. Huntington and F. Seitz, Phys. Rev. 61, 315 (1942).
[5] T. H. Blewitt and R. R. Coltman, Phys. Rev. 82, 769 (1951).

sufficiently well understood theoretically to make it profitable to carry out some calculations concerning the effect of radiation on elastic properties.

II. THE PHYSICAL MODEL

As stated above, changes in physical properties caused by irradiation are pictured as the result of random displacement of atoms. A perfect lattice is assumed in which radiation creates lattice vacancies and interstitial atoms. These disturbances will be preserved in their metastable positions provided the specimen is kept at a sufficiently low temperature to prevent annealing. The number of interstitials and vacancies will be assumed to be small enough so that interaction between the distrubances may be neglected. The problem is then to calculate the elastic coefficients of a crystal lattice containing a given small fraction of interstitials and vacancies.

Two characteristic systems will be investigated. One is the close-packed face-centered cubic lattice in which primarily the closed-shell repulsive interactions determine the elastic constants.[6] This description is suitable for the noble metals and the calculations will be carried out for copper. It will be assumed that the interstitial lodges in the geometrically favorable position, namely, in the body-centered position of the face centered unit cube. The second system is that typified by the alkali metals, namely the body-centered cubic. The calculations will be carried out for sodium. In this system both attractive and repulsive interactions must be taken into account.[6] Again, it will be assumed that the interstitial lodges at the geometrically favorable position, namely, in the center of the face of the body-centered unit cube. The calculations will be carried out for the undistorted lattice first. Relaxation around the lattice disturbances is calculated and discussed in Sec. VI.

The elastic coefficients of a homogeneous material are calculable if the atomic interactions are known as a function of the distance of separation of the atoms. A radiation damaged material is, however, locally inhomogeneous. It is very difficult to take proper account of this inhomogeneity. In the present approximation, therefore, the real material was replaced by an approximately equivalent homogeneous material in which the interactions ascribable to the lattice disturbances are smeared over the whole crystal. Thus, the geometry of the original lattice is retained but the potential energy of the system is modified according to the number of contacts formed and broken by the creation of interstitials and vacancies.

It is evident that quite drastic approximations have been made in order to carry out the calculations with a reasonable amount of labor. It will be seen from later sections that the results are quite clear-cut and the present approximation is considered adequate in indicating the direction and the order of magnitude of the changes in elastic coefficients to be expected from "frozen in" radiation damage.

III. MATHEMATICAL FORMALISM

The elastic coefficients of a crystal are given by the second derivatives of the elastic potential energy per unit volume with respect to the strains. Fuchs[6] discusses the derivation of these equations and further details may be found in unclassified reports by the writer.[7] Only the final working equations will be given here. It has been found that summation over nearest neighbors is sufficient for the face-centered cubic lattice, while nearest and next nearest neighbors must be taken into account in the body-centered cubic system.[6,7]

The final working equations are:

Face centered cubic, nearest neighbors,

$$\begin{aligned} A &= r_e^2(d^2U/dr^2)_{r_e} + 7r_e(dU/dr)_{r_e} \\ 2B &= r_e^2(d^2U/dr^2)_{r_e} + 3r_e(dU/dr)_{r_e} \\ K &= 2C/\Omega_0 = (24/9\sqrt{2}r_e)(d^2U/dr^2)_{r_e}, \end{aligned} \tag{1}$$

where Ω_0 = volume per atom = $\delta^3/4$, and r_e = interatomic distance = $\delta/\sqrt{2}$.

Body-centered cubic,

	Nearest neighbors	Next nearest neighbors
A	$\frac{16}{3}r_e\left(\frac{dU}{dr}\right)_{r_e}$	$+\frac{4}{\sqrt{3}}r_e\left(\frac{dU}{dr}\right)_{2r_e/\sqrt{3}} + \frac{8}{3}r_e^2\left(\frac{d^2U}{dr^2}\right)_{2r_e/\sqrt{3}}$
$2B$	$\frac{16}{9}r_e\left(\frac{dU}{dr}\right)_{r_e} + \frac{8}{9}r_e^2\left(\frac{d^2U}{dr^2}\right)_{r_e}$	$+\frac{4}{\sqrt{3}}r_e\left(\frac{dU}{dr}\right)_{2r_e/\sqrt{3}}$
K	$\frac{2C}{\Omega_0} = \frac{\sqrt{3}}{r_e^3}\left(\frac{dU}{dr}\right)_{r_e} + \frac{2}{\sqrt{3}}\frac{1}{r_e}\left(\frac{d^2U}{dr^2}\right)_{r_e}$	$+\frac{3}{2}\frac{1}{r_e^3}\left(\frac{dU}{dr}\right)_{2r_e/\sqrt{3}} + \frac{2}{\sqrt{3}}\frac{1}{r_e}\left(\frac{d^2U}{dr^2}\right)_{2r_e/\sqrt{3}}$

(2)

where Ω_0 = volume per atom = $\delta^3/2$, r_e = interatomic distance = $\sqrt{3}\delta/2$, $U(r)$ = potential energy per atom, $A = (c_{11}-c_{12})\Omega_0$, $2B = c_{44}\Omega_0$, $2C = K = \frac{1}{3}(c_{11}+2c_{12})\Omega_0$, c_{ij} = elastic coefficients in dynes/cm², and K = bulk modulus.

[6] K. Fuchs, Proc. Roy. Soc. (London) **A151**, 585 (1935); **A153**, 622 (1936).

[7] G. J. Dienes, North American Aviation Report No. SR-80 (1951); North American Aviation Report No. SR-125 (1951).

TABLE I. The elastic coefficients of Cu calculated by Eq. (3), in dynes cm^{-2} (low temperature). $D_0=2.8\times10^{-8}$ erg/atom, $r_e=2.55\times10^{-8}$ cm, and $\rho=0.200\times10^{-8}$ cm.

	Calculated	Experimental[a]
$c_{11}-c_{12}$	5.1×10^{11}	5.1×10^{11}
c_{44}	8.6×10^{11}	8.2×10^{11}
K	1.33×10^{12}	1.39×10^{12}

[a] Data from references 6 and 10.

IV. THE ELASTIC COEFFICIENTS OF COPPER AND SODIUM

Fuchs[6] has made a careful quantum-mechanical study of the cohesive forces and elastic coefficients in copper and the alkali metals. He has applied and extended the earlier work of Wigner and Seitz[8] and Seitz[9] on the cohesive forces in sodium and lithium. Two of his conclusions, important for the purpose of the present paper, may be stated as follows: 1. In copper the elastic coefficients are primarily determined by the closed shell repulsive interactions. This, apparently, holds even for the compressibility although one may expect purely volume forces to be of importance. 2. In the alkali metals both attractive and repulsive energies must be taken into account.

In neither case did Fuchs arrive at a simple function for U which could be conveniently used in the present calculations. Huntington and Seitz,[10] in their theoretical study of self-diffusion in copper, point out that a simple exponential function of the Born and Mayer type can be used satisfactorily to represent the repulsive interactions. This result, combined with the results of Fuchs' study, suggests that the elastic constants of copper may be adequately described by assuming U to be given, as a function of distance, r, by the relation

$$U=D_0e^{-r/\rho}, \tag{3}$$

where D_0 and ρ are adjustable constants. A single exponential function is an adequate approximation in this case because the second derivative of the attractive part of the potential energy is small compared to that of the repulsive part and can, therefore, be neglected.

This same approximation cannot be used for the alkali metals. To carry out the proposed calculation, it is important to find some simple function for U which can be used for calculating the elastic coefficients of alkali metals. Slater suggests[11] that a Morse function is a rather good approximation for the interatomic potential in metals. More recently Pauling[12] found that a Morse potential function can be used to calculate the compressibility of metals as a function of pressure. Consequently, it was thought that for sodium a function U may be used, given by

$$U=D_0[1-e^{-a(r-r_e)}]^2. \tag{4}$$

The use of the Morse potential function for describing the elastic coefficients of the alkali metals is discussed in detail in an unclassified report by the writer:[13] It is sufficient to state here that Eq. (3) has been found satisfactory for copper and Eq. (4) for sodium. The constants of Eqs. (3) and (4) have been calculated and the calculated elastic coefficients were found to be in good agreement with experimental values. The pertinent data are collected in Tables I and II. For sodium[14] it was necessary to sum over both nearest and next nearest neighbors.

It is concluded from these results that the elastic coefficients are quite well described by the atomic interaction potentials represented by Eqs. (3) and (4) for copper and sodium, respectively. It should be emphasized that, in both cases, only two adjustable constants (D_0 and ρ, and D_0 and a, respectively) are employed to fit three elastic constants. The equilibrium interatomic distance r_e is considered to be known and fixed.

V. INTERSTITIALS AND VACANCIES IN COPPER AND SODIUM

Sufficient background information is now at hand to carry out the theoretical estimate proposed in Sec. II. The calculations for copper will be described first since this metal represents the simpler case.

Let the fraction of interstitials produced by radiation be denoted by x. In the absence of any annealing the fraction of vacancies left behind is also x. In creating a vacancy 12 normal contacts are broken. Formation of an interstitial in the body-center position of the face-centered copper lattice requires 14 new contacts, 6 of them $(\sqrt{2}/2)r$ away and 8 of them $(\sqrt{3}\sqrt{2}/2)r$ away. Following the physical discussion of Sec. II, the total repulsive potential energy per atom may then be written,

$$U=(1-x)D_0\exp(-r/\rho)+x(6/12)D_0\exp[-(\sqrt{2}/2)r/\rho]+x(8/12)D_0\exp[-(\sqrt{3}\sqrt{2}/2)r/\rho]. \tag{5}$$

TABLE II. The elastic coefficients of Na calculated by Eq. (4), in dynes cm^{-2} (room temperature).[a] $D_0=5.19\times10^{-14}$ erg/atom, $r_e=3.68\times10^{-8}$ cm, and $a=1.06\times10^{8}$ cm.

	Calculated	Experimental[b]
$c_{11}-c_{12}$	1.159×10^{10}	1.159×10^{10}
c_{44}	4.26×10^{10}	4.26×10^{10}
K	4.15×10^{10}	4.20×10^{10}

[a] The elastic coefficients of Na at low temperature (see reference 14) (80°K) can also be satisfactorily fitted using $D_0=6.84\times10^{-14}$, $r_e=3.68\times10^{-8}$, and $a=1.087\times10^{8}$.
[b] Data from R. F. S. Hearmon, Revs. Modern Phys. 18, 409 (1946).

[8] E. P. Wigner and F. Seitz, Phys. Rev. 43, 804 (1933); 46, 509 (1934).
[9] F. Seitz, Phys. Rev. 47, 400 (1935).
[10] H. B. Huntington and F. Seitz, Phys. Rev. 61, 315 (1942).
[11] J. C. Slater, *Introduction to Chemical Physics* (McGraw-Hill Book Company, Inc., New York, 1939), pp. 450–456.
[12] L. Pauling, Science 111, 461 (1950).
[13] G. J. Dienes, North American Aviation Report No. SR-125 (1951).
[14] S. L. Quimby and S. Siegel, Phys. Rev. 54, 293 (1938).

If one neglects lattice relaxation and volume effects, the elastic coefficients of the damaged crystal are calculable from Eqs. (5) and (1) with all the derivatives evaluated at r_e. Physically this means that the change in repulsive energy has been spread out over the whole crystal and, in effect, the damaged lattice has been replaced by an equivalent homogeneous face-centered cubic lattice for which the repulsive interactions are given by Eq. (5) in place of Eq. (3).

In addition to the assumptions and approximations discussed so far, a further assumption is implicit in these calculations. Equation (5) assumes that the repulsive potential energy function, Eq. (3), fitted to the perfect lattice, remains valid over the considerably shorter interaction distances used in Eq. (5). From present knowledge of interaction forces it is impossible to estimate the degree of approximation involved.

The calculations indicated above have been carried out. The changes in the elastic coefficients are evidently proportional to x (fraction of interstitials or vacancies). It is of interest to give the results for two concentrations, $x=0.01$ (1 percent) and $x=0.05$ (5 percent), covering the range of concentration expected in irradiated materials. For consistency, the comparison is made relative to the calculated elastic constants of Table I. The results are summarized in Table III. In addition to the changes in the three fundamental elastic coefficients the corresponding values for the two Young's moduli are also given. Young's moduli, corresponding to the shear moduli c_{44} and $\frac{1}{2}(c_{11}-c_{12})$, are defined by

$$E_1=9Kc_{44}/(c_{44}+3K)$$
$$E_2=9K\cdot\tfrac{1}{2}(c_{11}-c_{12})/[\tfrac{1}{2}(c_{11}-c_{12})+3K].$$

The data in Table III indicate that large changes in the elastic moduli of copper are to be expected as a result of the creation of interstitials and vacancies. The higher elastic coefficients are entirely due to the presence of interstitials. Vacancies alone decrease the elastic coefficients. The effect of vacancies is easily calculable using the first term of Eq. (5) for U. Performing such a calculation it was found that 1 percent vacancies decrease the elastic coefficients very closely by 1 percent indicating that this change is primarily a bulk effect. These general results are physically to be expected as long as it is reasonable to derive the elastic properties from the closed shell interaction. If it is valid to consider irradiation to result in interstitials and vacancies then radiation damage is expected to increase the elastic coefficients in a metal such as copper and the increase in the elastic coefficients is primarily a measure of the number of interstitial atoms.

The calculations for sodium, a body-centered cubic lattice, are carried out in an analogous manner with the modification that a Morse potential is to be used for U [Eq. (4)], and both nearest and next nearest neighbors are to be counted in calculating the elastic coefficients from U as shown by Eq. (2). In creating a vacancy 14 normal contacts are broken. Formation of an interstitial in the face-centered position of the body-centered sodium lattice requires the formation of 2 new contacts $(1/\sqrt{3})r$ away and 4 new contacts $(\sqrt{2}/\sqrt{3})r$ away. Analogous to Eq. (5), therefore, the total potential energy per atom may be written

$$U=(1-x)D_0\{1-\exp[-a(r-r_e)]\}^2 +x(2/14)D_0\{1-\exp[-a(r/\sqrt{3}-r_e)]\}^2 +x(4/14)D_0\{1-\exp[-a(2r/\sqrt{3}-r_e)]\}^2. \quad (6)$$

The elastic coefficients are then calculated directly from Eq. (2) using the expression for U given above.

The calculations indicated above have been carried out. The changes in the elastic coefficients are proportional to x and the results are again given for two concentrations ($x=0.01$ and $x=0.05$). For consistency, the comparison is made relative to the calculated elastic coefficients of Table II. The results are summarized in Table IV.

As Table IV shows, the predicted effects for sodium, calculated on the basis of a Morse function interaction, and in the absence of relaxation, are of the same order of magnitude as for copper calculated from the repulsive interactions. The effect of vacancies alone has also been determined in sodium. As in the case of copper, vacancies alone decrease the elastic coefficients and the change is again essentially a bulk effect, i.e., 1 percent vacancies decrease the elastic coefficients very closely by 1 percent. Thus, for sodium also, the increase in the elastic coefficients is primarily a measure of the number of interstitial atoms.

TABLE III. Effect of interstitials and vacancies on the elastic coefficients of copper (in dynes cm^{-2}).

	$x=0.00$	$x=0.01$	$x=0.05$
$c_{11}-c_{12}$(unirrad.)	5.1 $\times10^{11}$		
$c_{11}-c_{12}$(irrad.)		5.3 $\times10^{11}$	6.1 $\times10^{11}$
$\Delta(c_{11}-c_{12})$		0.2 $\times10^{11}$	1.0 $\times10^{11}$
$\Delta(c_{11}-c_{12})/(c_{11}-c_{12})$		3.9%	19.6%
c_{44}(unirrad.)	8.6 $\times10^{11}$		
c_{44}(irrad.)		9.4 $\times10^{11}$	12.6 $\times10^{11}$
Δc_{44}		0.8 $\times10^{11}$	4.0 $\times10^{11}$
$\Delta c_{44}/c_{44}$		9.3%	46.5%
K(unirrad.)	1.33 $\times10^{12}$		
K(irrad.)		1.45 $\times10^{12}$	1.93 $\times10^{12}$
ΔK		0.12 $\times10^{12}$	0.6 $\times10^{12}$
$\Delta K/K$		9.0%	45.0%
E_1(unirrad.)	2.125$\times10^{12}$		
E_1(irrad.)		2.32 $\times10^{12}$	3.11 $\times10^{12}$
ΔE_1		0.195$\times10^{12}$	0.985$\times10^{12}$
$\Delta E_1/E_1$		9.2%	46.3%
E_2(unirrad.)	1.355$\times10^{12}$		
E_2(irrad.)		1.417$\times10^{12}$	1.655$\times10^{12}$
ΔE_2		0.062$\times10^{12}$	0.3 $\times10^{12}$
$\Delta E_2/E_2$		4.56%	22.1%

VI. RELAXATION EFFECTS

Relaxation of the atoms around the lattice disturbances has so far not been taken into account. These atomic readjustments can be of considerable impor-

TABLE IV. Effect of interstitials and vacancies on the elastic coefficients of sodium (in dynes cm^{-2}).

	$x=0.00$	$x=0.01$	$x=0.05$
$c_{11}-c_{12}$(unirrad.)	1.159×10^{10}		
$c_{11}-c_{12}$(irrad.)		1.218×10^{10}	1.454×10^{10}
$\Delta[c_{11}-c_{12}]$		0.059×10^{10}	0.295×10^{10}
$\Delta[c_{11}-c_{12}]/(c_{11}-c_{12})$		5.1%	25.5%
c_{44}(unirrad.)	4.26×10^{10}		
c_{44}(irrad.)		4.37×10^{10}	4.81×10^{10}
Δc_{44}		0.11×10^{10}	0.55×10^{10}
$\Delta c_{44}/c_{44}$		2.6%	13.0%
K(unirrad.)	4.15×10^{10}		
K(irrad.)		4.42×10^{10}	5.5×10^{10}
ΔK		0.27×10^{10}	1.35×10^{10}
$\Delta K/K$		6.5%	32.5%
E_1(unirrad.)	9.58×10^{10}		
E_1(irrad.)		9.87×10^{10}	11.17×10^{10}
ΔE_1		0.29×10^{10}	1.59×10^{10}
$\Delta E_1/E_1$		3.0%	16.6%
E_2(unirrad.)	3.21×10^{10}		
E_2(irrad.)		3.35×10^{10}	4.01×10^{10}
ΔE_2		0.14×10^{10}	0.8×10^{10}
$\Delta E_2/E_2$		4.4%	24.9%

tance, particularly in the alkali metals.[15] The atoms around an interstitial will certainly move outwards to accommodate the interstitial atom. Similarly, the atoms around a vacancy tend to move toward the empty lattice site. If these atomic motions are relatively large, the increase in the elastic constants calculated in the previous section may be a serious overestimate.

The outward motion of the atoms around an interstitial in copper is illustrated in Fig. 1. The repulsive interactions of the interstitial with its nearest neighbors push the atoms outward while the neighbors of the moving atom tend to restore it to its normal lattice position. Balance between these two forces will lead to an equilibrium displacement. The calculation is best carried out by finding the minimum in the potential energy of the whole system as a function of displacement, Δr. The displacement Δr is taken to be the same percentage of the atom to interstitial distance for each moving atom, that is, uniform distortion is assumed. This calculation is analogous to the one given by Dienes[16] for alkali halide crystals.

In Fig. 1 part of the next cell in one direction is illustrated in order to show which atoms are assumed to remain at their lattice sites. The interstitial itself has fourteen neighbors which become displaced—six in the face-centered positions and eight at the corners of the cube. All atoms further away than these fourteen are assumed to suffer no displacement (Fig. 1). Each of these moving neighbors has twelve contacts which are changed by relaxation and must be evaluated. Of these twelve those which are not nearest neighbors of the interstitial are stationary. However, the nearest neighbors of the moving atom which are also nearest

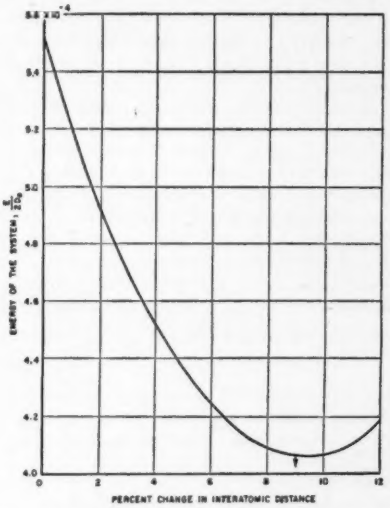

FIG. 2. Determination of equilibrium relaxation around an interstitial in copper.

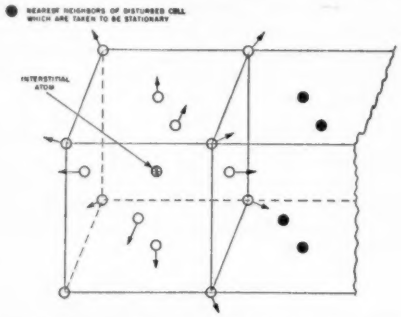

FIG. 1. Relaxation of atoms around an interstitial in copper.

neighbors of the interstitial have been displaced and their interactions were counted from the displaced position. These are the interactions which one must not count twice in the summation.

As an example of the procedure consider an atom normally in the face-centered position. After displacement the following interactions have changed and have been taken into account: (a) Interaction with interstitial. (b) Interaction with four nearest neighbors of the displaced face-centered atom which themselves have not moved (solid circles in Fig. 1). (c) Interaction with eight nearest neighbors of the displaced face-centered atom which themselves have been displaced. Similarly, for a corner atom the interactions are: (d) Interaction with interstitial. (e) Interaction with nine

[15] H. R. Paneth, Phys. Rev. **80**, 708 (1950).

[16] G. J. Dienes, J. Chem. Phys. **16**, 620 (1948).

nearest neighbors of the displaced corner atom which themselves have not moved. (f) Interaction with three nearest neighbors of the displaced corner atom which themselves have been displaced.

The summation required for evaluating the energy of the system evidently contains a large number of terms and is best accomplished by a point-by-point calculation for various values of Δr. The results are shown in Fig. 2 where the energy of the system, in units of $E/2D_0$, is plotted against the percentage change in interatomic distance, r. The minimum occurs at an outward equilibrium displacement of 9 percent.

Analogous calculations have been performed for relaxation inward around a vacant lattice site. The results are shown in Fig. 3 where the minimum is shown

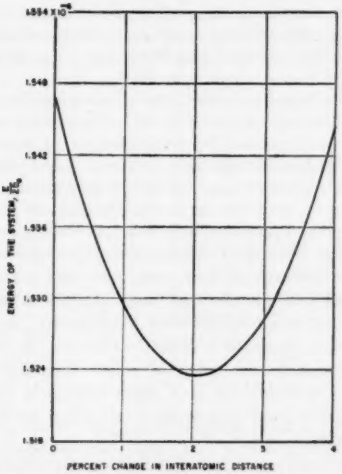

FIG. 3. Determination of equilibrium relaxation around a vacancy in copper.

to occur at an inward equilibrium displacement of 2 percent.

The equilibrium displacements having been determined, the total repulsive energy per atom, U, Eq. (5), can now be corrected for relaxation by taking into account all the altered interactions. Since the relaxation around a vacancy is small and the influence of the vacancies upon the elastic constants is also small, the relaxation corrections were applied only to the atoms surrounding the interstitial. From this point on the calculation is identical to that given in the previous section. The results show that the relaxation effects in copper decrease the influence of the interstitials, i.e., the increase in moduli resulting from the interstitials is not as large in the presence as in the absence of relaxation. The changes are, however, not large enough to modify any of the conclusions given in Sec. V, that is,

TABLE V. Effect of interstitials and vacancies on the elastic coefficients of copper (in dynes cm^{-2}).

Elastic coefficient	$x=0.00$[a]	$x=0.01$ Without relaxation	$x=0.01$ With relaxation
$c_{11}-c_{12}$	5.1×10^{11}	5.3×10^{11}	5.3×10^{11}
$\Delta(c_{11}-c_{12})$		0.2×10^{11}	0.2×10^{11}
$\Delta(c_{11}-c_{12})/(c_{11}-c_{12})$		3.9%	3.9%
c_{44}	8.6×10^{11}	9.4×10^{11}	9.2×10^{11}
Δc_{44}		0.8×10^{11}	0.6×10^{11}
$\Delta c_{44}/c_{44}$		9.3%	7.0%
K	1.33×10^{12}	1.45×10^{12}	1.42×10^{12}
ΔK		0.12×10^{12}	0.09×10^{12}
$\Delta K/K$		9.0%	6.8%

[a] x = fraction of interstials = fraction of vacancies.

the presence of interstitials in copper leads to a large increase in the elastic moduli even after relaxation. The results are summarized in Table V.

Relaxation effects in sodium are calculated in an analogous manner to that given for copper in the previous section except that the geometry is that of a body-centered cubic lattice and the interatomic interaction function is the Morse function [Eq. (4)]. The outward relaxation around an interstitial is illustrated in Fig. 4. The most important effect comes from the relaxation of the six nearest neighbors of the interstitial. Each of the moving atoms has fourteen contacts which must be taken into account, care being exercised in not counting twice the neighbors of the interstitial.

The total energy *vs* displacement curve is shown in Fig. 5. The minimum occurs at an outward equilibrium displacement of 30 percent. Evidently, relaxation around an interstitial in the more open body-centered cubic structure is far greater than in the close-packed copper lattice. Physically, this is a reasonable result.

Similar calculations for a vacent lattice site indicated that the lattice shows no relaxation around a vacancy within the accuracy of the nearest neighbor approximation. Since the influence of the vacancies is small to start with a more detailed calculation was not carried out.

Evaluation of the elastic constants in the relaxed lattice gave the results in Table VI. Comparison with

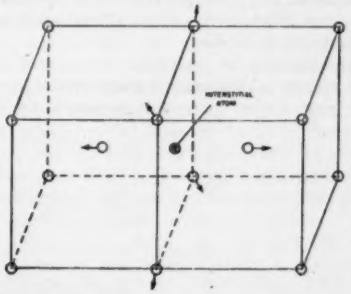

FIG. 4. Relaxation of atoms around an interstitial in sodium.

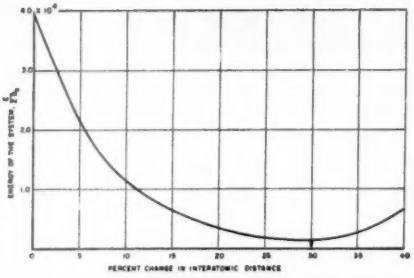

FIG. 5. Determination of equilibrium relaxation around an interstitial in sodium.

the unrelaxed lattice shows that atomic readjustments in the body-centered cubic lattice of sodium reduces the effect of the interstitial essentially to a bulk effect.

VII. SUMMARY

1. An approximate theoretical treatment is given of the change in elastic constants of simple metals caused by the presence of a given small fraction of interstitial atoms and vacancies. The elastic constants are calculated from interatomic potentials employing a simple exponential function for copper and a Morse function for sodium. Relaxation effects are taken into account.

2. A crystal containing interstitial atoms and vacancies is locally inhomogeneous. The major approximation of the theory is the replacement of the inhomogeneous lattice by an approximately equivalent homogeneous material in which the interactions ascribable to the lattice disturbances are smeared over the whole crystal. Thus, the geometry of the original lattice is retained in the present calculations, but the potential energy of the system is modified according to the number of contacts formed and broken by the creation of interstitials and vacancies.

3. The theoretically calculated changes in elastic coefficients are large in copper even in the presence of relaxation. In sodium, however, which has the more open body-centered structure, the relaxation around the interstitial is quite large. This atomic readjustment reduces the effect of the lattice disturbances to the magnitude of a bulk effect.

4. The presence of interstitial atoms and vacant lattice sites in a close-packed cubic crystal, such as copper, results in an appreciable increase in the elastic moduli. Vacancies alone decrease the elastic moduli by a magnitude corresponding essentially to a bulk effect. The increase in elastic coefficients, therefore, is due to the presence of interstitial atoms, with the increase being several orders of magnitude larger than would be predicted from a simple bulk effect.

5. The theoretically predicted effects should be easily observable experimentally provided interstitial atoms are, in fact, produced by irradiation, or by any other means, such as perhaps cold work at very low temperatures. To prevent annealing which may occur rapidly at room temperature the lattice disturbances must be produced and preserved at low temperatures.

6. The theoretical results strongly suggest that changes in elastic constants may serve as a useful and powerful tool for distinguishing between interstitial atoms and vacant lattice sites. Furthermore, since the mechanical properties of solids are known to be changed by irradiation, the study of elastic constants as a function of irradiation is of direct interest in yielding information about one of the fundamental mechanical properties.

Note added in proof:—Preliminary experiments by Bowman and Tarpinian (private communication, February, 1952) indicate that Young's modulus of copper increases by as much as 10 percent upon heavy cyclotron irradiation.

TABLE VI. Effect of interstitials and vacancies on the elastic coefficients of sodium (in dynes cm^{-2}).

Elastic coefficient	$x=0.00$[a]	$x=0.01$ Without relaxation	$x=0.01$ With relaxation
$c_{11}-c_{12}$	1.159×10^{10}	1.218×10^{10}	1.166×10^{10}
$\Delta(c_{11}-c_{12})$		0.059×10^{10}	0.007×10^{10}
$\Delta(c_{11}-c_{12})/(c_{11}-c_{12})$		5.1%	0.6%
c_{44}	4.26×10^{10}	4.37×10^{10}	4.29×10^{10}
Δc_{44}		0.11×10^{10}	0.03×10^{10}
$\Delta c_{44}/c_{44}$		2.6%	0.7%
K	4.15×10^{10}	4.42×10^{10}	4.23×10^{10}
ΔK		0.27×10^{10}	0.08×10^{10}
$\Delta K/K$		6.5%	1.9%

[a] x = fraction of interstitials = fraction of vacancies.

ACKNOWLEDGMENT

The writer is indebted to Miss E. Stratton for performing many of the detailed calculations and to M. M. Mills and S. Siegel for stimulating discussions during the course of this investigation.

Superconductivity of the Isotopes of Tin*

E. MAXWELL
National Bureau of Standards, Washington, D. C.
(Received December 26, 1951)

The superconducting transition temperatures of six samples of tin with masses ranging from 113.58 to 123.01 were measured by a magnetic method and found to obey a relation of the form $M^{0.500}T_c = \text{const.}$ The critical field curves for the samples of mass 113.58, 118.05, and 123.01 were determined between 1.4°K and 3.8°K and observed to be geometrically similar to about 1 part in 800. From this it is concluded that the electronic specific heat in the normal state is independent of mass, and that the thermodynamic functions derived from the critical field curves also have the similarity property.

I. INTRODUCTION

THE possible existence of an isotope effect in superconductivity was first explored by Kamerlingh-Onnes and Tuyn,[1] and again almost twenty years later by Justi.[2] These investigators looked for differences in the transition temperatures of ordinary lead (atomic weight 207.22) and uranium lead (atomic weight 206.15), but reported negative results. Since the transition of lead occurs at 7.2°K, a region in which precise determination and regulation of the temperature is difficult, it was considered worthwhile to re-examine the question at the National Bureau of Standards using some of the pure mercury isotope 198.[3] Its transition temperature was found to be about 0.02°K higher[4] than natural mercury (atomic weight 200.6). At about the same time, Reynolds, Serin, Wright, and Nesbitt[5] independently found similar shifts in the transition temperature for some samples of mercury enriched in isotopes of mass 199, 202, and 204, respectively.

In view of the fact that the earlier investigators had reported negative results for lead it was important to ascertain whether or not the effect was common to all superconductors or a special property of mercury alone. Accordingly, several samples of enriched isotopes of tin and thallium were obtained from the Atomic Energy Commission, and the existence of the isotope effect was verified for these metals as well. Some of the preliminary results have been reported elsewhere.[6–8] More recently the isotope effect was observed in lead also by Olsen[9] and by Reynolds and Serin.[10] It now appears that the earlier negative results of Kammerlingh-Onnes and Justi were perhaps due to insufficient resolving power in temperature.

It was shown by Reynolds, Serin, and Nesbitt[11,12] that the data for mercury could be approximately represented by the relation $M^{\frac{1}{2}}T_c = \text{constant}$. Furthermore, theoretical treatments by Fröhlich[13] and Bardeen[14] appeared, which were based on interaction between electrons and lattice vibrations and which specified that $T_c \sim M^{-\frac{1}{2}}$. (Fröhlich had developed his theory prior to his knowledge of the isotope effect.) In view of these developments tin appeared to be worth careful study, since the range of stable isotopes was large (112–124) and since for many purposes it was a more ideal material to work with than mercury. (The difficulty of realizing strain-free mercury specimens had complicated the problem of making precise measurements.) The present paper is an account of the critical field measurements thus far completed on tin isotopes.

II. EXPERIMENTAL DETAILS

The critical field measurements were made by observing the magnetic transitions of the capillary wire specimens in a longitudinal magnetic field. The general features of the apparatus are shown in Figs. 1 and 2. The method depends on the change in magnetic susceptibility of the specimen when it passes from the superconducting to the normal state and makes use of a ballistic type of flux measurement. The specimen is located inside a pick-up coil and the change in flux threading the coil is observed when the magnetic field is interrupted. A null method is employed in which the change of induction in the pick-up coil is balanced by an equal change in induction through a set of compensating coils. The final balancing is done with a variable mutual inductometer.

The apparatus is designed to accommodate six samples, each with its own pick-up coil. In practice, anywhere from three to five samples were used in any one experiment, and one of the unused pick-up coils was employed as a fixed compensating coil.

* Supported by the ONR.
[1] H. Kamerlingh-Onnes and W. Tuyn, Leiden Communications No. 160 (1922).
[2] E. Justi, Z. Physik. **42**, 325 (1941).
[3] The suggestion of looking for a mass dependence in superconductivity was also made independently to us by Professor K. F. Herzfeld.
[4] E. Maxwell, Phys. Rev. **78**, 477 (1950).
[5] Reynolds, Serin, Wright, and Nesbitt, Phys. Rev. **78**, 487 (1950).
[6] E. Maxwell, Phys. Rev. **79**, 173 (1950). See also references 17, 18, and 19.
[7] E. Maxwell, Proc. Natl. Bur. Standards Symposium on Low Temperature Physics, March 27–29, 1951 (to be published).
[8] E. Maxwell, Report on Conference for Very Low Temperature Physics, Oxford, England, August 22, 1951.
[9] Marianne Olsen, Nature **168**, 246 (1951).
[10] Reported by C. A. Reynolds at Conference for Very Low Temperature Physics, Oxford, England, August 22, 1951.
[11] Reynolds, Serin, and Nesbitt, Phys. Rev. **78**, 813 (1950).
[12] Serin, Reynolds, and Nesbitt, Phys. Rev. **80**, 761 (1950).
[13] H. Fröhlich, Proc. Phys. Soc. (London) **A63**, 778 (1950); also Phys. Rev. **79**, 845 (1950).
[14] J. Bardeen, Phys. Rev. **79**, 167 (1950); **80**, 567 (1950).

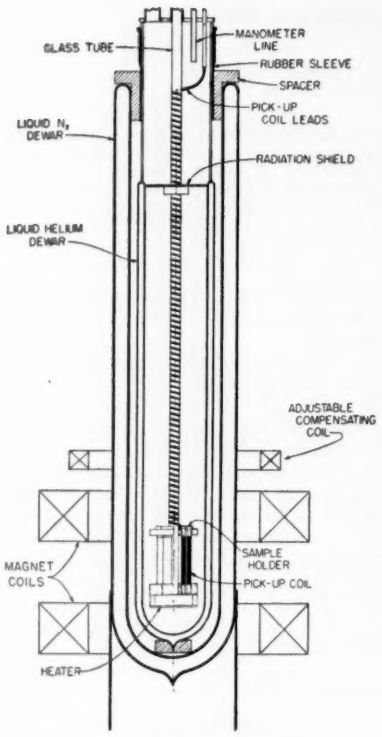

FIG. 1. Cross section of apparatus used for determining critical fields.

The technique of measurement was as follows: The temperature was held constant and the magnetic field set to the desired level by adjusting the magnet current. The circuit was then balanced by adjusting the variable mutual inductance M until no deflection was observed on the ballistic galvanometer when the magnet current was interrupted. In this way the change in mutual inductance between the magnet and the pick-up coil could be observed as the specimen went from the superconducting to the normal state. The change was of the order of 40 to 100 μh with the specimens used in these experiments.

In some of the earlier measurements a deflection method was employed in which the system was balanced when the specimen was either in the normal or the superconducting state and the galvanometer deflection recorded at all other points in the transition. This method is somewhat more rapid, but not as precise as the null method. Except where otherwise noted, the data reported here were taken by the null method.

For measurements in weak fields, where maximum sensitivity was desired, the ballistic galvanometer was a Leeds and Northrup type 2285x which had a period of 7 sec, resistance of 32 ohms, and a critical damping resistance of 110 ohms. The over-all sensitivity of the apparatus was of the order of 2000-mm deflection per cgs unit of magnetic moment. The short time zero instability was less than 0.1 mm. In strong fields where sensitivity was not important it was convenient to use a Leeds and Northrup type 2290 galvanometer with a 37-sec period. Since this galvanometer was highly overdamped in the circuit arrangement used, it was essentially a fluxmeter and eliminated "double-kicks" which were a nuisance whenever the shorter period galvanometer was used for strong field measurements. The "double-kicks" were caused by the fact that the voltage pulses induced in the sample and compensating coils had slightly different shapes so that as a balance was approached the galvanometer deflected first in one direction and then in the opposite because of its fast response. This made it difficult to decide when the system was balanced. With the fluxmeter the final deflection was proportional to the net change in flux and the balancing procedure greatly simplified. The sensitivity was, however, reduced by about a factor of five.

The pick-up coils were wound with 39,000 turns of No. 44 Formex wire on Bakelite forms and had a resistance of about 80 ohms at liquid helium temperatures. This resistance was about optimum for the shorter period galvanometer.

The Helmholtz coil magnet produced a field of 128.8 oersted/ampere which was homogeneous in the volume occupied by the samples to within 0.2 percent. All three components of the earth's field were balanced out by an auxiliary pair of Helmholtz coils to better than 1 milli-oersted.

Temperatures were measured by vapor pressure thermometry using the 1949 Mond Laboratory tables. A mercury manometer was used above 2.4°K, while below 2.4°K a butyl pthalate oil manometer was used

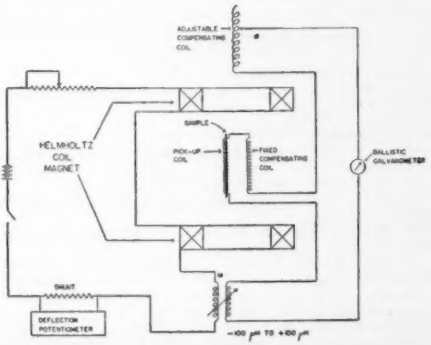

FIG. 2. Simplified circuit arrangement.

for greater sensitivity. The vacuum side of the oil manometer was continuously evacuated by a butyl pthalate diffusion pump. The oil manometer was frequently checked against the mercury manometer and gave results reproducible to ± 0.1 mm oil. Corrections were made for the temperature variation of the density of the oil and mercury during all observations.

When working in the He I region, corrections were also made for the hydrostatic head of liquid helium above the samples. Because of the poor heat conductivity of He I the helium in the lower part of the Dewar can assume a slightly higher temperature than the liquid at the surface. The maximum temperature that can be assumed is that corresponding to the pressure of the vapor at the liquid surface plus the pressure head of the liquid column. (A heater was used at the bottom of the Dewar for stirring purposes which automatically insured that boiling took place at the lower end of the Dewar and fixed the temperature at the value determined by the hydrostatic head.) The head correction varied from a few thousandths of a degree at 4.2° to about 0.01° just above the lambda-point.

The tin isotopes were obtained from the Atomic Energy Commission in the form of SnO_2. These were reduced to the pure metal by heating in a hydrogen atmosphere.[15] The tin metal was then cast in the form of capillary wires by first melting the metal in vacuum, allowing the molten tin to flow into Pyrex capillaries and sealing off under vacuum. In order to prevent the wires from breaking up it was necessary to degas the molten tin as far as possible. This was done by running the molten metal in and out of the capillary several times. After about a dozen trials, enough gas would be removed so that the capillary wire would not be broken up by gas bubbles. The specimens were then remelted by placing the Pyrex capillaries in a furnace which was slowly raised up, allowing the samples to recrystallize as single crystals. Although no detailed examinations of crystal structure have been made, it seems reasonable that the wires are either single crystals or several large crystals.

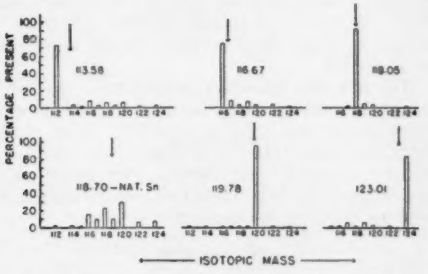

FIG. 3. Distribution of isotopic masses in the samples.

[15] The chemistry was kindly performed for us by Mr. E. L. Weise of the Inorganic Chemistry Section of the Natl. Bur. Standards.

TABLE I. Critical field data for six samples of Sn.

Sample	Atomic mass[a]	Chemical purity	T_c,°K 3-14-51	T_c,°K 7-6-51	H_0	H_0/T_c
112–1	113.58±0.01	99.58[b]	···	3.8082	312.59	82.06
116–1	116.67±0.03	99.69[b]	3.7708	···	···	···
118–1	118.05±0.02	99.19[b]	3.7444	3.7440	307.70	82.21
Sn–2	118.70(nat.)	99.996	3.7419	···	···	···
120–1	119.78±0.05	99.90[b]	3.7238	···	···	···
124–1	123.01±0.08	99.91[c]	3.6669	3.6633	300.97	82.16

[a] The exact atomic masses of the individual isotopes were used in calculating the average masses of these samples.
[b] Oxide.
[c] Metal.

The isotopic purities of the samples are given in Fig. 3 and the chemical purities in Table I. The chemical purity refers to the state of the oxides as furnished by the AEC except as otherwise indicated. The reduction process probably reduced the impurity content, but no analyses of the metal itself are available except for the enriched Sn^{124} sample. The spectrochemical analysis of this sample showed less than 0.1 percent impurity content, so it is likely that the metals as finally refined were considerably purer than the analysis of the oxides indicated.

Since the critical fields for the different isotopes differed by only very small amounts, great emphasis was placed on precision in making the measurements. The general procedure used was to have from three to five samples in the apparatus during any one experiment and to observe the transition of each successively as the field was gradually increased, while the temperature was held constant. By this procedure the differences in critical field were determined rather more precisely than was possible for the absolute values themselves. This fact may be put to advantage by basing the detailed interpretation of the data on the differences $\Delta H(T)$ and ΔT_c, where $\Delta H(T)$ is the difference in critical field for a pair of isotopes as a function of temperature, and ΔT_c is the difference in zero-field transition temperatures.[16] A truly differential measurement to determine these quantities directly would be very desirable but was not feasible. An approach to this was made in the $\Delta H(T)$ measurement in which it was possible to determine the critical fields of the different samples in fairly rapid succession, so that temperature drifts were practically eliminated.

Since magnetic transitions always have a finite width and since the separation in critical fields between isotopes is small, the detailed interpretation of the transition curve is of some importance. The customary procedure in the past has been to take the half-point in the transition, the field at which the magnetic moment of the specimen has half of its maximum value. This, however, corresponds to a point in the intermediate state instead of the ideal phase equilibrium curve, and is moreover a function of the width of the transition curve, which in turn is governed by the

[16] I am indebted to Dr. D. Shoenberg for pointing this out to me.

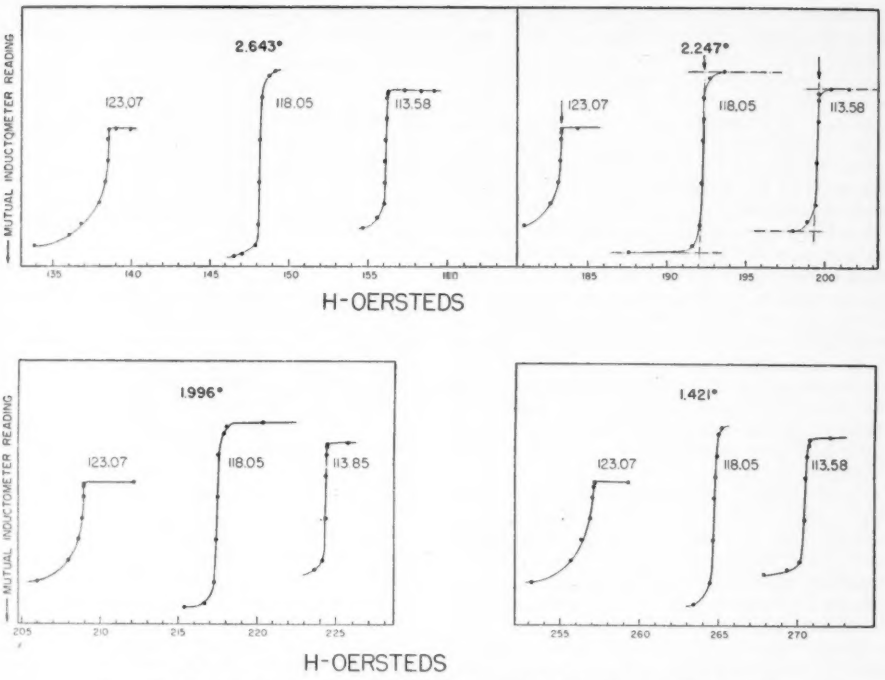

FIG. 4. Typical transitions at constant temperature. The method of selecting the equilibrium value of the field is illustrated in the data for 2.247°.

detailed geometry of the specimen. In this work the transition field was taken as the point at which the sample becomes completely normal, as interpreted by the arrows on the curve for 2.247° in Fig. 4. There is always a small amount of rounding to the curve on the high field side, the reason for which is not known, but is thought to be due to a secondary feature.

The rounding at the start of the transitions was interpreted as due to penetration of the field at the ends of the specimens due to the sharp edges. The length to diameter ratio of the specimens was of the order of 100:1, and consequently the effective demagnetization factor must have been the result of the effect of the sharp edges or other secondary features. The rounding was most noticeable in the sample of mass 123.07, which is somewhat irregular near the ends.

The procedure finally adopted was to trace out carefully each transition curve, point by point. It would normally take about fifteen to twenty minutes for each sample, so that for a group of three samples an hour might elapse between start and finish. As a check on slow drifts, a typical point on the steep part of each transition curve was selected and rapidly checked in succession on each of the three samples after all three curves had been traced out at a given temperature. In this way the field differences could be accurately established. The errors in the differential field measurements are estimated to be less than 0.6 oersted at 1.4°K and somewhat lower at higher temperatures. This estimate is an upper limit which includes such factors as uncertainty in selecting the true critical fields from the transition curves and not merely the precision with which changes in the applied magnetic field could be measured, which was of the order of a few hundredths of an oersted.

The zero field transition temperatures were determined by taking a series of measurements in weak fields and extrapolating to zero field. Some of the transitions were observed in fields of the order of 1 oersted. Some of these samples were redetermined several times over a period of four months and showed shifts of only a few thousandths of a degree.

III. RESULTS

The critical field data observed in these experiments are summarized in Tables I and II and Figs. 5, 6, 9, and 10. The data in Table II were obtained using the null method described in Sec. II and are plotted in

Fig. 5. In Fig. 6 the data in the neighborhood of zero field are plotted to an enlarged scale. The diamond shaped points are observations made by the null method. The other points are earlier observations made by the deflection method in three different runs. The tails on the plotted points indicate the over-all widths of the transitions. The transition field is taken as the field at which the specimen becomes completely normal as interpreted in Fig. 4. The average slope at the transition temperature, $(dH_c/dT)_{T_c}=147$ oersteds/°K, and is the same for all samples to within 4 percent.

The transition temperatures given in Table I are the intercepts of the curves of Fig. 6, and two separate sets of data are given corresponding to observations made on two different days. These are the best data. (The results of the other two sets of observations were incomplete and hence were not used.) For the purpose of finding the exponent in the mass-temperature relation, the two sets of data were considered separately, thus minimizing the effects of systematic errors.

The temperatures reported here are somewhat higher

TABLE II. Critical field data for Sn isotopes (field in oersteds).

T°K	H_c(113.58)	H_c(113.58) $-H_c$(118.05)	H_c(113.58) $-H_c$(123.01)
3.787	3.13	...	...
3.722	12.64	9.52	...
3.656	22.02	9.40	20.93
3.251	78.04	8.85	19.51
3.018	107.22	8.45	18.75
2.643	151.66	7.72	17.26
2.456	171.99	7.52	16.65
2.247	193.89	7.01	15.85
1.996	216.66	6.65	14.94
1.723	240.92	5.95	13.91
1.421	262.97	5.61	13.21
0(extrapolated)	312.40	4.89	11.62

than those reported by Lock *et al.*[17] and Bär *et al.*[18] on separated isotopes of tin but are consistent with those of Reynolds, Serin, and Nesbitt.[19] These divergencies may be due in part to differences in the purities of the materials, in part to systematic differences in thermometry and to differences in the method of selecting the critical fields. Except for the purity these considerations are of only secondary importance for the relative transition temperatures.

IV. INTERPRETATION

The critical field curves for the samples of mass 113.58, 118.05, and 124.01 are given in Fig. 5. These curves are definitely not parabolic, as may be seen in

[17] Lock, Pippard, Shoenberg, Allen, and Dawton, Nature **166**, 1071 (1950). Also Lock, Pippard, and Shoenberg, Proc. Symposium on Low Temperature Physics, Natl. Bur. Standards, March 27, 1951 (to be published), and by the same authors, Proc. Cambridge Phil. Soc. **47**, Part 4, 811 (1951).

[18] Bär, Mendelssohn, Olsen, Allen, and Dawton, Nature **166**, 1072 (1951).

[19] Reynolds, Serin, and Nesbitt, Proc. Symposium on Low Temperature Physics, Natl. Bur. Standards (March 27, 1951) (to be published).

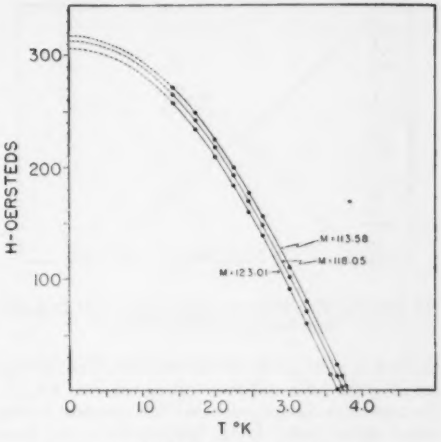

FIG. 5. Critical field curves for tin isotopes.

Fig. 7 where H is plotted against T^2 for the sample of mass 113.58. Although the parabola is a good fit below 2.7°K, it is clearly inadequate between 3°K and the transition temperature. It was found that the data could be nicely fitted by a three-constant equation, such as a hyperbola of the form

$$[(H_c-k)/a]^2+(T/b)^2=1, \tag{1}$$

or a cubic

$$H_c=H_0-AT^2+BT^3. \tag{2}$$

For the sample of mass 113.58 the constants A, B, and H_0 in Eq. (2), determined by a least squares adjustment, were $A=26.3445$, $B=1.26076$, $H_0=312.593$. (It is convenient to carry six figures for computation purposes, although the last two are not physically significant.)

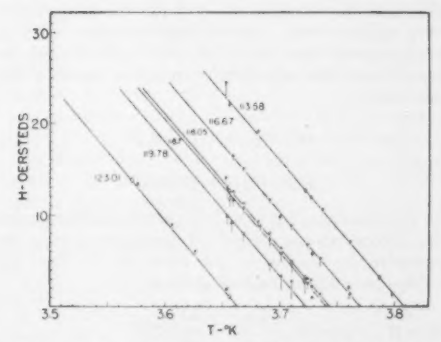

FIG. 6. Critical field curves for tin isotopes in small fields. □—data of March 14, 1951; △—data of April 17, 1951; ○—data of May 3, 1951; ◇—data of July 6, 1951. The points ◇ are probably most reliable. The vertical lines indicate the width of the transition.

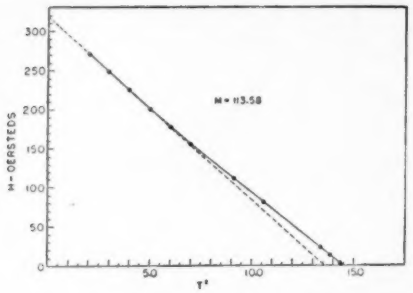

FIG. 7. Plot of H_c vs T^2 for tin sample with $M=113.58$ showing departure from parabolic behavior.

Figure 8 is a deviation plot of the differences between the observed fields and those calculated from Eq. (2). The root-mean-square deviation is 0.27 oersteds. Adding higher order terms to the polynomial would have reduced the mean square deviation but was not done since it would also have imparted an oscillatory character to the critical field curve. The absolute value of the deviation was under 0.5 oersted and therefore within the estimated experimental error.

A preliminary trial with the hyperbola of Eq. (1) suggested that an equally good fit might be obtained. However the fitting of a hyperbola in the least squares sense was not attempted, since it would have involved much more labor and offered no special advantage.

The critical field curves of Fig. 5 are geometrically similar, i.e., they can be described by a universal critical field curve of the form

$$h_c=f(t), \tag{3}$$

where $h_c=H_c/H_0$, $t=T/T_c$, and further H_0/T_c is the same for all curves. This is in agreement with Lock, Pippard, and Shoenberg.[17] As shown by them, the difference in critical fields for a pair of isotopes is a very sensitive test of geometrical similarity. This is advantageous since the differences in critical field are known more precisely than the absolute values of the field itself.

Let

$$H_{c1}=H_{01}-A_1T^2+B_1T^4 \tag{2a}$$

and

$$H_{c2}=H_{02}-A_2T^2+B_2T^4 \tag{2b}$$

be the equations of critical field curves for two samples of different atomic weight. If these two curves are geometrically similar in the sense of (3) then the difference in critical fields is given by

$$H_c=H_{c1}-H_{c2}=H_{01}\frac{\Delta T_{12}}{T_{c1}}+A_1\frac{\Delta T_{12}}{T_{c2}}T^2 -B_1\frac{\Delta T_{12}}{T_{c2}}\left(2+\frac{\Delta T_{12}}{T_{c2}}\right)T^4, \tag{2c}$$

where T_{c1} and T_{c2} are the transition temperatures of samples 1 and 2, respectively, and $\Delta T_{12}=T_{c1}-T_{c2}$. (Sample 2 is assumed to have the greater atomic mass.) Equation (2c) determines ΔH_c in terms of the observed zero field transition temperature difference ΔT_{12}. The test for geometrical similarity consists in comparing the observed values of ΔH_c with those computed according to Eq. (2c).

Figure 9 shows this comparison for $\Delta H(113.58, 123.01)$ and $\Delta H(113.58, 118.05)$, respectively. The agreement is considered good. The observed ΔH_c's lie somewhat below the calculated values at the lower end of the temperature scale, but the deviations are of the order of half an oersted and within the limit of error. For geometrically similar curves $\Delta H_0/H_0=\Delta T/T_c$. $\Delta H_0/H_0$ is about 6 percent lower than $\Delta T/T_c$ for the pair 113.58–118.05, while for the pair 113.58–123.01 it is within 3 percent. This is about the correct order of magnitude to be accounted for by experimental error and indicates that the curves are geometrically similar to approximately one part in 800.

Geometrical similarity implies that the ratio H_0/T_c is constant for the different isotopes. Fröhlich[13] and

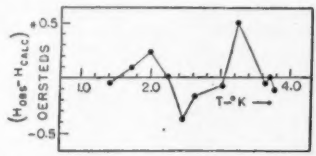

FIG. 8. Deviations of observed critical field for $M=113.58$ from the equation $H_c=312.593-26.3445T^2-1.26076T^4$.

Bardeen[14] have predicted that $H_0\sim M^{-\frac{1}{2}}$, as the result of theories based on interaction of electrons and zero-point vibrations, and consequently when geometrical similarity obtains $T_c\sim M^{-\frac{1}{2}}$. Figure 10 is a logarithmic plot of the data of Table I in which straight lines have been fitted separately to the two sets of data. These two determinations yield slopes of 0.487 ± 0.026 and 0.522 ± 0.028 (the precision indexes are the standard deviations) or a mean slope of 0.505 ± 0.019. The standard deviations give an indication of the internal consistency of the data, but it should be realized that the possible effects of purity, strain, and similar physical properties are unknown and are difficult to evaluate. Nevertheless it is clear that these results are highly consistent with the relation $T_c\sim M^{-\frac{1}{2}}$, and consequently lend support to the hypothesis that superconductivity is intimately associated with the interaction of electrons with zero point lattice vibrations.

If the reduced critical field is a universal function of the reduced temperature for all isotopes, as expressed by (3), it follows that the thermodynamic quantities which depend on the critical field can also be written as universal functions of the reduced temperature when properly normalized. The entropy difference, latent

heat, and specific heat difference per mole are given by

$$S_n - S_s = -(V_m/4\pi)H_c(dH_c/dT) \tag{4a}$$

$$Q = -(TV_m/4\pi)H_c(dH_c/dT) \tag{5a}$$

$$C_n - C_s = V_m\{(T/4\pi)H_c(d^2H_c/dT^2) + (T/4\pi)(dH_c/dT)^2\}, \tag{6a}$$

where V_m is the molar volume. The corresponding reduced equations are

$$s_n - s_s = \frac{S_n - S_s}{H_0(H_0/T_c)} = -V_m \frac{h}{4\pi}\frac{dh}{dt} \tag{4b}$$

$$q = \frac{Q}{(H_0^2/8\pi)} = -2th\frac{dh}{dt}V_m \tag{5b}$$

$$c_n - c_s = \frac{C_n - C_s}{T_c(H_0/T_c)^2} = V_m\left\{\frac{t}{4\pi}h\frac{d^2h}{dt^2} + \frac{t}{4\pi}\left(\frac{dh}{dt}\right)^2\right\}. \tag{6b}$$

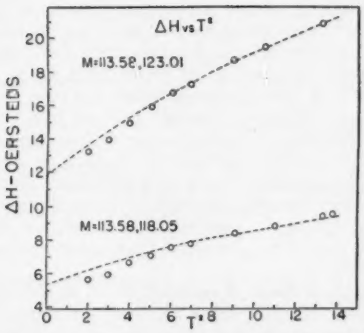

FIG. 9. Plot of ΔH_c vs T^2 for the pairs of tin samples with masses (113.58, 123.01) and (113.58, 118.05). Dotted curve calculated from Eq. (4).

In Eqs. (4b), (5b), and (6b), $h = H_c/H_0$ and $t = T/T_c$ are the reduced critical field and temperature. The quantities s, q, and c, defined as indicated in terms of S, Q, and C, are universal functions of h and t and apply to all the isotopes. This follows as a consequence of the similarity property.

The temperature dependence of the entropy and specific heat differences can be determined directly from the explicit relation for the critical field as per Eqs. (4) and (6). If $H(T)$ is given by a polynomial the entropy and specific heat differences will contain a linear term in T plus higher order terms. (For the case of a parabola[20-22] only linear and cubic terms are present.) The linear term is generally identified with the entropy or specific heat of the electrons in the normal state. The

[20] J. A. Kok, Leiden Communications 77a (1934).
[21] C. J. Gorter and H. Casimir, Physik. Z. 35, 963 (1934).
[22] A. Sommerfeld, Z. Physik 118, 467 (1941).

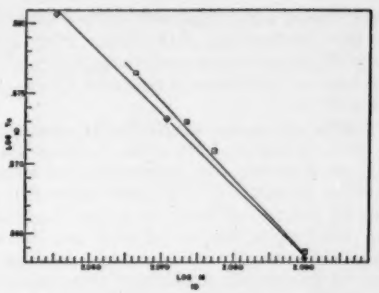

FIG. 10. Plot of $\log_{10}T_c$ vs $\log_{10}M$ for tin isotopes. The best value of α in the formula $M^\alpha T_c$ = constant is $\alpha = 0.505 \pm 0.019$.

coefficient of the linear term is given by

$$\gamma = -\lim_{T\to 0}\frac{V_m}{8\pi}\frac{d^2H_c^2}{dT^2} = -\lim_{T\to 0}\frac{V_m}{8\pi}\frac{H_0^2}{T_c}\frac{d^2h_c^2}{dt^2}. \tag{7}$$

$H_c(T)$ is given by Eq. (2) and $h_c(t)$ by

$$h_c(t) = H_c/H_0 = 1 - at^2 + bt^4, \tag{8}$$

where

$$a = (A/H_0)T_c^2, \quad b = (B/H_0)T_c^4.$$

Consequently

$$\gamma/V_m = (H_0/T_c)^2(a/2\pi), \tag{9}$$

an expression given previously by Sommerfeld[22] (and by Daunt, Horseman, and Mendelssohn[23] for the special case of a parabolic field relation).

The similarity feature of the critical field curves implies that both H_0/T_c and a are independent of atomic mass, and to the extent that this is quantitatively correct, it follows from (9) that γ/V_m is also independent of mass. H_0/T_c is constant to about one part in 800. An estimate of the variability of a may be obtained by comparing the calculated equation for $\Delta H_c(T)$ with the observed data,[24] and is of the order of 1.5 percent. Hence if no other sources of error are present, γ/V_m may be assumed independent of mass to about 1.5 percent. (There is, however, some further uncertainty in a due to the fact that there is a certain amount of choice in fitting an equation to the empirical critical field data; a will vary somewhat depending on whether the coefficients in the equation are chosen for best fit at low temperatures, or near the critical temperature, or whether the mean square deviation over the entire temperature range is minimized. This is simply

[23] Daunt, Horseman, and Mendelssohn, Phil. Mag. 27, 754 (1939).

[24] $\Delta H_c(T) = \Delta H_c(0) + mT^3 - nT^5$,
where
$$m = H_{01}\frac{a_2}{T_{c_1}^3} - H_{02}\frac{a_1}{T_{c_1}^3}.$$
If critical field curves are geometrically similar $a_2 = a_1$. If $a_2 \neq a_1$,
$$m_{obs} - m_{calc} = (H_{02}/T_{c_1}^3)(a_2 - a_1).$$

another way of saying that $(d^2H_c^2/dT^2)$ is determined with less certainty than $H_c(T)$ itself.) If the atomic volume V_m is also independent of mass,[25] then γ itself is the same for all isotopes, a conclusion also given by Lock *et al.*[17]

Using the numerical values $H_0/T_c=82.1$ oersteds/K°, $V_m=14.2$ cm³ and $a=1.223$ in Eq. (9) gives $\gamma=4.46\times10^{-4}$ cal/deg²/mole. The direct calorimetric measurements[26] of Keesom and Van Laer[27] determine γ as $4.0\pm0.4\times10^{-4}$ cal/deg²/mole, which is good agreement.

As stated above, the critical field data presented here are not adequately represented by a parabola, and hence the specific heat and entropy differences cannot be accurately described in terms of simply linear and cubic terms but must contain other higher terms as well. The entropy difference which follows from (2) and (4a) is

$$S_n-S_s=(V_m/4\pi)(2H_0AT-3BH_0T^2-2A^2T^3+5ABT^4-3B^2T^5). \quad (10)$$

It is also of interest to examine these data in terms of the Gorter-Casimir two-fluid theory.[21] From this point of view the electron assembly in the superconducting state is considered as a two-phase system, a "crystallized" phase of zero entropy consisting of the superconducting electrons and a "gaseous" phase consisting of normal electrons which have a finite entropy given by the Sommerfeld theory. The entropy of the "gaseous" phase per mole of superconductor is

$$S_{n_{el}}=\gamma Tx^\alpha, \quad (11)$$

where x is the fractional concentration of normal electrons at temperature T and α is a constant. The condition that the free energy be a minimum leads to the relations

$$x=(2\beta/\alpha\gamma)^{1/(\alpha-1)}T^{-2/(\alpha-1)} \quad (12)$$

and

$$T_c^2=(2\beta/\alpha\gamma), \quad (13)$$

where T_c = the transition temperature, and β is the free energy difference per mole between normal and superconducting phases at absolute zero and hence

$$\beta=(H_0^2/8\pi)\cdot V_m.$$

It will be seen that (13) is identical in form to (9) and that $\alpha=1/2a$.

If $\alpha=\frac{1}{2}$

$$x^\alpha\sim T^2 \quad (14)$$

$$S_{n_{el}}\sim T^3 \quad (15)$$

and the critical field curve is parabolic. The present data for tin show that the critical field is not parabolic, and that α is 0.409 instead of $\frac{1}{2}$. In general it follows from (11) and (12) that

$$S_{n_{el}}\sim T^{-(\alpha+1)/(\alpha-1)}. \quad (16)$$

Hence from our data $S_{n_{el}}\sim T^{2.4}$.

Daunt[28] has shown that the temperature dependence of the penetration depth can be deduced from the Gorter-Casimir thermodynamical model if the square of the penetration depth is assumed to be inversely proportional to the density of superconducting electrons. It follows that

$$(\lambda_0/\lambda)^2=1-t^{-2/(\alpha-1)}, \quad (17)$$

where λ_0 = penetration depth at 0°K, and λ = penetration depth at reduced temperature t. When $\alpha=\frac{1}{2}$ the familiar[29] fourth power law is obtained for the temperature variation of the penetration depth. For $\alpha=0.409$, the result indicated by the present data for tin, the temperature variation would follow a 3.4-power law, with an uncertainty of perhaps 5 percent in the exponent. Whether or not this divergence from the fourth power is significant is hard to say, since on the one hand the penetration depth measurements are probably not precise enough to exclude the possibility of a 3.4 power, and on the other hand the model from which (17) is derived may be only a crude approximation to the truth.

Finally, it should be remarked that if an equation of the form of (17) does hold, then the temperature dependence of the penetration depth is independent of isotopic mass.

It is a pleasure to acknowledge the valuable assistance of Mr. O. S. Lutes in the conduct of these experiments and in the calculation of the data and of Mr. W. B. Hanson, who assisted in some of the early experiments. I am indebted to Mr. E. L. Weise of the Chemistry Division of the National Bureau of Standards for his skillful preparation of the pure metal samples from the oxides and to Mr. J. M. Cameron of the Applied Mathematics Division of NBS for valuable statistical analysis. Finally, we thank the AEC for its cooperation in furnishing the enriched isotopes which made this study possible, and Dr. W. F. Meggers of NBS for lending us the Hg^{198} used in the original experiment.

[25] V_m may be slightly mass dependent because of the anharmonicity of the zero-point vibrations. This, however, should be a very small effect and may be estimated by assuming that a small increase in zero-point energy has the same effect in dilating the lattice as the same addition of thermal energy at a higher temperature. This argument suggests that the effect is only of the order of 0.002 percent per mass unit.

[26] W. H. Keesom and P. H. Van Laer, Leiden Communications 252b (1938).

[27] The uncertainty of ±0.4 is our own estimate based on the spread in their observed data.

[28] J. G. Daunt, Phys. Rev. **72**, 89 (1947). Phys. Rev. **74**, 985 (1948).

[29] Daunt, Miller, Pippard, and Shoenberg, Phys. Rev. **74**, 842 (1948); also J. M. Lock, Proc. Roy. Soc. (London) **A208**, 391 (1951).

Chemical Effects in Nuclear Magnetic Resonance and in Diamagnetic Susceptibility*

NORMAN F. RAMSEY
Harvard University, Cambridge, Massachusetts

(Received December 26, 1951)

An expression for the magnetic shielding of nuclei in solids and in molecules is developed, and an approximation is obtained that is particularly suited to substances containing heavy atoms. The temperature dependence of the magnetic shielding which arises when there are several low-lying states of the molecules is discussed. It is shown that only slight changes in the various formulas make them applicable to the diamagnetic susceptibility.

1. INTRODUCTION

IN the author's original paper[1] on chemical shifts and magnetic shielding, the development was limited to systems which on the average were cylindrically symmetric about the direction of the magnetic field, such as molecules in states whose axis of quantization was parallel to the magnetic field. A more general expression not subject to this limitation and hence applicable to crystals is obtained in the present paper.

In the earlier paper,[1] the general expression for the shielding [Eq. (6) of that paper[1]] contained two apparently quite different types of terms, each of which would have to be calculated separately by approximate methods in actual problems. In the present paper, it is shown that by a suitable gauge transformation an alternative approximate form for this expression can be obtained in which one of these types of terms (the second-order paramagnetism terms) vanish for electrons tightly bound to any of the atoms in the molecule.

Finally, in the earlier paper,[1] it was assumed that there were no alternative states separated from the ground state by an energy comparable to kT for which the magnetic shielding was different. Consequently, no temperature dependence of the shielding was indicated. Although for most molecules this assumption is valid and the magnetic shielding is temperature independent, a few cases of temperature dependent magnetic shielding have been observed. The treatment of the present paper will cover such cases as well and, in addition, is applicable to the temperature dependence of the diamagnetic susceptibility.

2. MAGNETIC SHIELDING CALCULATION

Consider a polyatomic molecule or crystal which in the absence of an external field has no resultant electron spin or electron orbital angular momentum. Since the nuclei are massive compared to the electrons, the nuclei can be treated classically to a very good approximation. In particular, in the first phases of the calculation the nuclei will be considered to be approximately stationary, attracting centers whose orientation is specified by λ. As is discussed in the earlier paper,[1] the effects of electron spin can be omitted in the subsequent discussion; except in cases of accidental degeneracies, the magnetic shielding fields from the electron spins should be of higher orders of smallness than the other contributions calculated here. It should be noted, however, that this result arises from the fact that magnetic shielding by definition is concerned only with effects proportional to the external magnetic field $\mathbf{H}$. Consequently, any direct contribution of the electron spins to the shielding field which arises in a second-order perturbation calculation will depend on matrix elements of the interaction between $\mathbf{H}$ and the electron spins which are nondiagonal in the resultant electron spin. If, however, $\mathbf{H}$ is uniform over the entire molecule such matrix elements vanish. As recently discussed by Ramsey and Purcell[2] while considering the shielding of the interaction between two nuclear magnetic moments in the same molecule, the effect of the electron spins must be included when $\mathbf{H}$ is not uniform over the molecule.

If the origin of the coordinate system is taken at the nucleus where the shielding is to be evaluated, if $\boldsymbol{\mu}$ is the magnetic moment of that nucleus, and if $\mathbf{H}$ is the external magnetic field, the vector potential for the kth electron at position $\mathbf{r}_k$ may be taken as

$$\mathbf{A}_{kl}=\tfrac{1}{2}\mathbf{H}\times\mathbf{r}_k+\boldsymbol{\mu}\times\mathbf{r}_k/r_k^3-\tfrac{1}{2}\mathbf{H}\times\mathbf{R}_{kl}, \tag{1}$$

where $\mathbf{R}_{kl}$ is a purely arbitrary constant and arises from the arbitrariness of the gauge of the vector potential. With this vector potential and with $(-e)$ as the charge of the electron, the Hamiltonian operator for the electrons of the system is

$$\mathcal{H}=\sum_{k=1}^{n}\frac{1}{2m}\left[\frac{\hbar}{i}\nabla_k+\frac{1}{2}\frac{e}{c}\mathbf{H}\times[\mathbf{r}_k-\mathbf{R}_{kl}]+\frac{e}{c}\frac{\boldsymbol{\mu}\times\mathbf{r}_k}{r_k^3}\right]^2+V. \tag{2}$$

By an expansion and a few simple transformations of vector products, this can be written as

$$\mathcal{H}=\mathcal{H}^{(0)}+\mathcal{H}^{(1)}+\mathcal{H}^{(2)}, \tag{3}$$

where

$$\begin{aligned}\mathcal{H}^{(0)}&=-\textstyle\sum_k(\hbar^2/2m_k)\nabla_k^2+V,\\ \mathcal{H}^{(1)}&=-\textstyle\sum_k\mathbf{H}\cdot\mathbf{m}_{kl}^0-\sum_k 2\boldsymbol{\mu}\cdot\mathbf{m}_{k0}^0/r_k^3,\\ \mathcal{H}^{(2)}&=(e^2/8mc^2)\textstyle\sum_k(\mathbf{H}\times[\mathbf{r}_k-\mathbf{R}_{kl}]+2\boldsymbol{\mu}\times\mathbf{r}_k/r_k^3)^2,\end{aligned} \tag{4}$$

* This work was partially supported by the joint program of the ONR and AEC.

[1] N. F. Ramsey, Phys. Rev. **77**, 567 (1950) and **78**, 699 (1950).

[2] E. M. Purcell and N. F. Ramsey (to be published).

with

$$\mathbf{m}_{kl}{}^{0}=-(e\hbar/2mci)[\mathbf{r}_k-\mathbf{R}_{kl}]\times\nabla_k$$

and

$$\mathbf{m}_{k0}{}^{0}=-(e\hbar/2mci)\mathbf{r}_k\times\nabla_k. \tag{5}$$

Therefore, by the usual second-order perturbation theory[1,3] and by use of the well-known transformation reducing the scalar product of two vector products, if W_λ' is the sum of the energy terms linear in $\boldsymbol{\mu}$ and $\mathbf{H}$, one obtains

$$W_\lambda'=\boldsymbol{\mu}\cdot\boldsymbol{\sigma}_\lambda{}^{d}\cdot\mathbf{H}, \tag{6}$$

where $\boldsymbol{\sigma}_\lambda{}^{d}$ is the dyadic

$$\begin{aligned}\boldsymbol{\sigma}_\lambda{}^{d}=&(e^2/2mc^2)(n\lambda|\textstyle\sum_k\{\mathbf{1}^{d}(\mathbf{r}_k-\mathbf{R}_{kl})\cdot\mathbf{r}_k\\&-(\mathbf{r}_k-\mathbf{R}_{kl})\mathbf{r}_k\}/r_k{}^{3}|n\lambda)-4\ \mathrm{Re}\textstyle\sum_{n'\lambda'}{}'[1/(E_{n'}-E_n)]\\&\times[(n\lambda|\textstyle\sum_k\mathbf{m}_{k0}{}^{0}/r_k{}^{3}|n'\lambda')(n'\lambda'|\mathbf{m}_{kl}{}^{0}|n\lambda)].\end{aligned} \tag{7}$$

It is of interest to note that the terms of the first type in (7) can be given a simple physical interpretation. If an electron at position $\mathbf{r}_k$ moves with angular velocity $\boldsymbol{\omega}$ about a point $\mathbf{R}_{kl}$, then the magnetic field at the origin resulting from this motion is

$$\begin{aligned}\mathbf{H}'=&-(e/c)[\boldsymbol{\omega}\times(\mathbf{r}_k-\mathbf{R}_{kl})]\times\mathbf{r}_k/r_k{}^{3}\\=&[\{e^2/2mc^2\}\{\mathbf{1}^{d}(\mathbf{r}_k-\mathbf{R}_{kl})\cdot\mathbf{r}_k\\&-(\mathbf{r}_k-\mathbf{R}_{kl})\mathbf{r}_k\}/r_k{}^{3}]\cdot[2mc\boldsymbol{\omega}/e].\end{aligned} \tag{8}$$

Therefore, the terms of the first part of (7) correspond to the magnetic field at the position of the nucleus being shielded by circulations of the electrons about the points $\mathbf{R}_{kl}$ with angular velocity $e\mathbf{H}/2mc$. As the points $\mathbf{R}_{kl}$ are arbitrary, the axes of the circulation are therefore arbitrary. At first sight this seems surprising, since the magnitude of the field clearly depends on the location of this axis. The explanation of this apparent anomaly is that $\mathbf{R}_{kl}$ also enters in the terms of the second type since $\mathbf{m}_{kl}{}^{0}$ depends on $\mathbf{R}_{kl}$, and any changes in the terms of the first type which result from a change in the values of $\mathbf{R}_{kl}$ are just exactly compensated by the corresponding changes in the terms of the second type. It should, of course, be noted that expression (7) provides only the electronic magnetic shielding contribution to shifts in nuclear resonance frequencies. In molecules in specific orientation states and in crystals, there are also, in general, much larger and more conspicuous shifts because of magnetic interactions of the nuclear spins, nuclear quadrupole interactions, etc. In general these depend differently on the external field than does the magnetic shielding, and their effects can be calculated by well-established methods.[4,5]

In many problems only a single component of the dyadic, say the zz component, is of interest. This is the case, as an example, for a molecule in the presence of a magnetic field along the z axis in case the orientation state of the molecule is on the average symmetrical about the z axis, as when it is specified by the magnetic quantum number relative to that axis. However, even for crystals, if only the magnitude of the field at the nucleus is of interest, it is given to the first approximation by the zz component of the dyadic only. If the zz component of $\boldsymbol{\sigma}_\lambda{}^{d}$ is called σ_λ, Eq. (7) gives

$$\begin{aligned}\sigma_\lambda=&(e^2/2mc^2)(n\lambda|\textstyle\sum_k\{(x_k-X_{kl})x_k\\&+(y_k-Y_{kl})y_k\}/r_k{}^{3}|n\lambda)\\&-4\ \mathrm{Re}\textstyle\sum_{n'\lambda'}{}'[1/(E_{n'}-E_n)]\\&\times[(n\lambda|\textstyle\sum_k m_{zk0}{}^{0}/r_k{}^{3}|n'\lambda')(n'\lambda'|m_{zkl}{}^{0}|n\lambda)].\end{aligned} \tag{9}$$

It should be noted that if $\mathbf{R}_{kl}$ is taken as zero the above result is that given in the previous papers.[1,3] In fact, one can derive (9) in an alternative fashion by starting with Eq. (6) of the earlier paper,[1] which was based on a particular gauge corresponding to $\mathbf{R}_{kl}=0$, and by transforming the coordinates to express the angular momentum $(-2mc/e)m_{zk}{}^{0}$ about the origin in terms of the angular momentum about the point $\mathbf{R}_{kl}$ in a fashion similar to that of Van Vleck[6] in showing the invariance of the magnetic susceptibility of molecules to the choice of the origin.

If the problem, in addition to being cylindrically symmetric about the field, is also on the average spherically symmetric as when all states of different possible magnetic quantum numbers are equally occupied, Eq. (9) reduces on the average to

$$\begin{aligned}\sigma_\lambda=&(e^2/3mc^2)(n\lambda|\textstyle\sum_k\{(1/r_k)-(\mathbf{R}_{kl}\cdot\mathbf{r}_k/r_k{}^{3})\}|n)\\&-(4/3)\ \mathrm{Re}\textstyle\sum_{n'}{}'[1/(E_{n'}-E_n)]\\&\times[(n|\textstyle\sum_k\mathbf{m}_{k0}{}^{0}/r_k{}^{3}|n')\cdot(n'|\mathbf{m}_{kl}{}^{0}|n)].\end{aligned} \tag{10}$$

3. MOLECULES WITH HEAVY ATOMS

The previous expressions have the disadvantage that all electrons in the molecule or crystal must be included in the calculation, even though it is physically apparent that electrons tightly bound to distant nuclei will make only a small contribution. In the above formulation this result is achieved by virtue of the terms of the first type in (7) approximately canceling terms of the second type for such electrons. Since, however, in most problems each type of term would be calculated only approximately, it is important to obtain an expression in which the result for such electrons does not appear as a very small difference in two large approximately calculated quantities.

Let N_K electrons form complete shells that are so tightly bound to the Kth nucleus that their mean potential is approximately spherically symmetric about the Kth nucleus, and let N_S electrons be all the remaining electrons which cannot be considered to be bound overwhelmingly to any single atom in the molecule. Then select $\mathbf{R}_{kl}$ to be $\mathbf{R}_K$, the radius vector to the Kth nucleus, if k corresponds to one of the N_K electrons tightly bound to the Kth nucleus, and let

[3] N. F. Ramsey, Phys. Rev. **83**, 540 (1951).
[4] Kellogg, Rabi, Ramsey, and Zacharias, Phys. Rev. **57**, 677 (1940).
[5] R. V. Pound, Phys. Rev. **79**, 685 (1950).
[6] J. H. Van Vleck, *Electric and Magnetic Susceptibilities* (Oxford University Press, London, 1932), pp. 275–276.

$\mathbf{R}_{kl}$ remain arbitrary for the N_S electrons not tightly bound to any nucleus. With this selection and with the spherical symmetry of the potential about the Kth nucleus, there will be no nondiagonal matrix elements of the orbital angular momentum operator $(-2mc/e)\mathbf{m}_{kK}$ about the Kth nucleus for any of the N_K electrons tightly bound to the Kth atom. Consequently, Eq. (7) reduces approximately to the following expression,

$$\sigma_\lambda=(e^2/2mc^2)\sum_K(n_K\lambda|\sum_{k=1}^{N_K}\{1^d(\mathbf{r}_k-\mathbf{R}_K)\cdot\mathbf{r}_k-(\mathbf{r}_k-\mathbf{R}_K)\mathbf{r}_k\}/r_k^3|n_K\lambda)+(e^2/2mc^2)(n_s\lambda|\sum_{k=1}^{N_S}\{1(\mathbf{r}_k-\mathbf{R}_{kl})\cdot\mathbf{r}_k-(\mathbf{r}_k-\mathbf{R}_{kl})\mathbf{r}_k\}/r_k^3|n_s\lambda)-4\,\mathrm{Re}\sum_{n_s\lambda'}[1/(E_{ns'}-E_n)]\times[(n_s\lambda|\sum_{k=1}^{N_S}\mathbf{m}_{k0}/r_k^3|n_{s'}\lambda')(n_s'\lambda'|\mathbf{m}_{kl}^0|n_s\lambda)]. \quad (11)$$

For the tightly bound electrons, therefore, the high frequency or second-order paramagnetic terms vanish. Equation (11) can be reduced to forms similar to (9) and (10) if the appropriate symmetries are applicable.

In the preceding paragraph the electrons were treated as if they were distinguishable, despite the fact that the wave functions must be antisymmetric in all the electrons. However, a similar result to the above can be obtained in a more complicated fashion if one adopts any of the methods of treating molecules in a suitably antisymmetric fashion, such as that of Slater,[7] provided the wave functions of the electrons tightly bound to any nucleus are approximately orthogonal to the remaining wave functions.

4. TEMPERATURE DEPENDENCE

The previous discussion has all been for a single electronic ground state n of the molecule. For most molecules, there is only a single electronic state possible within an energy range at all comparable to kT from the ground state, so that the previous expressions apply directly to most molecules and the magnetic shielding should be independent of the temperature, as usually is found to be the case.[8]

However, it has been found experimentally by Proctor and Yu,[8] and by Packard and Arnold[9] that in some cases there is a temperature dependence of the magnetic shielding. From the point of view of the above analysis, this presumably corresponds to there being several low-lying states for each of which the shielding, σ, is slightly different. Then, as the temperature is changed, the distribution between the states, and consequently, the average value of σ are altered.

[7] J. C. Slater, Phys. Rev. **38**, 1112 (1931).
[8] W. G. Proctor and F. C. Yu, Phys. Rev. **81**, 20 (1951).
[9] M. E. Packard and J. T. Arnold, Phys. Rev. **83**, 210 (1951).

The form of the temperature dependence to be anticipated can readily be obtained for any of the above shielding expressions. Since the cases in which temperature dependent effects have been observed are those which are such that on the average the distribution of the molecular orientation is spherically symmetric, only the temperature dependence that should arise from (10) will be discussed.

Assume that for states $n=0, 1, \cdots, g$ the quantity $\exp(-E_n/kT)$ is appreciable, while for the remaining states it is negligible. Then the weighted mean average of σ can be written as,

$$\bar{\sigma}=\sigma_1+\sigma_2+\sigma_3,$$

where

$$\sigma_1=C\sum_{n=0}^{g}\exp(-E_n/kT)(e^2/3mc^2)\times(n|\textstyle\sum_k\{(1/r_k)-(\mathbf{R}_{kl}\cdot\mathbf{r}_k/r_k^3)\}|n),$$

$$\sigma_2=-\frac{4}{3}C\,\mathrm{Re}\sum_{n=0}^{g}\exp(-E_n/kT)\sum_{n'=g+1}^{\infty}[1/(E_{n'}-E_n)]\times[(n|\textstyle\sum_k\mathbf{m}_{k0}^0/r_k^3|n')\cdot(n'|\sum_k\mathbf{m}_{kl}^0|n)], \quad (12)$$

$$\sigma_3=-\frac{4}{3}C\,\mathrm{Re}\sum_{n=0}^{g-1}\sum_{n'=n+1}^{g}[\exp(-E_n/kT)-\exp(-E_{n'}/kT)][1/(E_{n'}-E_n)]\times[(n|\textstyle\sum_k\mathbf{m}_{k0}^0/r_k^3|n')\cdot(n'|\sum_k\mathbf{m}_{kl}^0|n)]$$

and where,

$$C=1/\sum_{n=0}^{g}\exp(-E_n/kT).$$

It should be noted, however, that a single sharp line will be observed at the shifted frequency only if a molecule makes transitions between the different states $n=0, 1, \cdots, g$ at a sufficiently rapid rate that the Larmor precession of the nucleus occurs in the average field at the nucleus. In other words, collision narrowing[10] needs to occur. As discussed by Purcell, Bloembergen, and Pound,[10] if τ_c, the correlation time for the transitions, is short, the width of the resonance will be of the order $4\tau_c/\pi T_2''$,[2] where T_2' is the transverse relaxation time in the absence of collision narrowing, so $1/T_2''$ is of the order of $\gamma H\Delta\sigma$ where $\Delta\sigma$ is the spread of the σ-values among the g lowest states. Therefore, the resonance width in the presnt case from this effect alone will be $4(\gamma H\Delta\sigma)^2\tau_c/\pi$.

The first reported temperature-dependent magnetic-shielding constants were those of the cobalt nucleus in $K_3Co(CN)_6$, $Co[C_2H_4(NH_2)_2]_3Cl_3$, and $Co(NH_3)_6Cl_3$, which were shown by Proctor and Yu[8] to be such that for a temperature increase from 20°C to 80°C the resonance frequency increased by 0.015 percent or about 1 kc out of 7000 kc. In these same molecules the chemical

[10] Purcell, Bloembergen, and Pound, Phys. Rev. **73**, 704 (1947).

shift is large, with the resonance frequency for the last being 1.0083 times that of the first. The simultaneous occurrence both of the large chemical shift and of the temperature dependence indicates the existence of low-lying levels. Unfortunately, not enough data on the experimental temperature dependence are available as yet to determine the energy of the levels. However, the sign of the shift is enough to eliminate one very simple and attractive possibility. This possibility is that there might be only a single low-lying state in addition to the ground state, and that the existence of this level might be responsible both for the temperature dependence and for the large magnitude of σ which would then be chiefly the result of σ_3. In this case Eq. (12) would reduce approximately to

$$\sigma_3 = -(4/3)\,\mathrm{Re}[1/(E_1-E_0)][(0|\textstyle\sum_k \mathbf{m}_{k0}{}^0/r_k{}^3|1) \cdot (1|\textstyle\sum_k \mathbf{m}_{k1}{}^0|0)]\left[\frac{1-\exp\{-(E_1-E_0)/kT\}}{1+\exp\{-(E_1-E_0)/kT\}}\right]. \quad (13)$$

If this relation applied, E_1-E_0 could be calculated from the temperature dependence and $(0|\sum \mathbf{m}_{k0}{}^0/r_k{}^3|1) \cdot (1|\sum \mathbf{m}_k{}^0|0)$ could be calculated from the data. However, (13) would lead to a decrease in resonance frequency with increasing temperature which is just opposite to the observed results[8] with the cobalt compounds. Therefore, the simple relation (13) is not applicable in this case and the more complicated general relation (12) must be used.

The other important temperature shift so far reported is that of Packard and Arnold,[9] in which they observe in ethyl alcohol that the resonance of the hydrogen in the OH radical shifts markedly with temperature even though the magnitude of the shift itself is not unusually large. This suggests that the shift is not because of terms of the type σ_3 but instead to terms of the type σ_1 and σ_2. Liddel and Ramsey[11] have recently suggested a mechanism for the production of suitable low-lying alternative states in the process of molecular association in the liquid. Such association is usually assumed to be via a hydrogen bond affecting the hydrogen in OH, so it is quite reasonable that this hydrogen should be the one to have its temperature affected. It is important to note that since this mechanism depends on the molecular association of several molecules, it is dependent on the concentration of the liquid. Therefore, the temperature dependence will not be given simply by Eq. (12) which was derived for a single molecule. Instead, the various theories[12,13] for the equilibrium of the association must be used. The temperature dependence of the magnetic shielding in this case should in fact provide experimental information on the temperature dependence of the association equilibrium.

5. DIAMAGNETIC SUSCEPTIBILITIES

If the dyadic, ξ^d, is the diamagnetic susceptibility of the molecule or crystal, expressions for ξ^d can be obtained analogous to each of the preceding formulas for σ^d provided only that in each expression for σ^d the $r_k{}^3$'s that occur are replaced by unity, except that in Eqs. (10) and (12) $1/r_k$ is also replaced by $r_k{}^2$. Thus, (10) with $\mathbf{R}_{kl}$ set equal to zero leads to a diamagnetic expression similar to that of Van Vleck.[6] As a further example, the diamagnetic susceptibility of a molecule with g low-lying excited states is given by the following expression corresponding to (12),

$$\xi = \xi_1 + \xi_2 + \xi_3, \quad (14)$$

where

$$\xi_1 = C\sum_{n=0}^{g} \exp(-E_n/kT)(e^2/3mc^2) \times (n|\textstyle\sum_k\{r_k{}^2 - \mathbf{R}_{kl}\cdot\mathbf{r}_k\}|n),$$

$$\xi_2 = -(4/3)C\,\mathrm{Re}\sum_{n=0}^{g}\exp(-E_n/kT)\sum_{n'=g+1}^{\infty}[1/(E_n-E_0)] \times[(n|\textstyle\sum_k \mathbf{m}_{k0}{}^0|n')(n'|\sum_k \mathbf{m}_k{}^0|n)],$$

$$\xi_3 = -(4/3)C\,\mathrm{Re}\sum_{n=0}^{g-1}\sum_{n'=n+1}^{g}[\exp(-E_n/kT) - \exp(-E_{n'}/kT)][1/(E_{n'}-E_n)] \times[(n|\textstyle\sum_k \mathbf{m}_{k0}{}^0|n')\cdot(n'|\sum_k \mathbf{m}_{kl}{}^0|n)].$$

Measurements of the diamagnetic susceptibilities of the cobalt molecules such as $K_3Co(CN)_6$ for which the magnetic shielding is temperature dependent[8] would be of great interest, as Van Vleck[14] has also pointed out. The diamagnetic susceptibility would presumably be temperature dependent as well, with the nature of the dependence being given by (14), in contrast to the usual observations that such susceptibilities are temperature independent. In fact, (14) provides an expression for the temperature dependence of the susceptibility that is frequently called the temperature independent paramagnetism.

[11] U. Liddel and N. F. Ramsey, J. Chem. Phys. (to be published).
[12] J. H. Hildebrand and R. L. Scott, *Solubility of Non-Electrolytes* (Rheinhold Publishing Corporation, New York, 1950), p. 192.
[13] O. Redlich and A. T. Kister, J. Chem. Phys. **15**, 854 (1947).
[14] J. H. Van Vleck, Physica **17**, 281 (1951).

Letters to the Editor

PUBLICATION of brief reports of important discoveries in physics may be secured by addressing them to this department. The closing date for this department is five weeks prior to the date of issue. No proof will be sent to the authors. The Board of Editors does not hold itself responsible for the opinions expressed by the correspondents. Communications should not exceed 600 words in length and should be submitted in duplicate.

Size Effects and Diamagnetism in Finite Systems

M. F. M. OSBORNE AND M. C. STEELE
Naval Research Laboratory, Washington, D. C.
(Received February 27, 1952)

DINGLE[1] has reported a diamagnetism for a finite system of free electrons in weak fields $[H<c(2m\zeta)^{\frac{1}{2}}/eR\sim 5/R]$ in contradiction to a conclusion previously inferred by one of us.[2] We have examined this problem for a cylindrical container using the methods of lattice point problems in the theory of numbers,[3] and have been able to verify the order of magnitude of Dingle's results, thus resolving this controversy.

We have also examined by the same methods the case for strong fields ($H\gtrsim 5/R$) and find, in addition to the Landau and de Haas-van Alphen terms, a non-oscillatory diamagnetic moment per unit volume,

$$M/V=K(2m)^{1/2}e^{3/2}\zeta^{1/2}/Rh^{1/2}c^{3/2}H^{1/2}, \qquad (1)$$

where $K\sim 0.02$, ζ is the Fermi energy, R is the radius of the cylinder in cm, and H is the magnetic field strength in gauss.

This term arises from the quantization of orbits which intersect the walls of the container, and hence, may be called a surface diamagnetism. It approaches the Dingle diamagnetism as $H\to 5/R$. Quantization of these orbits also contributes oscillatory terms to the moment which are in most cases negligible compared to the de Haas-van Alphen effect.

The moment in Eq. (1) is larger than the Landau moment for properly chosen fields and specimen sizes, and hence, may well be observable. Thus if $R\sim 1$ cm, and $\zeta\sim 1$ volt, this moment is $\geq$ the Landau moment for $H\lesssim 300$ gauss. If $R\sim 10^{-3}$ cm, this moment is $\geq$ the Landau moment for $H\lesssim 10{,}000$ gauss. Thus it should be possible to observe this effect.

Experimental evidence[4] on the size effect in the diamagnetism of small unoxidized particles appears to be not in agreement with this or Dingle's theory. However, for the applicability of the above calculations, it is essential that the particles be electrically insulated from each other, so that the wave functions are truly bounded by the surface of the particles.

Details of these calculations will be reported subsequently.

[1] R. B. Dingle, Phys. Rev. **82**, 966 (1951).
[2] M. F. M. Osborne, Phys. Rev. **81**, 147 (1951).
[3] M. C. Steele, Proc. of the International Conference on Low Temperature Physics, Oxford, August 22–28, 1951, p. 137.
[4] H. Lessheim, Current Science **5**, 119 (1936).

Hyperfine Structure of the Spectra of Gadolinium and Zirconium

S. SUWA
Institute of Science and Technology, Komaba, Meguro-ku, Tokyo, Japan
(Received February 27, 1952)

THE hyperfine structure of the gadolinium spectrum in the visible region was studied, using a water-cooled hollow cathode discharge tube (the cathode contained gadolinium oxide) and a Fabry-Pérot etalon; and the previous measurement of Klinkenberg[1] was greatly improved and extended.

TABLE I. Hyperfine structure of the spectrum of gadolinium.

Type	λ(A)	Combination*		Hfs (10^{-2} cm^{-1}) a	b	c	d
A	4401.8	$4f^7 6s^2 5d a^9D_3-$	y^9F_4	0(6)	59(6)	116(10)	161(4)
	4373.8	$4f^7 6s^2 5d a^9D_4-$	y^9F_5	0(6)	58(6)	111(10)	157(4)
B	4435.1	——		0(7)	74(8)	143(10)	192(3) 233(2)
	4008.3	$4f^7 6s^2 5d a^9D_3-4f^7 5d^2 6p z^{11}G_3$		0(6)	79(6)	150(10)	207(3)
	3974.8	$4f^7 6s^2 5d a^9D_4-4f^7 5d^2 6p z^{11}G_7$		0(6)	87(6)	160(10)	223(3)
C	5617.9	$4f^7 6s^2 5d a^9D_2-4f^7 6s 5d 6p e^9F_2$		0(8)	37(10)	72(10)	115†
	5155.8	$4f^7 6s 5d^2 a^{11}F_3-4f^7 5d^2 6p z^{11}G_7$		0(8)	41(10)	81(10)	129†
	5103.4	$4f^7 6s 5d^2 a^{11}F_7-4f^7 5d^2 6p z^{11}G_8$		0(8)	42(10)	82(10)	130†
	5015.0	$4f^7 6s 5d^2 a^{11}F_8-4f^7 5d^2 6p z^{11}G_9$		0(8)	43(10)	86(10)	143†

* See reference 2.
† The d-component of type C appeared as a weak tail. Its edge on the high frequency side is shown.

Hyperfine structures of some Gd I lines[2] that were measured in the present investigation are listed in Table I. Numbers in parentheses indicate visually estimated intensities. The lines of type A were observed to consist of four components, of which a, b, and d were assigned to Gd^{160}, Gd^{158}, and Gd^{155}, respectively, while c was regarded as the result of superposition of the Gd^{157} and Gd^{156} components; in these lines both of the splittings of the Gd^{157} and Gd^{156} components are very small. In the lines of type B the hyperfine structures were similar to those of A-type lines, except that in the former type the d-component showed a measurable broadening. In the lines of type C, the d-component appeared as a weak tail broadened continuously from c towards higher frequency side and unresolved weak background was also observed between the components b and c; a, b, and c were interpreted as caused by the even isotopes Gd^{160}, Gd^{158}, and Gd^{156}, respectively, and the weak background and the tail as caused by the odd isotopes Gd^{157} and Gd^{155}.

As to the isotope shift, the ratios

$$r_1=\Delta\nu(Gd^{157}-Gd^{160})/\Delta\nu(Gd^{158}-Gd^{160})=1.94\pm 0.25$$

and

$$r_2=\Delta\nu(Gd^{155}-Gd^{160})/\Delta\nu(Gd^{158}-Gd^{160})=2.71\pm 0.02$$

were determined from the structure of λλ4401.8 and 4373.8. The distances $b-a$ in several lines show that the isotope shift per one 6s-electron in the neutral atom per addition of two neutrons[3] is 0.046 ± 0.005 cm^{-1} for $Gd^{158}-Gd^{160}$.

In λ5015.0 ($4f^7 6s 5d^2 a^{11}F_8-4f^7 5d^2 6p z^{11}G_9$), which is most suited for determining the nuclear moments of the odd isotopes, intensity distribution of the components caused by the odd isotopes indicates that the spins of both isotopes are $\frac{3}{2}$ or greater. Assuming that the above-mentioned ratios r_1 and r_2 are the same in all lines with respect to the centers of gravity of the components of the odd isotopes, the total splittings for Gd^{157} and Gd^{155} in λ5015.0 were estimated. Neglecting any splitting of the initial term, and using the Goudsmit-Fermi-Segrè formula for the 6s-electron in the term $4f^7 6s 5d^2 a^{11}F_8$, a rough estimate of the magnitudes of the magnetic moments of Gd^{157} and Gd^{155},

$$|\mu(Gd^{157})|=0.3\pm 0.2 \text{ nm}, \quad |\mu(Gd^{155})|=0.25\pm 0.15 \text{ nm},$$

was obtained, although the signs of the magnetic moments and the spins for both isotopes could not be determined.

In the study of the hyperfine structure of the spectrum of Zr I, the cathode contained powdered zirconium and was cooled with liquid air. In some lines, shift of the components caused by the even isotopes Zr^{90}, Zr^{92}, and Zr^{94} was detected, although complete resolution was not attained owing to the Doppler broadening of the components. For example, in the line λ4081.2 ($4d^3 5s^2 F_6-4d^3 5p z^5 D_4$)[4] the distance $Zr^{90}-Zr^{94}=0.020\pm 0.003$ cm^{-1} was measured, the Zr^{90} component lying on the higher frequency side.

The hyperfine structure of Zr^{91}, which isotope is known[5] to have a spin of 5/2, was also observed in some lines. Recently Arroe,[6] using an enriched isotope of Zr^{91}, measured the hyperfine

splittings of several terms. Using Arroe's data for the interval factor $A(4d^3 5s^6F_8) = -0.0078$ cm^{-1} (which are naturally more accurate than the present measurements), the value $a(5s) = -0.078$ cm^{-1} was obtained; and putting this into the Goudsmit-Fermi-Segrè formula, the value of the magnetic moment

$$\mu(Zr^{91}) = -1.1 \pm 0.3 \text{ nm}$$

was obtained.

The writer wishes to express his sincere thanks to Professor K. Murakawa for kind consultations. He would also like to express his appreciation for the kindness of Professor J. E. Mack who supplied the very pure sample of gadolinium which was used in the present work.

[1] P. F. A. Klinkenberg, Physica **12**, 33 (1946). Recently P. Brix and H. D. Engler, Naturwiss. **38**, 214 (1951), have studied the isotope shift in the Gd I spectrum, and found that the complex $4f^7$ contributes nothing to the isotope shift.
[2] The Gd I and Gd II spectra were classified by H. N. Russell, J. Opt. Soc. Am. **40**, 550 (1950).
[3] K. Murakawa and J. S. Ross, Phys. Rev. **83**, 1272 (1951).
[4] C. C. Kiess and H. K. Kiess, J. Research Natl. Bur. Standards **6**, 621 (1931).
[5] O. H. Arroe and J. E. Mack, Phys. Rev. **76**, 873 (1949).
[6] O. H. Arroe, *Studier over Spektrallinisers Struktur Med Anvendelse af Koncentrerede Isotoper* (Copenhagen, 1951).

Radiations from Ne^{19} and Na^{21}†

G. Schrank and J. R. Richardson
University of California, Los Angeles, California
(Received March 3, 1952)

THE half-lives, β-spectra, and accompanying γ-rays have been measured for the positron emitters Ne^{19} and Na^{21} with a 180° beta-ray spectrometer and a NaI crystal gamma-ray spectrometer. Calibration of the former was accomplished with the Cs^{137} conversion line and the 2.36-Mev β^+ spectrum[1] of Zn^{65}, while Na^{22} and Co^{60} were used with the latter. The samples were prepared from the reactions $F^{19}(p, n)Ne^{19}$ in BaF and CsF and $Mg^{24}(p, \alpha)Na^{21}$ in magnesium metal.

By means of a special probe it was possible to transfer the sample from the cyclotron to the spectrometer in about 30 seconds. With the β-spectrometer counting rate being recorded automatically the sample was allowed to decay for about two half-lives, the spectrometer field changed to a second value, and the sample then allowed to die out. These two decay rates were plotted on log paper using the previously determined half-life and so two relative values of momentum *vs* activity were obtained. Returning to a fiducial field value with each sample allowed data for a complete momentum plot to be accumulated.[2] It is clear that this method is useful with short-lived activities for which: (1) monitoring the total activity is unsatisfactory because the method of production does not insure the same ratio of "desired" to total activity for each sample and; (2) the time necessary to change the spectrometer field $\gtrsim$ the half-life.

Ne^{19} and Na^{21} exhibited half-lives of 18.5±0.5 sec and 22.8±0.5 sec, respectively, while the allowed Kurie plots gave end points of 2.18±0.03 Mev and 2.50±0.03 Mev, respectively.[3-7] Because of the necessity of source thickness the Kurie plots curved upward at lower energies and so masked possible low energy β^+ groups. Consequently, a search for accompanying γ-rays was made with a NaI crystal spectrometer. Whereas Ne^{19} was exposed to the crystal for about three half-lives as soon after production as possible, it was necessary to wait about 60 sec after bombardment before exposing Na^{21} in order to allow the competing shorter Al activities to die out. Several photographs with different numbers of exposures on each showed the 0.51-Mev annihilation line superimposed upon the expected continuous γ-distribution, but no line was detected above 0.51 Mev for either Ne^{19} or Na^{21}.

Comparison of ft values for this series of transitions ($T_z = -\frac{1}{2} \rightarrow T_z = +\frac{1}{2}$) shows most of them to be in the range 3 to 4×10^3. While Na^{21} falls within this range Ne^{19} with $Z=10$ is the notable exception[8] of the group having the lowest ft value at 1.8×10^3. Since differences in radial distributions are not expected to cause this much variation here, the proper choice of ground states from the shell models together with tensor or axial interaction should eliminate this difference. An experimental point at $Z=20$ would be of interest.

† Assisted by the joint program of the ONR and AEC.
[1] Huber, Medicus, Preiswerk, and Steffen, Helv. Phys. Acta **20**, 495 (1947).
[2] G. Schrank and J. R. Richardson, Phys. Rev. **81**, 660 (1951).
[3] E. Pollard and W. W. Watson, Phys. Rev. **58**, 12 (1940).
[4] White, Delsasso, Fox, and Creutz, Phys. Rev. **56**, 512 (1939).
[5] L. Rosenfeld, *Nuclear Forces* (Interscience Publications, New York, 1948), p. 377.
[6] Blaser, Boehm, Marmier, and Scherrer, Helv. Phys. Acta **24**, 465 (1951).
[7] H. B. Willard and J. K. Bair, Bull. Am. Phys. Soc. **27**, No. 1, 54 (1952).
[8] A. M. Feingold, Revs. Modern Phys. **23**, 10 (1951).

Crystal Structure of the Ferroelectric Phase in $PbZrO_3$ Containing Ba or Ti

Gen Shirane* and Sadao Hoshino
Tokyo Institute of Technology, Oh-okayama, Tokyo, Japan
(Received February 13, 1952)

A RECENT investigation[1] of $(Pb92.5\text{-}Ba7.5)ZrO_3$ has shown that this solid solution transforms, with rising temperature, from an antiferroelectric phase to a ferroelectric one at 175°C and further to a paraelectric phase at 200°C. The present authors have been studying the crystal structure of this ferroelectric phase in the same ceramic that was used for the previous dielectric study.

A series of powder photographs with rising temperature was taken with Cu $K\alpha$ radiation by using a high temperature camera of radius 5.5 cm. The Debye lines show pseudo-cubic features in the whole temperature range. The high order reflection lines in the photograph taken at 190°C show very small but definite line splittings: among them the (422) and (332) groups can be effectively used for the structure determination. In order to explain these line splittings, three possible lattice types are considered, namely, tetragonal, orthorhombic, and rhombohedral, corresponding to modifications of the perovskite structure. It has been proved that all of the multiplets can be well explained by assuming a rhombohedral lattice with $a = 4.153$A and $\alpha = 89°\,51'$. This conclusion is strongly supported by the behavior of the (400) group, which shows no multiplet structure besides the single $K\alpha_1 K\alpha_2$ doublet.

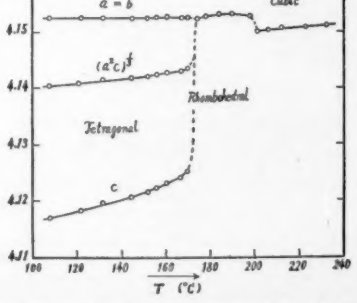

FIG. 1. Lattice spacing *vs* rising temperature for $(Pb92.5\text{-}Ba7.5)ZrO_3$.

Attention should be called here to the remarkable intensity anomalies observed in this photograph. Firstly, the relative intensities of reflections with odd values of $(h^2+k^2+l^2)$ to those with even values are anomalously large when compared with the case in the cubic phase. Secondly, we found a peculiar intensity relation among a certain line group; for example, the intensity of the $(430)(\bar{4}30)$ reflections is much stronger than that of the $(\bar{4}30)(4\bar{3}0)$ reflections, whereas their intensity ratio should be equal if the atoms occupied the special positions in the unit cell. These anomalies can be well understood when we assume that Zr (or Pb) ions are displaced along the [111] direction. This displacement is the most plausible one to be expected in the ferroelectric rhombohedral lattice. Such a structure is similar to that observed in $BaTiO_3$ below $-70°C$.[2] This conclusion seems to be rather unexpected, because all of the other perovskite type ferroelectrics, such as $BaTiO_3$,[2] $PbTiO_3$,[3] and $KNbO_3$,[4] show lattice changes in the following sequence for falling temperature: cubic—tetragonal —orthorhombic—rhombohedral.

The temperature change of the lattice spacing of $(Pb_{92.5}Ba_{7.5})ZrO_3$ was calculated from the (510) group and is shown in Fig. 1. Below 175°C the structure has a tetragonal lattice with $c/a<1$, giving superstructure lines like those observed in pure $PbZrO_3$. These superstructure lines disappear at the antiferroelectric to ferroelectric transition at 175°C.

It has been known that $Pb(Zr\text{-}Ti)O_3$ compositions show a similar ferroelectric phase[5] to that observed in $(Pb\text{-}Ba)ZrO_3$. In the previous x-ray study of $Pb(Zr_{95}\text{-}Ti_5)O_3$,[6] however, we were unable to determine the structure of this ferroelectric phase, though we found very small splittings of the Debye lines. A re-examination of this structure was carried out with a high purity specimen of the same composition, which is ferroelectric between 150° and 230°C. The structure of this ferroelectric phase has now turned out to be also rhombohedral, with $a=4.143$A and $\alpha=89°\,51'$ at 200°C. We found, in this phase also, similar intensity anomalies to those observed in the corresponding phase in $(Pb_{92.5}\text{-}Ba_{7.5})ZrO_3$.

We wish to express our sincere thanks to Professor S. Miyake and Professor Y. Takagi for very illuminating suggestions and also to Mr. E. Sawaguchi and Mr. K. Suzuki for their helpful discussions.

* Now at Department of Physics, Pennsylvania State College, State College, Pennsylvania.

[1] G. Shirane, Phys. Rev. **84**, 854 (1951).
[2] H. F. Kay and P. Vousden, Phil. Mag. **40**, 1019 (1949).
[3] G. Shirane and S. Hoshino, J. Phys. Soc. Japan **6**, 265 (1951).
[4] E. A. Wood, Acta Cryst. **4**, 353 (1951).
[5] G. Shirane and A. Takeda, J. Phys. Soc. Japan **7**, 5 (1952).
[6] Shirane, Suzuki, and Takeda, J. Phys. Soc. Japan **7**, 12 (1952).

$\beta-\gamma$ Polarization Correlation in Sb^{124}

ROBERT STUMP
Department of Physics and Astronomy, Kansas University, Lawrence, Kansas
(Received March 3, 1952)

IT is well known that there is an angular correlation between the direction of the highest energy β-particle (2.29 Mev) and the succeeding γ-ray (0.60 Mev) in the decay of Sb^{124}.[1-3] As a consequence of the existence of this correlation, it may be shown that the γ-ray will exhibit a polarization correlation. The $\beta-\gamma$ angular correlation depends upon the spins of the nuclear states involved in the decay, and upon the matrix element of the β-decay. On the other hand, the $\beta-\gamma$ polarization correlation depends only on the observed angular correlation, and the parity change (yes or no) of the γ-transition. Thus a measurement of the polarization leads to a unique assignment for the parity of the level from which the 0.60-Mev γ-ray is emitted.

In general, if the angular correlation has the form $W(\theta)=1+\alpha\cos^2\theta$ then the γ-ray emitted at $\theta=\pi/2$ (i.e., perpendicular to the direction of the preceding β) will be polarized. The polarization is given in terms of the number of quanta polarized in the θ-direction, J_θ, and the number in the ϕ-direction, J_ϕ. Then $J_\theta/J_\phi=(1+\alpha)/(1-\alpha)$ in case the γ-radiation is dipole or quadrupole radiation with no change in parity, and the reciprocal of this if there is a change in parity.[4] Hence, to determine the parity change it is necessary to know only the angular correlation coefficient α, and whether J_θ/J_ϕ is experimentally greater or less than one.

The observation of the polarization correlation of Sb^{124} was made with an arrangement similar to that of Metzger and Deutsch,[5] with the source and β-detector in a vacuum chamber to avoid the effect of scattering of the β-particles. The source was a thin film of Sb^{124} (supplied by Oak Ridge National Laboratory) which was evaporated on an aluminum backing, then stripped off and mounted on Nylon. The detector was a thin crystal of anthracene connected by a Lucite light pipe to a photomultiplier tube outside the chamber.

The polarization detector consisted of a scintillation counter with a large anthracene crystal to scatter the radiation by Compton collision, and two sodium iodide scintillation counters to detect the scattered radiation. The polarization of the γ-ray was determined by the anisotropy of the Compton scattering from the anthracene crystal.

The measurement of the polarization correlation consisted of determining the rate of triple coincidences between the β-particle, the γ-, and the scattered γ-rays, for two scattering directions. The triple coincidence rate with the scattering direction perpendicular to the plane of the β-particle and γ-ray is N_θ. The rate with the scattering direction in the plane of the β-particle and γ-ray is N_ϕ. The angle between the β and γ was always $\pi/2$. From the anisotropy in scattering predicted by the Klein-Nishina formula it is obvious that N_θ/N_ϕ has the same significance (although not the same size, because of inefficiency in the polarization detector) as does the term J_θ/J_ϕ in determining the parity change.

Since the decay of Sb^{124} is complex, aluminum absorbers were placed directly in front of the β-detector to eliminate the low energy β-particles which do not contribute to the correlation.[3] The ratio of the observed triple coincidence rates with ~ 200 mg/cm^2 of aluminum was $N_\theta/N_\phi=0.93\pm0.04$ and with ~ 400 mg/cm^2 of aluminum was $N_\theta/N_\phi=0.89\pm0.11$. Since the angular correlation coefficient $\alpha\simeq-0.4$, these data indicate that the γ-transition must occur with no change in parity. This result is in agreement with the decay scheme proposed by Stevenson and Deutsch to explain their angular correlation results.[3] It is also in agreement with the empirical rule of Goldhaber and Sunyar[6] that the first excited state of an even-even nucleus has spin two, even parity.

Measurements of the $\beta-\gamma$ polarization correlation are now being made on other nuclei in whose decay a $\beta-\gamma$ angular correlation has been observed.

[1] S. L. Ridgway, Phys. Rev. **78**, 821 (1950).
[2] J. R. Beyster and M. L. Wiedenbeck, Phys. Rev. **79**, 169 (1950).
[3] D. T. Stevenson and M. Deutsch, Phys. Rev. **83**, 1202 (1951).
[4] D. R. Hamilton, Phys. Rev. **74**, 782 (1948).
[5] F. Metzger and M. Deutsch, Phys. Rev. **78**, 551 (1950).
[6] M. Goldhaber and A. W. Sunyar, Phys. Rev. **83**, 906 (1951).

New Technique for the Determination of Photonuclear Cross Sections*

LESTER L. NEWKIRK†
Institute for Atomic Research and Department of Physics, Iowa State College, Ames, Iowa
(Received February 21, 1952)

A NEW technique for measuring photonuclear cross sections has been developed and applied to the $Cu^{63}(\gamma,n)Cu^{62}$ and $C^{13}(\gamma,n)C^{11}$ reactions up to 60 Mev. Induced radioactivity is employed to monitor the synchrotron beam. A mechanical device, called an oscillator, slides a test sample and a similar monitor

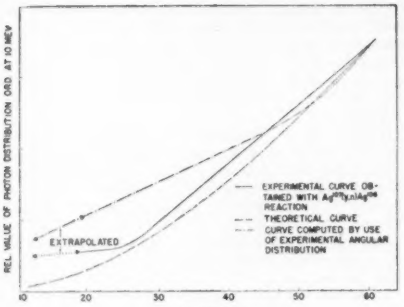

FIG. 1. Comparison of the theoretical and the experimental photon distributions. For each distribution, the relative photon ordinate values at a photon energy of 10 Mev have been plotted against the corresponding electron energy values.

sample alternately into the beam so that while one sample is being irradiated the other is shielded from the beam by a lead shield. As the oscillator changes position, the electron energy of the synchrotron is switched alternately between two values. After many oscillations have occurred, there will be two radioactive samples available for counting, each having been irradiated at different electron energies. From one run to another, the monitor sample is always irradiated at the same electron energy, but the test sample is irradiated at various electron energies. Thus, if irradiation and counting conditions are unchanged from run to run, any random or long period changes in beam intensity will show up in the monitor sample activities n_m.

All test sample activities are corrected to the values they would have had if a standard-beam intensity, as represented by one of the n_m, had been present while they were being irradiated. The ratio of the test sample activity to the monitor sample activity is plotted against electron energy to give a relative activation curve corresponding to constant injection conditions.

The photon distribution proposed by Schiff[1] was used, but the ordinates of the respective spectra of this distribution require adjustment. This was done in the present work by obtaining with the oscillator an activation curve for a reaction whose cross section is known. The $Ag^{107}(\gamma, n)Ag^{106}$ reaction[2] was used for this purpose here, although other "secondary standards" may prove useful in later applications of this method. In order to minimize

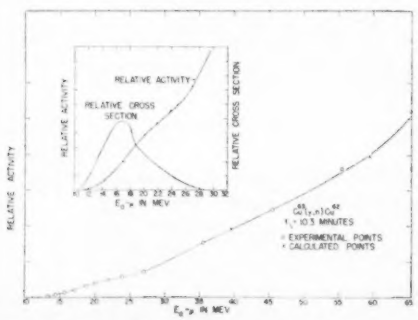

FIG. 2. Relative activation curve and cross-section curve for the $Cu^{63}(\gamma, n)Cu^{62}$ reaction. The cross section is plotted as a function of the photon energy and the activation data are plotted as a function of the electron energy of the synchrotron.

the effects of possible errors in the silver cross section upon the adjustment of the photon distribution, activation data were obtained from 60 Mev down only to 19.5 Mev, since below this energy the silver cross section differs appreciably from zero. A plot of the relative photon ordinate at 10 Mev against the corresponding electron energies is shown in Fig. 1.

In order to analyze the activation curves obtained for the $Cu^{63}(\gamma, n)Cu^{62}$ and $C^{12}(\gamma, n)C^{11}$ reactions (Figs. 2 and 3), it was necessary to extrapolate the photon ordinate curve down to 12.5 Mev. The cross sections computed by the use of such an extrapolated curve were found to be affected only slightly by the manner of performing the extrapolation. For this reason, the extrapolation is believed to be a good one and was found to yield results in good agreement with work done elsewhere.[1-3] The adjusted distribution may be used to analyze any activation curve obtained with the oscillator.

The relative cross sections for these reactions were computed by the total spectrum method of Johns *et al.*[1] (photon energy intervals of 1-Mev width were used). If an absolute cross section were desired, it would be necessary to make only one additional run under absolute monitoring and counting conditions. To determine if the cross sections obtained here are consistent with activation results at higher energies, the cross sections were used

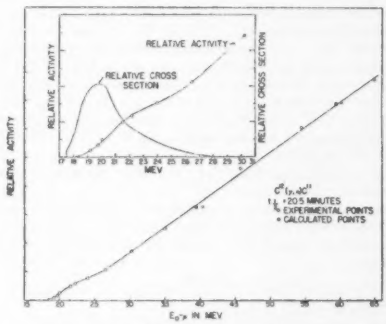

FIG. 3. Relative activation curve and cross-section curve for the $C^{12}(\gamma, n)C^{11}$ reaction. The cross section is plotted as a function of photon energy and the activation data are plotted as a function of the electron energy of the synchrotron.

to calculate activation results at electron energies of 39.5 Mev and 59.5 Mev. The results are plotted in Figs. 2 and 3 and show good agreement with the experimental activation results.

The shape of the experimental curve shown in Fig. 1 may, in itself, be of some interest. For comparison, a theoretical curve for the photon intensity at 10 Mev is also shown. The theoretical curve was computed by use of the Bethe-Heitler[4] integrated cross section, multiplied by the fraction of the total bremsstrahlung intensity striking the sample as computed from the theoretical angular distribution given by Schiff.[5] Experimental intensity-angle distribution results obtained here by the activation of copper were also used to determine a curve for comparison with the theoretical one (see Fig. 1). The discrepancy between the two computed curves is caused partly by the fact that at the lower energies the experimental distributions were narrower than the theoretical ones, as shown by a comparison in which the respective ordinate values of the theoretical and experimental distributions were normalized to agree at 0°. In addition, the calculation involving the experimental angular distribution was complicated by the presence of small secondary photon beams to either side of the main beam. The disagreement of the adjusted photon distribution, as obtained by the silver reaction, with the theoretical distribution is caused partly by the factors mentioned

above. In addition, such effects as loss of electrons in the orbit and multiple traversals of the target by some electrons may be responsible for some of the disagreement.

When it occurs, the loss of a substantial number of electrons in the orbit is detected by a photomultiplier tube, and it appears as "grass" on the oscilloscope at the control desk. Activation data were taken only when the loss of electrons appeared to be inappreciable, as indicated by a negligible amount of grass.

It is a sincere pleasure to acknowledge the cooperation, during the course of the experiment, of Dr. L. Jackson Laslett who originally suggested the method used to monitor the beam. Appreciation is also extended to Mr. Don Steward and Mr. Philip Phipps for their assistance in preparing the table of photon values.

* Contribution No. 169 from the Institute for Atomic Research and Department of Physics. Work performed in the Ames Laboratory of the AEC.
† Now at Hughes Aircraft Company, Culver City, California.
[1] Johns, Katz, Douglas, and Haslam, Phys. Rev. **80**, 1062 (1950).
[2] B. C. Diven and G. M. Almy, Phys. Rev. **80**, 407 (1950).
[3] Haslam, Johns, and Horsley, Phys. Rev. **82**, 270 (1951).
[4] H. Bethe and W. Heitler, Proc. Roy. Soc. (London) **A146**, 83 (1934).
[5] L. I. Schiff, Phys. Rev. **70**, 87 (1946).

The Role of Turbulence in the Evolution of the Universe

G. GAMOW
George Washington University, Washington, D. C.
(Received February 25, 1952)

IT can be considered now as an unquestionable truth that "*from one to ten thousand million years ago, the matter of the (known) spiral nebulae was compressed into a relatively restricted space, at the time the cosmic processes had their beginning*" and that during that stage "*the density, pressure, and temperature of matter must have reached absolutely enormous proportions*" since "*only under such conditions can we explain the formation of heavy nuclei and their relative frequency in the period system of elements.*"[1]

A detailed study of the conditions obtained during the early stages of the expansion process[2] leads to the conclusion that the temperature and density at the age t (in seconds) were given by the expressions:

$$T=1.5\times10^{10}/t^{\frac{1}{2}}\text{°K}, \quad \rho=\rho_0/t^3, \tag{1}$$

where ρ_0 is a constant to be adjusted by considering the nuclear building-up processes and has a numerical value of the order of magnitude 10^{-3} g cm^{-3} sec^3.

It is important to notice that during these early stages of expansion, the mass density of radiation quite considerably exceeded that of matter. Thus, for example, we find from Eq. (1) that at $t=900$ sec (15 min), $\rho_{rad}\cong0.5$ g cm^3 and $\rho_{mat}\cong10^{-8}$ g cm^3. Under these conditions, when radiation was predominant, matter was deprived of any possibility of condensing under the action of gravitational forces. It is, thus, reasonable to assume that the originally uniform gaseous material could start to break up into individual gas clouds (protogalaxies) only during the era when the density of radiation sank below the density of matter. The observational fact that the present distances between the neighboring galaxies exceed their geometrical dimensions by a factor of about a hundred suggests that the break-up must have taken place at a time of about one hundredth of the present age, and that at that time the mean matter density of the universe was comparable with the present matter density, 10^{-31}, inside of the galaxies. Using $t=3\times10^7$ years$\cong10^{15}$ sec in Eq. (1), we find $T\cong500$°K and $\rho_{rad}\cong10^{-28}$. This is indeed comparable with the present intragalactic density as well as with the result given by the density formula in Eq. (1). In order to find the sizes and masses of condensations we must insert the values of T and ρ for $t=10^{15}$ sec into the well-known Jeans' formula for gravitational instability. By doing so we find for the diameters and masses of condensations the values of $\cong10^6$ light years and $\cong10^9$ sun masses, which are in agreement with the hypothesis that the original condensations were the gaseous protogalaxies. It cannot be emphasized too strongly that all the numerical values derived above are off by an order of magnitude or even more from the actually observed values. This can easily be due, however, to the highly preliminary nature of the calculations.

An important point in applying the classical Jeans' formula to our case is that it is derived specifically for a nonexpanding gas, whereas our model is rapidly expanding. This point was investigated by the author in collaboration with Drs. S. Ulam and N. Metropolis (unpublished), with the unfortunate result that the expected condensations would never form in the originally homogeneous material, unless there are some additional physical factors favoring large-scale fluctuations of density. The attempts to provide for such an additional factor by considering the effect of radiation pressure (similar to the Spitzer-Whipple theory of stellar origin) have also failed. Thus, it seems at present that the only way of understanding the formation of gaseous protogalaxies lies in the assumption of extensive turbulent motion in the primordial expanding material.[3] Such turbulent motion would result in strong density fluctuations leading to compression eddies of all different sizes in accordance with Kholmogoroff's spectral law of turbulence. If such an assumption is made, we can easily see how gravity forces, which become of importance as soon as the radiation density sinks below the matter level, could grab the condensation eddies of suitable sizes to form the protogalaxies of proper masses and geometrical dimensions.

The existence of such turbulent motion in the primordial material of the universe is, in fact, strongly suggested by the recent studies by H. Shapley and C. D. Shane of the space distribution of galaxies in the observed part of the universe.

Although Reynold's number for the universe is always sufficiently large to expect the presence of turbulent motion, it is, however, difficult to see how such a motion could originate in a uniformly expanding homogeneous material. Thus, it may be well to introduce the primordial turbulence on a postulatory basis along with the original density of matter and the rate of expansion.

[1] Address by Pope Pius XII to the Pontifical Academy of Sciences on November 22, 1951 (Tipografia Poliglotta Vaticana, Rome, 1951).
[2] G. Gamow, Phys. Rev. **70**, 572 (1946); Alpher, Bethe, and Gamow, Phys. Rev. **73**, 803 (1948); G. Gamow, Nature **162**, 680 (1948); R. Alpher and R. Herman, Phys. Rev. **84**, 60 (1951).
[3] C. F. von Weizsäcker, Astrophys. J. **114**, 165 (1951).

Thermal Conductivity of Carbons and Graphite

S. MROZOWSKI
Department of Physics, University of Buffalo, Buffalo, New York
(Received February 25, 1952)

THE purpose of this note is to direct attention to some interesting characteristics of materials commonly known under the name of carbons, which make them in a certain sense unique among nonmetallic thermal conductors. In spite of their great practical importance they have not yet been systematically studied. The best available data are those of Powell and Schofield;[1] the two heavy curves in Fig. 1 represent the temperature dependence of the conductivity for polycrystalline graphite (G) and for a baked carbon (B) as roughly obtained from their work. The graphite curve is extended to lower temperatures following the results of Buerschaper.[2] The room temperature conductivity of polycrystalline graphite is definitely smaller than half of that of a single graphite crystal along the graphitic planes. In fact Pirani and Fehse[3] found for carbon filaments with well-aligned crystallites of graphite a conductivity higher than that of copper! Although the anisotropy of a single crystal certainly is not as large as for the electric conductivity ($\rho_\perp/\rho_{\parallel}\sim10^6$), the main heat transfer occurs probably for polycrystalline materials in a zigzag path along the graphitic planes. The curve (G) is of the general type observed for nonmetallic crystals, the conduction being chiefly the result of transfer of elastic vibrations via valence bonds, with a negligible contribution from the conduction by the free

electrons (except possibly in the highest temperature range, where the curve (G) seems to flatten out and even rise).

Recently Mizushima and Okada[4] pointed out that the conductivity of baked carbons (B) is to be interpreted similarly to the conductivity of glasses.[5] The mean free path Λ of the elastic vibrations being limited by the size of the microcrystallites Λ_0 and being consequently independent on temperature, the conductivity κ has to vary proportionally to the specific heat C_v (according to Debye's formula $\kappa = \frac{1}{3} \cdot C_v \cdot v \cdot \Lambda$). The curve ($B$) seems to be reasonably similar in shape to the specific heat curve obtained by Magnus.[6]

It is expected that at very low temperatures a similar region should be observed for polycrystalline graphite. In general, for any sample, as long as the mean free path of the phonons Λ is limited by the microcrystalline dimensions Λ_0, the conductivity κ should increase proportionally to C_v. A maximum should be

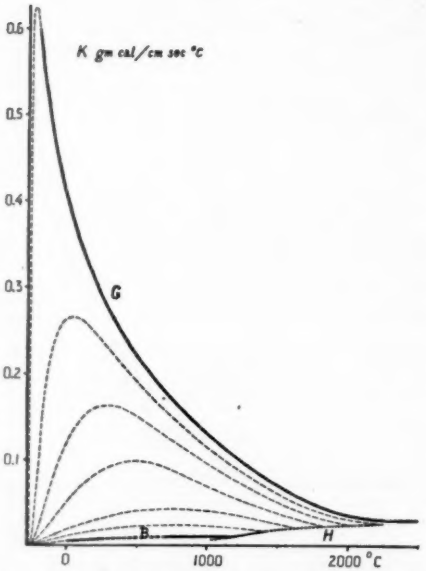

FIG. 1. Observed (continuous) and predicted (dashed) heat conductivities for variously heat-treated carbons as function of temperature. G—polycrystalline graphite, B—baked carbon, H—the heat-treatment curve.

reached at temperatures for which the lattice scattering $1/\Lambda_L$ (phonon-phonon interactions) becomes comparable to the boundary scattering $1/\Lambda_0$. For still higher temperatures the conductivity should decrease as for large nonmetallic crystals ($\kappa \sim 1/T$). This general behavior is well known from the work of de Haas and Biermasz and of Casimir. Until now maxima have been observed only at very low temperatures. Carbons, however, can be made with microcrystalline sizes ranging from 25A up to several thousands, thus making possible a study of all intermediate cases between large nonmetallic crystals and such amorphous substances as discussed by Kittel.[5] A system of expected intermediate curves has been added in Fig. 1; since the positions of the maxima are determined by the microcrystalline sizes ($T_{max} \sim 1/\Lambda_0$), it is estimated that for commercial carbons heat-treated to about 1800–2200°C ($\Lambda_0 \sim$ 100–200A), maxima should be found somewhere in the range between room temperature and 500°C.

The comparison of the low temperature part of the curve (G) (dashed) with curve (B) shows that the conductivity of baked carbons is smaller by a factor of 1000 (or more). Since crystallite sizes differ by a factor of not more than 100, and the specific heat and velocity of the waves v cannot depend very strongly on crystallite size, it is clear that in addition to the pure boundary scattering there must be present some other source of resistance to the heat flow in the baked carbons. It is easily seen that the transfer of heat from crystal to crystal is hampered by the relatively small number of valence bonds connecting the crystallites, the situation being quite similar to the case of the flow of electric current.[7] Consequently the conductivity curves do not join the graphitic curve at high temperatures, and no reliable estimate of the crystallite sizes can be made for baked carbons by application of the Debye formula.

[1] R. W. Powell and F. H. Schofield, Proc. Phys. Soc. (London) **51**, 153 (1939).
[2] R. A. Buerschaper, J. Appl. Phys. **15**, 452 (1944).
[3] M. Pirani and W. Fehse, Z. Elektrochem. **29**, 168 (1923).
[4] S. Mizushima and J. Okada, Phys. Rev. **82**, 94 (1951).
[5] C. Kittel, Phys. Rev. **75**, 972 (1949).
[6] A. Magnus, Ann. Physik **70**, 303 (1923).
[7] S. Mrozowski, Phys. Rev. **85**, 609 (1952).

The Radiation Characteristics of Cm^{240} and Cm^{241}†

G. H. HIGGINS AND K. STREET, JR.
Radiation Laboratory and Department of Chemistry, University of California, Berkeley, California
(Received February 25, 1952)

IN an attempt to extend the earlier work on the neutron deficient curium isotopes,[1,2] the isotopes of mass numbers 242, 241, and 240 were produced in varying ratios by bombarding Pu^{239} with helium ions.

Carrier-free samples of curium which had been chemically purified by ion-exchange techniques were volatilized onto platinum counting disks for study. The decay of the alpha-particles, and also the conversion and Auger electrons accompanying orbital electron capture, were followed on a windowless proportional counter. Decay of alpha-particles of specific energies was followed on the 48-channel differential pulse analyzer.[3]

When the bombardment energy was between 30 and 40 Mev, activities with three different half-lives were observed. These were the 27-day 6.25-Mev alpha-activity previously reported[1] and assigned to Cm^{240}, a 35-day 5.89-Mev alpha and electron capture activity, and the well-known 162-day 6.08-Mev alpha-activity of Cm^{242}.

Some of the curium samples which were proportionately richer in Cm^{240} were allowed to decay for known periods of time and an americium fraction was separated chemically. Samples were prepared and counted in the same manner as those of the curium. No activity other than a small amount of Am^{241} (about 0.001 percent of that present in the target material) which had followed the curium chemistry in the initial separations was detected. Thus, less than 0.5 percent of the Cm^{240} decayed by electron capture to produce the 52-hour activity of Am^{240}.

When the bombardment energy was between 25 and 28 Mev, only the 35-day and 162-day activities were observed. At these energies the $(\alpha, 2n)$ reaction would be expected to predominate, while the $(\alpha, 3n)$ should be in such low incidence that products of it would not be detected. For this reason the 35-day activity was assigned to Cm^{241}.

The ratio of the number of electron capture disintegrations to the number of alpha-disintegrations in the 5.89-Mev group was calculated to be between 360 and 460. The number of electron capture disintegrations was determined by assuming the same counting efficiency for the radiations accompanying the electron capture disintegration process of Cm^{241} as for those of U^{231},[4] and the number of alpha-disintegrations was determined from geometrical considerations, assuming 100 percent counting efficiency.

The values above indicate only the precision of the measurements, and errors in the assumed counting efficiency could change the numbers by factors of two or more. The partial alpha half-lives calculated from these branching ratios are 35 and 45 years.

While the 5.89-Mev group apparently accounts for more than 75 percent of the observed alpha-disintegrations which decay with a 35-day half-life, it seems likely from the alpha-systematics[5] that the ground-state transition energy would be between that of Cm^{242} (6.08 Mev) and Cm^{240} (6.25 Mev), but particles in this energy range are as yet unobserved.

We wish to express our appreciation to Dr. Glenn T. Seaborg for his continued interest in this work.

† This work was performed under the auspices of the AEC.

[1] Seaborg, James, and Ghiorso, *The Transuranium Elements: Research Papers* (McGraw-Hill Book Company, Inc., New York, 1949), Paper No. 22.2, National Nuclear Energy Series, Plutonium Project Record, Vol. 14B, Div. IV.
[2] K. Street, Jr., Ph.D. Thesis, University of California, 1949.
[3] Ghiorso, Jaffey, and Weissbourd, *The Transuranium Elements: Research Papers* (McGraw-Hill Book Company, Inc., New York, 1949), Paper No. 16.8, National Nuclear Energy Series, Plutonium Project Record, Vol. 14B, Div. IV.
[4] Crane, Ghiorso, and Perlman (to be published).
[5] Seaborg, Perlman, and Ghiorso, Phys. Rev. 77, 26 (1950).

Short-Range Protons from the Deuteron Bombardment of Li^6*

R. W. Gelinas and S. S. Hanna
Department of Physics, Johns Hopkins University, Baltimore, Maryland
(Received February 28, 1952)

THE 4.6-Mev state in Li^7 has been observed in the inelastic scattering of protons, deuterons, and alphas from Li^7 [1] and in the $Be^9(d, \alpha)Li^7$ reaction.[1,2] We have examined the spectrum of short-range protons from the $Li^6(d, p)Li^7$ reaction in a region corresponding to this excitation in Li^7. Thin targets of natural lithium, evaporated onto 1000A nickel foils, were bombarded with deuterons of energies 0.91 and 1.03 Mev, and the reaction products were observed at 90° and 110°. Detection was by means of nuclear plates in a magnetic spectrograph employing a second-order focus.[3] The observations reported here extend from an excitation energy of 4.30 to 4.80 Mev in Li^7.

In the first observation [Fig. 1(a)] a weak group of protons is observed in the correct location to be identified with the $Li^6(d, p)Li^7$ reaction. However, a search was made for the proton group from $N^{14}(d, p)N^{15}$, $Q=0.300\pm0.005$ Mev,[4] which would appear in this region. The observation was made with a lithium target, freshly prepared but then exposed to a pure nitrogen atmosphere. This procedure produces satisfactory nitrogen targets and the resulting nitrogen group appears in (*b*) in addition to the group attributed to lithium. Curves (*c*) and (*d*) were obtained at a lower bombarding energy, without and with a nitrogen contamination, respectively. In observation (*d*) the magnetic spectrograph was rotated to 110° to produce a further shift in energy of the proton groups. With the positive identification of the nitrogen group the relative shift in energy with angle and bombarding energy for the other group identifies it as a proton group from $Li^6(d, p)Li^7$. Each curve was obtained from a single three-inch nuclear plate, and the energy scale was determined from the deuterons scattered elastically from Li^7, which are shown (at reduced scale) in Fig. 1(c). The four observations yield an average $Q=0.410\pm0.015$ Mev for the lithium reaction and an excitation energy in Li^7 of 4.610 ± 0.020 Mev. This value agrees with our previous determination of 4.62 ± 0.02 Mev from the $Be^9(d, \alpha)Li^7$ reaction.[2] A value of $Q=0.296\pm0.015$ Mev is obtained for the nitrogen group, which agrees with the value obtained by Malm and Buechner.[4]

In all four spectra a continuous proton background is observed which is above the level expected from instrumental scattering alone. The rapid fall of the background below about 0.84 Mev in curve (*c*) is interesting in connection with a possible

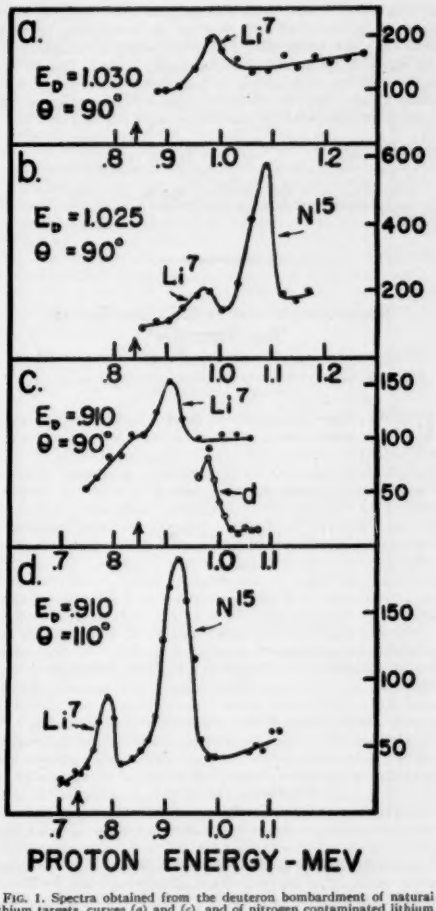

FIG. 1. Spectra obtained from the deuteron bombardment of natural lithium targets, curves (*a*) and (*c*), and of nitrogen contaminated lithium targets, curves (*b*) and (*d*). Li^7 and N^{15} designate, respectively, the $Li^6(d, p)Li^7$ and the $N^{14}(d, p)N^{15}$ reactions.

$Li^6(d, t)Li^5(p)He^4$ reaction. If the Q for $Li^5(p)He^4$ is taken as 1.8 Mev,[5] the mass of Li^5 becomes 5.01395 (instead of 5.0136[6]). This leads to a $Q=0.755$ Mev for the $Li^6(d, t)Li^7$ reaction. The minimum energy for a proton from the disintegration of a recoiling Li^5 nucleus is then 0.84 Mev for the conditions of curve (*c*). This is in excellent agreement with the observed point at which the background begins to fall, and the falling part of the curve is consistent with the great breadth of the Li^5 ground state. In curve (*d*) the minimum proton energy is calculated to be 0.73 Mev, and below this value the background is observed to decline, but the presence of the nitrogen peak makes the structure of the background above this value much less certain. In each graph the arrow marks the calculated position of minimum proton energy (neglecting the breadth of the Li^5 ground state). Unfortunately the measurements in (*a*) and (*b*) do not extend down to this value. The investigation of this background was extended to higher

energies (above 3 Mev) in an attempt to observe the upper limit which should be about 2.20 Mev for the bombarding energies used. The observations showed a general decline in background in this region of the spectrum. Unfortunately a sharp limit in the weak background could not be established in the presence of strong groups from carbon and oxygen which, if they do not actually interfere, contribute to the instrumental background.

* Assisted by a contract with the AEC.
[1] H. E. Gove and J. A. Harvey, Phys. Rev. **82**, 658 (1951).
[2] Gelinas, Class, and Hanna, Phys. Rev. **83**, 1260 (1951).
[3] D. R. Inglis, Phys. Rev. **78**, 104 (1950).
[4] R. Malm and W. W. Buechner, Phys. Rev. **80**, 771 (1950).
[5] Hornyak, Lauritsen, Morrison, and Fowler, Revs. Modern Phys. **22**, 291 (1950).

Spectroscopic Isotope Shift and Nuclear Shell Structure*

G. BREIT
Yale University, New Haven, Connecticut
(Received March 4, 1952)

FROM a theoretical standpoint views of nuclear shell structure, NSS, present the difficulty of reconciliation of a one-body, individual particle approach with the apparent existence of many particles within each other's range of force. An analogy with the theory of solids brought out by Weisskopf[1] is helpful in removing some of the contradiction. In the similar atomic electron problem the exclusion principle plays an important role, as in Weisskopf's explanation; in addition the geometrical relations, which make orbits that are added with higher Z have larger radii, also matter, producing an ordering according to values of the principal quantum number n. In the present note it is speculatively considered whether the centrifugal barrier associated with high values of the azimuthal quantum number L contributes to the possibility of assigning the usual shell structure quantum numbers as reasonably "good" quantum numbers. The considerations are based on empirical evidence from the spectroscopic isotope shift, SIS, which shows marked irregularities at the closure of nuclear neutron shells.[2] The recent finding of an anomaly in the addition of two neutrons after the completion of the neutron number 126 substantiates the view[3] that magic numbers and anomalies in the SIS are intimately connected, as mentioned by Kopfermann and Brix themselves.[2] A way of correlating the facts which appears adequate for explaining the apparent goodness of the NSS quantum numbers is as follows: (A) It is supposed that there exists a nuclear core[4] and that for even Z the protons form a part of it. (B) The radius of the core is smaller than the radius of the maximum of $|r\psi|^2$ for the $1i_{13/2}$ neutrons when $Z\sim 80$ and the $1h_{11/2}$ neutrons when $Z\sim 50$. (C) Within the core the neutrons with higher L move somewhat as hypothesized by Weisskopf; outside the core neutrons move essentially as free particles. (D) The density of the core is approximately constant.

The second part of (C) is hardly a hypothesis, since on a sphere of radius $1.5\times 200^{1/3}\times 10^{-13}$ cm one can arrange 14 neutrons at distances of $\sim 0.83\times 10^{-13}$ cm from each other. The jump in the SIS at $N=126$ is explicable as the result of adding two $1i_{13/2}$ neutrons to Pb^{208} to form Pb^{208} and two $2g_{9/2}$ neutrons to Pb^{208} to form Pb^{210}. Taking the radius to be $\hbar/(Mmc^2)^{1/2}$ the centrifugal potential barrier, B, for i neutrons is 21 mc^2 and the neutron density of an i neutron falls off by a factor 1/2.7 in a fractional radius change $\Delta r/r\sim 1/13$. For g neutrons $B=10$ mc^2 and $\Delta r/r\sim 1/9$. The ratio of surface thicknesses affected is $\sim(21/10)^{1/2}=1.45$ on the JWKB approximation. The agreement of this number with the observed ratio 1.5 in the SIS of the (210−208)/(208−206) differences is probably fortuitous but there is seen to be no difficulty in accounting for the observed magnitude of the effect. For $N=82$, $B\sim 20$ mc^2 for an h neutron and $\Delta r/r\sim 1/11$. The ratio of core thicknesses affected by h and by f neutrons is $\sim(20/12)^{1/2}=1.58$. It should be remarked that if the $f_{7/2}$ neutrons were to have a maximum of their radial density distribution slightly inside the core, a much larger ratio would result; the neutron density at the core surface and the core thickness affected would both be larger. The observed jump in the SIS on closing $N=82$ corresponds to a factor ~ 4. The existence of further anomalies close to $N=90$ suggests that the above explanation must be combined with other considerations, and there is a strong suggestion[5] of the participation of the effect of deviations from spherical symmetry for such nuclei. It is not intended, therefore, to explain all of the anomalies as an effect of a change in the penetrability of the core to the neutron wave function. The fact that the calculated isotopic shift is usually larger than the observed fits with the proposed outlying character of the $1i_{13/2}$ shell for $N=126$; the SIS in most of the isotopes Pb, Hg, Tl has presumably to do with the addition of i neutrons and the usual calculations assume a uniform density model of the nucleus, overestimating the expected effect. The general possibility of such a connection has already been noted by Kopfermann. The considerations on the effect of the centrifugal barrier presented above increase the probability of this view. For stable elements with $Z\cong 50$, the above picture when combined with the Bethe-Levinger-Courant view[6] of $\gamma-n$ and $\gamma-p$ reactions gives an increase in $\sigma(\gamma-n)/\sigma(\gamma-p)$ for these elements in comparison with the value of this quantity for lighter elements.[7] A proton in the nuclear core has to move through an envelope of neutrons before emergence, so that there results an increased probability of neutron emission as a result of collisions.

An obvious objection to the explanation of irregularities in the SIS is found in the fact that the spin of Pb^{207} is 1/2 and that this value cannot be explained as the spin of the $i_{13/2}$ shell with one missing neutron. On the other hand this objection disappears if one supposes that in Pb^{207} a neutron from an inner shell, perhaps the $3s_{1/2}$ shell, has been promoted to the $1i_{13/2}$ shell. The observed direction of staggering of the SIS could then be thought of as being partially caused by a decrease in nuclear volume produced by promoting the neutron from a penetrating to an external orbit. Since there is another way[8] of explaining odd-even SIS staggering, a quantitative consideration appears to be too difficult at this time.

It is desired to acknowledge a helpful discussion with Maurice Goldhaber regarding the plausibility of postulating the $1i_{13/2}-2g_{9/2}$ competition.

* Assisted by the joint program of the ONR and AEC.
[1] V. Weisskopf, Science **113**, 101 (1951.)
[2] P. Brix and H. Kopfermann, Festschrift Akad. Wiss. Göttingen, Math.-physik. Kl., 17 (1951).
[3] Brix, Buttlar, Houtermans, and Kopfermann, Nachr. Akad. Wiss. Göttingen, Math.-physik. Kl., Nr. 7 (1951). The writer would like to express his indebtedness to Professor H. Kopfermann for the opportunity of seeing the results before their publication.
[4] T. Schmidt, Z. Physik **106**, 358 (1937).
[5] P. Brix and H. Kopfermann, Z. Physik **126**, 344 (1949). Considerations regarding supplementary considerations have been discussed by Breit, Arfken, and Clendenin, Phys. Rev. **78**, 390 (1950).
[6] J. S. Levinger and H. A. Bethe, Phys. Rev. **78**, 115 (1950); see especially p. 128.
[7] H. Wäffler and O. Hirzel, Helv. Phys. Acta **21**, 200 (1948); G. Friedlander and M. L. Perlman, Phys. Rev. **74**, 442 (1948); **75**, 988 (1949); J. Halpern and A. K. Mann, Phys. Rev. **83**, 370 (1951); A. K. Mann and J. Halpern, Phys. Rev. **82**, 733 (1951).

jj-Coupling in Nuclei

B. H. FLOWERS*
Department of Mathematical Physics, The University, Edgbaston, Birmingham, England
(Received February 21, 1952)

ACCORDING to the Mayer-Jensen spin-orbit coupling shell model of nuclear structure,[1,2] the states of a single nucleon moving in the average field of the rest of the nucleus are defined by the quantum numbers $nljm$, the degeneracy in j being destroyed by strong spin-orbit forces. One is, therefore, led to investigate the splitting of the states of the nuclear configuration $(l_j)^N$ under the influence of central forces considered as a perturbation.

It can be shown[3] that, if forces are of sufficiently short range, the energies of configurations of maximum isotopic spin (i.e., those consisting of neutrons only, or of protons only) may to a fair degree of approximation be given in terms of the eigenvalues of Casimir's operator[4] for the group of symplectic transformations which leave invariant the form

$$\sum_{m=-j}^{j}(-1)^{m-\frac{1}{2}}\phi_1(m)\phi_2(-m),$$

representing the zero-order eigenfunction of two particles having resultant $J=0$. In this way, a classification of states is obtained[5] according to their seniority s, defined in analogy with Racah[5] as being the smallest value of N for which a state of given symplectic symmetry appears.

With short-range forces of arbitrary exchange nature (provided they are attractive for the ^1S interaction of two like nucleons) the lowest state in this approximation will have $s=0$ or 1 according as N is even or odd. From this, it follows immediately that the lowest level of the configuration $(l_j)^N$ has $J=0$ or $J=j$ according as N is even or odd, as found empirically by Jensen *et al.*,[1] and Mayer,[2] and verified to be so in a number of cases by Mayer[6] for a contact interaction.

Using the powerful group-theoretical methods of Racah[7] and of Jahn[8] the wave functions, properly antisymmetrized and classified according to seniority, have now been obtained for all the states of the configurations of 2, 3, and 4 particles of a given kind, neutron or proton, for $j=3/2$, 5/2, and 7/2. (The work is being extended to 5 and 6 particles in special cases, and to $j=9/2$.) In terms of the fractional parentage coefficients the energy matrices may be written down immediately in the form of Slater integrals.

The relative positions of levels have been studied as a function of the range of the interaction, using for definiteness Gaussian wave functions $\chi_l\sim r^l\exp[-\frac{1}{2}(r/a_0)^2]$, and a Gaussian potential $V(r)\sim\exp[-(r/a)^2]$ with a "symmetric" exchange operator, the range then being measured by a/a_0. Putting $\langle r^2\rangle_{Av}=r_0^2A^{\frac{2}{3}}$, where A is the atomic weight, and $r_0=1.4\times10^{-13}$ cm, and taking $a=2.2\times10^{-13}$ cm, one obtains for the $1d$ and $1f$ shells $a/a_0\approx0.9$ as a rough measure of the range of the force relative to the nuclear extension. However, the ordering of levels has been studied for ranges $0\leq a/a_0\leq2$, and thereby Kurath's[9] results have been confirmed and considerably extended.

There are several interesting consequences regarding the low-lying states of nuclei which it is the main purpose of this note to report. A detailed report will follow elsewhere.

1. *Even-even nuclei.* The lowest excited states of a configuration $(l_j)^N$ with even N belong to seniority $s=2$, which includes the levels $J=2, 4, \cdots, 2j-1$, in that order with $J=2$ lowest; all have even parity. This is the most likely explanation of the Goldhaber and Sunyar rule,[10] that the first excited state of even-even nuclei has $J=2$ and even parity. Recently Robinson and Madansky[11] have observed the first two excited states of Ce^{140}; these are found to have $J=2$ and 4 in accordance with the above predictions. Several other instances are also quoted by these authors.

2. *Light nuclei.* For heavy nuclei, due to the Coulomb forces, the isotopic number is large, so that neutrons and protons have different configurations each having maximum isotopic spin; for these nuclei our discussion applies so far only to the interactions within the separate configurations. On the other hand, for the light nuclei whose isotopic number is small, particularly those with $M_T=0$ or $\frac{1}{2}$, it is proper to consider configurations $(l_j)^N$ of neutrons and protons mixed. In the case of the odd-odd nuclei, for sufficiently short-range interaction the lowest state is $J=0$; but for ranges of interest, i.e., $a/a_0\gtrsim0.7$, the lowest state is $J=2j$. In any case, these two states are close in energy, and isomeric transitions are likely. It is of interest to find that both Sc^{44} and Sc^{46}, presumably with $f_{7/2}^1$ and $f_{7/2}^5$ configurations, are isomeric.[10] For the odd mass nuclei in this region similar conclusions can be reached: e.g., in the case of $d_{5/2}^3$, the lowest state is $J=5/2$ only for ranges $\lesssim0.95$, for beyond this point the state $J=13/2$ is lowest; and similarly in the case of $f_{7/2}^3$ the 19/2-state competes with the 7/2-state. The cross-over point occurs in the region of the actual range; and the complete absence of such high spins among the observed ground states raises considerable doubt whether the conditions of jj-coupling are properly established in the light nuclei with masses $\lesssim50$. The work of Jahn[8] and the present author[12] on the other hand, shows that the correct spin values for light nuclei are obtained without ambiguity in LS-coupling, assuming small spin-orbit coupling. The transition point presumably lies in the f-shell, in the region of magic number 28, and work continues to attempt to establish such a transition more definitely. The discovery of isomeric transitions among the odd mass nuclei in this region, with $\Delta J=6$ and no parity change, would be a decisive factor.

It is a pleasure to acknowledge the assistance of Mr. A. R. Edmonds with the numerical work involved, and the encouragement of Professor R. E. Peierls. This letter is published by permission of the Director, Atomic Energy Research Establishment, Harwell, England.

* On leave of absence from the Atomic Energy Research Establishment, Harwell, England.

[1] Hazel, Jensen, and Suess, Phys. Rev. **75**, 1766 (1949); Z. Physik **128**, 259 (1950).
[2] M. G. Mayer, Phys. Rev. **75**, 1969 (1949) and **78**, 16 (1950).
[3] B. H. Flowers, Harwell Report, A.E.R.E. T/R 713, 1951 (to be published in Proc. Roy. Soc., London).
[4] H. Casimir, Proc. Koninkl. Nederland Acad. Wetenschap. **34**, 844 (1931).
[5] G. Racah, Phys. Rev. **63**, 367 (1943).
[6] M. G. Mayer, Phys. Rev. **78**, 22 (1950).
[7] G. Racah, Phys. Rev. **76**, 1352 (1949).
[8] H. A. Jahn, Proc. Roy. Soc. (London) **A205**, 192 (1951).
[9] D. Kurath, Phys. Rev. **80**, 98 (1950).
[10] M. Goldhaber and A. W. Sunyar, Phys. Rev. **83**, 906 (1951).
[11] B. L. Robinson and L. Madansky, Phys. Rev. **84**, 1067 (1951).
[12] B. H. Flowers, Proc. Roy. Soc. (London) **A210**, 497 (1952).

Color-Center Formation in NaCl Containing Ag^+

E. Burstein, J. J. Oberly, B. W. Henvis, and Margaret White*
Crystal Branch, Metallurgy Division, Naval Research Laboratory, Washington, D. C.
(Received February 1, 1952)

NEW data on color-center formation in NaCl-Ag^+ indicate that at room temperature electrons are trapped at complex Ag^+-centers, whereas at liquid nitrogen temperature electrons are trapped primarily at single Ag^+ ions to form Ag^0 atoms.[1] The pertinent data may be summarized as follows:

(1) NaCl-Ag^+ exhibits Ag^+ absorption bands at 2090A and 2180A[2] which become narrow and decrease in magnitude when the temperature is lowered to that of liquid nitrogen. An additional band appears at 2300A for Ag^+ concentrations above 0.05 wt percent which also becomes narrow but differs from the others by increasing in magnitude with decreasing temperature.

(2) For low Ag^+ concentrations x-irradiation at room temperature yields color-center bands at 2750A, 3050A, and 3300A[3] in

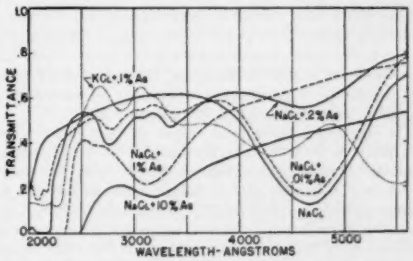

FIG. 1. Transmittance of NaCl, NaCl-Ag^+, and KCl-Ag^+ at room temperature after x-irradiation for 5 minutes at room temperature.

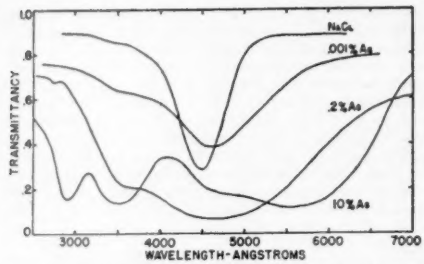

FIG. 2. Transmittancy (relative to the unirradiated crystal) of NaCl and NaCl-Ag^+ crystals at liquid nitrogen temperature after x-irradiation at liquid nitrogen temperature. The pure crystal was irradiated for 45 minutes, while the others were irradiated for only 5 minutes.

addition to the F band, M band, and V band, the latter band being superposed upon the Ag^+ bands. With increasing Ag^+ concentration the M band no longer appears, the F band weakens until it is completely suppressed, and the character of the Ag color-center bands changes (Fig. 1).[4]

(3) Optical bleaching of the F band enhances the Ag color-center bands. Illumination in the 2750A band bleaches it and strengthens the 3300A band and the F band. Similarly, illumination in the 3300A band bleaches it and strengthens the 2750A band.

(4) X-irradiation at liquid nitrogen temperature of crystals with low Ag^+ concentrations yields a strong, broad band at 4800A and a weaker band at 3700A (Fig. 2) which disappear on warming to room temperature. Illumination in the 4800A band bleaches it and also weakens the 3700A band. With increasing Ag^+ concentration the 3700A band increases relative to the 4800A band and additional bands are formed at 2900A and 5600A which are also unstable at room temperature.

The Ag^+ bands at 2090A and 2180A in NaCl-Ag^+ are most probably due to $4d^{10}-4d^9 5s$ transitions between states of the same parity which are forbidden in Ag^+ located in a perfect NaCl lattice but which become allowed as a result of interactions with lattice vibrations. The 2300A band which appears at higher Ag^+ concentrations is probably due to excitations of clusters of Ag^+'s which are allowed because the symmetry about the Ag^+ is no longer cubic.

The Ag color-center bands which are formed by room temperature x-irradiation are due to allowed transitions of centers whose optical cross sections are comparable to that of the F center. Although one might expect Ag^0 atoms at normal Na^+ sites in NaCl to be stable, it does not seem possible to ascribe any one of these bands to such centers but rather to electrons trapped at complex Ag^+ centers whose concentrations are much lower than that of single Ag^+. Thus the 2750A and 3300A bands may be the result of F centers and M centers with neighboring Ag^+. The narrow 3050A band ($\approx$0.06-ev band width) which lies close in wavelength to the $^2S_{\frac{1}{2}}-{}^2P_{\frac{1}{2},\frac{3}{2}}$ Ag^0 doublet may, on the other hand, be due to Ag^0 atoms located at large lattice defects where they are only weakly coupled to the lattice. The bands formed at high Ag^+ concentrations are probably due to one or more electrons trapped at larger aggregates of Ag^+ and vacancies.

The very broad 4800A band formed at liquid nitrogen temperature is, on the other hand, attributed to electrons trapped at single Ag^+ to form Ag^0 centers at normal Na^+ sites. The weaker 3400A band is possibly due to trapped holes since it also disappears without the appearance or strengthening of other bands when the 4800A band is bleached optically. The most obvious explanation for the absence of a Ag^0 band in NaCl-Ag^+ at room temperature is that the Ag^0 center has a small thermal ionization energy due to the considerable repulsive interaction energy and to the overlapping of the charge distributions of the relatively large Ag^0 and the surrounding ions.

* Present address, 4301 54th Place, Bladensburg, Maryland.

[1] We are indebted to R. J. Ginther, L. R. Johnson, and W. Zimmerman for the NaCl-Ag^+ and KCl-Ag^+ specimens.

[2] A. Smakula, Z. Physik **45**, 1 (1927); M. Forro, Z. Physik **56**, 534 (1929).

[3] These bands were first reported by A. Smakula, Nachr. Akad. Wiss. Göttingen, Math.-physik. Kl., 110 (1929).

[4] E. Burstein and J. J. Oberly, Ninth Annual Conference on Physical Electronics, MIT (1949), p. 44.

[5] Schulman, Etzel, and Ginther, Conference on the Electrical and Optical Properties of Ionic Crystals, University of Illinois (1951), show that the 2300A band is due to Ag^+-Ag^+ pairs.

The Mechanism of the Trichel Pulses of Short Time Duration in Air*

LEONARD B. LOEB
Department of Physics, University of California, Berkeley, California
(Received February 25, 1952)

IN 1937, O'Day[1] observed that the apparently steady negative point corona in air at atmospheric pressure consisted of regular, relaxation, oscillator-like pulses. These pulses were independently discovered and studied in detail by Trichel.[2] Later studies of Loeb, Kip, Hudson, and Bennett,[3] and of English,[4] Loeb,[5] Miller and Loeb,[6] English and Loeb,[7] and finally of Bandel[8] have done much to clarify the mechanisms. It was recognized that the build-up of the discharge owing to inherent cathode instability[9] and a conditioning prethreshold Townsend[6,7] discharge was rapid and that the quenching of the ionization creating a pulse was caused by formation of a space charge of negative ions.[2,4,6] The repeat rate of the pulses thus depends on the creation and clearing time of negative ions from some vital region.[2,6] Difficulties were encountered when English[4] showed, by synchroscope studies of carrier movements in the point-to-plane gap, that at 760-mm pressure in air the total time for ionization and space charge choking was less than 4×10^{-7} sec. Matters became even worse when photomultiplier studies of such pulses in air by English[10] revealed that the rise of luminosity occurred in less than 1×10^{-8} sec, was nearly constant for 1.5×10^{-8} sec, and declined to zero in some 3×10^{-8} sec. Thus, choking took place in less than 2.0×10^{-8} sec. Studies of the fields along the axis of the gap[11] now permit better estimates of electron avalanche intensities before the positive ion space charges materially increase the ionization. The total ion creation in Trichel pulses has been measured by English[4] as well as estimated from Trichel's[2] data. It is close to 2×10^9 ions in the case considered. Other critical dimensions of the discharge had been derived by Loeb[5] and English and have recently been confirmed by Schindler and Weissler.[12] Minimum values of the second Townsend coefficient for photoelectric liberation from a cathode γ_p, as well as for the liberation by positive ion bombardment γ_i, have been observed at higher pressures in H_2 and N_2 by Lauer.[13] Very recently, Geballe and Harrison[14] have shown that in O_2 at field strength to pressure ranges of $X/p=30$ to $X/p=70$ electrons attach to O_2 by a dissociative attachment process, yielding O^- ions with a relatively constant cross section of 30×10^{-20} cm^2. With these data it is at once possible to account for the incredibly short time scale of the observations of English.[10] Using an exemplary corona with a 0.019-cm radius point and 3.1-cm gap at 760 mm in air, which starts at 5000 volts and yields 2×10^9 ions, the data[8] are as follows. The first avalanche starting from one electron creates about 6×10^4 ions and electrons. Distances involved in ionization are of the order of 4×10^{-2} cm/sec, and electron drift velocities at the lower X/p involved one of the order of 2×10^7 cm/sec. Avalanches thus occur in intervals of 2.0×10^{-9} sec. If γ for photon action is 5×10^{-4}, a minimum conservative[13] value at high X/p, then in 10 ionizing sequences, lasting 2.0×10^{-8} sec, there will be created 3.6×10^9 ions and electrons. In this time perhaps 0.01 of the positive ions have moved into the cathode surface in a continuously increasing stream and added their secondary emission to increase

the multiplication with a γ_i of the order of 1×10^8. Thus the rate of increase in luminosity is accounted for. Assuming a relatively sudden cessation of ionization, the decline in light intensity is that caused by emission from excited states, as recombination is negligible. If the choking starts gradually and builds up rapidly, the plateau of luminosity with decreasing excitation and radiation is accounted for. With average electron energies of the order of 3 ev in the fields of $X/p\sim30$ to 70, near the end of the negative glow region, the cross section for dissociative attachment in air is 6×10^{-20} cm^2.[14] The random electron velocity is of the order of 10^8 cm/sec. At 760 mm the rate of negative ion forming encounters is 1.6×10^8 per second and the average lifetime τ of electrons is 6×10^{-9} sec. The electrons will then be reduced to $1/e$ of their number in 0.06 cm if the drift velocity in this region is 1×10^7 cm/sec at an X/p of about 26. At worst this reduction will occur at 0.12 cm with an electron velocity of 2×10^7 cm/sec. The negative ion density, with center of charge at 0.12 cm from the cathode surface, is of the order of 5×10^{13} ions/cm^3.[15] This creates a field distortion superposed on that inferred at the height of the luminosity[5] sufficient to terminate all ionization. The ionization becomes negligible within 6×10^{-9} sec after the maximum ionization is reached. This is the rate of choking required, and the observations of English are now understood. The time duration of the quenching process is given by

$$\tau=1/(\sigma\bar{c}N_1p),$$

where σ is the attachment cross section, $\bar{c}$ the average random velocity, N_1 the number of attaching molecules per cm^3 at 1-mm pressure and p the pressure in mm. No data on the change of τ with these variables exists to date except the general observations of Weissler,[15] Miller and Loeb,[6] and Bandel[8] that pulses appear to last longer at high potentials, low pressures, or low percentages of O_2. It may be added that the distortion of the field[16] by the negative ion space charge is such that after the pulse, when excitation and ionization cease near the point, there is still excitation and some ionization on the anode side of the negative ion space charge. This pushes out into the gap as the space charge clears. The resulting potential distribution accounts for the intense and extensive fan-like positive column extending to 0.15 cm which characterizes Trichel pulses in air but is absent in coronas in N_2 and in air where no pulses occur.

* Supported by ONR contract.

[1] Marcus O'Day, verbal communication at the Electronics Symposium, University of Michigan, August, 1937.
[2] G. W. Trichel, Phys. Rev. **54**, 1078 (1938).
[3] Loeb, Kip, Hudson, and Bennett, Phys. Rev. **60**, 714 (1941).
[4] W. N. English, Phys. Rev. **74**, 170 (1948).
[5] L. B. Loeb, J. Appl. Phys. **19**, 882 (1948).
[6] C. G. Miller and L. B. Loeb, J. Appl. Phys. **22**, 614 (1951); **22**, 740 (1951).
[7] W. N. English and L. B. Loeb, J. Appl. Phys. **20**, 707 (1949).
[8] H. W. Bandel, Phys. Rev. **84**, 92 (1951).
[9] L. B. Loeb, Phys. Rev. **76**, 255 (1949).
[10] W. N. English, Phys. Rev. **77**, 850 (1950).
[11] Loeb, Parker, Dodd, and English, Rev. Sci. Instr. **21**, 42 (1950).
[12] M. Schindler and G. L. Weissler, Phys. Rev. **85**, 759(A) (1952).
[13] E. J. Lauer, J. Appl. Phys. (to be published).
[14] M. A. Harrison and R. Geballe, Phys. Rev. **84**, 1072 (1951).
[15] G. L. Weissler, Phys. Rev. **63**, 96 (1943).
[16] W. Finkelnburg and S. M. Segal, Phys. Rev. **83**, 582 (1951).

Electrodynamic Corrections to the Fine Structure of Positronium

ROBERT KARPLUS AND ABRAHAM KLEIN
Harvard University, Cambridge, Massachusetts
(Received February 20, 1952)

THE accuracy of experiments that are currently being carried out to measure the separation of the ground-state doublet of positronium[1,2] has called attention to the need for a more precise theoretical treatment of the problem. Investigations reported in the literature[3-5] have considered only the effects to order α^2Ry of the exchange of one virtual quantum between the electron and the positron. Electrodynamic corrections due to the exchange of two virtual quanta and relativistic corrections to the first-order calculation, each of relative order α, may be expected to amount to an appreciable fraction of a percent.[6]

The starting point of this investigation was an equation for the two-particle electron-positron wave function that was obtained by the obvious adaptation of Schwinger's derivation of the two-electron wave function.[6] The interaction operator appearing in this equation is formally the same as the one obtained by Bethe and Salpeter,[7] except for the occurrence of a term that describes the virtual annihilation force[8,6] between the electron and the positron.

The smallness of the fine structure effects makes it possible to treat them as perturbations on the two-particle system that is bound by the Coulomb potential.[9] Our problem is simplified by the fact that only the spin-dependent part of the perturbation energy in an S-state is needed for an evaluation of the experimentally accessible 1^3S-1^1S separation. We have, therefore, considered only the effect of the corrections on this separation.

It is possible to divide the result meaningfully into two parts: effects in which Dirac particles are always present (direct interaction) and effects that involve at least one intermediate state in which only photons are present (exchange interaction or virtual annihilation force). The former contribute an amount

$$\Delta E_1=\tfrac{1}{2}\alpha^2\mathrm{Ry}_\infty[1-\tfrac{1}{4}\alpha/\pi+\alpha/\pi]=\tfrac{1}{2}\alpha^2\mathrm{Ry}_\infty[1-\tfrac{1}{4}\alpha/\pi],$$

where the large term is the first-order effect of the Breit interaction,[9] the negative term includes relativistic and retardation corrections and the effects of the exchange of two virtual photons, and the last term represents the increase in the Breit interaction due to the anomalous magnetic moments[10] of the particles. The exchange interaction contributes

$$\Delta E_2=\tfrac{1}{2}\alpha^2\mathrm{Ry}_\infty[1-8\alpha/9\pi-4\alpha/\pi+2(1-\ln2)\alpha/\pi];$$

the large term is the first-order effect of the virtual annihilation force, the two negative terms arise, respectively, from the polarization of the vacuum by the virtual photon and from the interactions of the pair before and after the virtual annihilation, and the last term represents the contribution of two-quantum virtual annihilation. This last term, which is effective only in the singlet state, is really complex, the imaginary part corresponding to the width of the state due to the real decay rate[11]

$$(2\pi\tau)^{-1}=\alpha^3\mathrm{Ry}_\infty/h=1.28\times10^9\ \mathrm{sec}^{-1}.$$

Numerically the predicted separation is

$$\Delta E_1+\Delta E_2=(1.1666+0.8671)\times10^9\ \mathrm{Mc/sec}$$
$$=2.0337\times10^9\ \mathrm{Mc/sec}.$$

When the experiments of Deutsch are interpreted on the basis of a Zeeman effect that depends on the total magnetic moment $(e\hbar/2mc)(1+\alpha/2\pi)$ of each particle, the value of the separation obtained by him is

$$(2.037\pm0.003)\times10^9\ \mathrm{Mc/sec}.$$

Theory and experiment are thus in satisfactory agreement.

We are grateful to V. F. Weisskopf for calling our attention to this problem.

[1] M. Deutsch and E. Dulit, Phys. Rev. **84**, 601 (1951); M. Deutsch and S. C. Brown, Phys. Rev. **85**, 1047 (1952).
[2] T. A. Pond and R. M. Dicke, Phys. Rev. **85**, 489 (1952).
[3] V. B. Berestetski and L. D. Landau, J. Exptl. Theoret. Phys. (U.S.S.R.) **19**, 673 (1949). See also V. B. Berestetski, J. Exptl. Theoret. Phys. (U.S.S.R.) **19**, 1130 (1949).
[4] J. Pirenne, Arch. Sci. Phys. Nat. **28**, 233 (1946); **29**, 121, 207, and 265 (1947).
[5] R. A. Ferrell, Phys. Rev. **84**, 858 (1951) and Ph.D. thesis (Princeton, 1951). Dr. Ferrell kindly sent us a copy of his thesis.
[6] J. Schwinger, Proc. Natl. Acad. Sci. **37**, 452, 455 (1951).
[7] H. A. Bethe and E. E. Salpeter, Phys. Rev. **84**, 1232 (1951).
[8] We are indebted to Dr. E. E. Salpeter for making available to us a copy of his paper on "Mass Corrections to the Fine Structure in Hydrogen-like Atoms" prior to publication. We have found his ideas very helpful in our work.
[9] G. Breit, Phys. Rev. **34**, 553 (1929); **36**, 383 (1930); **39**, 616 (1932).
[10] J. Schwinger, Phys. Rev. **76**, 790 (1949).
[11] J. A. Wheeler, Ann. New York Acad. Sci. **48**, 219 (1946).

Emission of the Atmospheric Oxygen Bands in Discharges and Afterglows

LEWIS M. BRANSCOMB*
Harvard University, Cambridge, Massachusetts
(Received February 21, 1952)

THE atmospheric bands of oxygen result from an intercombination magnetic dipole transition with a probability of only 0.14 sec^{-1}.[1] Although well known in the solar absorption spectrum, this system was not observed in emission until 1947, when Kaplan[2] reported the (0, 0) and (0, 1) bands in an oxygen-enriched nitrogen afterglow. Subsequently, the bands have been produced in emission in CO-O_2 explosions,[3] in He discharge with a trace of O_2,[4] and in a high pressure glow discharge in pure O_2.[5] In addition the (0, 1) band is a prominent feature of the infrared spectrum of the night air-glow.[6,7]

Under appropriate conditions a sealed-off glass vessel containing spectroscopically pure O_2 at about 1-cm pressure will afterglow very strongly in the infrared. The afterglow spectrum from 3000 to 9100A contains only the (0, 0) and (0, 1) atmospheric bands (with heads at 7593.7 and 7685A, respectively) and a weak continuum. The rf electrodeless discharge which precedes the afterglow produces these forbidden bands with much greater intensity. This spectrum contains members of the $\Delta v=0$ progression up to $v'=4$, as well as O I lines. O I 8446.8A and the O I triplet at 7772A are very strong, indicating a high degree of dissociation of the O_2. The (0, 0) band of the direct discharge, photographed in a net exposure of about 30 minutes on a Baird two-meter grating, is shown in Fig. 1.

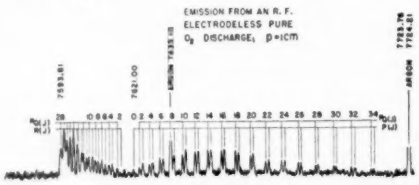

FIG. 1. The (0, 0) $^1\Sigma - {}^3\Sigma$ band of the forbidden oxygen atmospheric system produced in emission. The "rotational temperature" is 710°K.

The spectral composition and pressure requirement suggest that the energy producing the afterglow is stored in the high degree of dissociation and is released by three-body volume recombination. The "active oxygen" of the afterglow is also capable of heating to incandescence tiny flecks of metal for as long as 10 seconds in the afterglow. Because of the high probability of this metallic surface recombination, an electrodeless discharge is propitious for afterglow production.

The rotational and vibrational "temperatures" were measured in both the afterglow spectra and the direct discharge. The rotational distribution in the direct discharge follows very closely the Boltzmann formula with a "temperature" of 710°±10°K. The vibrational "temperature" is approximately the same, 670° ±80°K.[8] In the afterglow spectra the (1, 1) band does not appear on our plates, placing an upper limit on the vibrational "temperature" of the afterglow of about 450°K. Since the rotational "temperature" computed from the profile of the unresolved (0, 0) band in the afterglow is approximately room temperature (roughly 310°K), the excited oxygen molecules in the afterglow appear to attain thermal equilibrium before radiation, as would be expected from the low transition probability and the moderately high pressure.

The agreement between vibrational and rotational temperatures in the discharge and afterglow shows that many collisions occur before the excited molecule radiates. In excitation by molecule formation in three-body collisions, up to 3.5 volts of vibrational energy in the $^1\Sigma_g^+$ state must be removed before equilibrium is attained. Since vibrational energy relaxes much more slowly than rotation in O_2, we may expect the rotational temperature to agree with the gas kinetic temperature at pressures considerably lower than 1 cm Hg.

The rotational profile of the (0, 1) band of this system has been used by Meinel[6] and Dufay[7] to measure the temperature of the upper atmosphere at the altitude of the emitting layer, giving temperatures of 150°K and 130°K, respectively. The normal temperature behavior of the atmospheric bands in the direct discharge and in the afterglow substantiates the interpretations of Meinel and Dufay.

* Present address: National Bureau of Standards, Washington 25, D. C.
[1] G. Herzberg, *Spectra of Diatomic Molecules* (D. van Nostrand and Company, New York, 1950), second edition, p. 278.
[2] J. Kaplan, Nature **159**, 673 (1947); Phys. Rev. **78**, 82 (1950).
[3] Herman, Hopfield, Hornbeck, and Silverman, J. Chem. Phys. **17**, 220 (1949); J. Chem. Phys. **17**, 982 (1949).
[4] R. Herman and L. Herman, Compt. rend. **229**, 931 (1949).
[5] T. Herman and C. Weniger, Compt. rend. **230**, 940 (1950).
[6] A. B. Meinel, Pub. Astron. Soc. Pacific **60**, 373 (1948); Astrophys. J. **112**, 464 (1950).
[7] J. Dufay, Compt. rend. **231**, 1531 (1950); **232**, 426 (1951).
[8] The vibrational "temperature" is estimated by comparison of the (0, 0), (0, 1), and (1, 1) band intensities. The relative transition probabilities were taken from *Computation of the Intensities of Vibrational Spectra of Electronic Bands in Diatomic Molecules (Problem Rep. No. 27)* (The Computation Laboratory, Harvard University, Cambridge, Massachusetts, 1951).

Bardeen's Theory of Superconductivity and the *f*-Sum Rule

EDWARD N. ADAMS, II
Institute for Nuclear Studies, University of Chicago, Chicago, Illinois
(Received February 25, 1952)

BARDEEN'S[1,2] derivation of the London equation depends crucially on the assumption that the effective mass of a superconducting electron is very small and that as a consequence the Landau-Peierls diamagnetism is great enough to drive the magnetic field out of the metal. It will be shown below that on Bardeen's model the Landau-Peierls susceptibility is actually paramagnetic and would not, therefore, keep out the magnetic field. Bardeen's model may be characterized briefly as follows: The very weak electron-phonon interaction causes the continuum of levels at the top of the Fermi sea to split up into narrow bands. The superconducting electrons are a group of electrons which occupy the lowest of these bands. Rough arguments indicate that for at least some of these electrons the effective mass is very small. Bardeen argues that for superconductors the effective masses are so small that the Landau-Peierls diamagnetism becomes great enough to keep the magnetic field from penetrating the metal appreciably. In this case the wave functions of the electrons are not disturbed on account of the field and an old argument of London shows that the London equation is valid.

The Landau-Peierls susceptibility[3] can be written as

$$\chi = -\tfrac{1}{3}\mu_B{}^2 n(\zeta)\langle \alpha_{xx}\alpha_{yy} - \alpha_{xy}{}^2\rangle. \tag{1}$$

Here μ_B denotes the Bohr magneton, $n(\zeta)$ the density of energy levels at the Fermi surface, $\alpha_{\mu\nu}$ the ratio of the electron mass to the $\mu\nu$ component of the effective mass tensor, and the angular brackets denote an average over the free Fermi surface. x and y are directions perpendicular to the magnetic field. In a normal metal, for which the value of the angular bracket is of the order of unity, Eq. (1) gives a susceptibility of the order 10^{-6}. Therefore, in order to get a susceptibility large enough to keep the magnetic field out of the metal it is necessary that the angular bracket be of the magnitude 10^6 or larger, and positive. For the case of a weak interaction it is possible to express $\alpha_{xy}{}^2$ in terms of α_{xx} and α_{yy} and thus to obtain a simpler expression for the susceptibility. The relations we need can be obtained from the following two equations,[4] which are a consequence of the commutation relations among the p^μ and x^ν operators for the electron.

$$\Sigma_{n'}\, p_{nn'}{}^\mu p_{n'n}{}^\nu = \Sigma_{n'}\, p_{nn'}{}^\nu p_{n'n}{}^\mu, \tag{2a}$$

$$\Sigma_{n'}{}' \,(1/m[E_{n'}-E_n])(p_{nn'}{}^\mu p_{n'n}{}^\nu + p_{nn'}{}^\nu p_{n'n}{}^\mu) = \delta_{\mu\nu} - \alpha_{\mu\nu}{}^{(n)}. \tag{2b}$$

Equation (2b) is just a slightly generalized form of the f sum rule for metals. Suppose that the potential is very weak and that n denotes the lowest energy band. Then there is only one important term in each of the sums (2), *viz.*, the term in which n' denotes the first excited band. In this case one easily obtains from Eqs. (2)

$$2|p_{nn'^x}|^2 = m[E_{n'} - E_n](1 - \alpha_{xx}^{(n)}), \tag{3a}$$

$$2|p_{nn'^y}|^2 = m[E_{n'} - E_n](1 - \alpha_{yy}^{(n)}), \tag{3b}$$

$$2p_{nn'^x}p_{n'n}{}^y = 2p_{nn'^y}p_{n'n}{}^x = -m[E_{n'} - E_n]\alpha_{xy}^{(n)}. \tag{3c}$$

Multiplying (3a) by (3b) one gets the square of (3c) or

$$[\alpha_{xy}^{(n)}]^2 = (1 - \alpha_{xx}^{(n)})(1 - \alpha_{yy}^{(n)}). \tag{4}$$

From (4)

$$\alpha_{xx}\alpha_{yy} - \alpha_{xy}{}^2 = \alpha_{xx} + \alpha_{yy} - 1. \tag{5}$$

The left-hand side of Eq. (5) is just the quantity which occurs in the angular brackets of Eq. (1). It is clear from Eqs. (3) that if α_{xx} and α_{yy} are to have magnitudes much greater than unity, they must be negative numbers. In that case, however, the right-hand side of Eq. (5) is surely negative. It follows that Eq. (1) gives a paramagnetic and not a diamagnetic susceptibility.

The outcome of the argument is not changed if one takes into account the fact that the band in question is not the lowest band, on account of there being inner shell bands. One needs only to modify Eq. (4) by adding to each unity occurring therein an appropriate positive number of order of magnitude unity. The key point is that almost all of the contribution to the f sum comes from the term with the small energy denominator. Since the electron-phonon interaction is very much weaker than the interaction which binds the electron in the lattice, the energy denominator for a transition between two electron-phonon bands will be many orders of magnitude smaller than for a transitions between two normal lattice bands and the contribution to the f sum correspondingly larger. Thus the only important point for the argument is that the superconducting electrons occupy the lowest electron-phonon band.

In Bardeen's discussion of the susceptibility there is an indication[5] that perhaps his model requires very many electron-phonon bands to be occupied. In such a case the argument given above would not be relevant to Bardeen's theory. A careful examination of the papers[1,2] shows that Bardeen did not adopt this feature for his model but made all calculations on the assumption that the superconducting electrons are in a single band. It is concluded, therefore, that the calculations presented here do apply to Bardeen's theory and constitute a serious objection to the theory in its present form.

[1] J. Bardeen, Phys. Rev. **81**, 829 (1951).
[2] J. Bardeen, Phys. Rev. **80**, 567 (1950).
[3] R. Peierls, Z. Physik **80**, 763 (1933).
[4] E. N. Adams, II, Phys. Rev. **85**, 41 (1952). Equation (2b) above follows at once from Eq. (45a) of the reference.
[5] The remark referred to here follows Eq. (2.5) of reference 1.

Magnetic Moment of Se^{77}*

S. S. Dharmatti and H. E. Weaver, Jr.
Stanford University, Stanford, California
(Received February 29, 1952)

EMPLOYING a new nuclear induction apparatus which has higher sensitivity and stability than the one used in previous measurements and which will be described later, signals of Se^{77} were detected in a 12-molar solution of H_2SeO_3. Resonances of Se^{77} with an amplitude approximately seventy times that of the random noise were observed in SeO_2 and H_2SeO_3 dissolved in water without the addition of paramagnetic ions.

A comparison of the resonant frequency of Se^{77} with that of Na^{23} gave the result

$$\nu(Se^{77})/\nu(Na^{23}) = 0.72193 \pm 0.00002. \tag{1}$$

With the known[1] magnetic moment of Na^{23} and the fact that the spin of Se^{77} is $\frac{1}{2}$,[2] the sign and value of the magnetic moment were found to be

$$\mu(Se^{77}) = +0.53326 \pm 0.00005. \tag{2}$$

The fact that nuclear induction resonances of selenium were observed in solutions not containing additional paramagnetic ions suggests the possibility of the existence of some monatomic selenium in acid solutions[3] in a manner similar to acid solutions of tellurium.[4] The relatively narrow observed lines can possibly be attributed to the slight catalytic action of such monatomic and paramagnetic atoms.

We would like to express our gratitude to Professor F. Bloch for his continued interest in our work.

* Assisted by the joint program of the AEC and ONR.
[1] F. Bitter, Phys. Rev. **75**, 1326 (1949).
[2] S. P. Davis and F. A. Jenkins, Phys. Rev. **83**, 1269 (1951).
[3] *Textbook of Inorganic Chemistry*, edited by J. Newton Friend (Charles Griffin and Company, Ltd., London, 1931), Vol. VII, Part II, p. 290.
[4] S. S. Dharmatti and H. E. Weaver, Phys. Rev. **84**, 843 (1951).

The Mass Difference $Mg^{23} - Na^{23}$

H. B. Willard, J. D. Kington, and J. K. Bair
Oak Ridge National Laboratory, Oak Ridge, Tennessee
(Received February 27, 1952)

PROTONS from the 5.5-Mev electrostatic accelerator at Oak Ridge were used to measure the $Na^{23}(p, n)Mg^{23}$ threshold. White, Delsasso, Fox, and Creutz report this to be 4.78 ± 0.3 Mev.[1]

A thin metallic layer of sodium was evaporated (in place) on the 15-mil sheet tantalum backing of a rotating target. The neutrons emitted in the forward direction were detected by a threshold counter similar to that described by Bonner and Butler.[2] The proton energy was determined from a magnet current calibration curve based on well-known[3-5] resonances in the gamma-ray yield of the proton bombardment of fluorine. This method, described elsewhere,[6] is believed accurate to 0.2 percent. As an additional check, the $B^{11}(p, n)C^{11}$ threshold at 3.015 ± 0.003 Mev[7] and the $F^{19}(p, n)Ne^{19}$ threshold at 4.253 ± 0.005 Mev[6] were measured in the same magnet cycle of one of the present runs.

Figure 1 shows the $Na^{23}(p, n)Mg^{23}$ yield in the forward direction (uncorrected for the response of the neutron counter). The average value of the threshold for six magnet cycles on two freshly evaporated sodium targets is 5.091 ± 0.010 Mev; therefore, the Q value is -4.88 Mev. Taking the $n - H^1$ mass difference to be

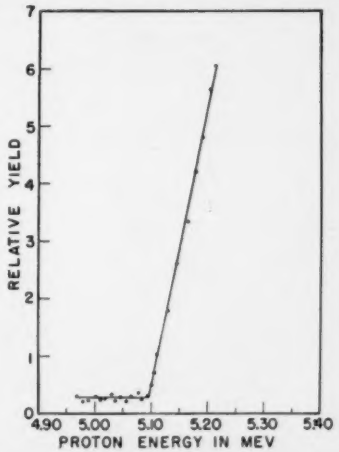

FIG. 1. The threshold for the $Na^{23}(p, n)Mg^{23}$ reaction.

0.782 Mev,[6] we find that $Mg^{23}-Na^{23}=0.0044_0$ amu. The positron from the disintegration of Mg^{23} has been observed with a maximum energy of 2.82 Mev.[1] The present threshold determination gives a maximum disintegration energy of 3.08 Mev.

[1] White, Delsasso, Fox, and Creutz, Phys. Rev. **56**, 512 (1939).
[2] T. W. Bonner and J. W. Butler, Phys. Rev. **83**, 1091 (1951).
[3] Chao, Tollestrup, Fowler, and Lauritsen, Phys. Rev. **79**, 108 (1950).
[4] A. H. Morrish, Phys. Rev. **76**, 1651 (1949).
[5] Herb, Snowdon, and Sala, Phys. Rev. **75**, 246 (1949).
[6] Willard, Bair, Kington, Hahn, Snyder, and Green (to be published).
[7] Richards, Smith, and Browne, Phys. Rev. **80**, 524 (1950).
[8] Li, Whaling, Fowler, and Lauritsen, Phys. Rev. **83**, 512 (1950).

Unified Description of Leptons

V. Votruba and M. Lokajíček
Institute for Theoretical Physics, Charles University, Prague, Czechoslovakia
(Received January 3, 1952)

In a recent paper by one of the authors[1] attention was called to the possibility that the lepton (in contrast to the nucleon) is a particle with isotopic spin 1.

Our first aim in the present paper is to show that the description of this lepton can be made independent of any special choice of the representation of the γ's and ξ's. We start with three independent Dirac fields ψ_a ($a=1, 2, 3$), which satisfy the following equations

$$\begin{aligned}&[\gamma_\mu(\partial_\mu+ieA_\mu/\hbar c)+\kappa]\psi_1=0,\\&[\gamma_\mu(\partial_\mu-ieA_\mu/\hbar c)+\kappa]\psi_2=0,\\&\gamma_\mu\partial_\mu\psi_3=0.\end{aligned}\tag{1}$$

These equations can be written in a compact form

$$[\gamma_\mu(\partial_\mu+ieA_\mu\xi_3/\hbar c)+\kappa\xi_3{}^2]\varphi=0,\tag{1'}$$

where ξ_3 is the third of the three Hermitian matrices

$$\xi_1=2^{-\frac{1}{2}}\begin{pmatrix}0&0&-1\\0&0&1\\-1&1&0\end{pmatrix},\quad \xi_2=2^{-\frac{1}{2}}\begin{pmatrix}0&0&-i\\0&0&-i\\i&i&0\end{pmatrix},$$
$$\xi_3=\begin{pmatrix}1&0&0\\0&-1&0\\0&0&0\end{pmatrix},\tag{2}$$

which satisfy the Duffin-Kemmer relations.

Now the "positron" field ψ_2 must be charge-conjugate to the "electron" field ψ_1, and the "neutrino" field ψ_3 must be self charge-conjugate. These conditions can be written in a compact form

$$\varphi'=C\bar{\varphi}=D\varphi,\tag{3}$$

where $\bar{\varphi}=\varphi^\dagger\gamma_4$, and C and D are matrices satisfying the relations

$$\begin{aligned}&C\gamma_\mu{}^T=-\gamma_\mu C,\quad C^T=-C,\quad C^\dagger=C^{-1},\\&D\xi_i=-\xi_i{}^TD,\quad D^T=D,\quad D^\dagger=D^{-1}.\end{aligned}\tag{4}$$

In the special representation (2) of the ξ's we obtain

$$D=\begin{pmatrix}0&1&0\\1&0&0\\0&0&1\end{pmatrix}.$$

The condition (3) is obviously compatible with (1').

The commutation relations of the field quantities can be written in either of the following three mutually equivalent forms

$$\begin{aligned}&\{\varphi_{a\alpha}(\mathbf{x}),(\bar{\varphi}(\mathbf{x}')\gamma_4)_{b\beta}\}=\delta_{ab}\delta_{\alpha\beta}\delta(\mathbf{x}-\mathbf{x}'),\\&\{\varphi_{a\alpha}(\mathbf{x}),\varphi_{b\beta}(\mathbf{x}')\}=-D_{ab}{}^\dagger(\gamma_4C)_{\alpha\beta}\delta(\mathbf{x}-\mathbf{x}'),\\&\{\bar{\varphi}_{a\alpha}(\mathbf{x}),\bar{\varphi}_{b\beta}(\mathbf{x}')\}=D_{ab}(C^\dagger\gamma_4)_{\alpha\beta}\delta(\mathbf{x}-\mathbf{x}').\end{aligned}\tag{5}$$

Equations (1'), (3), (4), and (5) are invariant with respect to the unitary transformation

$$\xi_i'=U\xi_iU^\dagger,\quad \varphi'=U\varphi,\quad D'=U^{\dagger T}DU^\dagger.\tag{6}$$

The description of the lepton is therefore independent of any special representation of the ξ's.[2]

The equations of motion (1') follows from the Hamiltonian

$$H=\tfrac{1}{2}\hbar c\int\bar{\varphi}[\gamma_j\partial_j+\kappa\xi_3{}^2+(ie/\hbar c)A_\mu\gamma_\mu\xi_3]\varphi d\mathbf{x}.$$

The charge and current density is $s_\mu=-\frac{1}{2}iec\bar{\varphi}\gamma_\mu\xi_3\varphi$.

The three charge-states of the lepton are to be defined as eigenstates of the operator ξ_3. The total energy of a free lepton field is then easily shown to be the sum of the (positive) energies of the electrons, positrons, and neutrinos, whereas the total charge is the algebraic sum of the charges of electrons and positrons.

The Hamiltonian of the interaction between the leptons and the nucleons is to be expected in the form

$$g\int(\bar{\Psi}\tau\Lambda\Psi)(\bar{\varphi}\xi\Lambda\varphi)d\mathbf{x},\tag{7}$$

where Λ is one of the five covariant Dirac operators. Now from (5), (3), and (4)

$$\begin{aligned}\bar{\varphi}(\mathbf{x})\xi_i\Lambda\varphi(\mathbf{x})&=\bar{\varphi}(\mathbf{x})(D\xi_iD^{-1})^T(C^{-1}\Lambda C)^T\varphi(\mathbf{x})+\delta(0)\mathrm{Sp}\xi_i\mathrm{Sp}(\gamma_4\Lambda)\\&=-\bar{\varphi}(\mathbf{x})\xi_i(C^{-1}\Lambda C)^T\varphi(\mathbf{x}),\end{aligned}$$

the latter because $\mathrm{Sp}\xi_i=0$. On calculating $(C^{-1}\Lambda C)^T$ one gets

$$(C^{-1}\Lambda C)^T=\begin{matrix}+\Lambda & \text{for} & \Lambda=1,\ \gamma_5,\ \gamma_\mu\gamma_5,\\-\Lambda & \text{for} & \Lambda=\gamma_\mu,\ \sigma_{\mu\nu}\end{matrix}$$

and therefore (7) vanishes identically in the cases of scalar, pseudoscalar, and pseudovector coupling.[3,4]

A unified description of the π-mesons ($\pi^\pm$, π^0) can be given on quite similar lines (using the Duffin-Kemmer β-formalism instead of the Dirac γ-formalism).

[1] V. Votruba, Phys. Rev. **85**, 141 (1952); cited as "*A*" below. This paper contains some errors which will be corrected in the present paper (see footnote 3 below). These corrections, however, do not invalidate the proposed picture of the lepton.

[2] It is easy to find the matrix U which transforms the representation (2) of the ξ's into the representation used in *A*. In this latter representation $D'=1$ and all the three fields ψ_a' become self charge-conjugate.

[3] This point was erroneously stated in *A*. The transcription of (*A*, 1) into (*A*, 1') has been verified, primarily, in the case of vector coupling and then unsoundly oversimplified to the case of scalar coupling. Scalar coupling between the leptons and the nucleons could be introduced in the form $(\boldsymbol{\tau}\cdot\boldsymbol{\xi}\psi)$ which is an awkward form, however. The sign of ξ_3 in (*A*, 7) and also the sign of the right-hand sides in the commutation relations of the λ's should be positive.

[4] *Addendum:* The true charge-conjugate lepton-field φ^s, for which $s_\mu(\varphi^s)=-s_\mu(\varphi)$, is generally given by $\vartheta\cdot\varphi$, where ϑ is a unitary and Hermitian matrix satisfying the relations $\vartheta^\dagger\xi_i\vartheta=(-1)^i\xi_i$ and transforming like the ξ's under (6). It is easily found that $\vartheta=1-\xi_1{}^2+\xi_2{}^2-\xi_3{}^2$. Only in the representation (2) is $\vartheta=D$ and $\varphi^s=\varphi'$. We are indebted to Professor G. Wentzel for valuable comments on our paper.

CONTENTS

THE PHYSICAL REVIEW

New Kind of Radio Propagation [illegible]
Bowen, G. F. Mc[illegible]

Magnetic Resonances in a [illegible]

Effects of Configuration [illegible]

Angular Distribution of [illegible]
Isotope Effect in [illegible]

Beta- and Gamma-Radiation [illegible]
Stars Initiated by High Energy [illegible]

Production of Positive Mesons by [illegible]
Further Results on the [illegible]

Measurement of the [illegible]

Shapes of Negative Beta-Spectra of [illegible]
Application of the Fermi Method to [illegible]

Solubility of He^3 in Liquid He^4
High Energy Collisions with the Production of Several [illegible]
Disintegration Schemes of I^{124}
Ferroelectricity and Antiferroelectricity in Ceramic [illegible]

Theoretical Estimate of the Binding Energies for the [illegible]

Superconductivity of the Isotopes of Tin
Chemical Effects in Nuclear Transformations and the Metastable Isomerism [illegible]

Letters to the Editor:

Slow Effects and Metastability in Nuclear Isomers [illegible]
Hyperfine Structure of the Spectrum of [illegible]
Relations between Spin and [illegible]
Crystal Structure of the [illegible]

$\beta-\gamma$ Polarization Correlation in [illegible]
New Transitions for the [illegible]
Role of Turbulence in the [illegible]
Thermal Conductivity of [illegible]
Radiation Chemistry of [illegible]
Short-Range Forces and [illegible]
Spectroscopic Terms of [illegible]
p-Coupling in Nuclei
Color-Center Formation in [illegible]

Mechanism of the Transformation of [illegible]
Nuclear-Isomeric Constants of the Rare Elements of [illegible]

Evolution of the Atmosphere [illegible]
Bardeen's Theory of [illegible]
Magnetic Moment of [illegible]
Mass Difference Rule [illegible]
Orbital Description of Nuclear [illegible]